

**Identification of cellular signaling events dysregulated in
Huntington's disease.**

A Thesis Submitted to the College of Graduate and Postdoctoral Studies
In Partial Fulfillment of the Requirements For
The Degree of Doctor of Philosophy
In the Department of Biochemistry
University of Saskatchewan,
Saskatoon

By
Akanksha Baharani

PERMISSION TO USE

In presenting this thesis in partial fulfillment of the requirements for the Doctoral degree in Biochemistry from the University of Saskatchewan, I agree that the Libraries of this University may make it freely available for inspection. I further agree that permission for copying of this thesis in any manner, in whole or in part, for scholarly purposes may be granted by the professor or professors who supervised my thesis work or, in their absence, by the Head of the Department or the Dean of the College in which my thesis work was completed. It is understood that any copying or publication or use of this thesis or parts thereof for financial gain shall not be allowed without my written permission. It is also understood that due recognition shall be given to me and to the University of Saskatchewan for any scholarly use of the findings described in my thesis.

Requests for permission to copy or to make other use of any material in this thesis, in whole or part, should be addressed to:

Head of the Department of Biochemistry
University of Saskatchewan
Saskatoon, Saskatchewan S7N 5E5

Dean
College of Graduate and Postdoctoral Studies
University of Saskatchewan
116 Thorvaldson Building, 110 Science Place
Saskatoon, Saskatchewan. SK- S7N 5C9
Canada

ABSTRACT

Huntington's disease (HD) is a fatal neurodegenerative disorder resulting from a CAG repeat expansion in the first exon of the gene encoding the Huntingtin protein (Htt) with physical, emotional, and cognitive symptoms. Current standard-of-care regimens for HD are limited to symptom-mitigating therapies with little potential for increasing the overall quality of life. As such, there is an imminent need for the development of more effective treatment options, efforts for which are enabled by a greater understanding of the molecular basis of disease initiation, progression, and pathology. Alterations in numerous signal transduction pathways in HD result from aberrant kinase signaling.

Protein phosphorylation is catalyzed by a class of enzymes called kinases, the cellular complement of which is referred to as its kinome. The kinases responsible for driving the fate of phosphoproteomes are central to elucidating various complex cellular events. The interactive capacity of the phosphate group makes the phosphorylated protein versatile in communicating. The study of kinome led to the development of a high throughput screening tool, peptide arrays. The arrays were exposed to lysates from cells / tissues where in the kinases from them phosphorylate the peptide spotted on the arrays. The degree of phosphorylation is measured for each spot on the array and compared to the controls thereby determining the upregulation or downregulation of signaling pathways in response to different biological treatments or conditions. The online tools used were a data analysis pipeline, Platform for Integrated, Intelligent Kinome Analysis-2 (PIIKA 2), and pathway analysis pipeline InnateDB. The kinases regulating the significantly (de)phosphorylating peptides were predicted through an online tool NetworKIN which utilized the output from PIIKA 2.

Peptide arrays were utilized to identify the dysregulated kinase signaling in a) Neural stem cells (NSC) using a previously designed array with 298 peptides b) R6/2 HD mouse model across key developmental time points using customized arrays with 1268 peptides. In an effort to investigate disease-associated changes in signal transduction activity, global patterns of kinase activity (kinome analysis) were characterized within a NSC line derived from a patient with a confirmed diagnosis of HD. As indicated by kinome analysis and independently verified by phosphorylation-specific antibodies, cytoskeletal signaling, and in particular LIMK1/cofilin/slingshot signaling, was dysregulated in HD NSC's. GSK3 β was reported as a

major upstream kinase potentially activated in the HD NSCs by NetworKIN analysis, an online tool. These changes in cytoskeletal associated signaling align with differences in dendrite formation between NSCs from HD and age-/sex-matched healthy controls (HC). Dendrites in the HD NSCs were 25% shorter relative to dendrites in control NSCs. The peptide array technique was then applied to R6/2 HD mouse model using the lysates from 8 key developmental time points (Embryonic 9 and 14; at birth; weeks 3, 4, 5, 7, 10) from both sexes. The subsequent confirmation of PI3K/AKT enhanced data transformation followed by pathway analysis revealed cytoskeletal dynamics as significantly dysregulated temporally. Changes in upstream regulators ROCK2 and PAK were prominent in the embryonic time points and LIMK1/cofilin/slingshot along with profilin showed alterations in the later time points especially the 3w and 4w, when the mutant huntingtin protein (mHtt) appears in the striatum the most affected cell type in HD brain. Collectively, these data highlight the potential role of cytoskeletal dynamics in HD pathology and shows that the targeted modulation of these signaling molecules may confer therapeutic benefit.

ACKNOWLEDGMENTS

I would like to thank the members of my committee for their invaluable suggestions and for taking the time to answer any questions. Dr. William J. Roesler for being patient and mentoring me throughout my graduate studies. Dr. Jeremy S. Lee for critically evaluating my progress and providing invaluable feedback. Dr. Darrell D. Mousseau for those long scientific discussions and sharing the same excitement for my research. Dr. Kevin E. Lukong for guidance and showing the confidence in my work. Dr. Heather L. Wilson for her amazing support and her ideas which made writing this thesis a great learning experience.

A heartfelt gratitude to Dr. Henry Daniell who always encouraged me to be brave and follow my passion. A special thank you to Dr. Zelan Wei for her unconditional support.

I would also like to thank the members of Napper Lab, for all the technical help and general comradery. I want to thank the personnel of the Dept. of Biochemistry and VIDO-InterVac for being supportive especially Cindy Thompson, Vasudevan Penugonde, Jaspreet Kaur, Deana Thunderchild, Barbara Stuckless, Maja Redekopp, Sherry Tetland, Dr. Colette Wheler, Julie Watt, Karen Labach, Shirley Lam, George Wong, Amiel Smith, Lisa Mess and Raf Jamil. Thank you Dr. Rajendra Kedlaya, Dr. Amrita Kaur and June Nichole for being so kind. I cherish the time spent with my friends and colleagues in Saskatoon especially Raghuveera Goel, Nilusha Malmuthuge, Aditya Mandapati, Sumudu Parera, Robert Brownlie, Rose Venne, Patricia Cano-Gonzales, Brenden Van Wyk, Yi Chen, Dinesh Wellawa, Elisa Martinez, Amit Gaba, Natasa Arsic, Paola Elizalde, Rahwa Osman, Kanupriya Pandey, and Soumya Sucharita.

On a more personal level, I would like to acknowledge my parents, my sisters and brothers in law for the support they have given me all these years my little nephews and niece for bringing joy in our lives. SAAVARR.

DEDICATION

This dissertation is dedicated to my parents Mr. Manohar Lal Baharani and Mrs. Laxmi Baharani.

For their endless love, support and encouragement.

TABLE OF CONTENTS

PERMISSION TO USE	i
ABSTRACT.....	ii
ACKNOWLEDGMENTS	iv
DEDICATION.....	v
TABLE OF CONTENTS.....	vi
LIST OF TABLES.....	x
LIST OF FIGURES	xi
LIST OF ABBREVIATIONS	xiv
1. REVIEW OF THE LITERATURE	1
1.1 Neurodegenerative disorder with polyglutamine repeats	1
1.1.1 CAG repeats in Huntington disease.....	1
1.1.2 Huntington disease: discovery and prevalence	4
1.1.3 Striatum: structure and function.....	5
1.1.4 Gain of function vs neurodevelopmental.....	6
1.1.5 Huntingtin protein expression and function.....	8
1.1.6 Structure of huntingtin protein and post-translational modifications on the protein	9
1.1.7 Cytoskeleton: structure and function	12
1.1.7.1 Actin.....	12
1.1.7.2 Microtubules	12
1.1.7.3 Intermediate filaments	13
1.1.7.4 Cytoskeletal abnormalities in Huntington’s disease	16
1.2 Phosphorylation mediated cellular signaling.....	18
1.2.1 Kinases.....	18
1.2.2 Kinome and phosphoproteome	19
1.3. Kinome profiling.....	19
1.3.1 Peptide arrays.....	20
1.3.2 Selection of peptide targets	21
1.3.2.1 DAPPLE	21

1.3.2.2 Peptide array design.....	22
1.3.3 Bioinformatic pipeline.....	26
1.3.3.1 Platform for Intelligent, Integrated Kinome Analysis (PIIKA 2).....	26
1.3.3.2 InnateDB.....	28
1.4 Neural stem cells in studying Huntington’s disease	29
1.5 Mouse models to study Huntington’s disease.....	30
1.5.1 R6/2 mouse model	30
1.6 Sex differences in neurodegenerative disorders	31
1.6.1 Sex differences in Huntington’s disease	32
2. HYPOTHESIS AND OBJECTIVES.....	34
2.1 Rationale and Hypothesis	34
2.2. Objectives	34
3. MATERIALS AND METHODS.....	35
3.1 Reagents and chemicals	35
3.2 Cell culture and tissue harvest	38
3.2.1 Cell culture harvest	38
3.2.2 Tissue harvest.....	38
3.2.2.1 Genotyping and PCR	39
3.2.2.2 R6/2 developmental time points for tissue harvest.....	42
3.3 Analysis of neuronal morphology by NeuroLucida 360.....	47
3.4 Peptide array technology.....	47
3.4.1 Peptide synthesis and spotting	47
3.4.2 Processing peptide array	49
3.4.3 Signal detection and bioinformatics analysis	49
3.4.3.1 Platform for Intelligent, Integrated Kinome Analysis (PIIKA 2).....	51
3.4.3.2 InnateDB.....	53
3.5 SDS-PAGE	54
3.5.1 Western blotting.....	54
3.5.2 Primary and secondary antibodies	55

3.6 NetworKIN	58
3.7 KinMAP	60
4. RESULTS	63
4.1 Human neural stem cells	63
4.1.1 Validation of peptide array targets	68
4.1.1.1 Cytoskeletal dynamics - LIMK1, Cofilin, Slingshot	69
4.1.2 NetworKIN	72
4.1.2.1 GSK3 β , MK2	73
4.1.3 KinMap	76
4.1.4 NeuroLucida 360	78
4.1.5 Discussion	80
4.2 R6/2 Huntington mouse studies	82
4.2.1 Validation of peptide array targets	82
4.2.1.1 Cytoskeletal dynamics	83
4.2.1.1.1 Rho-associated protein kinase (ROCK2)	88
4.2.1.1.2 p21 activated kinase (PAK)	92
4.2.1.1.3 Lim domain kinase (LIMK1)	97
4.2.1.1.4 Cofilin	101
4.2.1.1.5 Slingshot (SSH1L)	106
4.2.1.1.6 Profilin-1	110
4.2.1.1.7 AKT1	114
4.2.2 NetworKIN	119
4.2.3 KinMAP	119
4.2.4 Discussion	120
5. GENERAL DISCUSSION	123
5.1 Cytoskeletal dynamics dysregulated in HD NSCs and R6/2 mice	123
5.2 Limitations of kinome analysis	128
5.3 Proteome vs kinome: dysregulation in cytoskeletal dynamics	129

6. CONCLUSIONS.....	132
7. FUTURE DIRECTIONS	133
7.1 Kinome analysis of other neural tissues.....	133
7.2 Stem cells	133
7.3 Therapeutic strategies	134
REFERENCES	135
APPENDIX.....	156

LIST OF TABLES

Table 1.1 List of trinucleotide repeat disorders, genes involved, repeat size and tissues affected..	2
Table 3.1 List of reagents and chemicals.....	35
Table 3.2 Reagent supplier addresses	37
Table 3.3 List of stock solutions of chemicals/reagents.....	56
Table 3.4 List of primary antibodies used.....	57
Table 4.1 List of up regulated pathways in NSCs along with the P-values (<0.05) based on InnateDB pathway analysis.....	66
Table 4.2 List of down regulated pathways along with the P-values based on InnateDB pathway analysis.....	66
Table 4.3 List of peptides validated by Western blotting.....	68
Table 4.4 List of peptides selected for validation based on PIKA 2 output with fold changes and P-values for every time point and both sexes [male (M) and female (F)].....	85
Table 4.5 Summary of the significantly hyper- (pink) and hypo- (green) phosphorylated proteins based on Western blot results.....	118
Table 5.1 Comparative summary of the significantly hyper- (pink) and hypo- (green) phosphorylated proteins based on peptide array and Western blot results of R6/2 mouse model.....	124
Table 5.2 The percentage of peptides significantly (de) phosphorylated in the mouse and NSCs.....	126
Table 5.3 Main cytoskeletal defects observed in neurodegenerative disorders.....	131

LIST OF FIGURES

Figure 1.1 The length of CAG repeat is inversely related to the age of onset.....	3
Figure 1.2 Juvenile HD (JHD) accounts for 5-10% of all HD cases.....	4
Figure 1.3 Striatum is the major receptive component of the basal ganglia.....	6
Figure 1.4 Models of degeneration in HD.....	7
Figure 1.5 Schematic of a neuron depicting pathways dysregulated in HD.....	9
Figure 1.6 Schematic representation of Htt protein and its PTMs.....	11
Figure 1.7 The cell cytoskeleton.....	15
Figure 1.8 Schematic of neuronal structure and its cytoskeleton.....	17
Figure 1.9 DAPPLE pipeline.....	22
Figure 1.10 Overview of array design.....	23
Figure 1.11 Scanned image of a kinome microarray after incubation with cell lysate followed by staining.....	25
Figure 1.12 A general workflow of the software pipeline (PIIKA) for kinome analysis.....	27
Figure 3.1 The ovary-transplanted hemizygous female is recommended for breeding with B6CBAF1/J males.	40
Figure 3.2 Shown is the cauterized ovary on the right side (indicated by the forceps) of the mouse.....	41
Figure 3.3 Representative genotyping for HD-positive mice (lanes 1-8) and sex-determination (lanes 9-16).....	42
Figure 3.4 Timeline for peptide array analysis.....	43
Figure 3.5 Schematic of mouse brain depicting the anatomical location of the striatum.....	44
Figure 3.6 The panel shows the brain tissue harvested from different time points which were studied.....	46
Figure 3.7 Screenshot of the user interface of the DAPPLE2 web server.....	48
Figure 3.8 Kinome analysis with peptide arrays.....	50
Figure 3.9 Screenshot of the user interface of the PIIKA 2 web server.	52
Figure 3.10 Screenshot of the user interface of the InnateDB web server.....	53
Figure 3.11 Screenshot of the user interface of the NetworKIN web server.....	59
Figure 3.12 Screenshot of the user interface of the KinMap web server.....	61

Figure 3.13 Graphic representation of the Kinome tree with all families.....	62
Figure 4.1 Experimental outline.....	64
Figure 4.2 A Western blot analysis of phosphoproteins indicated the activation of cytoskeletal signalling pathways.....	70
Figure 4.2 B Schematic of actin polymerization and depolymerization.....	71
Figure 4.3A Western blot analysis of phosphoproteins confirmed the activation of specific intracellular signalling pathways revealed by NetworkKIN and it's upstream kinase.....	74
Figure 4.3B Schematic representing the microtubule stability.....	75
Figure 4.4 Dendrogram of the human kinome generated using KinMap represents the predicted kinases in HD NSCs.....	77
Figure 4.5 Neurolucida tracings of neurons in the healthy control and HD NSCs by averaging six fields to calculate relative neurite length, number of cell bodies and soma length.....	79
Figure 4.6 Molecular signaling involved in cytoskeletal organization.....	84
Figure 4.7 A Western blot analysis of the protein levels for phospho-ROCK.....	89
Figure 4.7B Western blot analysis of the protein levels for total-ROCK.....	90
Figure 4.10C Quantification of phospho-ROCK2 expression levels in brain samples of HD versus healthy control (HC) mice.....	91
Figure 4.8A Western blot analysis of the protein levels for phospho-PAK.....	94
Figure 4.8B Western blot analysis of the protein levels for total-PAK1/2/3.....	95
Figure 4.8C Quantification of phospho-PAK expression levels in brain samples of HD versus healthy control (HC) mice.....	96
Figure 4.9A Western blot analysis of the protein levels for phospho-LIMK.....	98
Figure 4.9B Western blot analysis of the protein levels for total-LIMK.....	99
Figure 4.9C Quantification of phospho-LIMK1 expression levels in brain samples of HD versus healthy control mice.....	100
Figure 4.10A Western blot analysis of the protein levels for phospho-cofilin.....	103
Figure 4.10B Western blot analysis of the protein levels for total-cofilin.....	104
Figure 4.10C Quantification of phospho-cofilin expression levels in brain samples of HD versus healthy control mice.....	105
Figure 4.11A Western blot analysis of the protein levels for phospho-SSH1L.....	107

Figure 4.11B Western blot analysis of the protein levels for t-SSH1L.....	108
Figure 4.11C Quantification of phospho-SSH1L expression levels in brain samples of HD versus healthy control mice.....	109
Figure 4.12A Western blot analysis of the protein levels for phospho-profilin.....	111
Figure 4.12B Western blot analysis of the protein levels for total-profilin.....	112
Figure 4.12C Quantification of phospho-profilin 1 expression levels in brain samples of HD versus healthy control mice.....	113
Figure 4.13A Western blot analysis of the protein levels for phospho-AKT1.....	115
Figure 4.13B Western blot analysis of the protein levels for total-AKT1.....	116
Figure 4.13C Quantification of phospho-AKT1 expression levels in brain samples of HD versus healthy control mice.....	117
Table 4.14 Summary of the significantly hyper- (pink) and hypo- (green) phosphorylated proteins based on Western blot results.....	118
Figure 5.1 Schematic representation of neuroprotective mechanisms of ER signaling.....	128
Figure 5.2 Quantitative proteomic analysis shows actin cytoskeleton pathway is enriched in HD relative to control.....	130
Figure 6.1 Schematic representation of cytoskeletal signaling resulting in neurite reduction in HD.....	132

LIST OF ABBREVIATIONS

ABP	Actin binding proteins
AKT	Protein kinase B (PKB), also known as AKT
ALS	Amyotrophic lateral sclerosis
ATM	Ataxia-telangiectasia mutated (ATM) protein
BDNF	Brain derived neurotrophic factor
CaMK	Calcium / Calmodulin-dependent Kinase
CaN	Calcineurin
CDK	Cyclin-dependent kinase
CK	Casein kinase
CNS	Central nervous system
COX17	Cytochrome c oxidase copper chaperone
CREB3	cAMP responsive element binding protein 3
DB	Database
DMEM	Dulbecco's modified eagle's medium
DMSO	Dimethyl sulfoxide
DRPLA	Dentatorubral-pallidoluysian atrophy
DSK	Dual specificity kinase
E	Embryonic
ECM	Extracellular matrix
EDTA	Ethylenediaminetetraacetic Acid
ELISA	Enzyme linked immunosorbent assay
ER	Estrogen receptor
ERK	Extra-cellular signal regulated kinase
F	Female
F-actin	Filamentous actin
FC	Fold change
G-actin	Globular actin
GDNF	Glial derived neurotrophic factor
GEF	Guanine nucleotide exchange factors

GSK3 β	Glycogen synthase kinase 3 β
HC	Healthy Control
HD	Huntington's Disease
HDAC	Histone Deacetylase
HSP	Heat shock proteins
<i>Htt</i>	Huntingtin gene
Htt	Huntingtin protein
IF	Intermediate filament
IGF1	Insulin like growth factor 1
M	Male
MAP	Microtubule associated protein
MAP2K4	Mitogen-Activated Protein Kinase Kinase 4
MAP3K14	Mitogen-Activated Protein Kinase Kinase Kinase 14
MAPK	Mitogen Activated Protein Kinase
mHtt	Mutant huntingtin
MJD	Machado–Joseph disease
MS	Mass spectrophotometry
MT	Microtubule
mTOR	Mammalian Target of Rapamycin
NES	Nuclear export signal
NSC	Neural Stem Cells
NT	No template
Ov	Ovary
P00	At birth
PBS	Phosphate Buffered Saline
PCR	Polymerase chain reaction
PEST	Proline, Glutamic/Aspartic acid, Serine, Threonine
PHOSIDA	Phosphorylation Site Database
PI3K	Phosphatidylinositol 3 kinase
PK	Protein kinase
PKA/G/C	Protein kinase A/G/C

PMSF	Phenylmethylsulfonyl fluoride
PNorm	Percentile normalization
PolyQ	Poly glutamine
p-p	Proline-proline
PP	Protein phosphatase
PPM	Metallo dependent phosphatases
PPP	Phosphoprotein phosphatases
PRD	Proline rich domain
PTEN	Phosphatase and tensin homolog deleted on chromosome 10
PTM	Post-Translational Modification
PTP	Protein tyrosine phosphatase
QNorm	Quantile normalization
ROS	Reactive oxygen species
RTK	Receptor tyrosine kinase
SBMA	Spinal-Bulbar Muscular Atrophy
SCA	Spinocerebellar ataxia
SDS-PAGE	Sodium Dodecyl Sulfate - Polyacrylamide Gel Electrophoresis
SGK	Serum and glucocorticoid induced kinase
SLC17A6	Solute Carrier Family 17 Member 6
SRY	Sex determining region on Y chromosome
SSH1L	Slingshot
ST	Striatum
STK	Serine/Threonine kinase
TK	Tyrosine Kinase
Tm	Tropomyosin
TrkB	Tyrosine kinase receptor B
vsn	Variance stabilization normalization
w	Week
WB	Western blotting

1. REVIEW OF THE LITERATURE

The main focus of this literature review are the important aspects of Huntington's disease and the kinome analysis utilized to understand the dysregulated kinase signaling.

1.1 Neurodegenerative disorder with polyglutamine repeats

Huntington's Disease (HD) is one of nine known neurodegenerative disorders (Table 1.1) with a polyglutamine (polyQ) expansion in their respective disease - causing protein (Pennuto *et al.*, 2009; Stoyas and La Spada, 2018) (Figure 1.1). HD is a progressive, autosomal dominantly inherited neurological disorder characterized by prominent motor, psychiatric, and cognitive disturbances resulting from the degeneration of striatal neurons (Haddad and Cummings, 1997). The other eight members of the CAG-polyglutamine disease family include spinal and bulbar muscular atrophy (SBMA), dentatorubral pallidoluysian atrophy, and six spinocerebellar ataxias (SCA 1, 2, 3, 6, 7, and 17) (Budworth and McMurray, 2013). All CAG - polyglutamine diseases are dominantly inherited, with the exception of SBMA, which is X-linked. The polyglutamine tract is believed to be the cause of the toxic gain of function of proteins that lead to the degeneration and death of specific neurons, mentioned in the Table 1.1. In HD striatal degeneration is the main cause of the disease process, but other structures such as the cortical and hippocampal neurons are also affected by mutant huntingtin (mHtt) (Landles and Bates, 2004). The intriguing aspect of polyglutamine disorders is that they all affect a specific subset of neuronal population, the mechanisms of which are poorly understood, which complicates studies identifying suitable therapeutic options (Cattaneo *et al.*, 2001; Fischbeck, 2001; Thomas, 2006).

1.1.1 CAG repeats in Huntington disease

The timing of onset of HD is determined by length of polyglutamine repeat. In the normal population, the *Htt* repeat size varies from 17-29. The expansion of CAG repeats beyond 39 causes the expanded polyQ sequence in the protein (Gusella *et al.*, 1983; Orr and Zoghbi, 2007). The defect in HD is the expansion of an unstable DNA segment containing polymorphic trinucleotide cytosine-adenine-guanine (CAG) repeats in the coding sequence. One copy of mHtt from either parent is sufficient to cause the disease. Repeats between 27-35 are referred to as intermediate

Table 1.1: List of CAG trinucleotide repeat disorders, genes involved, repeat size and tissues affected (Permission to use from Stoyas and La Spada, 2018).

<i>Disease</i>	<i>Gene</i>	<i>Normal (repeats)</i>	<i>Disease (repeats)</i>	<i>Neuropathology</i>
<i>Huntington's Disease</i>	<i>Htt</i>	6–35	36–250	Medium spiny neurons of striatum and cortical projection neurons
<i>Spinal and bulbar muscular atrophy</i>	<i>AR</i>	5-34	37-70	Lower motor neuron in spinal cord and bulbar region of brainstem
<i>Dentatorubral pallidoluysian atrophy</i>	<i>Atrophin-1</i>	7-35	49–88	Brainstem, cerebellar and deep midbrain structures
<i>Spinocerebellar ataxia 1</i>	<i>Ataxin-1</i>	6–44	39–83	Atrophy, gliosis and severe loss of Purkinje cells in cerebellum
<i>Spinocerebellar ataxia 2</i>	<i>Ataxin-2</i>	13–33	32–77	Purkinje and granule cells and gliosis of inferior olive and pons
<i>Spinocerebellar ataxia 3</i>	<i>Ataxin-3</i>	12–40	54–89	Spinocerebellar tract, brainstem and spinal cord
<i>Spinocerebellar ataxia 6</i>	<i>Ataxin-6</i>	4–18	19–33	Cerebellar atrophy, loss of Purkinje cells and cerebellar granule cells
<i>Spinocerebellar ataxia 7</i>	<i>Ataxin-7</i>	4–35	37–306	Retinal photoreceptors, cerebellar cortex, dentate nucleus, inferior olive and pontine nuclei
<i>Spinocerebellar ataxia 17</i>	<i>TBP</i>	25–42	43–66	Cortex, striatum and cerebellum and Purkinje cells

alleles, whereas 36-39 is incomplete penetrance and beyond 39 is referred to as complete penetrance (Chandra *et al.*, 2014). The repeat size is responsible for pathogenesis and individuals with higher repeats show earlier and more severe signs of the disease. Offspring of an HD parent have a 50% chance of inheriting the disease and there is an inverse relationship between the age of onset and the CAG repeat size (Figure 1.1). Notably a recent study pointed out that an uninterrupted sequence of CAG repeats is supposedly the most important factor in predicting the age of onset of HD (Genetic Modifiers of Huntington's Disease Consortium. Electronic address and Genetic Modifiers of Huntington's Disease, 2019; Wright *et al.*, 2019).

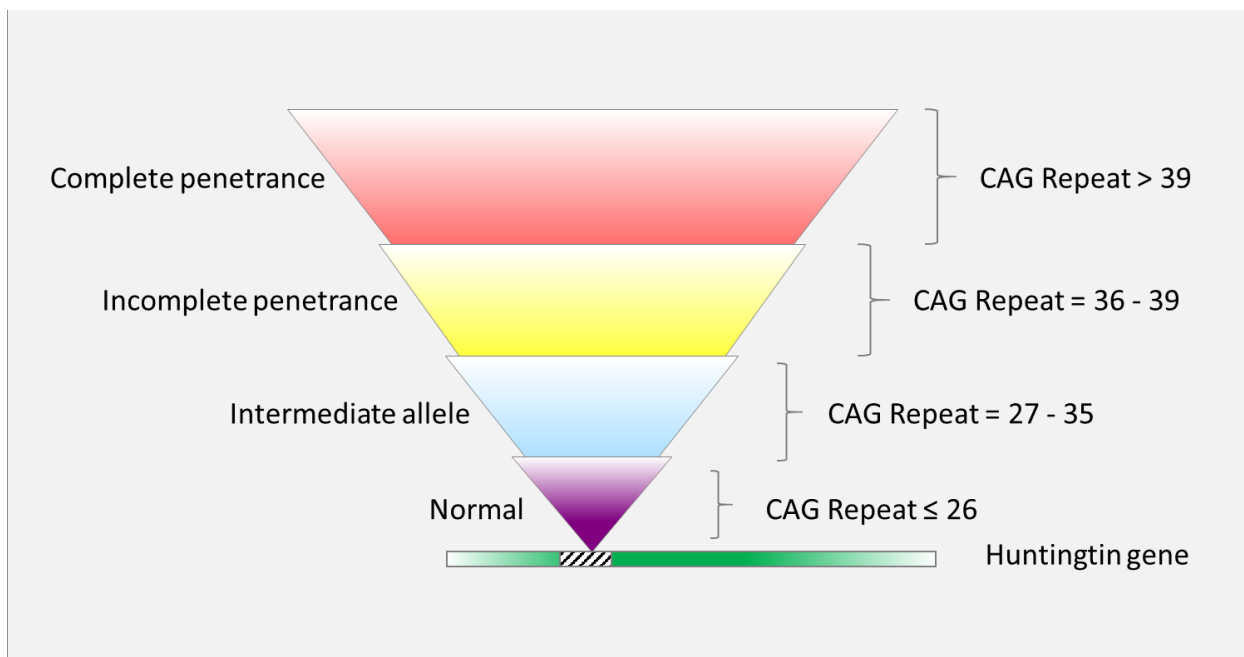


Figure 1.1: The length of CAG repeat is inversely related to the age of onset.

This is a schematic of how age of onset is determined by the number of CAG repeats. The normal gene contains ≤ 26 CAG repeats (purple). The intermediate allele contains 27-35 repeats (blue), but there is incomplete penetrance between 36-39 (yellow). HD is inevitable if the repeat size increases beyond 39 (red) (Permission to use from Chandra *et al.*, 2014).

1.1.2 Huntington disease: discovery and prevalence

Huntington's disease was first described by George Huntington an American physician, in 1872 after studying several affected individuals. As mentioned earlier HD polyQ expansion is attributed to a defect in a single gene - *huntingtin (Htt)* (Bertram and Tanzi, 2005). The median life expectancy after the onset of symptoms of the disease is approximately 21.4 years (Foroud *et al.*, 1999). Symptoms generally manifest in the fourth or fifth decade of life. Juvenile HD (JHD) accounts for 5-10% of all HD cases, and symptoms can occur even before the age of 21 (Quigley, 2017) (Figure 1.2). The polyQ repeat length is generally more than 60 in JHD, and such individuals do not survive more than 10-15 years after the onset of symptoms (Koutsis *et al.*, 2013; Quigley, 2017). The prevalence of HD is higher in the European population, compared to the East Asian population, and affects 5-7 individuals per 100,000 worldwide (Pringsheim *et al.*, 2012) and one in approximately 7,000 Canadians (<https://www.huntingtonsociety.ca/>).

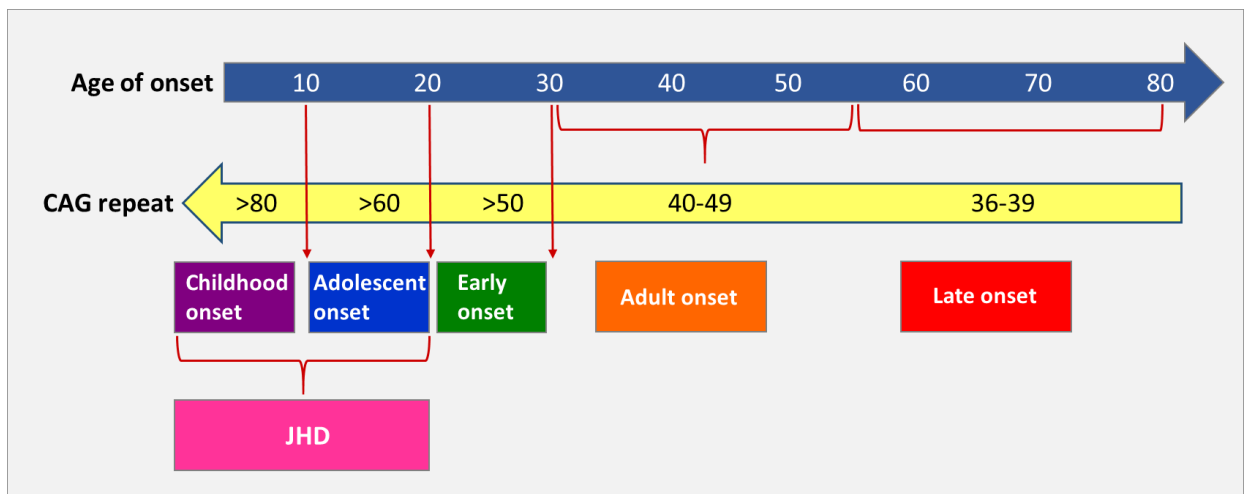


Figure 1.2: Juvenile HD (JHD) accounts for 5-10% of all HD cases.

Symptoms of juvenile HD occur in the late teens when the repeats size is more than 55. The adult and late onset of HD varies upon the CAG repeats (Permission to use from Nopoulos, 2016).

The discovery of the huntingtin gene was after more than 100 years of the first comprehensive description of adult-onset of the disease. The Huntington's Disease Collaborative Research Group (HDCRG) discovered the HD gene after 10 years of research (MacDonald *et al.*, 1993). The gene locus was mapped to chromosome 4p16.3 in the early 1980's, but it was first cloned in 1993 (MacDonald *et al.*, 1993). The disease is caused by mutation in the gene, IT15 (interesting transcript 15), containing 67 exons encoding a 3144 amino acid protein called "huntingtin" or "Htt". The mutation is an expanded trinucleotide repeat region in exon 1 of *huntingtin* (*Htt*).

1.1.3 Striatum: structure and function

HD is caused due to the degeneration of neurons in the striatum. In spite of the ubiquitous presence of Htt in neurons, it is uncertain why the striatal medium spiny neurons are principally vulnerable to the mHtt. The basal ganglia is comprised of the striatum, globus pallidus, subthalamic nuclei and substantia nigra. The circuitry of the basal ganglia is complex with multiple parallel loops that control and modulate cortical output. Striatum is the major receptive component of the basal ganglia, containing three nuclei, namely caudate, putamen and nucleus accumbens (Figure 1.3). The first to degenerate in HD is the caudate nucleus followed by putamen and then the nucleus accumbens in the later stages of the disease. The striatum has inhibitory GABAergic (Gamma aminobutyric acid) neurotransmitters. Almost 90% of the striatal neurons are medium spiny neurons that express GABA, while about 10% are interneurons. Apart from this, the striatum also widely expresses dopamine receptors. Cortico-striatal neurons and thalamo-striatal inputs are glutaminergic and afferents from the substantia nigra and the ventral tegmental area are dopaminergic (Andre *et al.*, 2010).

The primary function of the striatum is the regulation of motor movements and the organization of motor activity requires multiple synaptic inputs from the cortex, midbrain and thalamus. The striatum regulates both motor and non-motor activities such as cognition, language, emotion, and motivation.

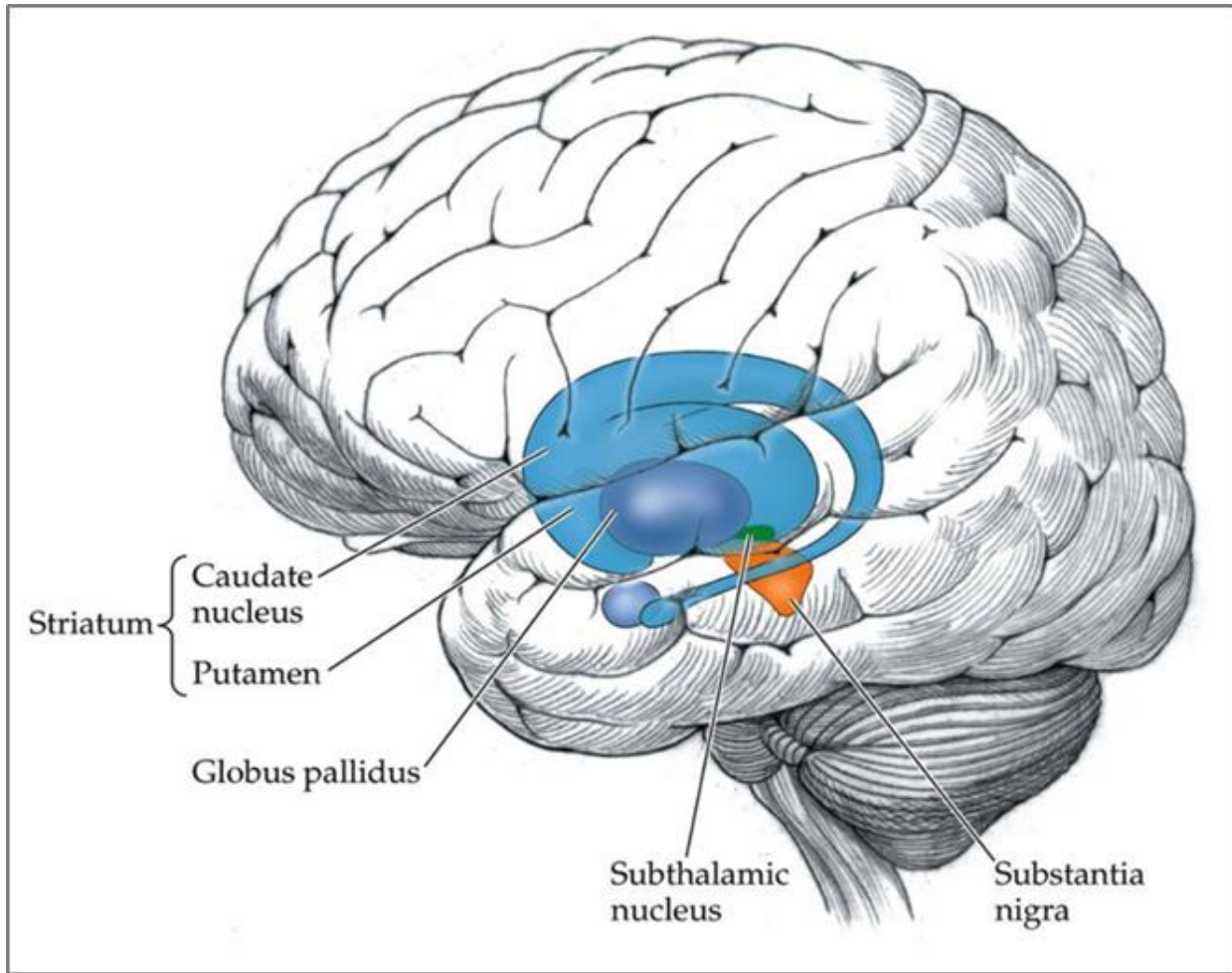


Figure 1.3: Striatum is the major receptive component of the basal ganglia.

This schematic represents the location of striatum in the human brain. Striatum consists of two structures putamen and caudate nucleus. (Permission to use from Biological Psychology 6e, Book -2010)

1.1.4 Gain of function vs neurodevelopmental disease

There are two concepts of neuronal degeneration, one the classic concept and second the neurodevelopmental concept of degeneration (Figure 1.4). The classic theory of HD is that the mHtt results in a gain-of-function and the toxicity is responsible for neuronal cell death. Conversely, the loss-of-function of normal Htt in tandem with the increase in mHtt accelerates the process. The current perception is that mHtt causes the disease due to accumulation of the toxic

protein in the cell, which ultimately leads to degeneration (Bowater and Wells, 2001; La Spada *et al.*, 1994; Orr and Zoghbi, 2007). Htt-deficient mice die early during embryonic development, while Htt +/- mice exhibit no or few neurological abnormalities therefore, emphasizing the gain-of-function as the cause of toxicity (Duyao *et al.*, 1995; Nasir *et al.*, 1995).

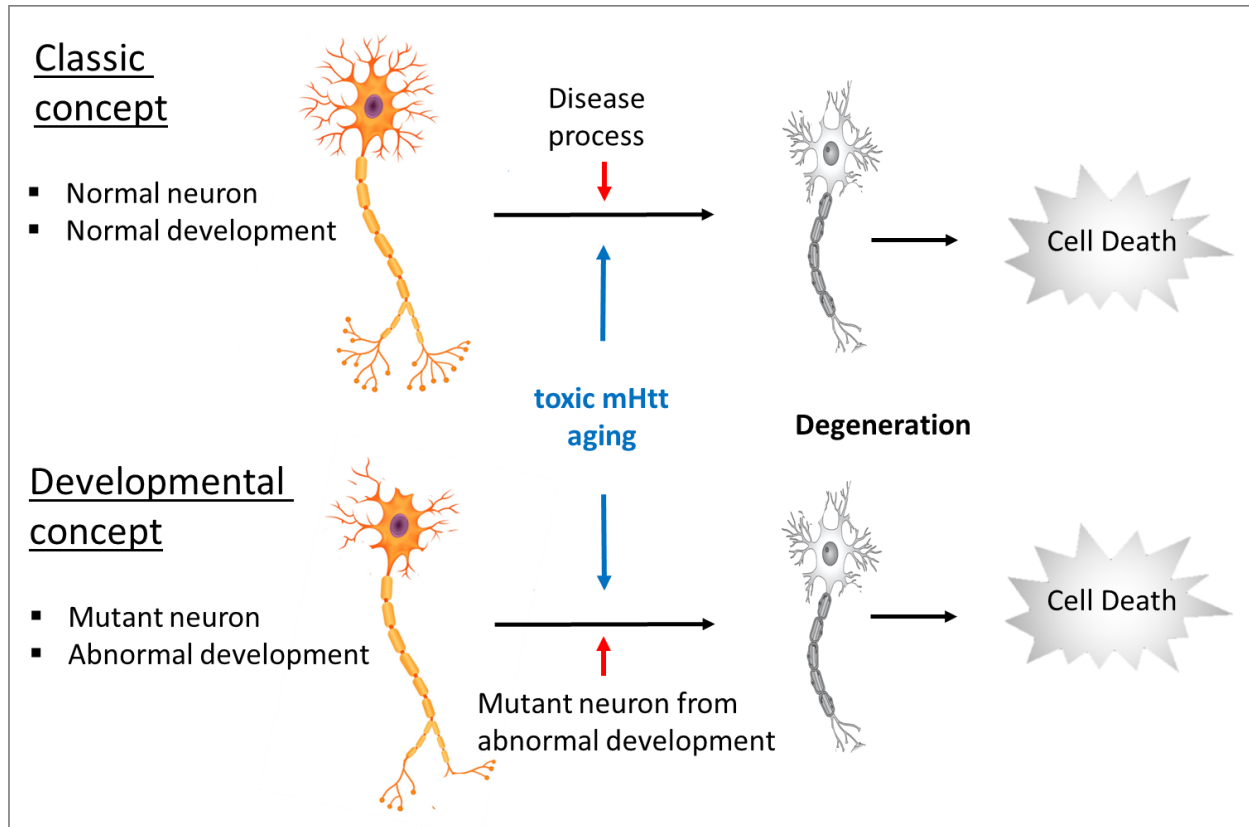


Figure 1.4: Models of degeneration in HD.

Schematic of the similarities / differences in classic and developmental concepts leading to degeneration in HD. Classic concept of degeneration suggests that normal neuron degenerates in the disease process due to the effect of mutant HD gene. Developmental concept is based on aberrant development, where the disease process begins with abnormal neuronal development, compensation leads to a mutant steady state, and degeneration occurs due to stress caused by factors such as maturation, aging, or toxic gene effects (Permission to use from Nopoulos, 2016).

Another theory is that the role of Htt in normal neural development is compromised due to mHtt, which is in itself a part of the disease process (Kerschbamer and Biagioli, 2015; Wood, 2018). The individual is able to deal with the toxic effects of the mHtt while there is sufficient normal Htt to balance the molecular changes. Eventually the balance tips in favor of mHtt due to maturation and aging processes, and this drives the faulty circuit towards degeneration. The developmental model needs further validation by experiments which are able to recapitulate the prodromal stage of the disease. Accurate identification of signaling changes in the earliest symptomatic stages of HD might lead to better biomarkers or therapeutic targets in treating HD.

1.1.5 Huntingtin protein expression and function

Htt is ubiquitously expressed but the specific vulnerability of striatal medium spiny neurons is unexplained. Htt is also expressed in various tissues outside the central nervous system (CNS) (Carroll *et al.*, 2015). A subset of the neural population is vulnerable to environmental changes and toxins, which ultimately promotes the loss of specific neuronal populations. Ring *et al.* performed a transcriptomic analysis utilizing the HD NSC model which revealed a dysregulation of genes involved in neuronal development and the formation of the dorsal striatum (Ring *et al.*, 2015), possibly suggesting the specificity of striatal degeneration. Multiple studies have shown that normal Htt is required for development and its importance in cell cycle, neuronal survival and stability (Schulte and Littleton, 2011). These functions are affected during the disease process as depicted in figure 1.5 resulting in altered protein folding, transcriptional dysregulation, aberrant interactions affecting the cytoplasmic processes and activation of apoptosis (Dayalu and Albin, 2015; Harjes and Wanker, 2003; Landles and Bates, 2004; Li and Li, 2004b). It has been shown that the Htt-deficient mice are embryonically lethal at day 8.5, whereas heterozygous mice display fewer neuronal anomalies therefore indicating its importance during development and survival (Duyao *et al.*, 1995; Nasir *et al.*, 1995; Zeitlin *et al.*, 1995). Huntingtin is a large protein that is ubiquitously expressed throughout the body, but its function still remains unknown though it has more than 200 known interacting partners (Parsons *et al.*, 2014; Schulte *et al.*, 2011; Tourette *et al.*, 2014).

with synaptic transmission, neurogenesis, apoptotic cell death, transcription, axonal transport and has 3235 interacting partners (Schulte *et al.*, 2011; Szebenyi *et al.*, 2003; Tourette *et al.*, 2014; Trushina *et al.*, 2003; Velier *et al.*, 1998). The gene consists of 67 exons and the polyQ tract [(Q(n)] begins at the 18th amino acid. In humans, the polyQ domain is followed by two proline rich regions [P(n)], whereas in mice, this number is six (Li and Li, 2004b; Saudou and Humbert, 2016) (Figure 1.6). The Htt protein contains HEAT (huntingtin, elongation factor 3, the PR65/A subunit of protein phosphatase 2A and lipid kinase Tor) repeat sequences. Each HEAT repeat is comprised of a 50 amino acid sequences and there are 28-36 such repeats in the Htt protein (Li and Li, 2004a). The HEAT repeats have a helical structure, which forms super helical structures with hydrophobic cores. These repeats are predicted to mediate various inter- and intra-molecular interactions, many of which are dissociated by proteolysis (Palidwor *et al.*, 2009). Bioinformatics analysis between amino acids 60 and 3,144 reported 16-36 HEAT repeats that are also required for protein-protein interactions (Palidwor *et al.*, 2009; Takano and Gusella, 2002; Tartari *et al.*, 2008; Warby *et al.*, 2008). Notably the domain organization of Htt by cryo-electron microscopy and their data indicated three domains, including N, C and a smaller bridge domain (Guo *et al.*, 2018). Proteins involved in microtubule dynamics possess HEAT repeats, which indicate that the repeats might play an important role in protein-protein interactions (Imarisio *et al.*, 2008). Structural studies have reported that Htt is an elongated superhelical solenoid with a diameter of ~200 Å (Colin *et al.*, 2008; Li and Li, 2004a) The N-terminal region is best studied as it contains the most vulnerable polyQ stretch and the rest of the protein is not as well characterized, which includes 66 amino acids 69 to 3,144, accounting for 97.8% of the protein (Schulte and Littleton, 2011). Apart from HEAT repeats there are four PEST - amino acids proline (P), glutamic acid (E) or aspartic acid (D), serine (S) and threonine (T) - domains containing proteolytic site (Ehrnhoefer *et al.*, 2011; Warby *et al.*, 2008). Both the wild type (WT) and mHtt contain proteolytic sites, and HD patient's show an increase in the proteolytic activity, which leads to the generation of multiple small N-terminal fractions containing polyQ repeats (Lecker *et al.*, 2006; Miller *et al.*, 2010). The N-terminal 17 amino acids are conserved in vertebrates (Tartari *et al.*, 2008). This region consists of an amphipathic α -helix which is critical for its maintenance in the endoplasmic reticulum (Atwal *et al.*, 2007). The main function for this region is the nuclear export signal (NES), which is also a target for multiple post-translational modifications (PTM) affecting the clearance of Htt and its subcellular localization (Atwal *et al.*, 2007) (Saudou and Humbert, 2016).

Htt undergoes multiple PTMs, including phosphorylation, acetylation, palmitoylation, ubiquitination and sumoylation. PTMs influence the aggregation, cellular properties, and toxicity of mHtt and therefore may contribute to HD pathogenesis (DeGuire *et al.*, 2018; Gauthier *et al.*, 2004). The Htt protein has several known phosphorylation sites as highlighted in Figure 1.6. These are well known sites for phosphorylation of the Htt protein and most are hypo-phosphorylated in the mHtt compared to the WT protein and the reduced phosphorylation has been associated with increased toxicity of the mHtt protein (Ehrnhoefer *et al.*, 2011; Ratovitski *et al.*, 2017).

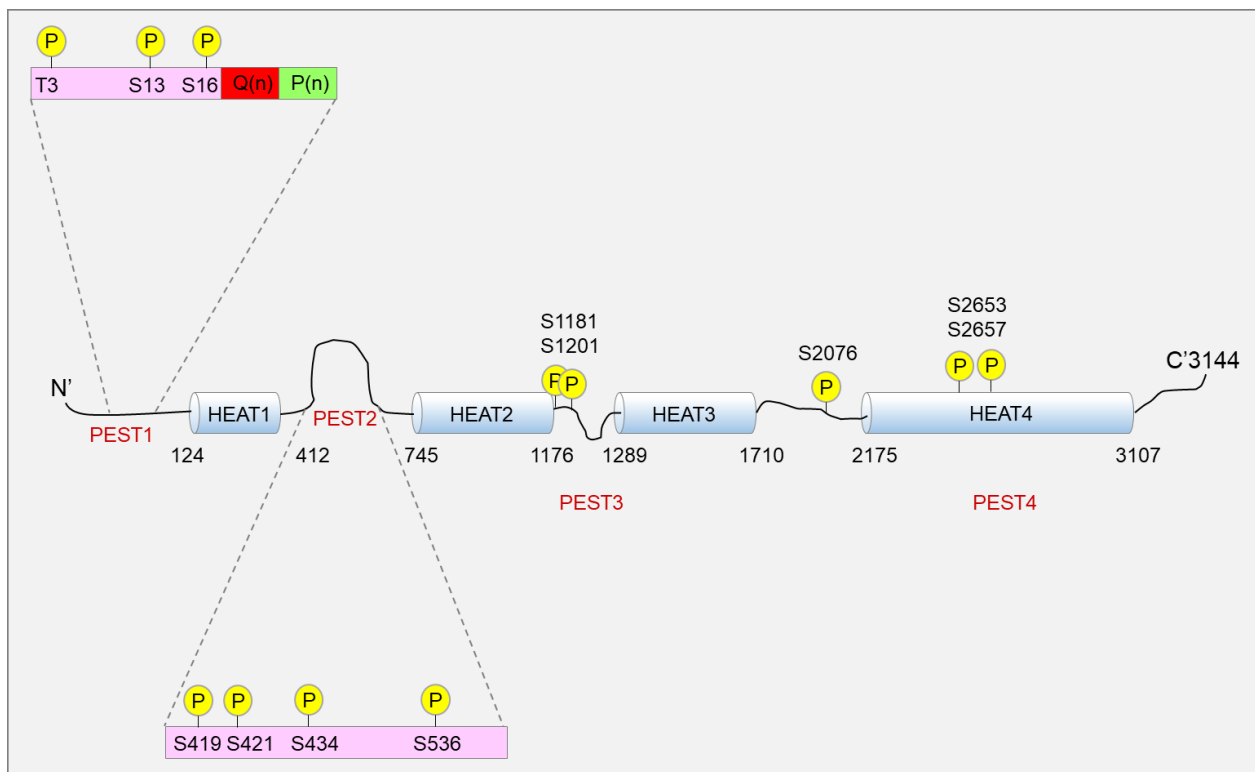


Figure 1.6: Schematic representation of Htt protein and its PTMs.

The schematic of the Htt protein represents from the N to the C terminus. Phosphorylation sites at threonine (T) or serine (S) residues are indicated in yellow. Polyglutamine tract is represented as Q(n) and polyproline as P(n). The HEAT domains are represented as blue cylindrical structures with PEST domains in between (Permission to use from Ehrnhoefer *et al.*, 2011).

1.1.7 Cytoskeleton: structure and function

The cytoskeleton is a network of protein-like fibers inside the cell, which help in maintaining its structure and function. These scaffolding networks help organize other intracellular components and enable transport within the cell. There are various components of the cytoskeleton, including actin (microfilaments), microtubules (MT) and intermediate filaments (IF). They are highly organized and well-coordinated structural features in normal cells. They are involved in major functions such as cellular movement, cell division and intracellular transport, which involves multiple protein-protein interactions.

1.1.7.1 Actin

Microfilaments are composed of actin polymers and multiple actin-binding proteins (ABP). Actin exists in two forms, monomeric or globular (G-actin) and polymeric or filamentous (F-actin), and binds to ATP which upon hydrolysis to ADP leads to the growth of the filament. Actin filaments are arranged in double helical polymers with a tropomyosin (Tm) polymer running along the major groove in the microfilament (Gunning *et al.*, 2008; Gunning *et al.*, 2015). The cellular events that require synchronized turnover and remodeling of actin filaments, such as motility, differentiation, division and membrane organization utilize actin microfilaments. These actin polymers and Tm interact with ABPs thus, generating a complex that forms the basis of the various cellular activities (Gunning *et al.*, 2015).

1.1.7.2 Microtubules

MTs are composed of α - and β -tubulin heterodimers. Both α - and β -tubulin associate into polymers and there exist different isotypes which have tissue- and development-specific expression. There are multiple β -tubulin isotypes that are evolutionarily conserved across species, but differ predominantly in their carboxy-terminal region. This region binds to multiple microtubule associated proteins (MAP) and is predicted to influence the MT activity and stability. The main function of the MTs are cellular growth, vesicular transport and mitosis. They are highly dynamic structures and their ability to polymerize and depolymerize in a regulated manner allows

the proper segregation of chromosomes during mitosis. The assembly and disassembly of MTs occurs by GTP hydrolysis only on the β -tubulin subunit, not the entire α / β heterodimer (Akhshi *et al.*, 2014; Fife *et al.*, 2014).

1.1.7.3 Intermediate filaments

IFs can be formed from 40 different protein subunits and are structurally different from the well-conserved globular proteins, actin and tubulin. IFs are divided into five different categories, including keratin, neurofilament, desmin, laminin and vimentin (Robert *et al.*, 2016). This categorization is based on the protein composition and its intracellular localization. IFs can extend from around the nucleus across the cytoplasm and be attached to the extracellular matrix (ECM) thus, forming an extensive network. This intricate network allows the coordination of multifunctional cytoskeletal activities by relaying information from within the cell to the exterior (Chang and Goldman, 2004).

The major function of the aforementioned cytoskeletal units is to maintain cell structure and motility. Altered cellular motility has been recently viewed as a hallmark feature of various neurodegenerative disorders. The process of cell motility can be broken down into four steps: protrusion, adhesion, contraction and retraction (Figure 1.7) (Fife *et al.*, 2014). Extracellular signals such as growth factors and chemokines generate a gradient that polarize the cell movement. The integrins, receptor tyrosine kinases (RTK) and cadherins after receiving these signals alter the activity of downstream Rho GTPase guanine nucleotide exchange factors (GEFs) which finally affect Rho GTPases which are the key players in regulating cytoskeletal dynamics (Jaffe and Hall, 2005). The extension of the actin filaments towards the extracellular signal is stabilized by the adhesions linking actin to the ECM proteins (Hall, 2012). This allows the protrusion and the adhesion of the cytoskeletal proteins toward the signal by various protein-protein interactions. The contraction allows the disassembly of the entire subset of proteins at the distal end of the cell thereby allowing the movement of the cell body forward and at the same time retracting the cell body and pushing it in the direction of cell movement (Hall, 2012). Rho GTPases are a family of 20 small G proteins regulating the cytoskeletal proteins and thereby influencing the cell cycle, cell polarity and cell migration (Jaffe and Hall, 2005). Rho GTPases function as a molecular switch where the GDP-bound form is inactive and the GTP-bound form is active (Jaffe and Hall, 2005).

The regulation of mammalian GTPases is complex since its inactivation is regulated by 67 GTPase proteins and inactivation by 82 GEFs, which act downstream of cell surface receptors (Rossman *et al.*, 2005). There are three well studied Rho GTPases, including Rho, Rac and Cdc42, which regulate actin assembly. Cdc42 is involved in the regulation of microtubule dynamics (Hall, 2012). Rho can recruit ROCK (Rho kinase) family kinases which are responsible for phosphorylating multiple cytoskeletal proteins (Hall, 2012; Jaffe and Hall, 2005). These interactions are involved in promoting actin stress fibre formation where another player cofilin is involved. Cofilin is downstream of the Rho GTPase pathway and along with the actin-related protein 2/3 (ARP2/3) complex, plays an important role in the generation of free actin filament ends thus resulting in actin filament remodeling by polymerization and depolymerization (Hall, 2012). Cofilin is inactivated when phosphorylated by LIM kinase 1 (LIMK1) and reactivated by dephosphorylation by a phosphatase Slingshot (SSH1L) (Mouneimne *et al.*, 2006; Soosairajah *et al.*, 2005). LIMK is downstream of the Rho GTPase effector proteins and its activity is highly regulated by the phosphorylation of the Rho kinases (ROCK1 and ROCK2) (Nakagawa *et al.*, 1996). Cofilin activity is tightly regulated and is required for chemotaxis (directed cell movement towards a chemoattractant), and for the reorganization of actin filaments, which move toward chemoattractant such as growth factors (Mouneimne *et al.*, 2006). Ultimately ROCK signaling influences cytoskeletal dynamics by phosphorylating the downstream targets, LIMK (LIMK1 and LIMK2), which along with its interaction with cofilin and the phosphatase SSHL (SSHL1 and SSHL2), probably determines the cellular response to a stimulus (Mouneimne *et al.*, 2006; Soosairajah *et al.*, 2005).

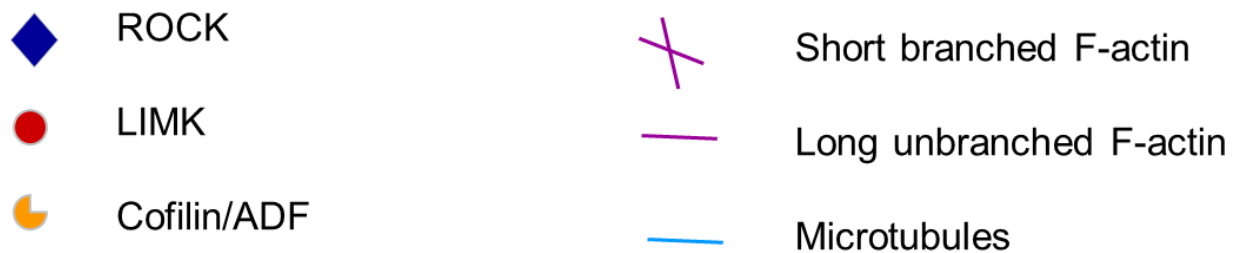
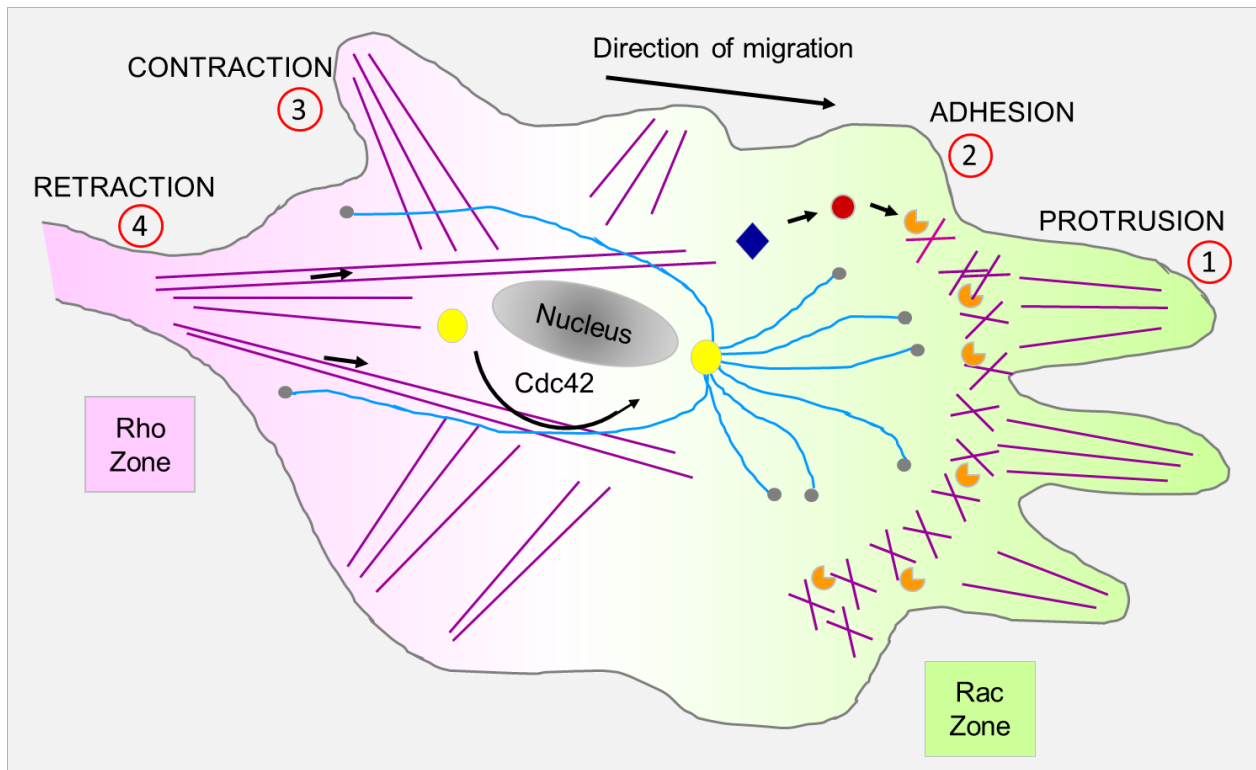


Figure 1.7: The cell cytoskeleton.

The schematic representation of the process of cell motility is broken down into four steps: protrusion, adhesion, contraction and retraction (1-4). F-actin is shown in purple (short, branched F-actin at the leading edge, and long, unbranched F-actin stress fibres at the rear). Microtubules are shown in blue. Cytoskeletal regulatory and associated proteins ROCK, LIMK and cofilin/ADF are also shown as blue, red and orange symbols. (Permission to use from Fife *et al.*, 2014).

1.1.7.4 Cytoskeletal abnormalities in Huntington's Disease

Neurons have two cytoplasmic extensions, including axons and dendrites and they require a specialized cytoskeleton to maintain their complex morphology in order for neural transmission to occur through these processes (Figure 1.8). A change in their neural morphology may affect the neural function and ultimately induce pathology. In neurons, the dynamic tubulin polymers are stabilized before forming axonal and dendritic extensions (Mitchison and Kirschner, 1988). The neuronal projections transport cargo bi-directionally along the microtubules, partnering along with the kinesins and motor proteins (Goldstein and Yang, 2000; Liot *et al.*, 2013). It is believed that mHtt interacts with the motor proteins that carry cargo, such as TrkB-containing vesicles, and reduces its interaction with the microtubules, which affects transport (Gauthier *et al.*, 2004; Li *et al.*, 1998). A number of studies utilizing HD mouse models (R6/1, R6/2, Q175 and KI140) have reported an increased tau phosphorylation involving the kinases that regulate it, including GSK3 and CamKII (Fernandez-Nogales *et al.*, 2015; Gratuze *et al.*, 2016). GSK-3 β is the major kinase to phosphorylate tau both in vitro and in vivo and a major microtubule-associated protein (Medina *et al.*, 2011). CamKII on the other hand is involved in activating the major phosphatase SSH1L which dephosphorylates cofilin thereby activating it (Zhao *et al.*, 2012). As discussed earlier the LIMK1, cofilin and SSH1L are involved in actin cytoskeletal reorganization. The levels of cofilin which is an upstream regulator of actin are perturbed in a number of neurodegenerative disorders such as AD, PD and Amyotrophic Lateral Sclerosis (ALS) (Eira *et al.*, 2016; Sainath and Gallo, 2015). There are a number of stressors in the cell that cause actin cytoskeletal dynamic arrest. Rod formations are seen in AD and PD and the activated cofilin saturates the actin filaments during stress and bundles them into rod-like structures, thereby ceasing actin polymerization and depositing these rods in the nucleus and cytoplasm (Minamide *et al.*, 2000; Zhao *et al.*, 2006). This process leads to the release of free ATP in the cell and once the stress is released, the rods dissociate almost immediately. Additionally, profilin (an actin binding protein), which has an opposite action to cofilin, is perturbed in ALS (Henty-Ridilla *et al.*, 2017; Kiaei *et al.*, 2018). Profilin has the opposite action to cofilin on actin, and binds to Htt at a proline-rich region adjacent to the expanded polyQ tract (Henty-Ridilla *et al.*, 2017; Zhao *et al.*, 2006). Thus, a number of studies have shown stress-related actin rod formation in a variety of neurodegenerative disorders, despite that the biology of the cofilin-actin rod formation is not well understood. Cofilin gene knockout is

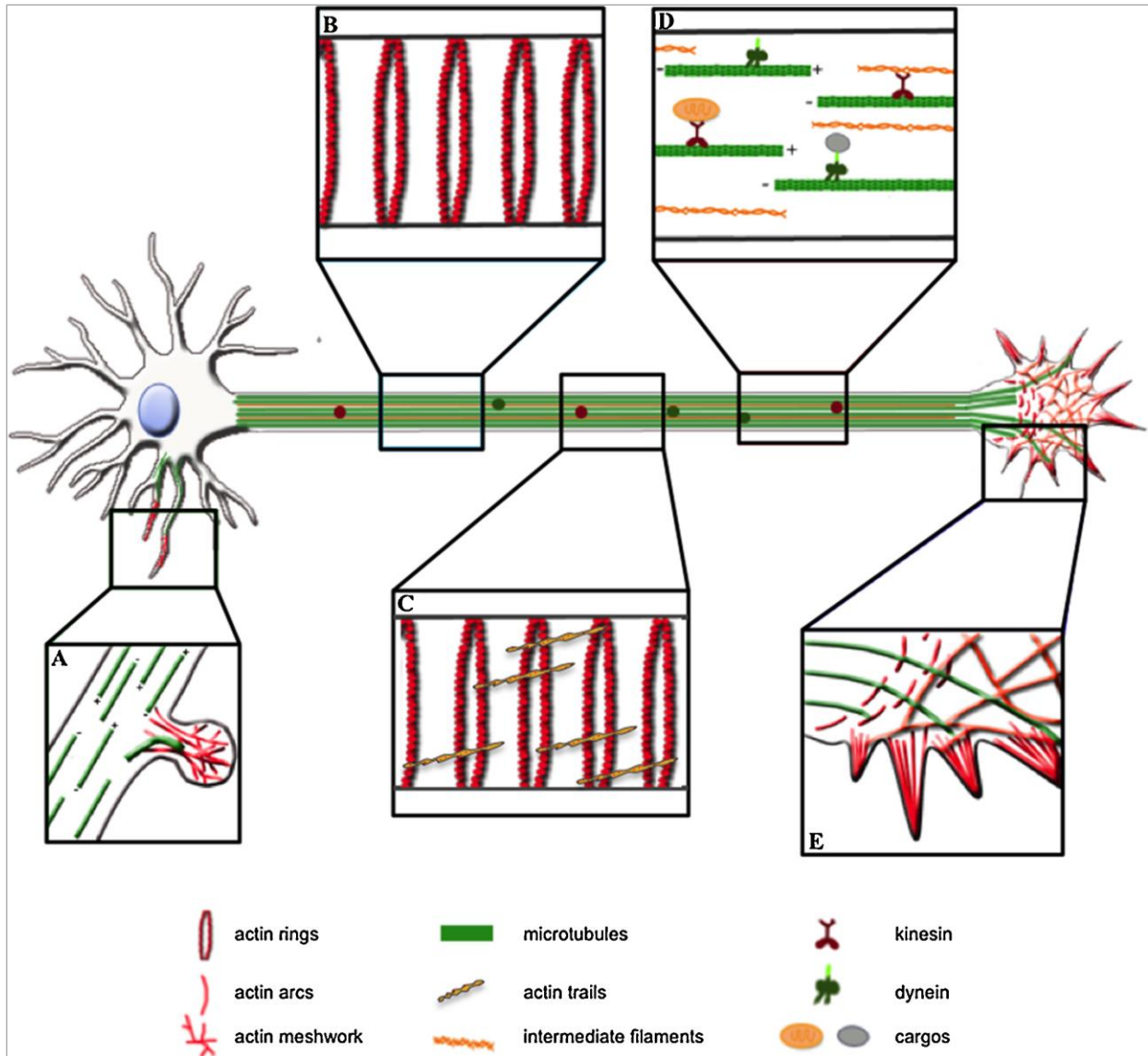


Figure 1.8: Schematic of neuronal structure and its cytoskeleton.

Neurons have a highly regulated cytoskeleton with actin, microtubules and intermediate filaments which are localized differently on the dendrites, spine and cell body (A), axon (B, C and D) and synapse and growth cone (E). Actin rings are seen across the axon and actin arcs form the structural basis of the synaptic end. Actin meshwork is found especially concentrated in the dendrites and the synaptic end. Actin trails are concentrated mostly in the axon. Microtubules are predominantly in the axon but they are also present in the dendrites and synapse. Intermediate filaments localized in the axon (Permission to use from Eira *et al.*, 2016).

embryonically lethal although one study suggested that the postnatal neurons in the forebrain showed that cofilin was required for the turnover of F-actin at the synapses (Gurniak *et al.*, 2005). An increase in calcium levels activate calcineurin (CaN), which dephosphorylates cofilin through the activity of the phosphatase, slingshot (SSH1L) (Zhao *et al.*, 2006). Therefore, a normal neuron requires proper cofilin functioning, which must be tightly regulated by upstream kinases and phosphatases (Bamburg and Bernstein, 2010). Thus among many other roles in the cell, Htt appears to be involved in key molecular interactions involving vesicular transport between the actin and microtubule cytoskeletons (Caviston and Holzbaaur, 2009).

1.2 Phosphorylation mediated cellular signaling

Protein phosphorylation is a significant PTM that regulates the dynamics of a protein allowing precise temporal control of its structure, function, and subcellular localization.

1.2.1 Kinases

Alterations in numerous signal transduction pathways in HD result from aberrant kinase signaling. The balance between kinase signaling pathways is important to maintain normal cellular processes, such as proliferation, neuronal plasticity, apoptosis, etc. Protein kinases have the ability to phosphorylate other proteins and regulate their function. Phosphorylation occurs through the addition of a phosphate group (PO₄) by a mechanism controlled by kinases. There are 518 human protein kinases classified according to the amino acid residue that they phosphorylate. The most phosphorylated residues are serine (Ser or S; 86.4%), threonine (Thr or T; 11.8%) and tyrosine (Tyr or Y; 1.8%). Once activated, these protein kinases lead to the phosphorylation of other proteins. Most of the kinases act on both serine and threonine (serine /threonine kinases; STKs), while others act on only tyrosine (tyrosine kinases; TKs). Phosphatases have the opposite function of kinases, and remove the phosphate group from the phosphoproteins. They hydrolyze the phosphoric acid monoesters into a phosphate group and a molecule with a free hydroxyl group. There are about 226 protein phosphatases that regulate phosphorylation events. A number of cellular molecules are activated and deactivated by phosphorylation / dephosphorylation events due to specific kinases and phosphatases acting on them, respectively.

1.2.2 Kinome and phosphoproteome

Cellular phosphorylation analyses can be divided into i) kinome and ii) phosphoproteome. The former focusses on the analysis of the protein kinases mediating phosphorylation, while the latter focusses on the targets of those kinases. The kinases responsible for driving the fate of phosphoproteomes are central to elucidating various complex cellular events. As discussed in the previous section cellular signaling events are largely controlled by phosphorylation / dephosphorylation thus play an important role in different cellular processes. Recent advances have facilitated studies of the global effects of phosphorylation, as well as studies of specific signaling pathways. This has been performed by mass spectrometric methods where after the enrichment of phosphorylated peptides/proteins, different methodologies such as ionization and fragmentation have been utilized for the mass-analysis of phosphorylated peptides. The physiological substrates for protein kinases are proteins and the specificity of the target is dictated by the conserved amino acid residues surrounding the phosphorylation site. Such conserved peptide sequences have been used in peptide arrays designed to study whole proteins by kinome analysis. The V_{\max} (the maximum rate at which an enzyme can catalyze a reaction) and K_m (the amount of substrate required for the enzyme to function at one half of its maximal rate) values are close to the natural substrates thus providing the ideal platform for studying these proteins. These peptides are chemically stable and easily produced commercially. They can be printed on glass slides and are cost effective, making them easily available for research studies.

1.3. Kinome profiling

The early 2000's marked the completion of the human genome project and a simultaneous review published in Science listed the protein kinase complement of the human genome and termed it the "Kinome" (Manning *et al.*, 2002). Protein phosphorylation by protein kinases (PK) is the most characterized signaling mechanism in eukaryotic cells. The majority of cellular proteins are phosphorylated, making this one of, if not the most important modification in cellular processes. As many as one-third of all the proteins are phosphorylated at any given time, which makes it a difficult undertaking to enumerate all such proteins. It can be simplified by looking at the substrates that each kinase phosphorylates in the human kinome. This can then be extrapolated to physiological and diseased states to gain a better understanding to provide therapeutic benefits

(Johnson and Hunter, 2005). A comparative analysis of genomes has determined that there are considerable differences among eukaryotes. The differences are highlighted by the variance in the number of kinases present in their genomes. For example the *Arabidopsis thaliana* genome contains 610 kinases, *Drosophila melanogaster* has 239 kinases, *Saccharomyces cerevisiae* has 115 kinases, and *Plasmodium falciparum* has 65 kinases (Peppelenbosch, 2012). The human kinome constitutes ~518 members (1.7% of protein coding genes) (Johnson and Hunter, 2005), of which the mouse has 510 orthologs, which accounts for ~98% similarity (Caenepeel *et al.*, 2004). Exploiting array technology for the development of drug targets for biologically important kinases has been utilized in large-scale screening processes. The most challenging aspect is that the appropriate kinase substrates have to be recognized and printed on the array, which is based on a literature search and examinations of online databases. The specificity of the kinase to phosphorylate the substrate produces a dataset that can be mined for unknown biological functions and potential drug targets in different diseases (Arsenault *et al.*, 2011; Arsenault *et al.*, 2012a; Guo *et al.*, 2014a; Jalal *et al.*, 2009; Sutherland *et al.*, 2013). Kinome analyses via peptide arrays have proven effective in understanding signaling events associated with a number of diseases, including neurodegenerative disorders such as prion (Arsenault *et al.*, 2012b) and Alzheimer's disease (Hoozemans *et al.*, 2012), cancer (Goel *et al.*, 2018; Labots *et al.*, 2016; Moser *et al.*, 2014; Parikh and Peppelenbosch, 2010), infectious diseases (Kindrachuk *et al.*, 2014; Mulongo *et al.*, 2014; Robertson *et al.*, 2014; Van Wyk *et al.*, 2016), and inflammation (Arsenault *et al.*, 2013a; Arsenault *et al.*, 2013b).

1.3.1 Peptide arrays

Peptide arrays were first developed in 1984, when they were synthesized on packed polyethylene rods (Geysen *et al.*, 1984). Protein can range from a few amino acids to hundreds of amino acids. The very short sequences of about 40-50 amino acids are referred to as peptides. Some of the current peptide array technologies are based on the concept of light-directed, spatially addressable chemical synthesis which was introduced in 1991 (Fodor *et al.*, 1991). SPOT synthesis (Synthetic peptide arrays on membrane supports) was developed in parallel in 1992 with the preparation of a series of predefined, chemically synthesized short peptide sequences on absorptive surfaces (Frank, 2002). Peptide arrays are an efficient technique with easy to synthesize peptides

that are regularly used to investigate PTMs *in vitro*. It is a simple, but powerful method to investigate PTMs by utilizing their intensity values after staining to study a treatment sample compared to a control in a rapid and cost effective manner.

1.3.2 Selection of peptide targets

1.3.2.1 DAPPLE

DAPPLE (<http://saphire.usask.ca/saphire/dapple/>) is a web based platform developed for phosphorylation site determination to predict the additional mouse phosphorylation events based on described phosphorylation events of other species (Trost *et al.*, 2013a) alongside the known human and mouse phosphorylation events based on published literature. A simple workflow of DAPPLE 2 shows that it predicts sites for different post-translational modifications in the proteome of the target organism selected and generates a list of predicted PTMs (Figure 1.9). The list for HD peptide array included over 270,000 peptides which were rationally selected and shortlisted to 1268 peptides providing an overall coverage of the major signaling pathways predicted or directly involved in HD.

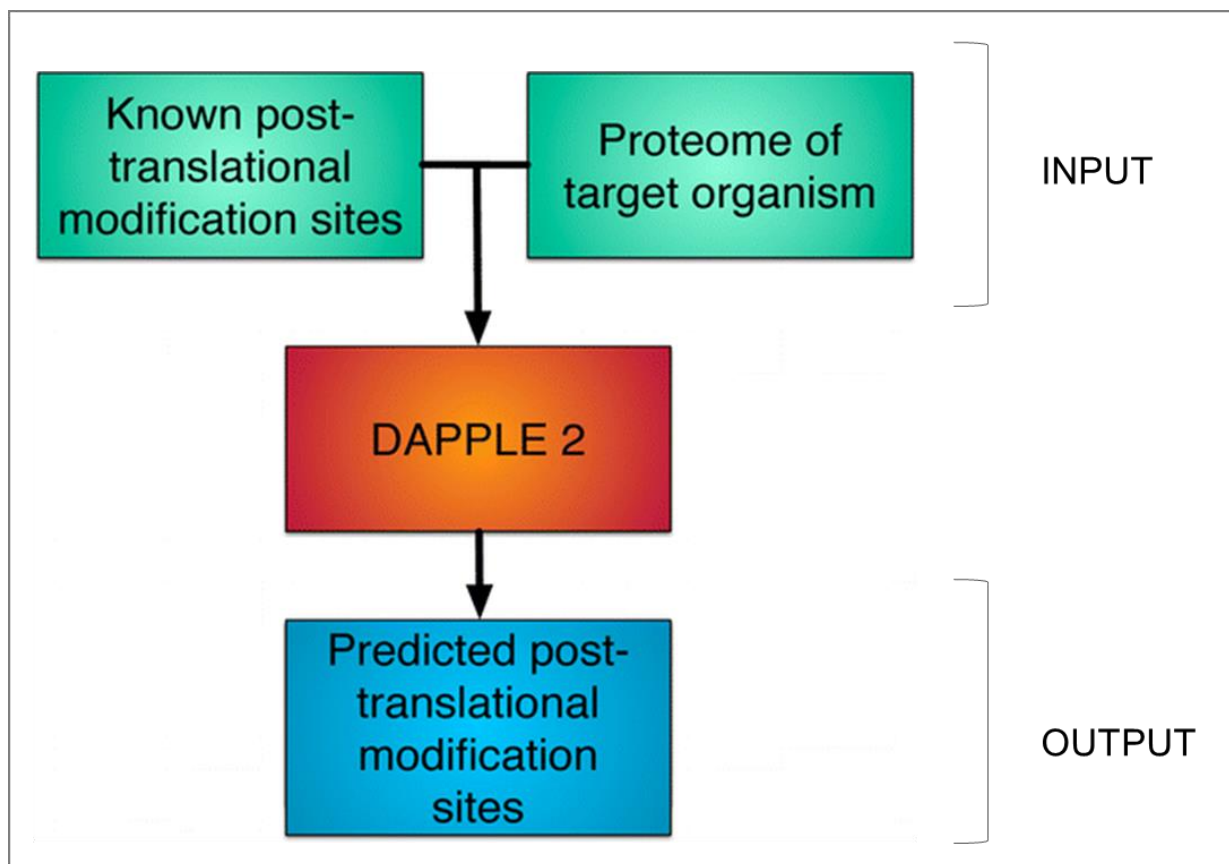


Figure 1.9: DAPPLE pipeline.

The flowchart shows that DAPPLE 2 predicts sites for post-translational modifications in the proteome of the target organism selected (input) and generates a list of predicted PTMs (output). The peptides are selected from this list to be printed on the array (Permission to use from Trost *et al.*, 2016).

1.3.2.2 Peptide array design

The array was designed by utilizing these unique peptide sequences, with a biological significance based on the literature. Custom peptide synthesis and printing was completed on a glass slide, and each array measured approximately 7.6 cm long and 2.5 cm wide as manufactured by JPT Peptide Technologies (<https://www.jpt.com/>) (Figure 1.10). The peptides are typically 15

amino acids long with the phosphoacceptor residue in the center, flanked by an equal number of residues on either side. Peptide array was divided into three grids / blocks of same set of peptides and each printed nine times (three in each block), making sure that there was no margin for error and there are enough technical replicates for statistical analysis. Each spot on the array contains many copies of the peptide sequence which is determined by the manufacturer. Ideally each peptide should have a central phosphoacceptor residue with the conserved sequence on either side but in some cases this cannot be possible. This is overcome by either printing shorter peptide

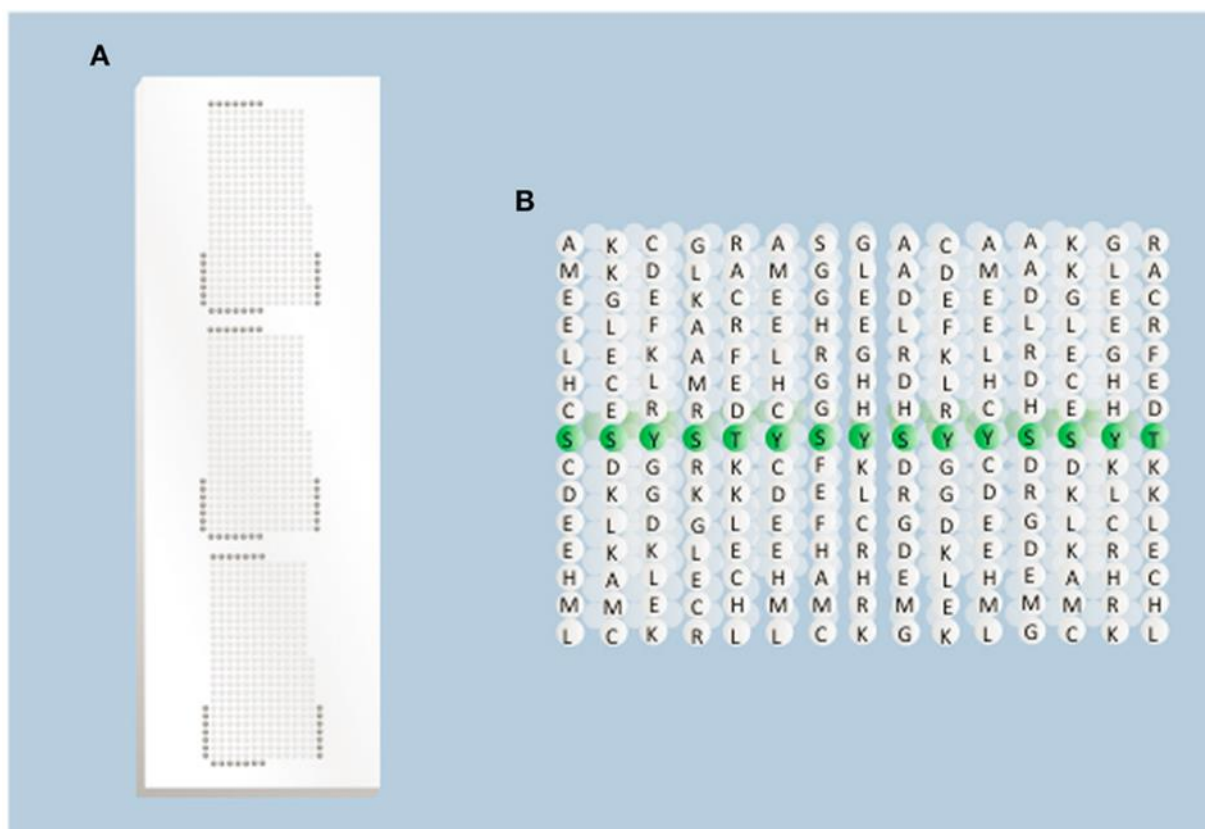


Figure 1.10: Overview of array design.

(A) Physical presentation of the peptides. Each spot on the array represents a different peptide sequence presented within a grid of the total population of peptides (kinase substrates) to be considered. Each grid is replicated three times to generate technical replicates of each spot. Dark gray spots on the edge of the grid represent control peptides for better visualization. (B) Peptides on the array. Each spot on the array represents a population of single peptides (typically 15 amino acids long) in which the central position is the phosphoacceptor residue represented here in green (Permission to use from Daigle *et al.*, 2014).

on the array or by having more residues on one side. Each peptide spot measured about 350 μ m in diameter and was separated by a distance of about 750 μ m. The peptide spotting was in a grid fashion surrounded by full length proteins and were printed on the periphery to aid in better visualization. The exact layout of arrays differ based on the peptides printed on it which can be from hundreds to thousands. The design and printing is completed by the commercial providers. The laboratory procedure for using these arrays are described in section 3.4. After the scanning the spots appear to be like as shown in Figure 1.11 A where the black spots are the one with little or no phosphorylation and spots with phosphorylation are green (Figure 1.13 B). The values of these emitted light intensities are read by an image scanner and are called “intensity values”. The stain binds non-specifically to the background hence the intensity values around the spot are considered as background values. The background intensity is subtracted from the foreground intensity (spot intensity value) and the resulting value indicates the level of phosphorylation of that particular peptide. It is difficult to measure the absolute levels of the phosphorylation with peptide arrays hence for any significant biological output from both treatment and control arrays are required. The treatment array minus control array intensity values can be used to determine the amount of phosphorylation of the peptide under study. Such peptide is termed as a “differentially phosphorylated” peptide and indicates whether the peptide is hyper- or hypo-phosphorylated when compared to control. The technical replicates mentioned earlier evaluate the random variation in the biological experiment. The same peptide is spotted three times in each block therefore there are nine in total across the three blocks and are termed as intra-array replicates. The technical replicates have three advantages i) phosphorylation measure of each peptide is averaged hence reducing random variation ii) peptides with random variation can be identified iii) these technical replicates check for the variation in the measurement of phosphorylation across different biological samples. Hence the sample size is important for determining the biological significance of a particular treatment / disease. The larger the sample size, the more definitive is the peptide array output since the variation in the different biological backgrounds due to treatment/ genetic background or any other anomaly does not lead to a potential data bias in the clustering pattern. The raw intensities obtained from the kinome dataset are normalized before meaningful information can be obtained, the details of which are described in the next section.

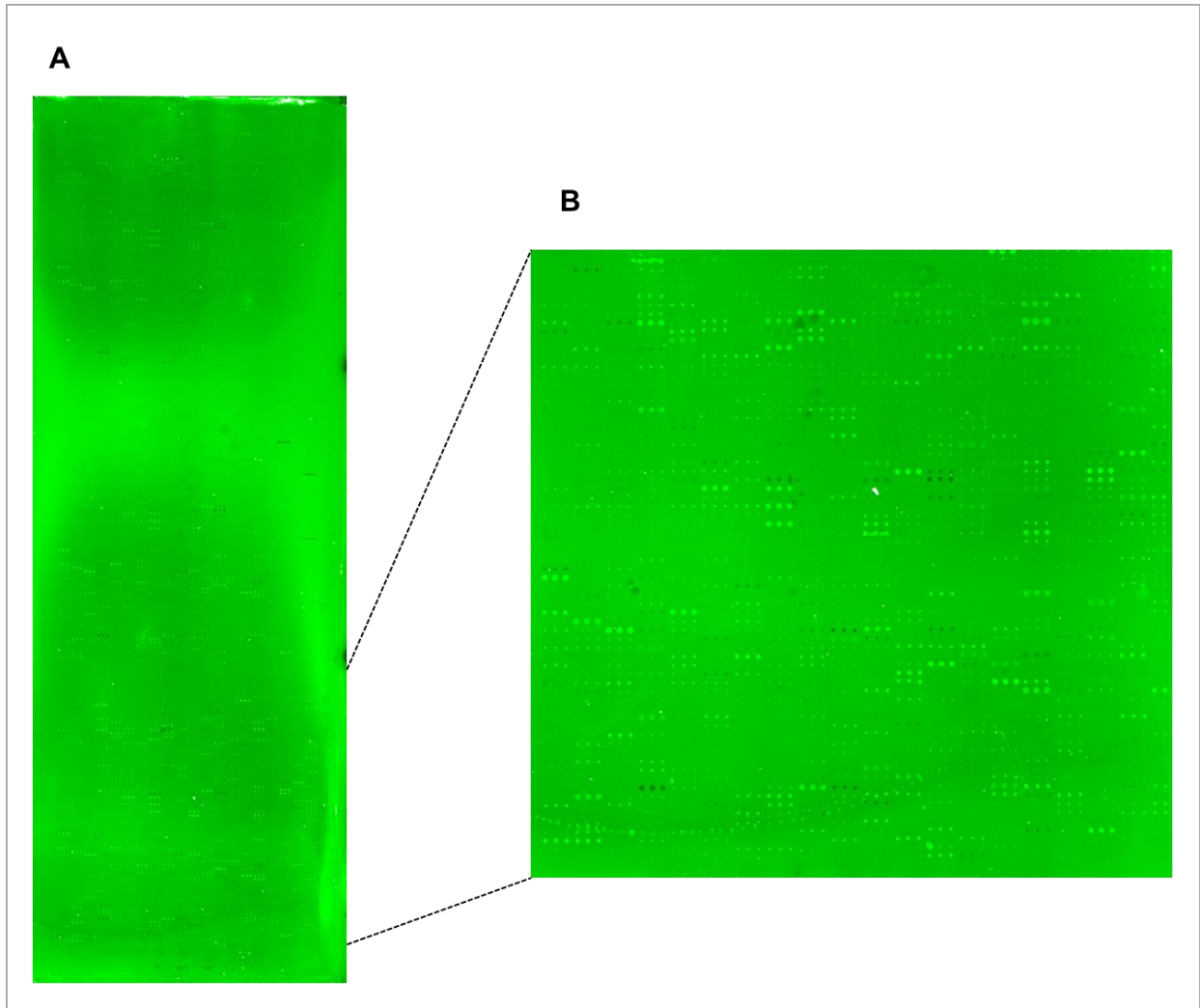


Figure 1.11: Scanned image of a kinome microarray after incubation with cell lysate followed by staining.

(A) The scanned image of a complete array. (B) Black spots contain peptides that underwent little or no phosphorylation, green spots represent moderate amounts of phosphorylation.

1.3.3 Bioinformatic pipeline

1.3.3.1 Platform for Intelligent, Integrated Kinome Analysis (PIIKA 2)

PIIKA 2 was designed to identify differentially phosphorylated peptides in the peptide arrays (Trost *et al.*, 2013b) (Figure 1.12). It was designed using a software program in the R environment. The input files contain the raw intensities from the genepix microarray and the output can be represented as t-test values or other visual representations, such as PCA plots, heatmaps, etc. The output files contain multiple column subheadings, but P-value and fold change (FC) were utilized which are considered to identify significantly differentially phosphorylated peptide (Li *et al.*, 2012). A t-test indicates the difference in the mean phosphorylation between the treatment and control but does not indicate the directionality / degree of difference (+/-), hence fold change. A liberal cut off ($P \leq 0.1/0.2$ and $FC > 1$) is used in kinome analyses to generate a large data set and avoid false positives. The P-value used for the cell line data was 0.1 and for the mouse model 0.2 which was based on the number of peptides printed in the array. The peptide array used for cell lines had 298 unique peptides and the mouse study used peptide array with 1268 peptides, hence the leniency in the P-value. T-test was performed using the R environment function in PIIKA 2, to generate the P-values taking into account the intensity values between the same peptides under treatment and control conditions. FC gives the magnitude of differences between the phosphorylation in the treatment and control. The pathway analysis software (InnateDB) uses both FC and P-value to determine the significant pathways dysregulated in the peptide array. PIIKA 2 uses the difference (not ratio) between the treatment and control to generate the FC. The transformed intensities are converted to FC values by using the formula:

$$\text{Fold change} = 2^d \quad [\text{where, } d = \text{average}_{\text{treatment}} - \text{average}_{\text{control}}]$$

A comparative analysis of various normalization methods (normalization by log2 (Log2), percentile normalization (PNorm), quantile normalization (QNorm), transformation by variance stabilization (vsn) (Huber *et al.*, 2002) was performed for normalizing the dataset thereby not altering the data relevance, verifying that vsn transformation is the best in preserving the raw data patterns. The raw data after processing by vsn revealed that it had the same distribution pattern as the raw data hence retaining the biological significance of the dataset. There are two main purposes

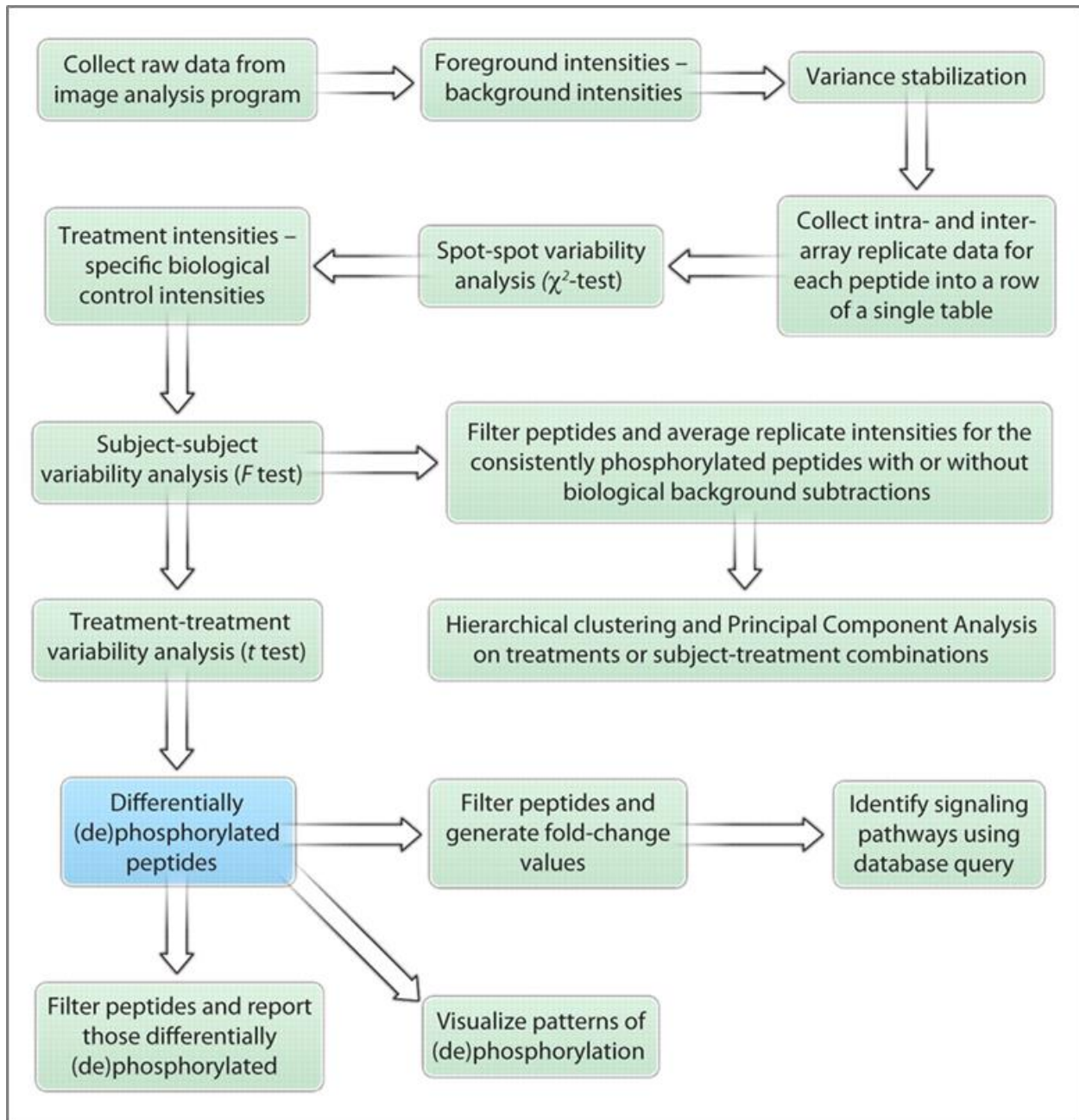


Figure 1.12: A general workflow of the software pipeline (PIIKA) for kinome analysis.

The flow of information and activity starts from the top left and follows the arrows. Rectangles with green background represent procedures, and the one with blue background represents intermediate results. The differentially phosphorylated peptide list was generated by comparing the test to control followed by normalization. This was used for all further bioinformatics analyses (Li *et al.*, 2012) (Reprinted with permission from AAAS).

of vsn. First, to normalize all measurements on the same scale and second to convert all negative intensity values to positive using a complex algorithm. To determine a significant differentially phosphorylated peptide, both the FC and the corresponding P-value are considered. This is because the FC could be due to a few (or one) significantly (de)phosphorylated peptides and a t-test P-value is required to confirm the replicate consistency. Finally, the FC and P-value should be used based on biological rather than mathematical considerations.

1.3.3.2 InnateDB

While t-tests determine whether the individual peptides are differentially phosphorylated and fold change determines the directionality of the change, pathway analysis determines whether the entire pathway is differentially modulated. This was done by another online tool InnateDB. InnateDB is equipped to analyze peptide array dataset and once the list of peptides is uploaded along with the P-value, FC and uniprot ID, this information is used to generate a list of biological pathways that are significantly upregulated or downregulated. InnateDB (<https://www.innatedb.com/>) is a platform that facilitates the analysis of mammalian, murine and bovine genes (Breuer *et al.*, 2013). It contains close to 200,000 molecular interactions that are experimentally validated, with 3000+ pathway annotations that allow a better understanding of the input dataset. In addition to these it also has 18000+ manually-curated interactions. InnateDB can be queried for specific pathways or in a high throughput fashion, incorporating multiple genes/protein dataset to perform a more complex analysis. Gene ID's are accepted from Uniprot, Ensembl, Ref Seq, Entrez gene in the InnateDB software. It can be used as a knowledgebase to perform pathway analyses, gene ontology analyses, and network analyses, among other search fields. All such interactions can be downloaded as visual tools, as well as in text-based formats (tab, csv, xls) to aid the user in interpreting their own data (Breuer *et al.*, 2013). The P-values in InnateDB are generated using the hypergeometric distribution test which confirms whether a pathway is statistically more over-represented in the uploaded dataset than expected by chance prior to correction for multiple testing. P-values are automatically corrected using the Benjamini and Hochberg or by a conservative Bonferroni correction. The output generated from InnateDB are over-represented pathways associated with the P-values from the input data. Since the InnateDB software generates output from various databases there are many canonical pathways

represented multiple times. The validation of these peptides is completed independently using other assays.

1.4. Neural stem cells in studying Huntington's disease

Molecular investigations of disease have benefited from tools such as stem cells, which can be differentiated into many lineages, including neuronal (Nelson *et al.*, 2010; Takahashi and Yamanaka, 2013), and enable drug screening to expedite the development of therapeutics for neurodevelopmental, neurodegenerative, and psychiatric disorders (Ardhanareeswaran *et al.*, 2017). Recently, the ability to generate induced pluripotent stem cells (iPSCs) from fully differentiated cells (such as skin fibroblasts) has opened many avenues for the advancement of medicine (Takahashi and Yamanaka, 2013). The precision with which fibroblasts can be reprogrammed to develop neuronal stem cells (NSCs) that form fully functional neurons has tremendous potential for screening potential treatments of neurodegenerative disorders (Ross and Akimov, 2014). Importantly, NSCs can be generated from HD patients within virtually all age-groups, rendering a convenient model to study the age-related pathogenesis of the disease (Koyuncu *et al.*, 2018; Ross and Tabrizi, 2011). Such NSCs can also be exploited to infer patient-specific therapeutic opportunities (Mu *et al.*, 2014; Ross and Akimov, 2014). Examinations of HD NSCs has led to observed differences in cellular pathways pertaining to oxidative stress, mitochondrial dynamics, transcriptional dysregulation, and gene expression (Consortium, 2012; Szlachcic *et al.*, 2015; Zhang *et al.*, 2010). iPSC models have been generated for other polyQ disorders and neurological diseases (Kikuchi *et al.*, 2017; Xie *et al.*, 2016; Yang *et al.*, 2016). While iPSC models have been used to examine individual or related signaling cascades (Mueller *et al.*, 2018; Nekrasov *et al.*, 2016; Szlachcic *et al.*, 2017), here we examine an HD patient-derived NSC line for changes in the patterns of multiple signaling cascades simultaneously using a kinome technology refined at our University (Arsenault *et al.*, 2011; Baharani *et al.*, 2017; Jalal *et al.*, 2009). The stem cells provide an opportunity to assess a neurological disease for which it is tough to access the tissue compared to the other tissues of the body. The development of the stem cell technology has allowed faster and more clinically relevant progress especially in the field of neurological diseases.

1.5 Mouse models to study Huntington's disease

To study human disease processes, transgenic mouse models have become a necessity (Brouillet *et al.*, 1999; Ferrante, 2009). Neurological disease models should be robust and have limited variability in mimicking human diseases. They should possess minimum discrepancies and should display similar neural abnormalities as observed in individuals affected with the specific neuronal disorder (Beal and Ferrante, 2004; Hersch and Ferrante, 2004). There are a number of mouse models used to study HD, and have been grouped in a broader umbrella of genetically modified mouse models and chemically induced lesion models. The chemically induced lesion models are induced with 3-nitropropionic acid or quinolonic acid (Ramaswamy *et al.*, 2007). The genetically modified mouse models are grouped into three sub-categories based on how they were developed. They include N-terminal transgenic animals, full-length transgenic models and knock-in transgenic mouse models. The N-terminal animals carry the 5' portion of the human Htt gene containing the CAG repeats. The full-length models have the full-length Htt sequence with the trinucleotide repeats. The knock-in models have CAG repeats of varying lengths, which are directly engineered into the mouse *Htt* locus. All models are similar in that they contain CAG repeats, but show differences in the HD phenotype (Ferrante, 2009; Figiel *et al.*, 2012). The N-terminal transgenic lines were the first HD mouse models generated and they are the most commonly used in HD research. The most studied among them is the R6/2 transgenic mouse model. Many preclinical studies have been completed utilizing these lines (Pouladi *et al.*, 2013) and it is one of the best characterized transgenic lines available (Mangiarini *et al.*, 1996).

1.5.1 R6/2 mouse model

R6/2 mouse model have a robust phenotype, a shorter life span (3-4 months), and well defined neurobehavioral and neuropathological findings hence they are widely used in HD research. The R6/2 lines were the first to be generated expressing the mutant human exon *Htt* (Mangiarini *et al.*, 1996). The N-terminal transgenic mice were generated by pronuclear injections, and thus, each transgene is integrated randomly at a unique site in the mouse genome. The human trinucleotide repeats in these transgenes are unstable, and thus, there is an increase in the number of repeats in both germ line and somatic cells in successive generations. Monitoring of the repeat

length is critical while maintaining colonies to reduce experimental variation (Cummings *et al.*, 2012).

R6/2 mice carry a small section of the 5' end of human Htt gene, which includes exon 1 with the CAG trinucleotide repeats. The stock is maintained with a CAG repeat of 120 +/- 5 repeat units. The N-terminal lines have a more prominent phenotype than the other mouse models. They develop neurological abnormalities more rapidly and show loss of motor coordination, tremors, hypokinesia, abnormal gait and premature death (Menalled *et al.*, 2009). The N-terminal mutant *Htt* fragment is sufficient to exhibit HD-like neuropathology in mice. R6/2 mice range in survival from 14-21 weeks, depending on the housing conditions (Li *et al.*, 2005; Wood *et al.*, 2010). Behavioural studies indicate that R6/2 mice exhibit deteriorating motor performance, reductions in body weight, and impaired dystonic movements that worsen with age (Figiel *et al.*, 2012). These mice also show a reduced brain weight (around week 4), decreased brain volume and expanded ventricles (around week 8.5), which are hallmarks of HD. These mice also exhibit a decrease in striatal volume and atrophy of the striatal neurons towards the end stages of disease (Ferrante, 2009). Htt aggregates increase with age, although they are reported to be present since birth, which is not observed in human HD patients. Such observations could be attributed to the presence of the truncated gene, which could be responsible for the aggravated phenotype. Similarities exist in the dysregulated cellular mechanisms of HD patients and R6/2 mice, including transcriptional regulation, proteolysis, apoptosis, mitochondrial function, and vesicular trafficking. R6/2 mice have substantial neuropathological similarities with HD patients, but do not have the same genetics. Nevertheless these mice have well characterized phenotypes and can be used for survival studies and clinical trials generating outcomes in as few as 3 months (Li *et al.*, 2005; Skotte *et al.*, 2018). R6/2 model exhibits a progressive HD phenotype, which is the closest to the human HD symptoms, and therefore, is considered the best model for therapeutic studies.

1.6 Sex differences in neurodegenerative disorders

The potential sex differences in Huntington's, Parkinson's and other neurodegenerative disorders on the onset of the disease and its progression are poorly understood. Animal models provide a great platform to understand the difference between the two sexes in the disease process as they allow the circumventing of the problems of standardization, i.e. the variation in the CAG

repeats and age matched samples which are difficult to obtain in the human patients. Recently, it was shown that these disorders have a bias (Kovtun *et al.*, 2004; Nyarko *et al.*, 2018; Quartey *et al.*, 2019; Smith and Dahodwala, 2014; Wooten *et al.*, 2004). The disease susceptibility, pathogenesis, and clinical presentation is different in males compared to females (Smith and Dahodwala, 2014). Such differences are being attributed to the female sex hormone, estrogen, having a protective effect on neurons (Bourque *et al.*, 2009; Siani *et al.*, 2017). The first report to comprehensively characterize the behavioral, physiological and neuropathological difference in HD mice reported atrophy of DARPP32(+) MSNs only in male transgenic HD rats (Bode *et al.*, 2008). DARPP32 is expressed in MSNs which also express dopamine D1 receptors. Dopamine is a neurotransmitter that controls movement, cognition and emotional functions. The dopamine transporter (DAT) membrane receptor is the key regulator of dopamine uptake at the synaptic cleft and studies have shown that estrogen has a protective effect in dopaminergic neurons (Cereda *et al.*, 2013; Simunovic *et al.*, 2010; van Dyck *et al.*, 1995). Differences in gene expressions between male and female brains have also been identified and those changes are anticipated even before the effect of the gonadal hormones (Dewing *et al.*, 2003). The male sex-determining region on the Y chromosome (SRY) is a transcription factor. *In situ* hybridization has shown SRY expression in the brains of rodents, and subsequent studies revealed that the regions with the highest expressions are the cortex, substantia nigra, and medial mammillary bodies (Dewing *et al.*, 2006). SRY exerts its influence on the biochemical properties of dopaminergic neurons, which in turn affects motor behaviour in male rats (Czech *et al.*, 2012). The loss of SRY in males leads to a significant reduction in dopamine function in the surviving neurons hence SRY may be an additional mechanism that regulates dopamine in males. Thus, the difference in molecular mechanisms between sexes can likely be attributed to the influence of sex chromosome genes (Carruth *et al.*, 2002; Dewing *et al.*, 2006).

1.6.1 Sex differences in Huntington's disease

Sex differences have not been well studied in HD with some research directing towards severe phenotype in females while the other report the opposite. A report studied the influence of sex on HD progression on 1267 patients with HD, wherein women showed slightly more severe phenotype and faster rate of progression in women (Zielonka *et al.*, 2013). This study revealed sex

differences in the severity of HD, where women exhibited lower motor and functional UHDRS (Unified Huntington's Disease Rating Scale) scores compared to males. UHDRS is an evaluation standard used to assess HD based on four clinical performance categories, including motor function, cognitive function, behavioral abnormalities, and functional capacity (Huntington, 1996). Multiple reports also suggested that the age of onset being higher in females than males (Roos *et al.*, 1991); however, the progression of disease was milder in women, compared to men (Chen *et al.*, 2009; Roos *et al.*, 1991). The loss of body weight has been reported in both males and female HD patients, however, the body mass index lower in males despite their higher calorific intake.

The repeats are highly unstable and longer when inherited from an affected father (Norremolle *et al.*, 1995). Males predominantly show an expansion of the repeats and the females show a contraction (Kovtun *et al.*, 2000). Another study compared 254 affected parent-child pairs with HD to determine the frequency of intergenerational CAG changes in the *mHtt* which reported expansions in the polyQ repeats when transmitted through the affected father (Kremer *et al.*, 1995). Another study revealed somatic and gonadal mosaicism which indicated towards the mitotic and meiotic instability in the polyQ repeats (Telenius *et al.*, 1994). The most neuropathological findings in HD are in the brain which exhibited the most somatic mosaicism followed by significant mosaicism in the sperm (Telenius *et al.*, 1994). A recent report demonstrated that increased age of the father was also associated with a higher frequency of CAG repeat expansions in sperm (Wright *et al.*, 2019) which supports previous findings (Chong *et al.*, 1997; Semaka *et al.*, 2013).

Female hormones are being considered as a neuroprotective therapy that delay the onset and reduce the severity of HD symptoms (Bode *et al.*, 2008). The overall results of such studies indicate that there is a complex sex effect on disease severity and the rate of HD progression (Zielonka *et al.*, 2013). There is still a considerable amount of research required to confirm which sex is most affected since there is evidence supporting both. This can be addressed if there is an inclusion of equal number of females and males in research trials and the dataset compared for similarities and differences. The assumption that results from males apply to females could result in a bias dataset because it fails to recognize the sex dependent effects in a research study (Beery and Zucker, 2011). Thus, such observations should be considered while designing future experiments and clinical trials (McCullough *et al.*, 2014).

2. HYPOTHESIS AND OBJECTIVES

2.1 Rationale and Hypothesis

The aberrant kinase signaling in HD has not been well characterized. There are multiple pathways that are dysregulated and the alterations might occur due to age, sex and disease progression which can be well understood if the differences are recapitulated by a global profiling of kinase signaling across all the key developmental time points in both sexes. The use of peptide arrays to identify the signaling pathways that are dysregulated in Huntington's disease will provide insight into these pathological mechanisms of the disease as well as rationale targets for therapeutic intervention.

The hypothesis states that multiple processes are dysregulated in HD due to aberrant kinase signaling that is modulated by age and sex. The objectives are outlined below.

2.2. Objectives

1. To design a HD specific peptide array for kinome analysis.
2. To identify potential pathways that are dysregulated in striatal tissue from R6/2 HD mice using peptide arrays and pathway analysis.
3. To validate the differentially phosphorylated peptides that are determined from the bioinformatic analysis of the peptide array data.

3. MATERIALS AND METHODS

3.1 Reagents and chemicals

The reagents and chemicals used in the experiments are provided in the Table 3.1 below along with the names and addresses of the manufacturer / supplier in Table 3.2.

Table 3.1: List of reagents and/or chemicals. The Table lists commercially procured reagents, chemicals and other materials to perform the experiments. The names of the supplier and catalogue number are also indicated.

Reagents and Chemicals	Supplier and Catalogue Number
(Ethylenedinitrilo) tetra acetic acid,	Sigma-Aldrich, E9884
100 bp ladder	NEB, N3231S
1kb ladder	NEB, N3232S
30% Acrylamide/Bis Solution 29:1	Biorad, 1610156
Acetonitrile	EMD Biosciences, 200-835-2
Ammonium Persulfate	Sigma-Aldrich, A3678
Aprotinin	Sigma-Aldrich, P2714
ATP	Sigma-Aldrich, FLAAS-5VL
BCA protein assay	Thermo Fisher, 23225
Bovine serum albumin	Sigma-Aldrich, 05470
Brij35	Sigma-Aldrich, 8.01962
Cryovials	VWR, 89092-262
DNA Polymerase	Thermo Fisher, F530S
DNeasy Blood & Tissue Kit	Qiagen, 69506
DPBS- No Ca ⁺² , No Mg ⁺²	Life Technologies, 14190
Ethyl alcohol	Fisher Scientific, S25310
Ethylene glycol-bis(2-aminoethylether)-N,N,N',N'-tetra acetic acid	Sigma-Aldrich, E3889
Glycerol	Sigma-Aldrich, G5516
Glycine	Fisher Scientific, S80028

Human Neural Progenitor Cells (hNPCs)	Axol, ax0016
Huntington's Disease Human Neural Progenitor Cells	Axol ax0211
Leupeptin	Sigma-Aldrich, L2884
Lifter slip	Fisher Scientific, 22 035 805
Magnesium chloride	Fisher Scientific, 232-094-6
Methanol	EMD Millipore, MX0475
N,N,N',N'-tetramethylethylenediamine (TEMED)	Sigma-Aldrich, T9281
Neural Maintenance Medium Kit.	Axol, ax0031
Neural Unlock™	Axol, ax0044
NewBlot Stripping Buffer for Nitrocellulose membrane	Li-COR, P/N 928-40030
Phenylmethylsulfonylfluoride	Thermo Fisher, 36978
Phosphatase inhibitor	Thermo Fisher, 78420
Phosphatase inhibitor	Thermo Fisher, 78428
Phosphatase inhibitor cocktail 3	Sigma-Aldrich, P0044
Phusion DNA Polymerase	Thermo Fisher, F530S
Precision Plus Protein™ Dual Xtra Standards	Biorad, 161-0377
Pre-stained protein ladder	Biorad,161-0375
Pre-stained protein ladder	Biorad,161-0377
PRO-Q, Diamond Phosphoprotein Stain	Invitrogen, P33300
Protease inhibitor	Thermo Fisher, 78430
Protein ladder	Biorad, 161-0375
RIPA Lysis Buffer System	Santa Cruz Biotechnology, sc24948
Sodium acetate	Sigma-Aldrich, S2889
Sodium chloride	Sigma-Aldrich, S9888
Sodium dodecyl sulfate	Sigma-Aldrich, L3771
Sodium fluoride	Sigma-Aldrich, 201154
Sodium orthovanadate	EMD Millipore, 567540
Sodium pyrophosphate	Sigma-Aldrich, S6422
Sure Bond™ Coating Solution	Axol, ax0041
Sure Boost	Axol, ax0045
Sure Growth	Axol, ax0047

Tris base	Fisher Scientific, BP152-5
Triton X-100	Fisher Scientific, AC215680000
Trypsin (Cell culture grade)	Fisher Scientific, SV3003101
Trypsin with EDTA	Life Technologies, 25300-054
Tween-20	Fisher Scientific, BP337500
β -Glycerophosphate	Cayman, 14405

Table 3.2: Reagent supplier addresses. This Table lists the names and addresses of all reagent/chemical suppliers.

Supplier	Address
Axol	Cambridge, United Kingdom
Bio-Rad	Hercules, California, USA
Cayman	Burlington , Ontario, Canada
Cell signaling technologies	Danvers, Massachusetts, USA
EMD Millipore	Danvers, Massachusetts, USA
Fisher Scientific	Walton, Massachusetts, USA
Invitrogen Life Technologies	Green Island, New York, USA
LI-COR, Odyssey	Lincoln, Newark, USA
New England Biolabs	Ipswich, Massachusetts, USA
Qiagen	Toronto, Ontario, Canada
Santa Cruz Biotechnologies	Santa Monica, California, USA
Sigma-Aldrich	St. Louis, Missouri, USA
Thermo Fisher Scientific	Logan, Utah, USA
VWR	Mississauga, Ontario, Canada

3.2 Cell culture and tissue harvest

3.2.1 Cell culture harvest

HD neural stem cells (NSC) with 45 CAG repeats (# ax0021) and iPSC-derived neural progenitor control cells (ax0016) were obtained from Axol Biosciences (Cambridge, U.K). Both cell lines were cultured according to the vendor's protocol. Prior to culturing cells, Axol Sure Bond coating solution (# ax0041) prepared in 1X PBS (without calcium or magnesium; D-PBS) was used to treat uncoated 6-well dishes by incubating in the solution overnight at 37°C. The cells were seeded at a density of 10,000-50,000 cells/cm² in Axol Neural Maintenance Media (# ax0031) supplemented with the Axol Sure Boost serum (# ax0045). Following two hours of incubation, the media was replaced with neural maintenance media supplemented with the Axol Sure Growth serum (# ax0047). Cells were cultured in this media for two days, and thereafter cultured in the Neural Maintenance Media alone. For passaging and harvesting cells, the culture dishes were rinsed with 1X PBS and cells were detached from the dish using the Axol Neural Unlock solution (# ax0044). A total of 10x10⁶ cells were harvested and prepared for either peptide array analysis or Western blotting (WB).

3.2.2 Tissue harvest

The R6/2 HD mouse model expresses a small N-terminal fragment with exon 1 of the huntingtin gene (Mangiarini *et al.*, 1996). The fragment contains approximately 120 +/- 5 CAG repeats, which generates a progressive (disease) phenotype. The model exhibits many of the behavioral and neuropathological features of HD and is well characterized, which makes it a perfect candidate for in-depth studies of the HD pathology using kinome analysis. PCR was used for genotyping during maintenance of colonies. Brain tissue (whole brain for embryonic and striatum for the rest) (Figure 3.4) were harvested, after sacrificing the mice for future experiments.

3.2.2.1 Genotyping and PCR

Animal care facility at VIDO-InterVac housed 20 breeding pairs of R6/2 transgenic mice, which were purchased from the Jackson Laboratory (#6494). Multiple breeding pairs were established between B6CBAF1/J males and ovary-transplanted hemizygous females (Figure 3.1 and 3.2). Ninety embryos and 169 pups were used for 518 genotyping reactions to confirm both the mutant *Htt* gene and *SRY* for sex determination. All newborn pups were genotyped and non-transgenic littermates were used as wild type controls, while presence of *SRY* was considered as male. DNA was extracted using a Qiagen kit (catalog number 60506). DNA extraction was completed using the skull from embryonic time points (E19 and E14) after harvesting the brains. I obtained ~2mm tail biopsies for the rest of the time points to extract the DNA. The genotype was assessed using PCR and amplifications were performed using Phusion DNA polymerase (2 U/ μ L), and dNTP mix with the following reaction and cycling conditions:

Reactions Components (20 μ l reaction):

Phusion DNA Polymerase (0.2uL), 10 mM dNTPs, 10 μ M Forward Primer (0.2 μ M), 10 μ M Reverse Primer (0.2 μ M), Template DNA (<100 ng), 5X Phusion GC Buffer, DMSO (0.6uL), 50 mM MgCl₂ solution, Nuclease-free water (to 20 μ l). Cycling Conditions:

1. Initial Denaturation	98 °C (30 seconds)
35 cycles of	
2. Denaturation	98 °C (15 seconds)
3. Annealing	58 °C (30 seconds)
4. Extension	72 °C (30 seconds)
5. Final extension	72 °C for 5 minutes
6. Hold	4°C



Figure 3.1: The ovary-transplanted hemizygous female is recommended for breeding with B6CBAF1/J males.

Shown is an ovary-transplanted female with the left ovary (indicated by the forceps) grafted from an HD female and the right cauterized to prevent any nonessential pregnancy (Image courtesy: VIDO-InterVac Animal care).



Figure 3.2: Shown is the cauterized ovary on the right side (indicated by the forceps) of the mouse.

The embryos in the transplanted ovary on the left are the F1 generation. Such embryos are further genotyped and the brains are harvested at different time points (Image courtesy VIDO-InterVac Animal care).

All PCR primers were purchased from Invitrogen Life Technologies (New York, USA). The following primer sequences were used: Forward, 5'-CCG CTC AGG TTC TGC TTT TA-3'; Reverse, 5'- TGG AAG GAC TTG AGG GAC TC-3'. The mutant *Htt* product was ~170 base pairs. The forward primer annealed upstream of the CAG repeat region and the reverse primer annealed in the transgene; therefore, indicating the presence or absence of the transgene. PCRs to determine the sex of pups were also performed under the same reaction conditions. The *SRY* primers were: Forward 5'-TTG TCT AGA GAG CAT GGA GGG CCA TGT CAA-3'; Reverse 5'-CCA CTC CTC TGT GAC ACT TTA GCC CTC CGA-3'. *SRY* primers amplified a product of ~ 273 base pair indicated a male sex, since they amplified a region of the Y-chromosome. The PCR products were separated by 1.5% agarose gel and imaged (Figure 3.3).

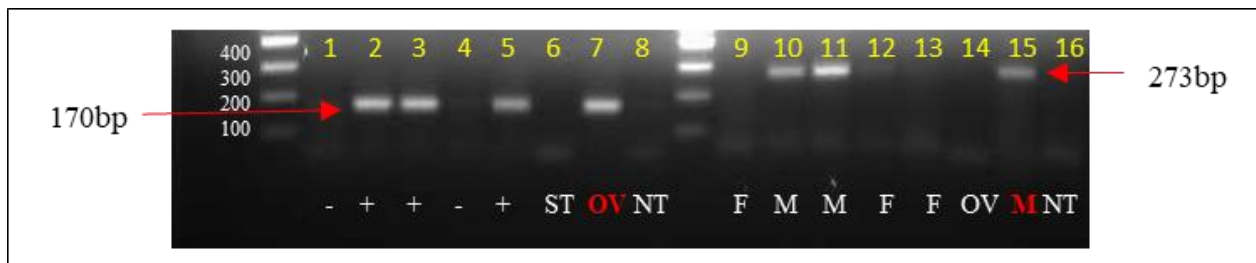


Figure 3.3: Representative genotyping for HD-positive mice (lanes 1-8) and sex-determination (lanes 9-16).

PCR products were generated for various samples (lanes 1-5 and 9-13), for positive control reactions from an ovary (lanes 7 and 14) to genotype HD-positive mice and tail snips of a male mouse (lane 15) for sex determination. No template controls (lane 8 and 16) were also incorporated. A striatum (lane 6) sample from another mouse species was used as a negative control. The PCR product size for HD genotypes was ~170 bp and sex determination was ~ 273 bp. ST=Striatum; NT=No template; OV=Ovary; F=Female, M=Male, + = presence of *mHtt*, - =absence of *mHtt*.

3.2.2.2 R6/2 developmental time points for tissue harvest

Age-matched R6/2 breeding pairs were purchased from Jackson Laboratories (<https://www.jax.org/>) and housed in the animal care facility of the Vaccine and Infectious Disease Organization - International Vaccine Center (VIDO-InterVac) at the University of Saskatchewan.

Animals were maintained with ad libitum access to food and water. The rooms were kept at a constant temperature (19°C-22°C) and humidity (40–50%) with a 12:12 h light/dark cycle. The breeding scheme included ovarian transplanted hemizygous females with the B6CBAF1/J males. R6/2 mice developed a progressive behavioral and neurological phenotype by 4-6 weeks of age, which mimics the onset of HD in humans. Both the HD and healthy control (HC) mice were grouped into sets of males and females. The different time points for the peptide array analysis were embryonic days 9 (E9) and 14 (E14), at birth (P₀), and weeks 3 (3w), 4 (4w), 5 (5w), 7 (7w) and 10 (10w) (Figure 3.4). The methodology for processing the peptide arrays is described in section 3.4. At embryonic time points, whole brains from both HD and HC littermate controls of both sexes were dissected and cryopreserved. The striatal tissues were dissected from the brains of mice at P₀ and weeks 3, 4, 5, 7, 10, and frozen at -80°C until further analysis (Figure 3.5).

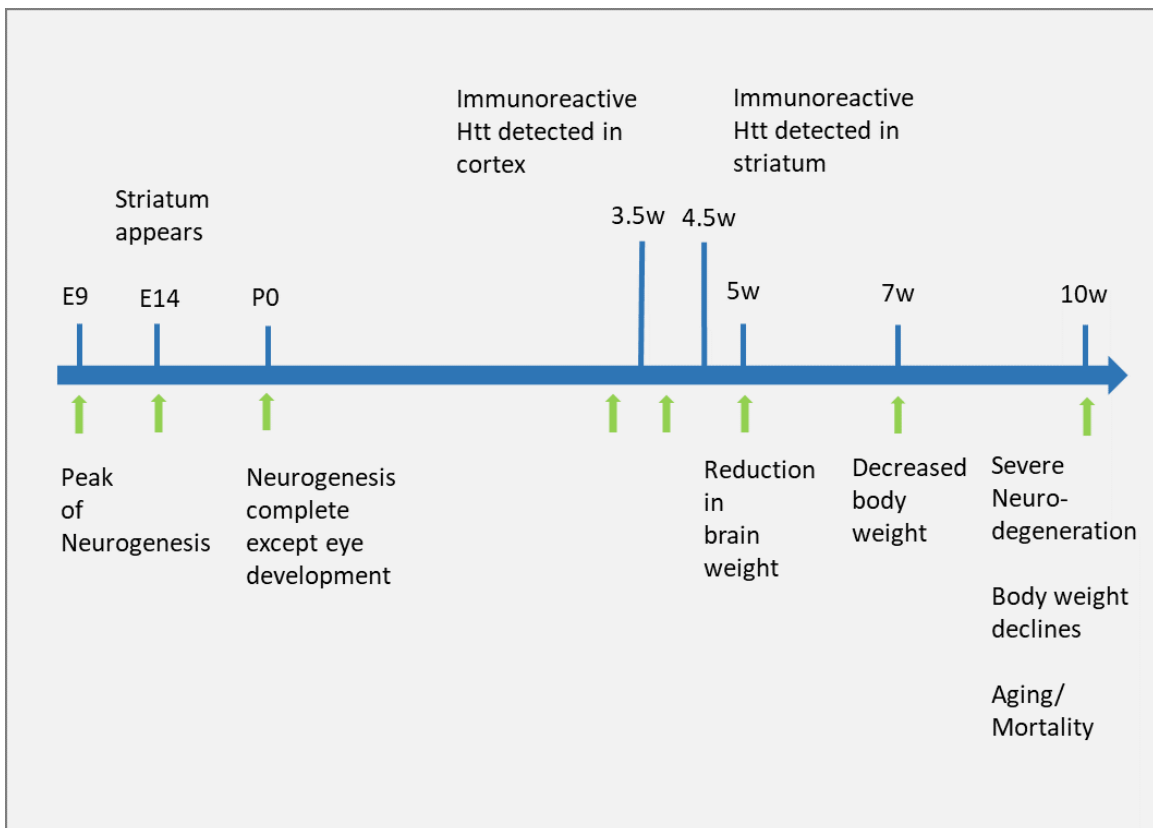


Figure 3.4: Timeline for peptide array analysis.

The different time points for the peptide arrays were embryonic days 9 (E9) and 14 (E14), at birth (P₀), and weeks 3 (3w), 4 (4w), 5 (5w), 7 (7w) and 10 (10w).

Tissues were harvested based on the key developmental time points which were divided into eight groups (E9, E14, P0, 3w, 4w, 5w, 7w, and 10w). The time points were chosen based on the neural development in the mouse. Embryonic day 9 is the peak of neurogenesis (Darlington *et al.*, 1999; Finlay and Darlington, 1995). Embryonic day 14 defines the beginning of the development of striatum, caudate and putamen (Fentress *et al.*, 1981). These neurons are the first ones to be affected by mHtt leading to the motor abnormalities. The striatum is involved in cognition, motor functions, planning and decision making; hence, the degeneration of the striatal neurons affects these actions. Neural development was complete at birth, except for the eyes, which open after birth. The mHtt appeared in the cortex at 3.5 weeks and the striatum at 4 weeks

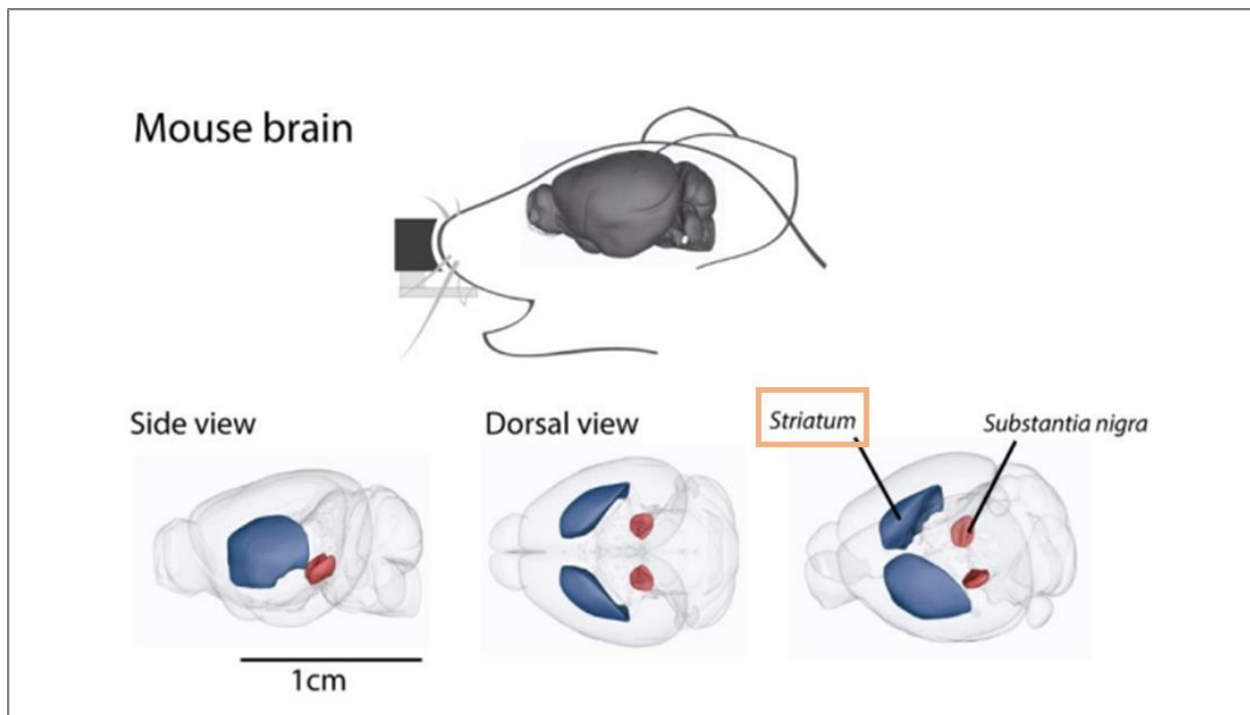


Figure 3.5: Schematic mouse brain depicting the anatomical location of the striatum. Shown is the side and the dorsal views of mouse brains. The location of the striatum is also shown in the figure whose neurons are primarily affected in HD. The striatal tissue is located underneath the cortex (Permission to use from Masini D *et al.*, 2018). (<https://openarchive.ki.se/xmlui/handle/10616/46182>).

(Mangiarini *et al.*, 1996). The 3- and 4-week time points were chosen to include the changes appearing in the brain just before the appearance of mHtt. At 5 weeks, the mice showed motor impairments (Mangiarini *et al.*, 1996). The loss of body weight was prominent around 7 weeks where the HD mice weighed about 60-70% less than their control siblings (Mangiarini *et al.*, 1996). The age of onset of HD symptoms is reported to aggravate between 9 and 11 weeks and the end point is between 10-13 weeks (Beal and Ferrante, 2004; Mangiarini *et al.*, 1996) . Therefore, the inclusion of 10 weeks was the last time point. Overall the selection of time points fell into two categories 50% understanding the initial stages of disease progression (E9-3w) and the rest 50% to recapitulating the signaling in the course of disease progression (4w-10w). Mice were euthanized by cervical dislocation and the brains were removed followed by the dissection of the striatum. Whole brains were harvested for embryonic time points (Figure 3.6). All tissues were collected in Eppendorf tubes, snap frozen on dry ice and stored at -80°C for peptide array or Western blot analyses the details of which are discussed in section 3.4 and 3.5 respectively.

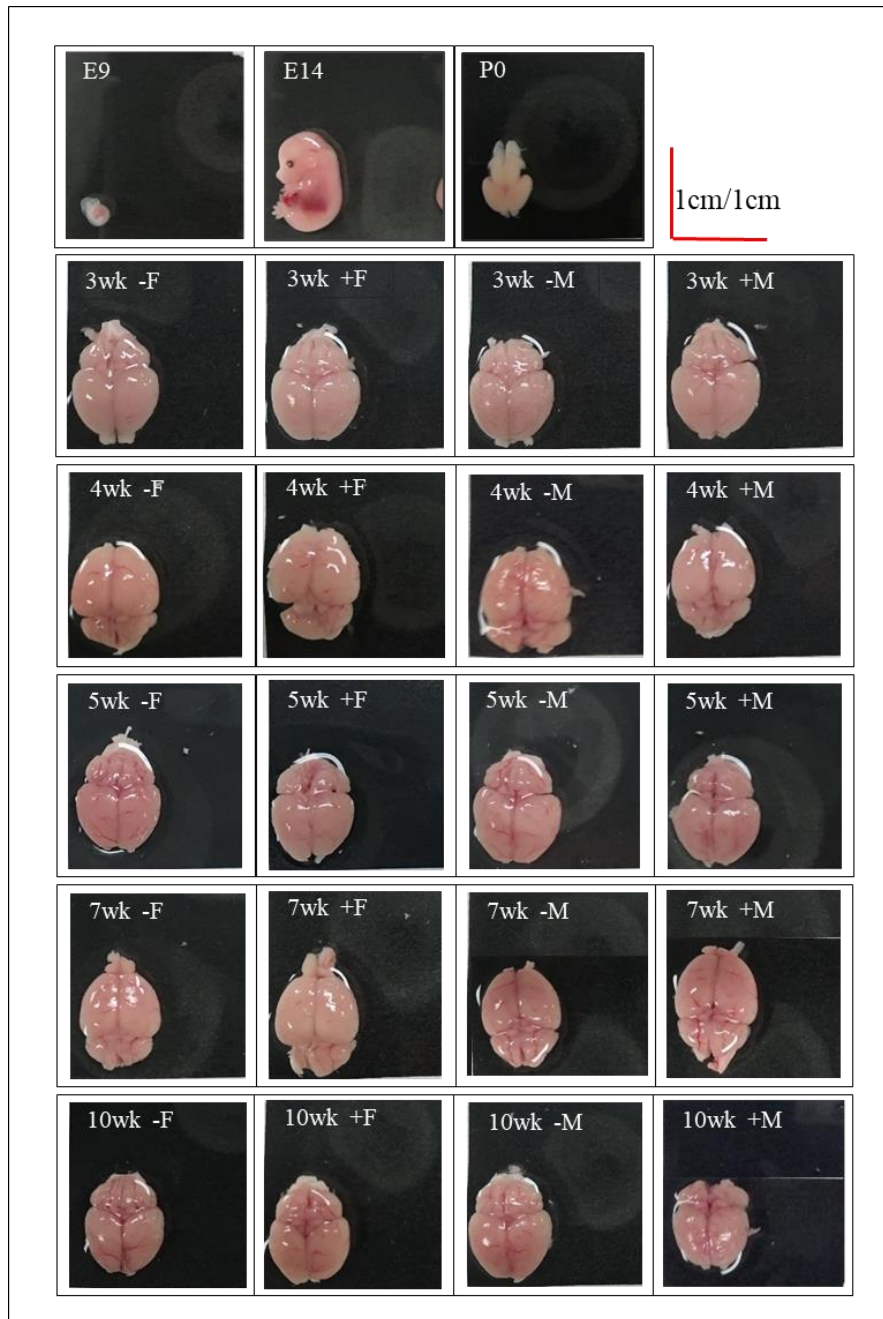


Figure 3.6: The panel shows the brain tissue harvested from different time points which were studied.

The top row shows the 9-day and 14-day embryos followed by a P0 brain. The rest of the panel comprises representative images indicating degeneration in the brain from 3 weeks to 10 weeks in both males and females. The first left column are “negative female” (-F) murine brains, i.e., healthy control (HC) females without mHtt. This is followed by “positive female” (+F) brain, i.e., with mHtt (HD). The following two columns are “negative male” (-M) followed by the extreme right column the “positive male” (+M). (Image courtesy VIDO – InterVac Animal care).

3.3 Analysis of neuronal morphology by NeuroLucida 360

Huntington's disease (HD) and healthy control (HC) neural stem cells (NSCs) were cultured in 6-well tissue culture dishes, as described earlier in section 3.2.1. Phase-contrast images of both cell lines were acquired at 20x magnification using the Olympus CKX41 light microscope. The acquired images were analyzed using NeuroLucida 360 software (MBF Biosciences, USA) (<https://www.mbfbioscience.com/neuroLucida360>) (Dickstein *et al.*, 2016). Quantitative evaluation of HD and HC NSCs morphology was performed, as described previously (Dickstein *et al.*, 2016), to determine neurite outgrowth, number of soma, and soma size. An average of six HC and HD fields were analyzed. Each image corresponds to a field from one well of a 6 well plate and the data are presented as the mean \pm SEM.

3.4 Peptide array technology

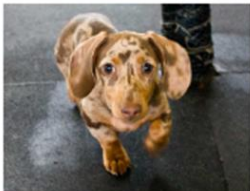
The peptide array technology was used to assess the global kinase profile in both the NSCs and the murine tissue. The array used for the cellular kinome profiling was a previously designed 298 peptide array and I designed the murine array which consists of 1268 peptides. The synthesis, spotting and general methodology are described below.

3.4.1. Peptide synthesis and spotting

The customized peptide microarrays described previously (Jalal *et al.*, 2009) were obtained from JPT peptide technologies GmbH (Germany). DAPPLE 2 was used to generate a list of 270,000 peptides from which a list of 1268 peptides were selected to print on the array. The peptides list with the peptide name, uniprot ID, target phosphosite and peptide sequence. These peptides were printed on a modified glass slide in replicates of 9, each measuring $\sim 350 \mu\text{m}$ with a spot concentration of 100 fmol/mm^2 . The peptides and the corresponding phospho-sites are listed in the (Supplementary Table S1) (Figure 3.7). Only the murine proteins (corresponding peptides) which have a human homolog were selected. The selection was completed by an in depth analysis of the published literature and utilizing web based online databases such as Phosphosite plus (Hornbeck *et al.*, 2012) (www.phosphosite.org), for phosphorylation events.

Home PTMs and databases About/help Contact

DAPPLE 2



Target organism

Select organism by:
Name Taxonomic ID

Please select the target organism for which you want to predict PTM sites:

PTM database

Select post-translational modification (PTM) type:

Select database:

Search Parameters

Select the search method. BLAST is more sensitive, while RAPSearch 2 is faster.

BLAST RAPSearch 2

Select the maximum number of results to return per known PTM site:

Enter your email address. Once DAPPLE 2 has finished running, you will receive an e-mail with a link to your results.

Figure 3.7: Screenshot of the user interface of the DAPPLE2 web server.

The target organism and is uploaded and the PTM selected using a dropdown menu. The results are emailed to the user after the selection is complete and submitted.

3.4.2 Processing peptide array

Briefly, 10^7 cells, either HD or HC NSCs, were harvested and pelleted by centrifugation at 7000xg for 10 minutes at 4°C. Murine whole brain (embryonic) and striatal tissue were weighed and ice cold kinome lysis buffer was added and allowed to soak for 10 minutes. A hand held homogenizer was used for disruption of the cell pellets and tissue. Cells were lysed in freshly prepared kinome lysis buffer [20 mM Tris pH 7.5, 150 mM NaCl, 1 mM EDTA, 1 mM EGTA, 1% Triton, 2.5 mM sodium pyrophosphate, 1 mM beta-glycerophosphate, 1 mM Na_3VO_4 , 1 mM NaF, 1 µg/ml Leupeptin, 1 µg/ml Aprotinin, 1 mM phenylmethylsulphonyl fluoride] and the crude lysates were centrifuged at 12000xg for 10 minutes (30 minutes for tissues) at 4°C. The supernatant or clarified lysates were transferred to fresh microcentrifuge tubes. Total protein concentration in the lysates was determined using the BCA protein assay (Pierce BCA protein assay kit, Thermo Fisher Scientific) and normalized using the appropriate volume of lysis buffer. Lysates were diluted to achieve a final protein concentration of ~1.5mg/ml and 80 µl of the clarified lysate was mixed with 10 µl of activation mix [50 % Glycerol, 50 µM ATP, 60 mM MgCl_2 0.05 % Brij35, 0.25 mg/ml BSA] in a separate microcentrifuge tube and incubated on ice for 10 minutes. The mixture was then applied on the peptide arrays. After incubation at 37°C for two hours in a humidified chamber, arrays were washed with 1X PBST (1% Triton in 1X PBS) followed by staining with a phosphoprotein solution (Pro-Q Diamond Phosphoprotein Stain, Invitrogen) for an hour in the dark at room temperature. The arrays were then washed by gentle shaking for 10 min in a de-staining solution comprised of 20% acetonitrile and 50 mM sodium acetate, pH 4.0. The de-staining process was repeated three times. A final wash was performed with ddH₂O and the arrays were air-dried (Figure 3.8).

3.4.3 Signal detection and bioinformatics analyses

The processed arrays were then scanned using a GENEPIX professional 4200A microarray scanner at 532 to 560 nm with a 580 nm filter. The signal intensity corresponding to each phosphorylated peptide on the array was determined using the Genepix software, and the raw data were analyzed using the PIIKA 2 (Platform for Intelligent, Integrated Kinome Analysis) online tool (<http://saphire.usask.ca/saphire/piika/index.html>) (Maattanen *et al.*, 2013b).

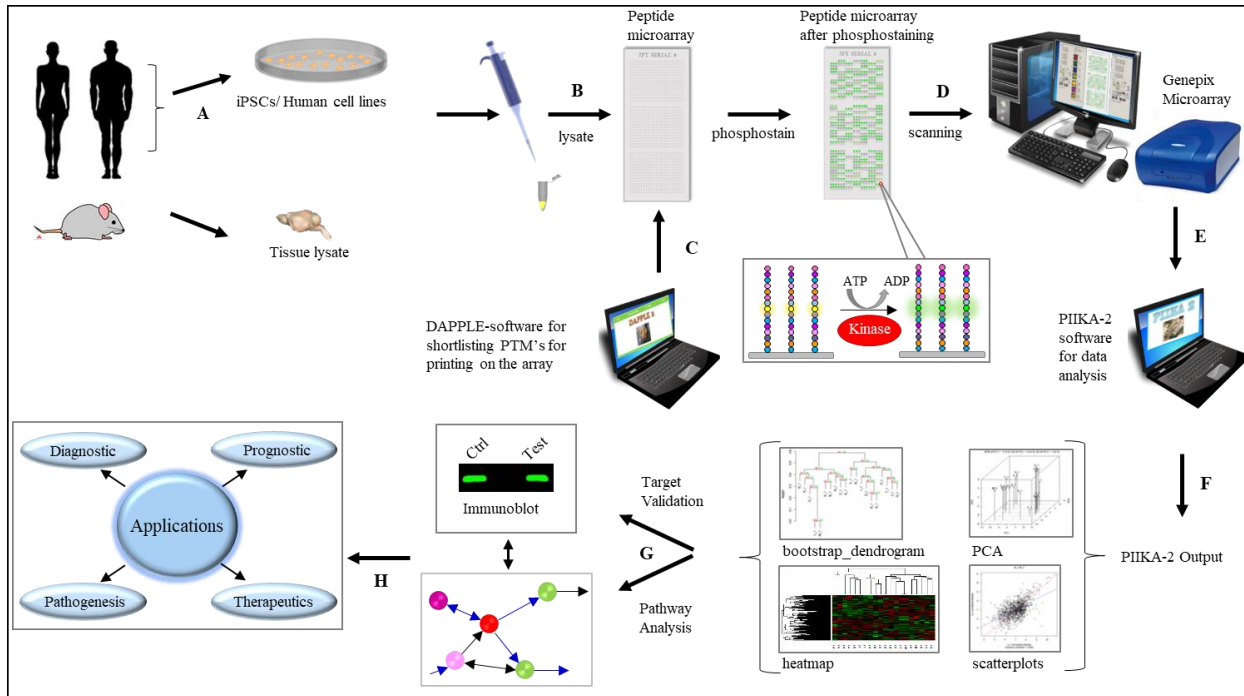


Figure 3.8: Kinome analysis with peptide arrays.

(A) Samples can represent cell lines, isolated cell types (like peripheral blood mononuclear cells) or tissues. (B) Cellular lysates are incubated on the array in the presence of ATP. (C) Arrays are either commercially purchased or generated through selection of peptides from online databases or phosphorylation site prediction software such as DAPPLE 2. (D) The signal from phosphostained or radio-labelled arrays are detected and quantified. (E) The output of the scanned arrays is analyzed by using software platforms such as PIKA 2 or other approaches. (F) Results from kinome analysis are depicted in different formats such as heatmaps and principal component analysis (PCA) plots. (G) Biological events suggested through kinome analysis are typically validated through independent approaches such as functional assays or phosphorylation specific antibodies. (H) Finally, results from the validation can be used for various applications (Baharani *et al.*, 2017).

3.4.3.1 Platform for Intelligent, Integrated Kinome Analysis (PIIKA 2)

The array was printed with technical replicates and the analysis was completed using PIIKA 2 software (Maattanen *et al.*, 2013b). This pipeline is specifically designed for the data collected from peptide arrays (Figure 3.9). The pipeline successfully handles the negative values, and without distorting the raw values, generates statistically significant outputs. The foreground and background mean values of each array were uploaded onto PIIKA 2. These values were utilized to perform statistical analyses and generate output files consisting of heatmaps, PCA plots, etc. After analyzing the outputs, I decided on the different validation strategies to be incorporated to determine the differential phosphorylation status of the peptides in the test sample (HD) versus the controls.




Click [here](#) for help regarding the files and parameters listed below.
The sample files mentioned below correspond to the sample data mentioned in the paper describing PIIKA 2.

PIIKA 2 is licensed under a [Creative Commons Attribution-NonCommercial-ShareAlike 4.0 International License](#). If you would like to use it for commercial purposes, please [contact us](#).

Step #1: Input files

No file chosen

No file chosen

No file chosen

(Required) Main input file
Contains the intensity values for your arrays.
[Sample file](#)

(Optional) Treatment-control combinations
Specifies the treatment-control combinations in your dataset.
[Sample file](#)

(Optional) Treatment-control combinations: for F-value visualization
Specifies the treatment-control combinations for F-value visualization files.
[Sample file](#)

Step #2: Required parameters

(Optional) If you are using a commercial off-the-shelf array, choose it here, and the number of technical replicates and the number of peptides will be automatically filled in. If you are using a custom array, ignore this option.

Number of technical replicates per unique peptide on the same array

Number of treatments

Number of unique peptides on the array

Number of inter-array replicates

Note: if you entered a value greater than 1 for this option, please use the button below to indicate whether the inter-array replicates represent biological replicates or technical replicates.

Step #3: Optional parameters

Omit background subtraction?
If you choose "yes", instead of subtracting the background measurements from the foreground measurements, only the foreground measurements will be used (although the background measurements must still be provided).

Normalization method

Distance metric for hierarchical clustering

Linkage method for hierarchical clustering

Perform chi-square test?
****Note that the default choice for this option is now "Yes"****

Perform F-test?
Applies only if your dataset contains 2 or more biological replicates.

Perform biological subtraction before performing F-test?
Applies only if you are performing an F test.

Perform random tree analysis? (REMINDER: If you select this option, you must name your samples as described in the [input guide](#) (e.g., A-1, A-2, B-1, B-2, etc.). Also, please expect to wait a few hours for your job to finish if you select this option).
Note: that to perform the random tree analysis, the number of inter-array replicates must be 1 (and thus the number of treatments must be equal to the number of arrays).
If you selected Yes for this option, please enter the number of random trees to generate (default = 2000).

Perform peptide subset analysis? (REMINDER: If you select this option, you must name your samples as described in the [input guide](#) (e.g., A-1, A-2, B-1, B-2, etc.). Also, please expect to wait a few hours for your job to finish if you select this option).
Note: that to perform the peptide subset analysis, the number of inter-array replicates must be 1 (and thus the number of treatments must be equal to the number of arrays).
If you selected Yes for this option, please enter the number of random trees to generate for the random tree tests (default = 1000).

If you selected Yes for this option, please enter the maximum number of peptides to include in a peptide subset. The smaller the number, the faster your job will complete (default = 50).

Value of alpha (false positive rate) for statistical significance testing

Estimated background probability that a peptide will be differentially phosphorylated

Step #4: E-mail address

(Required) Please enter your e-mail address here. Once your job is finished running, you will receive an e-mail with a link where you can download the results. Please note that your e-mail address may be saved for the purposes of tracking usage and of informing you of updates and bug fixes to PIIKA 2.

Step #5: Submit!

Figure 3.9: Screenshot of the user interface of the PIIKA 2 web server.

It involves five steps which includes uploading the file, the parameters for the analysis and the tests to be performed. The results are emailed to the user after the selection is complete and submitted.

3.4.3.2 InnateDB

Next, step was to perform functional gene enrichment analyses using the InnateDB online tool to map the dysregulated phosphorylated targets to cognate signaling pathways. The details of the online web tool are described earlier in section 1.3.3.2. InnateDB mapped these targets to various canonical signaling pathways and a $P \leq 0.05$ was used as a cut off for this analysis. Using phosphosite-specific information derived from PIKA 2, InnateDB further classified these pathways as either upregulated or downregulated. Consequently, a list of the potentially up and down regulated pathways were shortlisted using the P-values for both NSC and R6/2 dataset (Figure 3.10).

Figure 3.10: Screenshot of the user interface of the InnateDB web server.

The selection to perform pathway analysis is followed by uploading the file and the results can be downloaded.

3.5 SDS-PAGE

The independent validation of the significantly differentiated peptides; both in NSCs and murine study; based on the bioinformatics pipeline was performed by SDS-PAGE and Western blotting discussed in the following sections. Cell lysates (NSC) were prepared by first aspirating the media from the culture plates followed by gently rinsing the culture plates once with 1X PBS. The cells were then harvested using Axol neural unlock. This was followed by centrifuging to generate a pellet which was lysed in a freshly prepared RIPA lysis buffer (Table 3.4). The murine tissue (R6/2) samples were suspended in RIPA lysis buffer and sonicated with continuous 40 mA pulses for 3s five times on ice. Sonicated samples were centrifuged at $12,000 \times g$ at 4°C for 30 min and supernatant was collected for Western blot analysis. Protein samples were resolved via sodium dodecyl sulphate (SDS) Polyacrylamide gel electrophoresis (PAGE). SDS-PAGE was performed using the Mini-Protein 4 gel electrophoresis system (#165800FC, Bio-Rad, USA). Polyacrylamide gels (10%) with a 1.5 mm thickness were cast using the appropriate glass plates provided with the gel electrophoresis pack. The resolving gel comprised 10% acrylamide, 0.8% bis-acrylamide, 0.4% SDS, 375 mM Tris HCl pH 8.8, 0.16% (w/v) APS, 0.1% TEMED and H_2O . The stacking gel comprised 4% acrylamide, 0.8% bis-acrylamide, 0.4% SDS, 125mM Tris HCL pH 6.8, 0.24% (w/v) APS, 0.1% (w/v) TEMED and H_2O . The protein samples were boiled at 100°C for 5 minutes prior to loading onto 10-well gels. The gels were run in 1x SDS running buffer at a constant voltage of 100 volts until the bromophenol blue dye front passed through the gel.

3.5.1 Western Blotting

Gels were removed carefully from the glass plates after the electrophoresis. The stacking gels were discarded and the resolving gels were overlaid on a standard extra thick pre-cut filter paper (# 84783, Thermo Scientific) soaked in transfer buffer. Nitrocellulose membranes were cut to the size of the gel and soaked in transfer buffer then overlaid on the gels. This was covered with another pre-soaked standard extra thick filter paper and the entire assembly was placed in a gel holder cassette. The gel holder cassette was placed in the Western blotting electro blotting apparatus (Bio-Rad). This was filled with Western blotting 1x transfer buffer, pre cooled at 4°C .

Once the circuit was complete by attaching the lid, the protein transfer was run for 1.5 hours at 100 volts at 4°C.

After the protein transfer was complete, the nitrocellulose membrane was removed from the cassette and placed in another container with 5% skim milk on a rocking platform and incubated for 40 minutes at room temperature. After blocking, the membrane was rinsed in 1x PBS to remove the residual skim milk followed by the addition of primary antibody buffer (Table 3.4). Primary antibodies were prepared at appropriate dilutions (listed below) and the membranes were soaked in the antibody buffer for overnight incubation at 4°C on a rocker. The membranes were washed with 1x PBST buffer 3x for 5 minutes each and then incubated with the appropriate secondary antibody (LICOR goat anti mouse/ goat anti rabbit, as mentioned below). Secondary antibodies were diluted in secondary antibody buffer (Table 3.4) at a concentration of 0.0001 µg/mL and left at room temperature on a rocker for 1.5 hours. The membranes were washed 3x with 1x PBST (Table 3.3) for 10 minutes each and used for analysis on the LI-COR Odyssey infrared scanning instrument (LI-COR, USA). Image Studio™ Lite software (LI-COR, USA) linked to the LI-COR instrument was used to acquire the image at the appropriate laser intensities. The images acquired were transformed to grey scale and exported in the .jpeg and .tiff format for later use. The analysis was completed using the intensities estimated by the Image Studio™ Lite software. The expression of tubulin was obtained from the same blot as the primary antibody. The ratio of the both phospho and total protein over tubulin was used for normalizing. This was followed by a ratio of phospho over total protein to obtain a relative phosphorylation value for that particular protein and the comparative analysis was completed using t-test.

3.5.2 Primary and secondary antibodies

Primary antibodies listed in Table 3.4 were purchased from Abcam, Cell Signaling Technologies (Danvers, USA), Thermo Fisher Scientific (Massachusetts, USA), Cedarlane (Ontario, Canada), and Sigma-Aldrich (Massachusetts, USA). Secondary antibodies for Western blotting, including IR Dye-680RD IgG (#926-68071), IR Dye-800CW IgG (#926-32211) and IR Dye-800CW IgG, (#926-32210) were purchased from Li-COR Odyssey (Nebraska, United States).

Table 3.3: List of stock solutions of chemicals/reagents. Shown in in this Table is a list of stock solutions of specific chemicals/reagents and their composition.

Buffer/ Media	Composition
1x PBS (Phosphate buffered saline)	137 mM NaCl, 2.7 mM KCl, 8 mM Na ₂ HPO ₄ , 1.46 mM KH ₂ PO ₄ , pH 7.4.
1x PBST	1x PBS, 0.1% Tween-20 (v/v)
Blocking buffer	5% Skim milk in 1x PBS buffer (5 g Skim milk in 100 mL PBS buffer)
Primary antibody buffer	0.1% Tween-20, 5% BSA in 1x PBS
Secondary antibody buffer	0.1% Tween-20, 5% BSA in 1x PBS
Western blotting Transfer buffer	25 mM Tris, 192 mM glycine, pH 8.3, 20% methanol.
1X SDS PAGE Running buffer	25 mM Tris, 192 mM glycine, 0.1% SDS, pH 8.3.
RIPA lysis buffer	50 mM Tris-HCl, 150 mM NaCl, 0.1% SDS, 1% Triton X-100 and 0.5% sodium deoxycholate. Buffer supplemented with commercial protease and phosphatase inhibitor cocktails
Peptide Array Buffer	20 mM Tris pH 7.5, 150 mM NaCl, 1 mM EDTA, 1 mM EGTA, 1% Triton, 2.5 mM sodium pyrophosphate, 1 mM beta-glycerophosphate, 1 mM Na ₃ VO ₄ , 1 mM NaF, 1 µg/ml Leupeptin, 1 µg/ml Aprotinin, 1 mM phenylmethylsulphonyl fluoride
Refer to Table 3.1 for commercial source information	

Table 3.4: List of primary antibodies used. Shown in this Table are the names, and working concentrations/dilutions of primary antibodies used in Western blotting.

Primary Antibody	Working Concentration / Dilution
Anti PAK1 + PAK2 + PAK3 (CST 2604)	1:1000
Anti-AKT (CST 2938S)	1:1000
Anti-Cdk2 (ab 32147)	100 μ l at 0.128 mg/ml / 1:1000
Anti-Cofilin (CST 3313S)	1:1000
Anti-LIMK1 Abcam (ab 95186)	100 μ l at 0.2 mg/ml / 1:1000
Anti-MAKPAPK2 (CST 9329S)	1:1000
Anti-p38 (ab170099)	100 μ l at 0.273 - 0.288 mg/ml / 1:1000
Anti-Profilin 1 (CST 3237)	1:1000
Anti-PTEN Abcam (ab 31392)	100 μ g at 1 mg/ml / 1:1000
Anti-ROCK2 (CST 8236)	1:1000
Anti-Slingshot (Cedarlane SK6410)	1:500
Anti-TAB1 (ab 76412)	1:1000
Anti-ULK1 (CST 6888)	1:1000
Phospho AKT1 (CST 9018S)	1:500
Phospho Cdk2 (ab 194868)	100 μ l at 1.14 - 2.34 mg/ml / 1:500
Phospho Cofilin, (CST 5175S)	1:500
Phospho LIMK1 (ab 38508)	100 μ g at 1 mg/ml / 1:500
Phospho p38 (ab 60999)	100 μ g at 1 mg/ml / 1:500
Phospho PAK (ab 2477)	100 μ g at 1.94 mg/ml / 1:1000
Phospho Profilin 1 (ab 215752)	1:1000
Phospho PTEN (ab 131107)	1:1000
Phospho ROCK2 (ab 228008)	100 μ l at 0.13 mg/ml / 1:1000
Phospho TAB1 (Thermo PA5-12851)	1:500
Phospho ULK1(CST 8054S)	1:500
α -Tubulin (ab4074)	1 μ g/ml / 1:20,000
β -actin (sc 4778)	0.2 μ g/mL / 1:20,000

3.6 NetworKIN

The validation of the significantly differentiated peptides was completed by Western blotting using commercial antibodies. This was used to validate a single pathway proposed to be dysregulated in the disease. There were many other peptides in the NSC and murine output that could be validated but instead I took a high throughput approach. This allowed to summarize the results utilizing an online tool (NetworKIN) that predicts the upstream kinases that regulate the significantly phosphorylated peptides on the array.

NetworKIN (Version 3.0) platform was used to identify candidate kinases upstream of the phosphosites identified in our kinome analyses (Figure 3.11). The NetworKIN tool predicts the kinase substrate relationship (Linding *et al.*, 2008). The tool integrates information on various kinase-specific and phospho-binding domain-specific motifs derived from the NetPhorest database and uses STRING to improve the prediction of cellular kinase-substrate relationships (Linding *et al.*, 2008) (Miller *et al.*, 2008).

Significantly dysregulated (hyper-phosphorylated or hypo-phosphorylated phosphosites) were used to predict upstream kinases using the NetworKIN tool (<http://networkin.info/index.shtml>) (Version3.0) (Linding *et al.*, 2008). The original list was divided into two separate list and then uploaded individually on the NetworKIN online tool as hyper and hypo phosphorylated peptides. The resulting predicted annotations were filtered using a NetworKIN confidence score cut-off of 3.0 for the cell lines dataset and a NetworKIN score-difference cut-off of 4.0 for the mouse dataset. Since the mouse dataset comprised of 1268 unique peptides and the cell line 298 a higher cut off was used for it. The score-difference defined the maximum difference between the best prediction and the second-best prediction. The results can be downloaded in an excel format from the web. The identified kinases for both, hyper- and hypo-phosphorylated phosphosites were plotted on a mammalian kinase-dendrogram, for visual representation, generated using the KinMap_{beta} (Eid *et al.*, 2017).

NetworKIN switch to NetPhorest Home Download Help About

This is the high-throughput interface for NetworKIN. Click [here](#) to go back to the low-throughput version.

NetPhorest 2.1 Update
 We are happy to announce the release of NetPhorest 2.1, which fixes two major bugs that resulted in arbitrary scores from neural network predictors on SH2 domain, and partially arbitrary scores from neural networks on other domains. PSSM/scansite predictors remain unchanged. Both web and command line versions were affected. We recommend repeating any analysis performed before May XX, 2017.
[Learn more and download the updated binaries on the download page.](#)

Select the sequence database:
 Human - Uniprot 2013/12

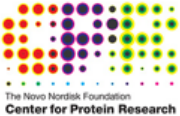
To download the sequence database(s) in fasta format, please visit the [download page](#)

Put modified sites below in the format:
 Protein ID, Position, Residue (space/tab delimited) Example: #1, #2, ProteomeDiscoverer

OR select a MaxQuant output file:

If you use any of the data from this web site please cite this article: [Horn et al., KinomeXplorer: an integrated platform for kinome biology studies. Nature Methods 2014 Jun;11\(6\):603-4.](#)



(C) 2005-2013 Rune Linding and Lars Juhl Jensen

Figure 3.11: Screenshot of the user interface of the NetworKIN web server.

The input files are uploaded and the score-difference cut-off is defined. The results can be downloaded after submitting the files.

3.7 KinMAP

The predicted kinases based on the NetworKIN online tool were mapped on a “kinome tree”, the details of which are described here. KinMap (<http://kinhub.org/kinmap/>) is a web-based tool to map kinases based on the kinome data. The software is built on the availability of a dataset that links them to the upstream kinases (Figure 3.12). The knowledge of the structural, biochemical, functional and disease association of a kinase is utilized to predict the upstream kinases. This platform facilitates a visual representation of the predicted kinases and represents such data on a kinome tree. The sophisticated kinome tree annotations also allow a comparison of the kinases between sexes, disease progression states, etc.; thus, providing more options for therapeutic interventions. KinMap supports multiple input and output formats and can recognize alternate kinase names thus making it extremely user-friendly. The names of the kinases can be manually inputted or uploaded on the web server. There are different symbols which can be color coded and used to represent the kinase. The size of the symbols can indicate their significance. These high quality pictures can be downloaded after submitting the data in different image formats.

Eight different families of enzymes (Figure 3.13) can be represented on the kinome tree, including:

1. AGC - Containing PKA, PKG, PKC families
2. CK - Cell/Casein Kinase
3. STE - Homologs of yeast Sterile 7, Sterile 11, Sterile 20 kinases
4. TKL - Tyrosine kinase-like - TKL
5. TK - Tyrosine kinase
6. CMGC- Containing CDK, MAPK, GSK3, CLK families
7. CAMK - Calcium/calmodulin dependent protein kinase - CAMK
8. APK - Atypical protein Kinases

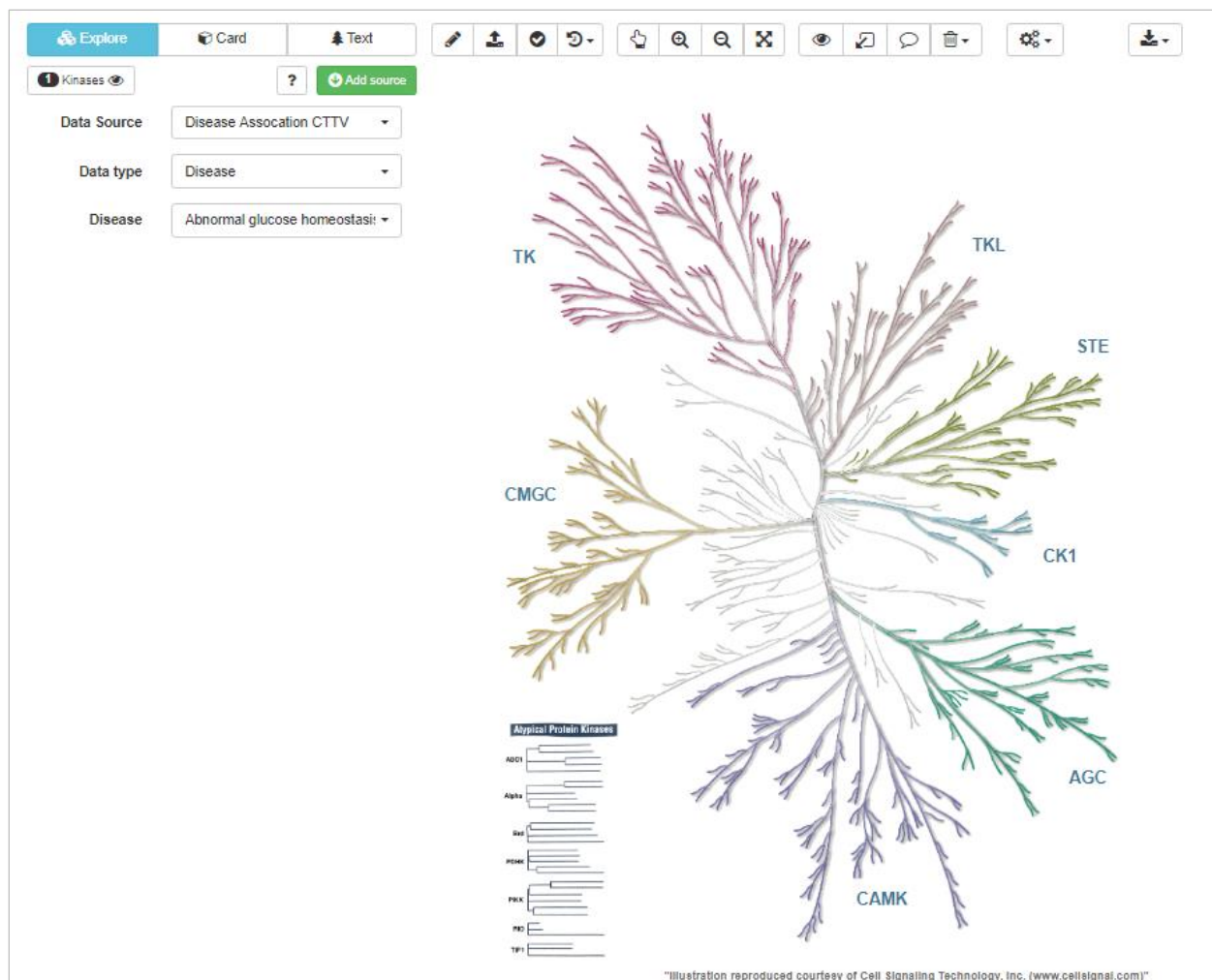


Figure 3.12: Screenshot of the user interface of the KinMap web server.

The input file can be uploaded manually or imported from an excel format and after submission the kinases are represented on the kinome tree. The annotated image of the human kinome tree can be downloaded in different formats (PNG and SVG) for use.

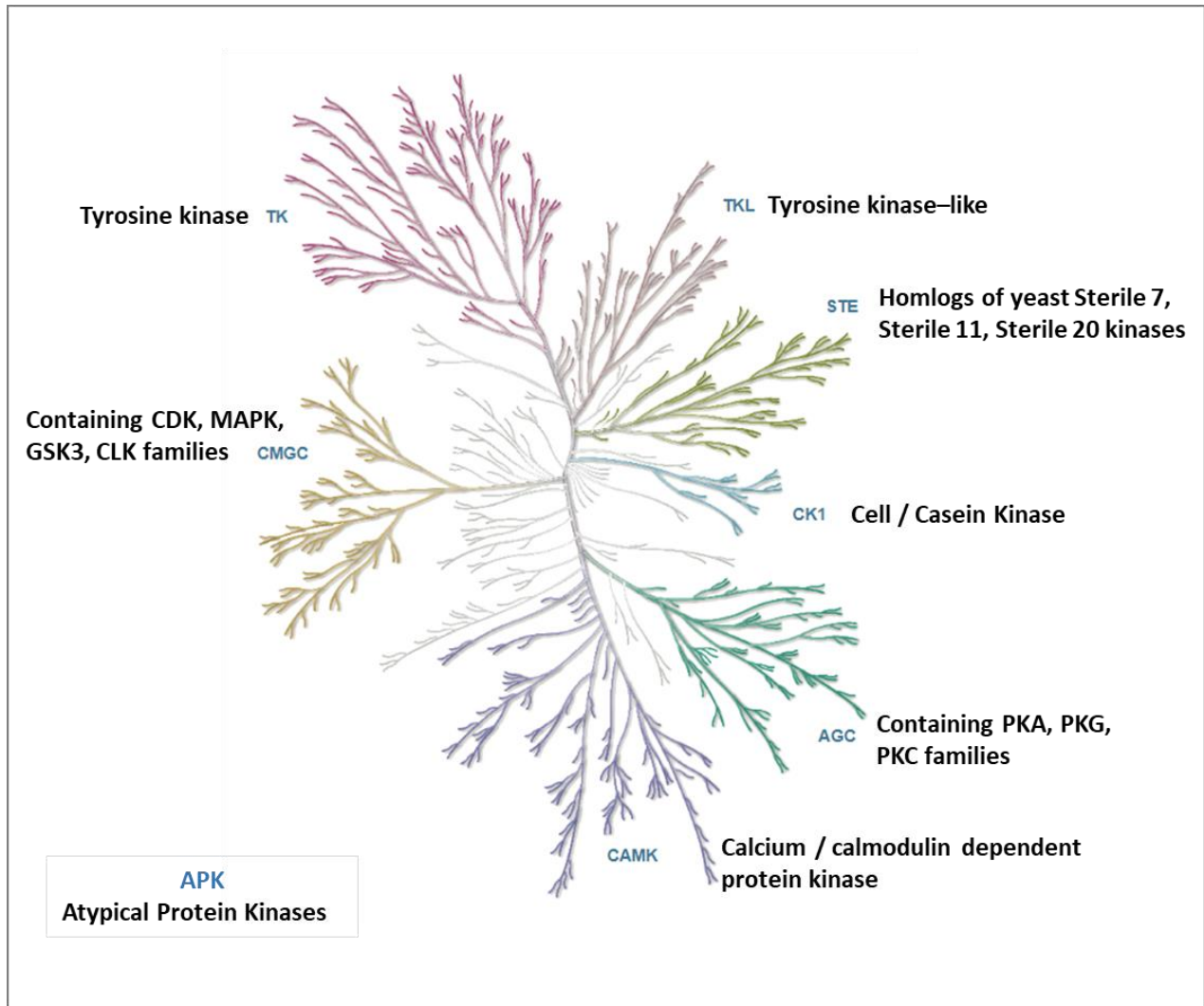


Figure 3.13: Graphic representation of the kinome tree with all families.

[Containing PKA, PKG, PKC families 2 (AGC), Cell/Casein Kinase (CK), Homologs of yeast Sterile 7, Sterile 11, Sterile 20 kinases (STE), Tyrosine kinase-like (TKL), Tyrosine kinase (TK), Containing CDK, MAPK, GSK3, CLK families (CMGC), Calcium/calmodulin dependent protein kinase (CAMK), Atypical protein Kinases (APK)].

4. RESULTS

The results discussed in this section have been generated by a mix of both experimental and bioinformatics analyses. For ease of explanation, Figure 4.1 outlines the different bioinformatics tools that were used to generate and validate the experimental data. The blue (input), light green (output) and dark green represent the bioinformatics tools used for the analysis of the experimental data. The red indicates the peptide array experiments using cell / tissue lysates, followed by validation using Western blotting.

4.1 Human neural stem cells

A previously designed peptide array comprising 298 unique peptides that represented well-characterized signaling proteins implicated in cell survival, proliferation, motility, and immune response-related pathways was used for kinome analysis (Arsenault *et al.*, 2012a). This array was used as a platform to screen for potential signaling differences in NSCs derived from an HD patient. As a biological control, HC NSCs were utilized. To ensure reproducibility and statistical rigor, arrays were designed to include a total of nine replicates of each unique peptide (Jalal *et al.*, 2009; Li *et al.*, 2012). Overall, our analyses led to the identification of a total of 128 peptides that demonstrated significant differences ($P < 0.1$) in their levels of phosphorylation between the HD and HC NSCs. Fifty-two of these differentially phosphorylated peptides were hyper-phosphorylated in HD compared to HC, while 76 were found to be hypo-phosphorylated. A peptide was selected for further analysis if its P-value was ≤ 0.1 with a fold change of $\pm > 1$ (Li *et al.*, 2012; Maattanen *et al.*, 2013a; Maattanen *et al.*, 2013b). This liberal threshold allowed to reduce the possibility of losing potential phosphorylated events while performing pathway analysis. Finally, the priority of kinome analysis is to identify biological events that are subsequently validated through independent approaches. This increases the likelihood of identifying kinases that are dysregulated based on significantly differentially phosphorylated peptides in the HD NSCs. The list of up- and down-regulated peptides along with their fold changes and P-values based on PIKA 2 output is provided in Supplementary Table S2.

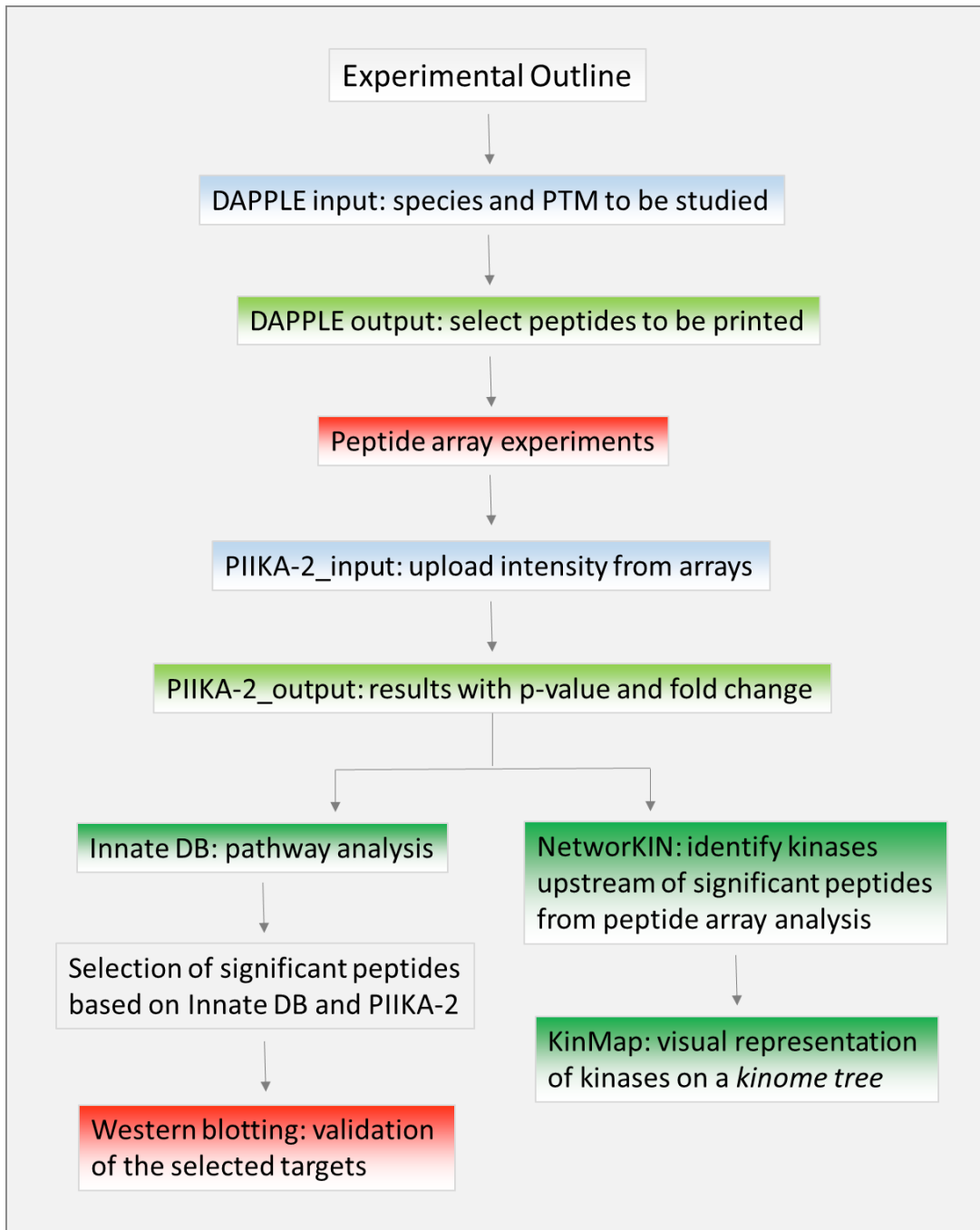


Figure 4.1: Experimental outline.

The flowchart outlines the general pipeline for the peptide array analysis, up to the validation step. The PIIKA outputs are divided into two where one follows the validation experiments (left) and the other follows the bioinformatics pipeline (right) used to predict the upstream kinases that are dysregulated in the disease process. Blue and green represents the online software tools utilized for the experiments. Red indicates the experiments performed to generate the data followed by validation. PTM here refers to phosphorylation events.

The next step was the functional gene enrichment analyses using the InnateDB tool to map the dysregulated phosphorylated targets to cognate signaling pathways. InnateDB mapped these targets to 24 canonical signaling pathways ($P \leq 0.05$). Using phosphosite-specific information derived from PIIKA 2, InnateDB further classified these pathways as either upregulated or downregulated (Breuer *et al.*, 2013). Consequently, four pathways as potentially upregulated and 20 pathways as potentially downregulated were identified (Table 4.1 and 4.2). The InnateDB output is presented in five columns for simplicity, as shown in the Tables below, which represents the pathway name followed by ID and the database that provided the information under the column source name which is followed by P-value and finally gene names involved in the pathway. InnateDB integrates information from a variety of external resources (PID, NID, KEGG etc.) thereby, supplementing its own curated interactions (Breuer *et al.*, 2013). Such factors make it necessary to broaden the search and carefully compare the outputs of both PIIKA 2 and InnateDB to identify common peptides that were significantly differentially phosphorylated for further validation by Western blotting (Table 4.3).

A number of pathways were listed in the output from InnateDB such as p53 mediated signaling, caspase cascade etc. The peptides dysregulated in the cytoskeletal pathway were the most prominent based on PIIKA 2, InnateDB and Neurolucida results, discussed later. The peptides selected for validation by Western blotting were LIMK1 and cofilin which are shown in the next section.

Table 4.1: List of up regulated pathways in NSCs along with the P-values (<0.05) based on InnateDB pathway analysis.

Pathway Name	Pathway ID	Source Name	P-value	Gene Symbols
Il12 and STAT4 dependent signaling pathway in Th1 development	4054	PID BIOCARTA	0.01	MAPK14, STAT4
p53 pathway	15289	PID NCI	0.03	AKT1, CDK2, MAPK14, MDM2, PPP2CA, TP53
p53 signaling pathway	597	KEGG	0.05	BAX, CASP3, CDK1, CDK2, MDM2, PTEN, TP53
IL2	15918	NETPATH	0.05	AKT1, BCL2, CDK2, CREB1, EIF4EBP1, FYN, JAK1, MAPK14, MKNK1, NFKB1, PIK3R1, PIK3R2, PTK2B, RELA, RPS6KB1, STAM2, STAT3, STAT4

Table 4.2: List of down regulated pathways in NSCs along with the P-values based on InnateDB pathway analysis.

Pathway Name	Pathway ID	Source Name	P-value	Gene Symbols
Caspase Cascade in Apoptosis	14995	PID NCI	0.01	ACTA1, AKT1, BAX, BCL2, CASP3, LIMK1, RIPK1, XIAP
Posttranslational regulation of adherens junction	15876	PID NCI	0.02	CASP3, CTNNB1, EGFR, FYN

stability and disassembly				
LPA receptor mediated events	15008	PID NCI	0.02	AKT1, CASP3, EGFR, NFKB1, PIK3R1, PTK2B, RELA
Apoptotic factor-mediated response	18658	REACTOME	0.03	CASP3, XIAP
Caspase cascade in apoptosis	4166	PID BIOCARTA	0.03	CASP3, XIAP
Integrin signaling pathway	4024	PID BIOCARTA	0.03	ACTA1, FYN
M-calpain and friends in cell motility	4086	PID BIOCARTA	0.03	ACTA1, EGFR
Nephrin/Neph1 signaling in the kidney podocyte	14899	PID NCI	0.03	AKT1, FYN
Phagosome	10394	KEGG	0.03	EEA1, NCF1
SMAC binds to IAPs	13396	REACTOME	0.03	CASP3, XIAP
SMAC-mediated apoptotic response	17242	REACTOME	0.03	CASP3, XIAP
SMAC-mediated dissociation of IAP: caspase complexes	13395	REACTOME	0.03	CASP3 , XIAP
Sema3A PAK dependent Axon repulsion	13910	REACTOME	0.03	FYN, LIMK1
Syndecan-3-mediated signaling events	15336	PID NCI	0.03	EGFR, FYN
Thromboxane A2 receptor signaling	14941	PID NCI	0.03	AKT1, EGFR
Viral myocarditis	8123	KEGG	0.03	CASP3, FYN
Follicle stimulating hormone	15929	NETPATH	0.03	AKT1, CREB1, EGFR, EIF4EBP1, FYN, MAPK14, MDM2, RELA

Fc gamma R-mediated phagocytosis	4359	KEGG	0.03	AKT1, CDC42, LIMK1, NCF1, PIK3R1, PIK3R2, PLCG2, RPS6KB1
Alpha6Beta4Integrin	15905	NETPATH	0.06	AKT1, CASP3, EGFR, EIF4EBP1, FYN, MAPK14, PIK3R1, PIK3R2, SMAD3
Trefoil factors initiate mucosal healing	4063	PID BIOCARTA	0.06	AKT1, CASP3, CHUK, CTNNB1, EGFR, IKBKB, PDPK1, PIK3R1, RELA

4.1.1 Validation of peptide array targets

The most prominent pathway that appeared to be dysregulated was the cytoskeleton represented by LIMK1 and cofilin on the peptide array. LIMK1 is the kinase that phosphorylates cofilin and phosphatase Slingshot dephosphorylates it. All the peptides were validated by Western blotting as shown below. It is more suitable to measure phosphorylation vs. the total expression of a protein, the ratio (relative phosphorylation) which was used to represent the difference between HC and HD (Bass *et al.*, 2017).

Table 4.3: List of peptides validated by Western blotting. Shown in this table are the names of the peptide followed by their P-values and fold change obtained from kinome analysis. The primary antibodies used were against the phosphosites, mentioned in the table.

Name	ID	Target	P-value	Fold change
Cofilin 1	P23528	S3	0.050	-1.71
LIMK1	P53667	T508	0.019	-1.56

4.1.1.1 Cytoskeletal Dynamics – LIMK1, Cofilin, SSH1L

LIMK1-T508 and cofilin-S3 were hypo-phosphorylated in the HD NSCs, thereby suggesting a third regulator, the phosphatase Slingshot (SSH1L) - in the actin cytoskeletal dynamics in HD NSCs (Figure 4.2A). The regulation of actin microfilaments found in neurons and their specific concentrations in the synaptic terminals, dendritic spines, and growth cones (Figure 1.8) (Fifkova and Delay, 1982) makes this trio (LIMK1-cofilin-SSH1L) an important regulator for the maintenance of the actin cytoskeleton (Figure 4.2B). Essential aspects of synaptic plasticity, neuronal morphology, and motility in the cell cycle in response to extracellular signals have all been associated with dynamic remodeling of actin monomers (dos Remedios *et al.*, 2003). Cofilin is inactivated by LIM kinase (LIMK)-mediated phosphorylation, which inhibits its interactions with actin filaments and actin monomers (Dawe *et al.*, 2003; Yang *et al.*, 1998). Its reactivation occurs through dephosphorylation by SSH1L-S978 (Niwa *et al.*, 2002). Cofilin is directly involved in actin dynamics and its hyper-phosphorylation leads to disintegration of the cytoskeletal structure of actin filaments (Wioland *et al.*, 2017).

The results obtained from the NSCs cannot be considered confirmatory since they are from a single sample. The results suggest that the hypo-phosphorylation of LIMK1 upstream of cofilin did not correlate with its function as a kinase phosphorylating cofilin. Another upstream regulator of cofilin is a SSH1L, which is a cofilin-S3-specific phosphatase that drives the negative feedback inhibition of LIMK1-mediated cofilin-S3 phosphorylation (Yang *et al.*, 1998). Here, both LIMK1 and SSH1L show reduced phosphorylation suggesting that they are in an inactive and active state respectively. Cofilin is hyperphosphorylated indicating that the kinase is active or the phosphatase is inactive. These results indicated a more complex mechanism for the contributions of SSH1L-LIMK1 in the regulation of cofilin. A previous study established that SSH1L and LIMK1 form a complex that leads to the dephosphorylation of LIMK1 and inhibition of its kinase activity (Soosairajah *et al.*, 2005). Furthermore, there might be crosstalk between the proteins of signaling cascades as both LIMK and Slingshot have isoforms. Profilin also affects the actin polymerization and depolymerization due to its interactions with cofilin (Minamide *et al.*, 2000; Wioland *et al.*, 2017). These results might not exactly corroborate the biology however they suggest that there is dysregulation in the phosphorylation status of the cytoskeletal proteins thus affecting actin dynamics. Further validation using different biological samples from patients might be able to resolve the output and provide significance to the values.

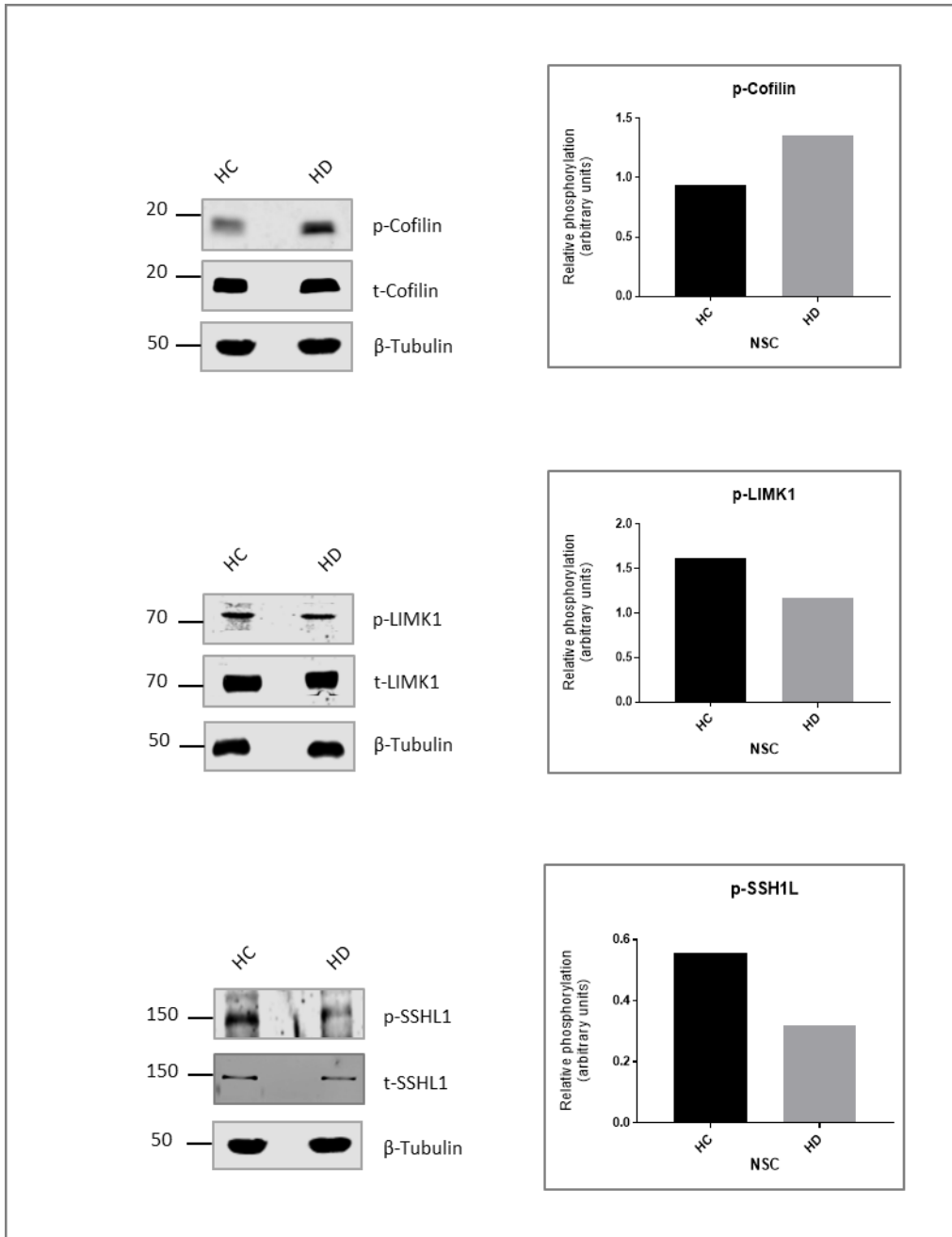


Figure 4.2A: Western blot analysis of phosphoproteins indicated the activation of cytoskeletal signalling pathways.

Representative blots along with the ratio of the phospho (p) to total (t) (relative phosphorylation) cofilin-S3, LIMK1-T508 and SSH1L-S978 in this study. Quantification of Western blot band intensities of the selected phosphorylated proteins and their respective total proteins were compared to β -tubulin. Values are from a single sample.

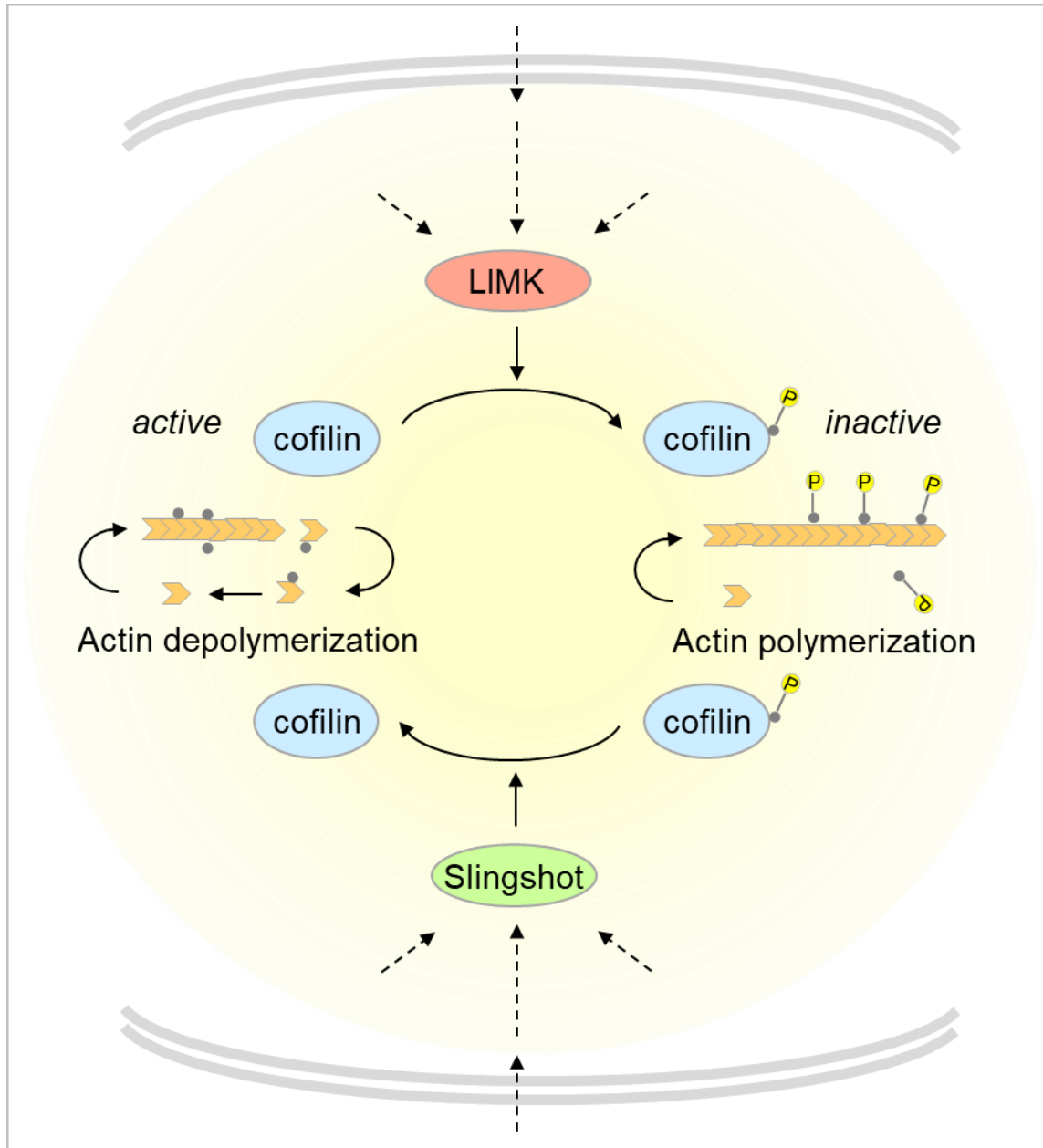


Figure 4.2B: Schematic of actin polymerization and depolymerization.

The kinase LIMK phosphorylates cofilin rendering it inactive leading to actin polymerization. The phosphatase slingshot activates cofilin by removing the phosphate. Both LIMK and Slingshot have upstream regulators shown here in dashed arrows which ultimately lead to their activation / deactivation.

4.1.2 NetworKIN

After validating the peptide array targets for cytoskeletal pathway by Western blotting, I set out to determine the upstream kinases that regulated these significantly differentially phosphorylated peptides. To do this I used a bioinformatics online tool, NetworKIN (<http://networkin.info/index.shtml>), which allows systematic matching of kinases to specific motifs. This greatly enhances the motif predictions and exploring cellular phosphorylation networks (Linding *et al.*, 2008). NetworKIN allows 60-80% prediction capability for *in silico* analyses, thus, increasing the probability of an accurate identification of a kinase responsible for a particular phosphorylation event (Linding *et al.*, 2008). NetworKIN analyses of significant upregulated peptides with a score of >3 resulted in 21 candidate kinases (Supplementary Table S3). The score-difference defined the maximum difference between the best prediction and the second-best prediction. These kinases are predicted to play a significant role in the progression of the disease process and can be explored as therapeutic targets. Kinases targeting multiple phospho sites were CK2 α (3 phosphosites, NetworKIN score range: 10.59 - 35.64), GSK3 β (3 phosphosites, NetworKIN score range: 6.17 – 9.20), GSK3 α (2 phosphosites, NetworKIN score range: 3.73 – 6.08), IKK α (2 phosphosites, NetworKIN score range: 17.18 – 17.33), JAK2 (2 phosphosites, NetworKIN score range: 3.41 – 8.07), MAP2K6 (2 phosphosites, NetworKIN score: 16.27), MAPK11 (2 phosphosites, NetworKIN score range: 8.71 – 13.04), MAPK8 (2 phosphosites, NetworKIN score range: 7.90 – 9.54), PKA α (2 phosphosites, NetworKIN score: 5.88), PKA β (2 phosphosites, NetworKIN score range: 8.64 – 8.65), PKA γ (2 phosphosites, NetworKIN score range: 8.64 – 8.65), Tyk2 (2 phosphosites, NetworKIN score range: 7.88 – 8.0). Similarly, the NetworKIN analyses of downregulated peptides with a score of >3 corresponded to 21 candidate kinases. Kinases with multiple phospho sites were PDHK1 (6 phosphosites, NetworKIN score range: 3.17 – 60.25), MAPK1 (4 phosphosites, NetworKIN score range: 5.97 – 31.24), PKB α (AKT1) (3 phosphosites, NetworKIN score range: 5.08 – 15.59), HIPK2 (3 phosphosites, NetworKIN score range: 3.30 – 4.27), Kit (2 phosphosites, NetworKIN score range: 29.90 – 30.11), MAPK11 (2 phosphosites, NetworKIN score: 5.82), MAPK3 (2 phosphosites, NetworKIN score range: 7.62 – 14.74), TRKA (2 phosphosites, NetworKIN score range: 24.44 – 24.35). Based on the analyses by NetworKIN, I sought to determine whether the WB analyses for one of the

predicted kinases, GSK3 β , and its upstream kinase, MK2, shows a difference in their phosphorylation status using phospho-specific antibodies.

4.1.2.1 GSK3 β and MK2

The analysis of the hyper phosphorylated peptide by kinome analyses and investigation by the NetworKIN platform predicted GSK3 β as one of the upstream kinases dysregulated in HD which is implicated in cytoskeletal changes (Figure 4.3A). An upstream regulator of GSK3 β is MK2, which has been implicated in the microtubule dynamics (Yuan *et al.*, 2010) was also investigated by WB (Figure 4.3B). Glycogen synthase kinase-3 is a serine/threonine protein kinase that is highly expressed in the brain. Phosphorylation of GSK3 β at S9 renders it inactive (Beurel *et al.*, 2015) and its abnormal phosphorylation of the microtubule-binding protein, tau, is suspected as a primary event in the formation of the neurofibrillary tangles in Alzheimer's disease brains (Mandelkow *et al.*, 1992). It is interesting to note similar dysfunctionalities are observed in the HD NSCs, a neurodegenerative disorder. Kobayashi *et al.* showed that the activation of LIMK1 by MK2 induces cell migration (Kobayashi *et al.*, 2006). When phosphorylated at S9, GSK3 β is enzymatically inactive and more likely to be degraded, whereas the phosphorylation of MK2 at T222 and T334 (by stress-activated kinases such as p38 α) induces MK2 enzymatic activity (Yuan *et al.*, 2010) (Figure 4.5B). The WB results indicated that the expression level of phosphorylated GSK3 β (S9) and MK2 (T222-p1 and T334-p2) were concurrently increased, suggesting the inactivation of GSK3 β which ultimately could contribute to the dysregulation of microtubule dynamics. The biological signaling can be confirmed with an increase in the sample size. The results depicted in Figure 4.3A are and not absolute but suggestive of a biological function, as they represent a single biological sample and cannot be represented in a statistically-significant format.

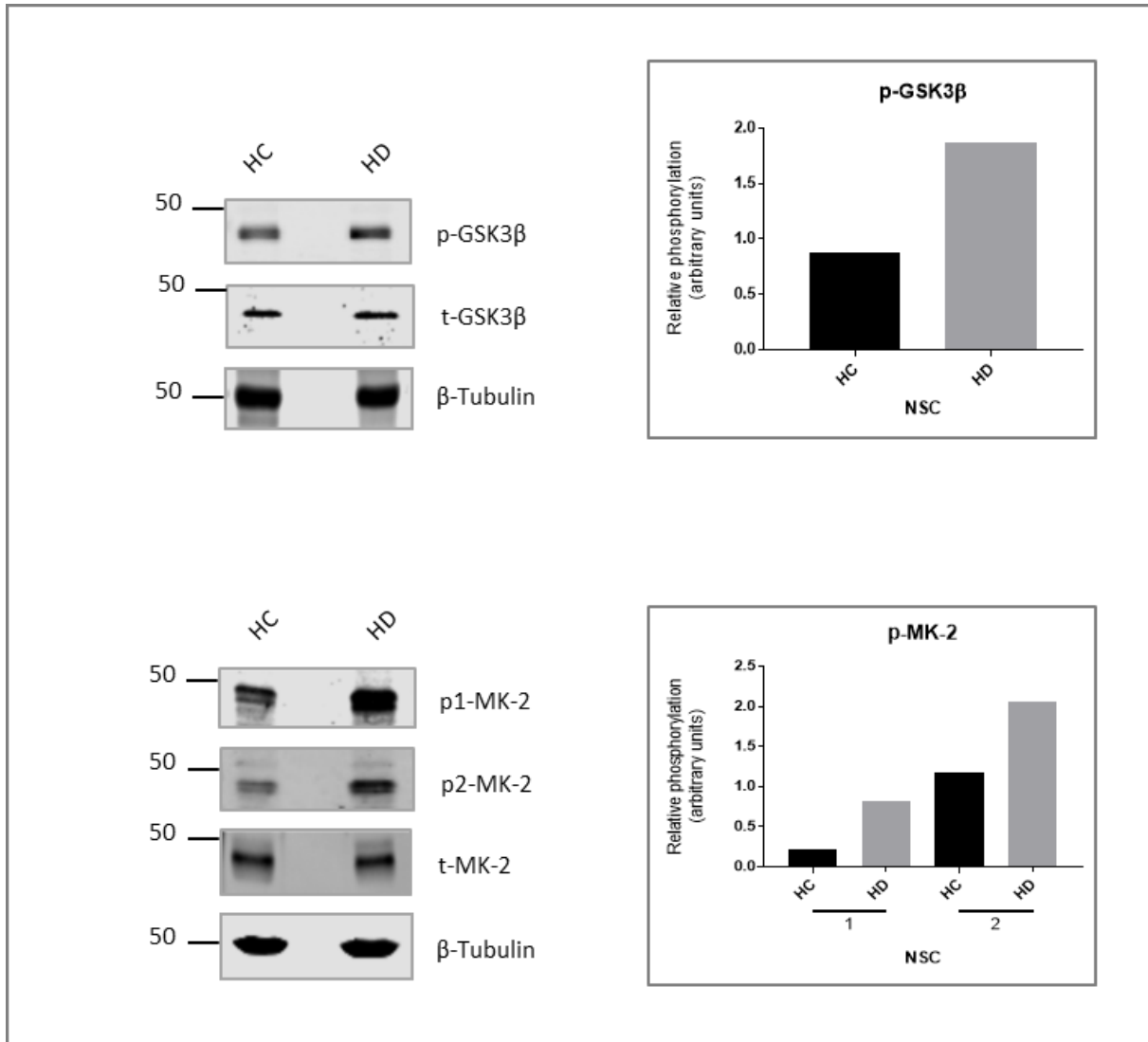


Figure 4.3A: Western blot analysis of phosphoproteins confirmed the activation of specific intracellular signalling pathways revealed by NetworKIN and its upstream kinase.

Representative blots along with the ratio of the phospho (p) to total (t) GSK3β-S9 as an output of *in silico* analysis based on the peptide array dataset. Western blot analysis of MK2 upstream of GSK3β with the ratio of the phospho (p) to total (t) MK2 (p1-T222, p2-T334). Quantification of Western blot band intensities of the selected phosphorylated kinases and their respective total proteins were compared to β-tubulin. Values are from a single sample.

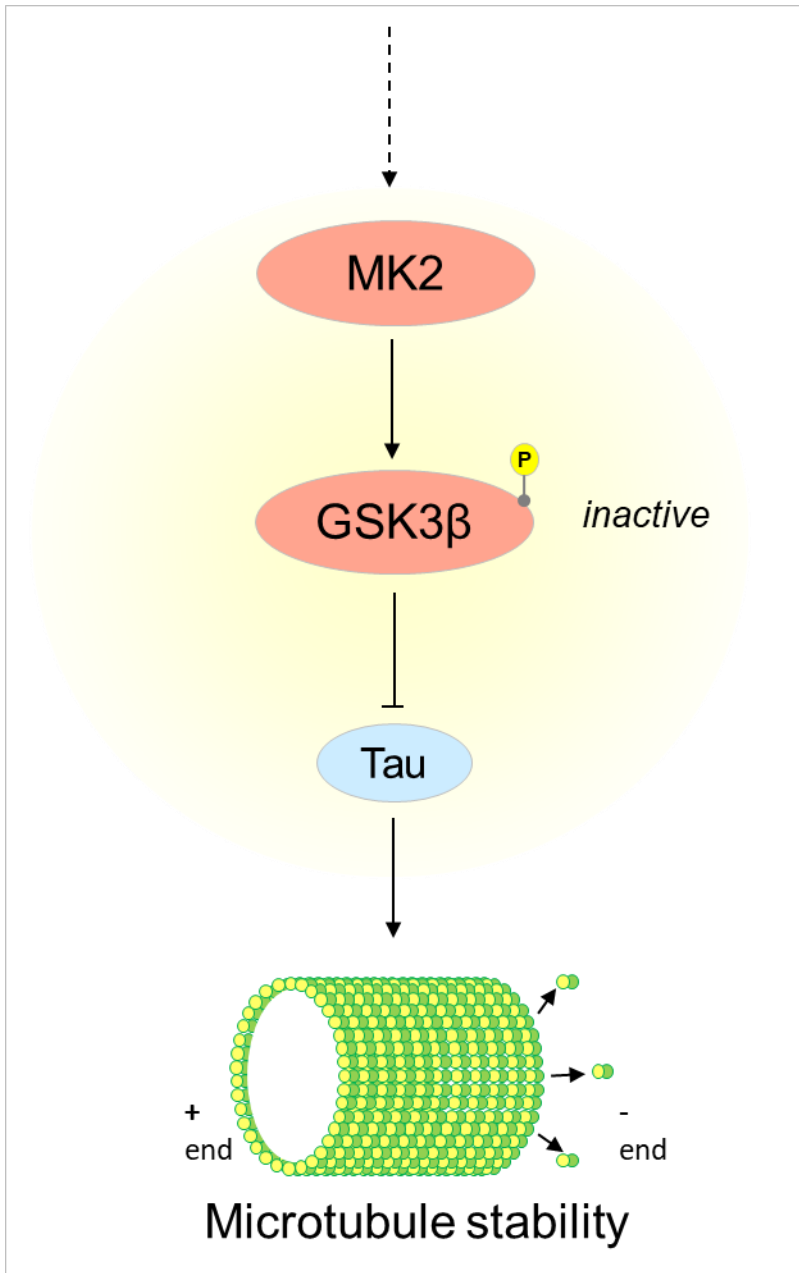


Figure 4.3B: Schematic representing the microtubule stability.

Phosphorylation of GSK3 β at S9 renders it inactive and its abnormal phosphorylation of the microtubule-binding protein. It is regulated by the upstream kinase MK2 which is a downstream effector of the ERK signaling shown as dashed arrow.

4.1.3 KinMap

A dendrogram of the human kinome was constructed using KinMap (Eid *et al.*, 2017). It highlighted the candidate kinases predicted to target the significantly differentially phosphorylated peptides on the array. The identified kinases for both, hyper- and hypo-phosphorylated phosphosites were uploaded on NetworKIN (Linding *et al.*, 2008), which predicted the kinases phosphorylating those peptides. The candidate kinases identified by NetworKIN analysis were selected based on a cut-off score of 10 and represented on the mammalian kinase-dendrogram, using the KinMap_{beta} online tool. The NSCs were obtained from a female patient, and hence, a circle was used to represent the dataset. The upregulated kinases were represented in red and downregulated in green. This is a simple visualization of a compound profiling dataset, which allowed us to answer complex questions pertaining to the involvement of the kinases in the disease. The in-depth analysis of these outputs also enables the identification of new avenues for kinases in drug development projects.

The dendrogram shows a wide distribution of the predicted kinases across different families, but the largest node size is seen on Atypical Protein Kinases (APK), whose functions are largely unknown (Manning *et al.*, 2002). The node size is proportional to the number of phosphosite targets of the kinases. In this study, two prominent APKs were predicted (black arrows, Figure 4.4), including ATM (Serine/threonine protein kinase ATM) (green) and PDHK1 (Pyruvate dehydrogenase (acetyl-transferring)] kinase isozyme 1) (red). Both play an important role by being activated during stress and apoptosis. ATM activates during DNA damage specifically checkpoint signaling upon double strand breaks (DSBs), whereas PDHK1 during mitochondrial dysfunction and protects the cells against apoptosis in response to hypoxia and oxidative stress (Barone *et al.*, 2009; Kato *et al.*, 2007; Lu *et al.*, 2014; Vallee *et al.*, 2018).

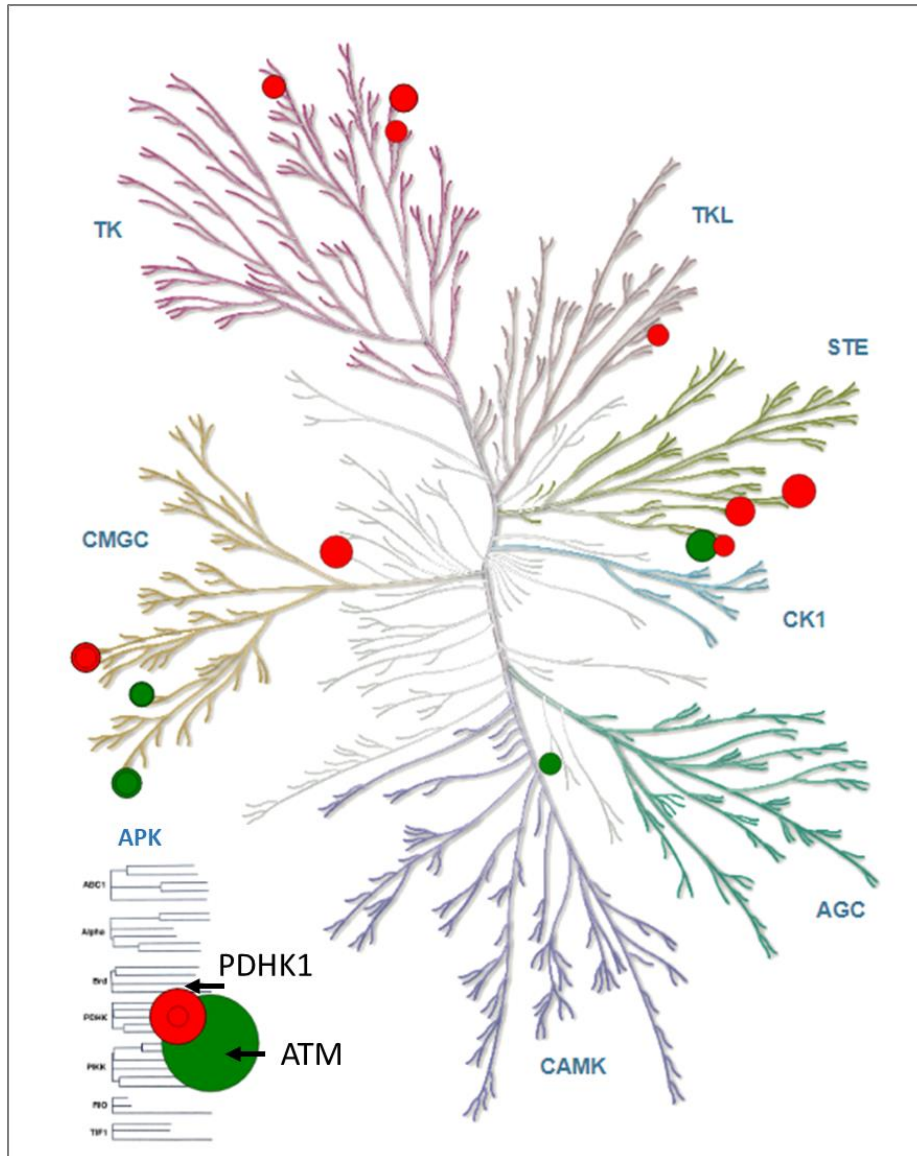


Figure 4.4: Dendrogram of the human kinome generated using KinMap predicts the kinases involved HD NSCs.

Dendrogram of the human kinome constructed using KinMap (Eid *et al.*, 2017), highlighting the candidate kinases predicted to target the upregulated and downregulated phosphosites in HD NSCs. Candidate kinases were identified by NetworKIN (Linding *et al.*, 2007) analysis. Node size is proportional to the number of the phosphosites targeted by the kinase. All major kinase families are annotated in the dendrogram and include: TK (Tyrosine Kinases), TKL (Tyrosine Kinase-Like), STE (Sterile kinases; homologs of the yeast STE7, STE11 and STE20 kinases), CK1 (Casein Kinase 1), AGC (comprising Protein kinase A/ PKA, PKG and PKC kinase sub-families), CAMK (Calcium/Calmodulin-dependent kinases) and CMGC (comprising cyclin-dependent kinase (CDK), mitogen-activated protein kinase (MAPK), glycogen synthase kinase (GSK) and CDC-like kinase (CLK) and APK (Atypical Protein Kinases).

4.1.4 NeuroLucida 360

Results from our kinome and WB analyses suggested that cofilin, LIMK1 and SSH1L were altered in HD NSCs (Figure 4.2). A correlation between LIMK inactivation and altered cytoskeletal dynamics has been observed (DiProspero *et al.*, 2004; Narayanan *et al.*, 2016), which affects the neurite morphology (Sainath and Gallo, 2015). Actin microfilaments have specific locations in the neurons and are particularly concentrated at the synaptic terminals, dendritic spines and growth cones (Gordon-Weeks, 1987; Matus *et al.*, 1982) (Figure 1.8). Neurons are polarized cells, and thus, rely on a strong cytoskeletal network to maintain the typical neuronal morphology that allows the proper functioning of the neuron and neuronal plasticity. Abnormal signal transduction could impact the cytoskeleton negatively and affect actin microtubule dynamics. Therefore, to determine whether dysregulated cofilin, LIMK1 and SSH1L in HD-derived NSCs could lead to altered neurite outgrowth an artificial reconstruction of the neuronal structure was completed. NeuroLucida 360 platform (Dickstein *et al.*, 2016), accurately traced and reconstructed intricate neuronal structures and quantitatively assessed the neuronal soma and neurite length associated with HD and normal NSCs. With this automatic neuron construction tool, one could completely reconstruct neurons and its complex network of dendrites, axons, etc., and using the detection algorithm, analyze the length of these extensions and the number of soma (cell bodies). This facilitated comparisons of the disease conditions to the control, providing a visual, numerical and analytical assessment of the disease progression. The results from six fields demonstrated a significant difference in neurite length between the HD and HC NSCs (Figure 4.5). The average neurite length of HD NSCs was found to be up to 25% shorter than the average neurite length of HC NSCs ($P < 0.002$). No significant difference was observed in the density and soma size between the corresponding NSCs, thus suggesting that about the same number of somas resulted in a sparser network of neurite branching in HD, compared to HC NSCs. Collectively, the data suggests that abnormal functioning of LIMK1, cofilin and SSH1L in HD-derived NSCs potentially leads to perturbed cytoskeletal dynamics in those cells and that this could predispose to poor neurite outgrowth in HD pathogenesis and eventually, to a loss of synaptic integrity.

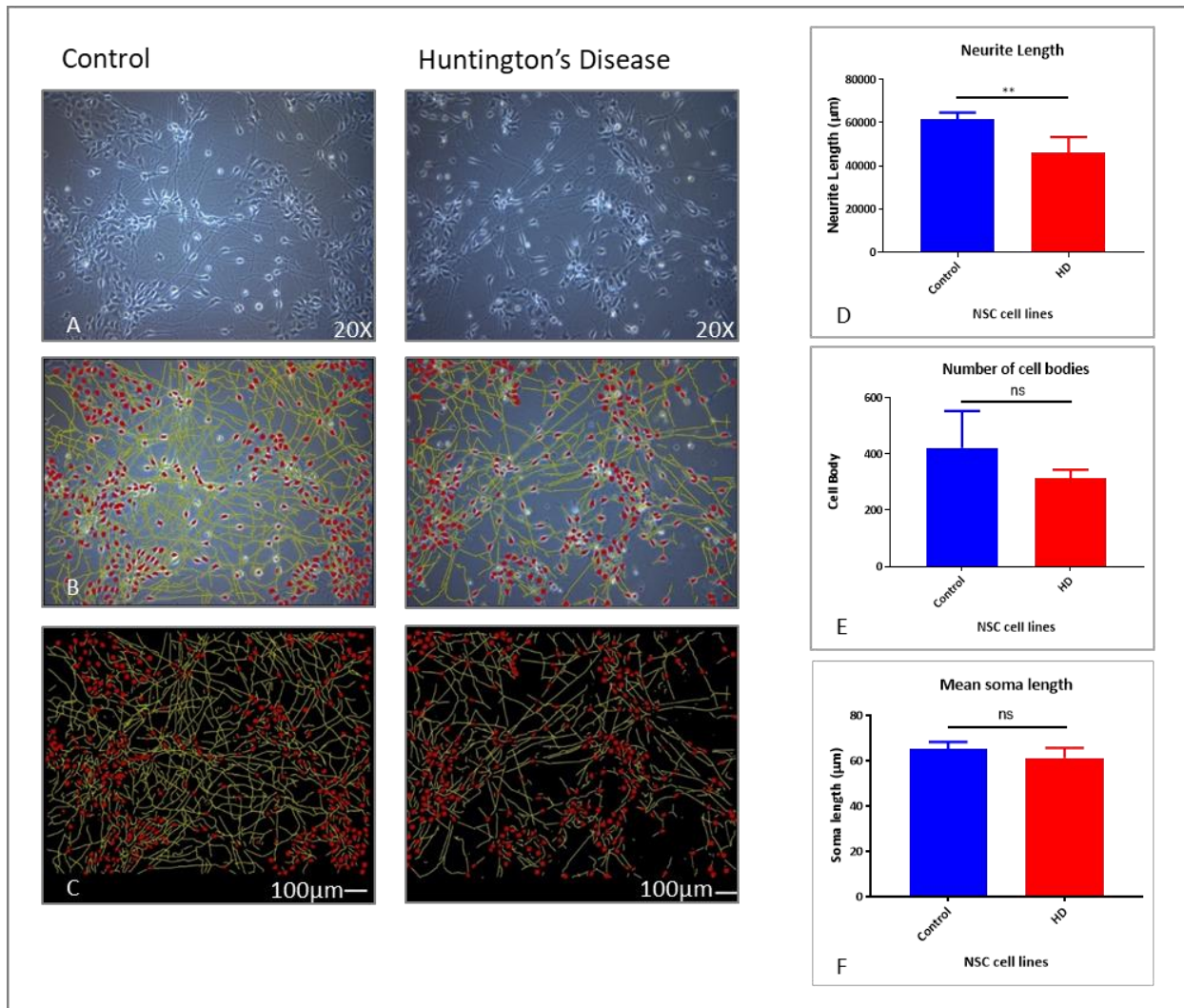


Figure 4.5: Neurolucida tracings of neurons in the HC and HD NSCs

(A) Representative image of HC and HD NSCs by averaging six fields. The indicated cell lines were cultured to approximately 80% confluence and phase-contrast images of the cells were acquired at 20x magnification using a light microscope. (B) Reconstruction of the neurite extensions were generated using Neurolucida 360 and the representative overlay indicating the soma and neurite extensions are shown here. (C) Reconstruction of the soma and cell body with the scale bar measuring 100µm. (D) Reconstruction was used for quantitative analyses of the total neurite length of six HC and HD images. (E) Quantification of the neuronal morphology in HD and HC NSCs. (F) Results from the analysis of mean soma lengths in both HD and HC NSCs. Bar graph shows mean \pm standard deviation, $**P < 0.005$, $n = 6$ experiments, unpaired t-test. HC = Healthy control, HD = Huntington disease.

4.1.5 Discussion

Herein, NSCs and R6/2 HD mice were used as a model to study the signaling aberrations underlying HD pathogenesis. Specifically, kinome analysis was applied to NSCs derived from the fibroblasts of a female HD patient with a clinically-diagnosed symptomatic age of onset of 48 years. This phosphorylation (peptide array) platform and kinome analysis represents a cost-effective and powerful high-throughput approach to probe for cognate and disease-specific kinases. Several models, including immortalized neuronal cell lines and transgenic mouse models, have been used to study HD pathology (Cisbani and Cicchetti, 2012; Ferrante, 2009). These models have provided critical information regarding HD pathogenesis, and are somewhat able to recapitulate the underlying molecular characteristics displayed in the HD patient brain and are an invaluable resource to allow for modelling disease pathologies.

Several recent studies have reported the dysregulation of cytoskeletal dynamics in neurodegenerative disorders, although the molecular mechanisms by which they occur are not always apparent (Goldberg, 2003; Guo *et al.*, 2014b; Heng *et al.*, 2010; Niwa *et al.*, 2002). LIM kinases are known to play a role in cytoskeletal dynamics (Briz and Baudry, 2014; Endo *et al.*, 2007). The LIMK family includes LIMK1, which is highly expressed in the brain, and LIMK2, which is ubiquitously expressed throughout the body (Proschel *et al.*, 1995; Takahashi *et al.*, 1998). These kinases are downstream effectors of Rho-GTPases and regulate the actin cytoskeleton architecture (Proschel *et al.*, 1995). Upregulation of LIMK1 increases axonal growth while its downregulation causes the opposite effect (Heng *et al.*, 2010; Koch *et al.*, 2014). The phosphorylation of LIMK1-T508 increases its activity and is associated with enhanced LIMK1-dependent regulation of actin cytoskeletal dynamics (Cuberos *et al.*, 2015; Petrilli *et al.*, 2014). LIMK1 is known to directly phosphorylate cofilin on S3, which inactivates cofilin and prevents its binding to actin (Yang *et al.*, 1998). In contrast, Slingshot phosphatase-1 also targets S3, and promotes cofilin (re)activation (Romarowski *et al.*, 2015). Loss of cofilin function due to phosphorylation at S3 impairs monomeric actin-turnover (G-actin) in the cytoplasm, leading to morphological deficits, as demonstrated in Figure 4.2B (Munsie *et al.*, 2012). The impairment of G-actin affects profilin that balances the F/G actin ratio which ultimately affects the actin polymerization (Posey *et al.*, 2018).

This study revealed hypo-phosphorylation of LIMK1 T508 in HD NSCs, but an increase in cofilin S3 phosphorylation. Hypo-phosphorylation of SSH1L was at S978, reduces its phosphatase activity and suggested the existence of a complex interplay of LIMK1-cofilin-SSH1L pathway. Such phosphorylation also likely contributes to the loss of actin integrity in HD as observed in other neurodegenerative diseases, including Alzheimer disease (Bamburg and Bernstein, 2016; Barone *et al.*, 2014). It is well established that the calcium levels in HD brains are elevated and contribute to cellular toxicity and death (Cheng *et al.*, 2003; Raymond, 2017; Wang *et al.*, 2005). Therefore, it is possible neuronal actin cytoskeletal dynamics and organization may be dependent on Ca²⁺ calcineurin - induced SSH1L activation and cofilin deactivation (Wang *et al.*, 2005). Another mechanism for dysregulation of SSH1L is the ROS- (Reactive oxygen species) dependent activation of the SSH1L-cofilin pathway which stimulates the SSH1L-dependent formation of cofilin-actin rods; therefore, affecting the actin dynamics (Kim *et al.*, 2009). All living cells generate ROS, which at a moderate concentration, play important physiological roles, but at high levels generate oxidative stress to which the central nervous system (CNS) is particularly vulnerable. Neurodegenerative disorders (NDD) are late-onset and prone to oxidative stress. Misfolded proteins accumulate as a result of stress and these proteins are vulnerable to modification by the carbonyl products of oxidative stress (Kim *et al.*, 2015; Liu *et al.*, 2017).

Overall, the neuronal tracings, kinome analysis and bioinformatics prediction suggest, among other things, differences in microtubule assembly (Figures 4.2-4.5) and the findings present evidence that cofilin dysregulation *via* SSH1L/LIMK1 inactivation is a potential molecular hallmark of HD pathology. NetworkKIN predicted GSK3 β , ATM and PDHK1 as one of the major upstream kinases, potentially activated in HD NSCs. These results suggest a complex interplay between the cytoskeletal proteins and its upstream kinases. The sample size was one hence it cannot be definitively suggested whether stress or DNA damage causes the dysregulated kinase signaling in HD though it is obvious that the phosphorylation of the key cytoskeletal proteins is affected.

4.2 R6/2 Huntington mouse studies

Alteration in the kinase signaling has been verified in various cellular and mouse models over the years in HD. R6/2 is a progressive mouse model of the disease, and hence, subtle changes in the disease process can be well documented. The onset of HD pathology in humans is generally triggered in their mid-40's, although it is known that the patients are born with the defective gene. This clearly suggests that the fate of HD patients is sealed by birth. How signaling is altered in the early stages of life is not clearly understood and leads to the question of whether these pathological defects affect neural development. This study focused on answering some of these questions by comparing global kinase signaling of HD and HC across major neural developmental time points using R6/2 mice. This was accomplished using whole brains for the embryonic time points. To understand the signaling defects in the other significant developmental milestones, striatal tissue was selected for the analysis which is the most affected in HD. These time points captured the various physiological changes in the disease process to study the biochemical changes due to (de)phosphorylation by the kinases, and the causes thereof.

4.2.1 Validation of peptide array targets

As discussed previously, I designed a custom 1268 peptide array (Supplementary Table S4) that represented signaling proteins implicated in cell-survival, proliferation, neural-development, cytoskeleton, energy metabolism, transcription and immune-related pathways. This array was used as the platform to screen for potential signaling differences in the neural tissue derived from age and sex matched R6/2 murine model of HD. Based on the peptide array and pathway analysis results there were five pathways that appeared to be significantly affected across the eight time points. They were i) Cytoskeletal dynamics; ii) Calcium signaling; iii) Transcription; iv) Cell cycle regulation; and v) Energy Metabolism. I selected significant peptides involved in cytoskeletal dynamics to validate by Western blotting as this pathway was also significantly affected in the human NSCs. This allowed a better understanding of the defective kinase signaling (kinome analysis) across significant developmental time points that lead to the disease symptoms in the R6/2 mouse model.

4.2.1.1 Cytoskeletal dynamics

The priority of kinome analysis is to identify targets that are validated by independent approaches, which in this case was Western blotting. In both cases the direct measurement is the extent of phosphorylation in the peptide / protein (array / WB). The distinction is that this study is attempting to capture the phosphorylation status of a peptide *in vitro* (array), and compare it to the phosphorylated protein *in vivo* (cell/tissue).

As discussed previously, the peptide was selected from the PIIKA 2 output for further analysis with a $P < 0.2$ and a fold change of $> \pm 1$ (Goel *et al.*, 2018; Maattanen *et al.*, 2013a; Maattanen *et al.*, 2013b) (Supplementary Table S5). This liberal threshold allowed us to avoid false positives while performing pathway analysis. As described earlier, the InnateDB tool was used to map the dysregulated phosphorylated targets to multiple cognate signaling pathways. Using phosphosite-specific information derived from PIIKA 2, these pathways were classified as upregulated or downregulated (i.e., positive fold change as up and negative as downregulated). This dataset was uploaded for pathway analysis to the InnateDB online tool and consequently this analysis identified different signaling pathways that were dysregulated across the different time points in the disease process (Supplementary Tables S6 and S7). In this case I had to verify that the significantly phosphorylated peptides selected were based on their differential phosphorylation status across time points, which meant that a peptide should have a significant change in its phosphorylation across at least half of the time points (4 out of 8). Overall, this analyses led to the identification of cytoskeletal signaling as the major dysregulated pathway in HD R6/2 neural tissues. Figure 4.6 shows the peptides that were validated by Western blot analysis, while Table 4.4 shows the fold changes and P-values that were derived from the PIIKA 2 output.

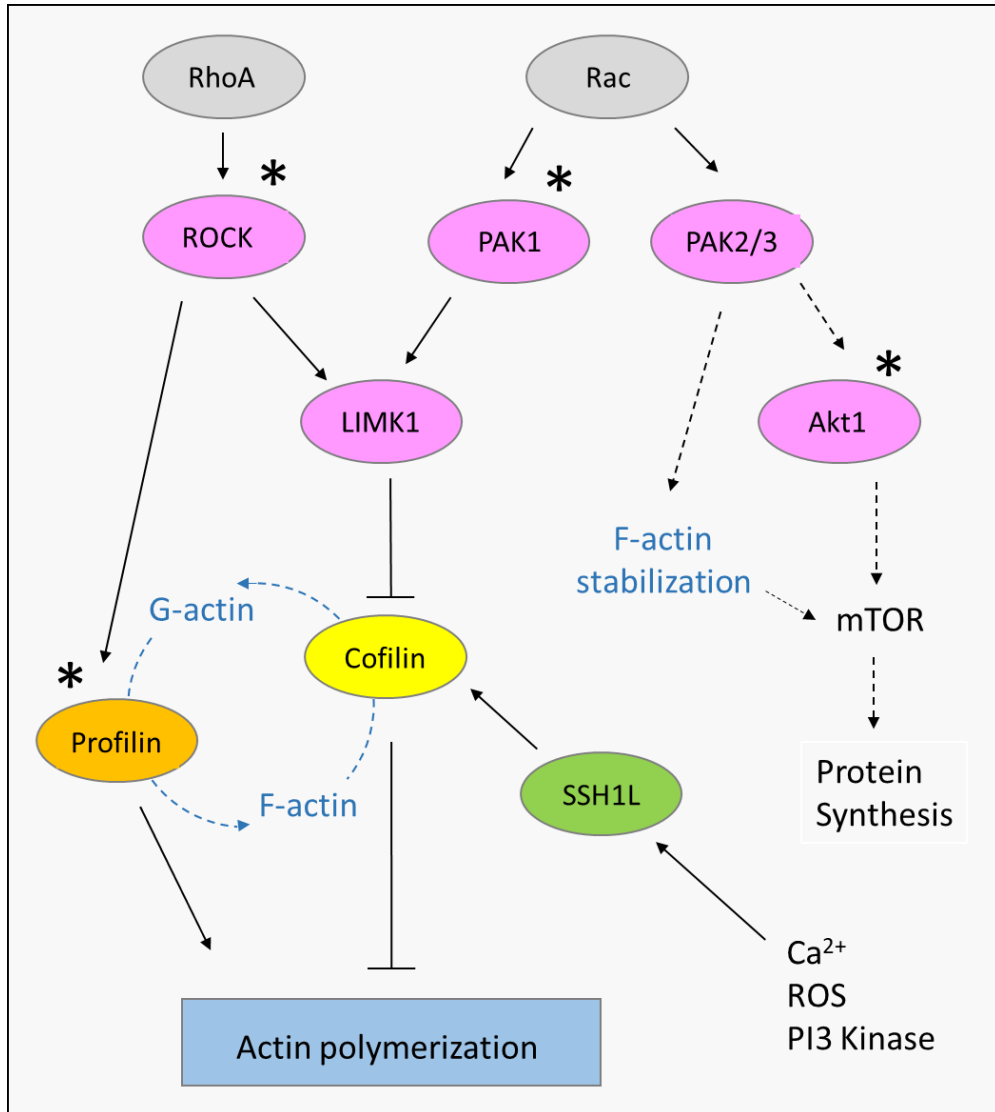


Figure 4.6: Molecular signaling involved in cytoskeletal organization.

This map illustrates the Rho kinase signaling pathway, the key effectors, and its downstream targets that ultimately affect actin polymerization. The molecules represented in pink and grey are kinases while profilin and cofilin have no such activity. Activation of ROCK and PAK lead to the phosphorylation and activation of LIMK thus allowing the phosphorylation of cofilin which leads to its deactivation. It's reactivated by the phosphatase SSH1L shown here in green. SSH1L is modified by multiple upstream regulators such as PI3K, ROS, calcium etc. Profilin (orange) and cofilin (yellow) are involved in maintaining the balance between F and G actin which regulates actin polymerization. * Represents the peptides that were selected for validation based on their significant differential phosphorylation in the peptide array. ROCK1=Rho associated protein kinase 1, PAK=p21 activated kinase, LIMK1=Lim domain kinase, SSH1L=slingshot phosphatase, ROS=Reactive oxygen species. G=globular, F=Filamentous, Ca²⁺ =Calcium, ROS=Reactive oxygen species.

Table 4.4: List of peptides selected for validation based on PIIKA 2 output with fold changes and P-values for every time point and both sexes [male (M) and female (F)]. The bold represent the time points with significant P-values. E = embryonic, P0 = at birth, w = week.

Name	ID	Target	Time point	Fold change	P-value
ROCK2	P70336	S1366	E9_F	1.41	0.02
			E9_M	1.04	0.41
			E14_F	- 1.09	0.31
			E14_M	1.31	0.08
			P0_F	1.16	0.10
			P0_M	1.07	0.35
			3w_F	1.33	0.10
			3w_M	- 1.09	0.32
			4w_F	- 1.26	0.07
			4w_M	- 2.26	0.01
			5w_F	1.62	0.01
			5w_M	- 1.03	0.45
			7w_F	- 1.03	0.44
			7w_M	- 1.07	0.37
			10w_F	- 1.20	0.21
			10w_M	- 1.09	0.32
PAK1	O88643	T423	E9_F	- 1.23	0.23
			E9_M	1.14	0.35
			E14_F	1.26	0.07
			E14_M	1.01	0.48
			P0_F	- 1.20	0.15
			P0_M	- 1.03	0.46
			3w_F	1.60	0.04
			3w_M	- 1.04	0.42
			4w_F	1.20	0.16

			4w_M	- 1.31	0.05
			5w_F	1.03	0.46
			5w_M	1.13	0.31
			7w_F	1.09	0.36
			7w_M	- 1.17	0.23
			10w_F	- 1.17	0.23
			10w_M	1.14	0.30
Profilin1	P62962	S138	E9_F	- 3.49	0.01
			E9_M	1.48	0.20
			E14_F	2.70	0.01
			E14_M	1.69	0.02
			P0_F	- 1.24	0.25
			P0_M	- 1.73	0.08
			3w_F	2.61	0.02
			3w_M	- 1.32	0.28
			4w_F	3.03	0.01
			4w_M	1.36	0.18
			5w_F	1.94	0.02
			5w_M	- 2.39	0.01
			7w_F	- 1.16	0.32
			7w_M	- 3.01	0.01
			10w_F	- 1.11	0.30
			10w_M	1.48	0.03
AKT1	P31750	S473	E9_F	1.64	0.09
			E9_M	- 3.62	0.01
			E14_F	2.04	0.01
			E14_M	1.05	0.41
			P0_F	- 1.81	0.01

			P0_M	1.03	0.46
			3w_F	- 1.34	0.13
			3w_M	- 1.12	0.31
			4w_F	- 1.69	0.03
			4w_M	- 1.04	0.44
			5w_F	- 1.31	0.26
			5w_M	1.82	0.02
			7w_F	- 1.04	0.45
			7w_M	- 1.41	0.15
			10w_F	1.25	0.20
			10w_M	- 1.49	0.02

4.2.1.1.1 Rho-associated protein kinase (ROCK2)

ROCK 2 is critical for maintaining the spine morphology and regulating neuronal actin, which ultimately modulates synaptic function. Dendritic spines are specialized structures required for normal synaptic physiology and have been shown to be altered in the HD state (Chelly and Mandel, 2001; Zhou *et al.*, 2009). Two mammalian ROCK homologs have been identified, including ROCK1 (also called Rho-kinase β) and ROCK2 (also known as ROK α) (Nakagawa *et al.*, 1996). The expression of ROCK2 is higher in the brain compared to ROCK1. ROCK2 knockout mice have a normal gross brain anatomy, but show changes in synaptic transmission (Zhou *et al.*, 2009). The actin cytoskeleton is altered in these mice thus making ROCK2 essential for the normal morphology and functioning of the synapses (Zhou *et al.*, 2009). It is known that ROCK2 can directly phosphorylate and activate LIM kinases, which in turn phosphorylate and inactivates cofilin thus affecting actin depolymerization (Maekawa *et al.*, 1999) (Figure 4.6). The phosphorylation of ROCK2 S1366 is conserved in vertebrates and is required for the activation of the enzyme (Chuang *et al.*, 2012). It is phosphorylated upon DNA damage, probably by ATM or ATR cellular kinases that are well-characterized in the DNA-damage response (Cara *et al.*, 2016).

Representative Western blots for both sexes at different developmental time points are shown below with phospho-ROCK2 (160kD) represented in Figure 4.7A and total-ROCK2 in Figure 4.7B. Assessments of the relative phosphorylation confirmed that phosphorylation of ROCK2 S1366 was significantly decreased in lysates derived from the whole brains of female HD mice at E9 and striatum at 10w. However, the relative phosphorylation of ROCK2 at S1366 in E14 females was significantly increased in HD. The other time points did not show any significant difference in the relative phosphorylation status of ROCK2 (Figure 4.7C), although the peptide array results indicated otherwise (Table 4.4).

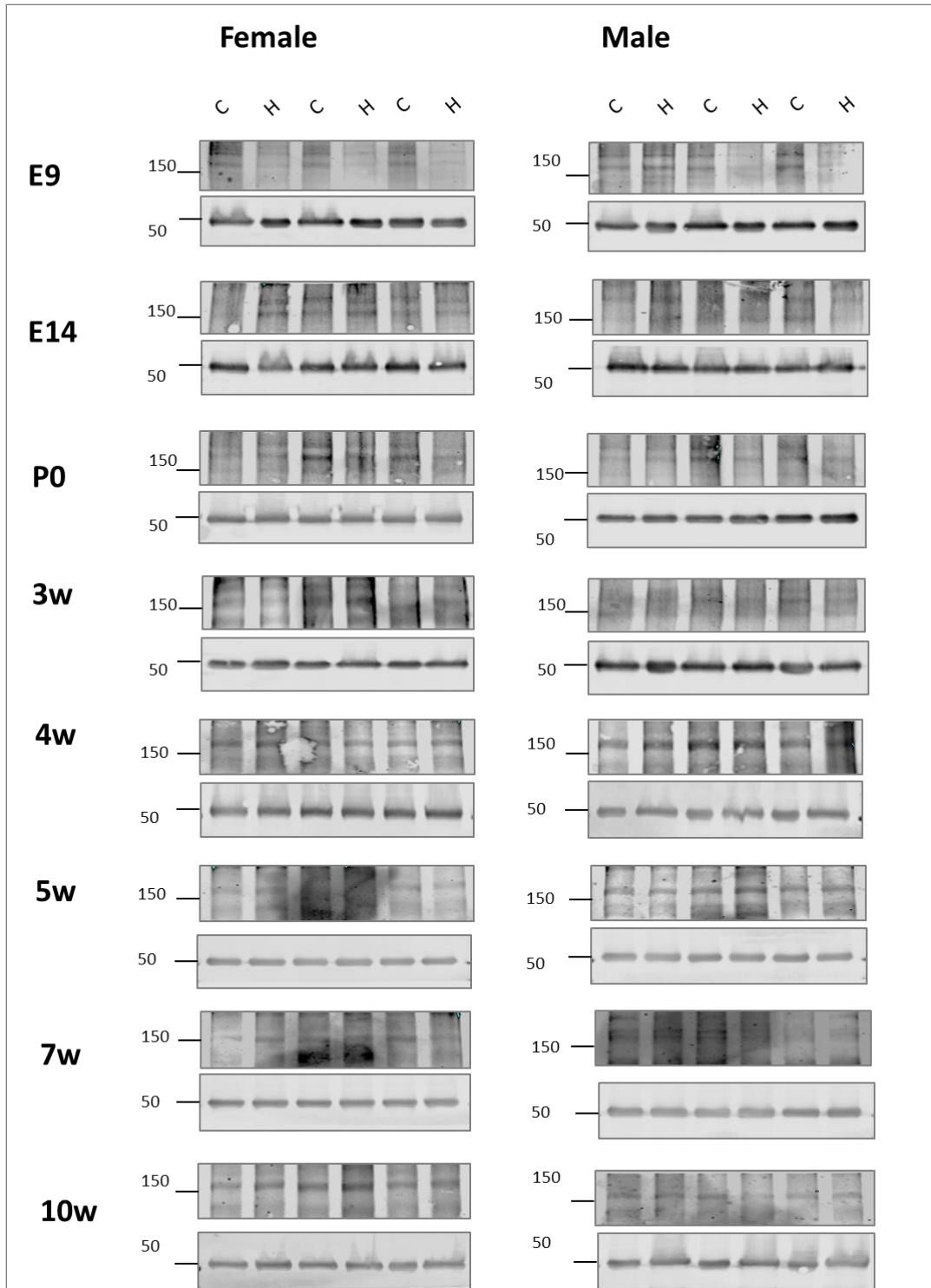


Figure 4.7A: Western blot analysis of phospho-ROCK protein levels.

Representative blots for phospho-ROCK (160kD) across eight time points and both sexes. The same membranes were also blotted for α -tubulin as a loading control (50kD). C = Control mouse, H = HD mouse, E = embryonic, P0 = at birth, w = week.

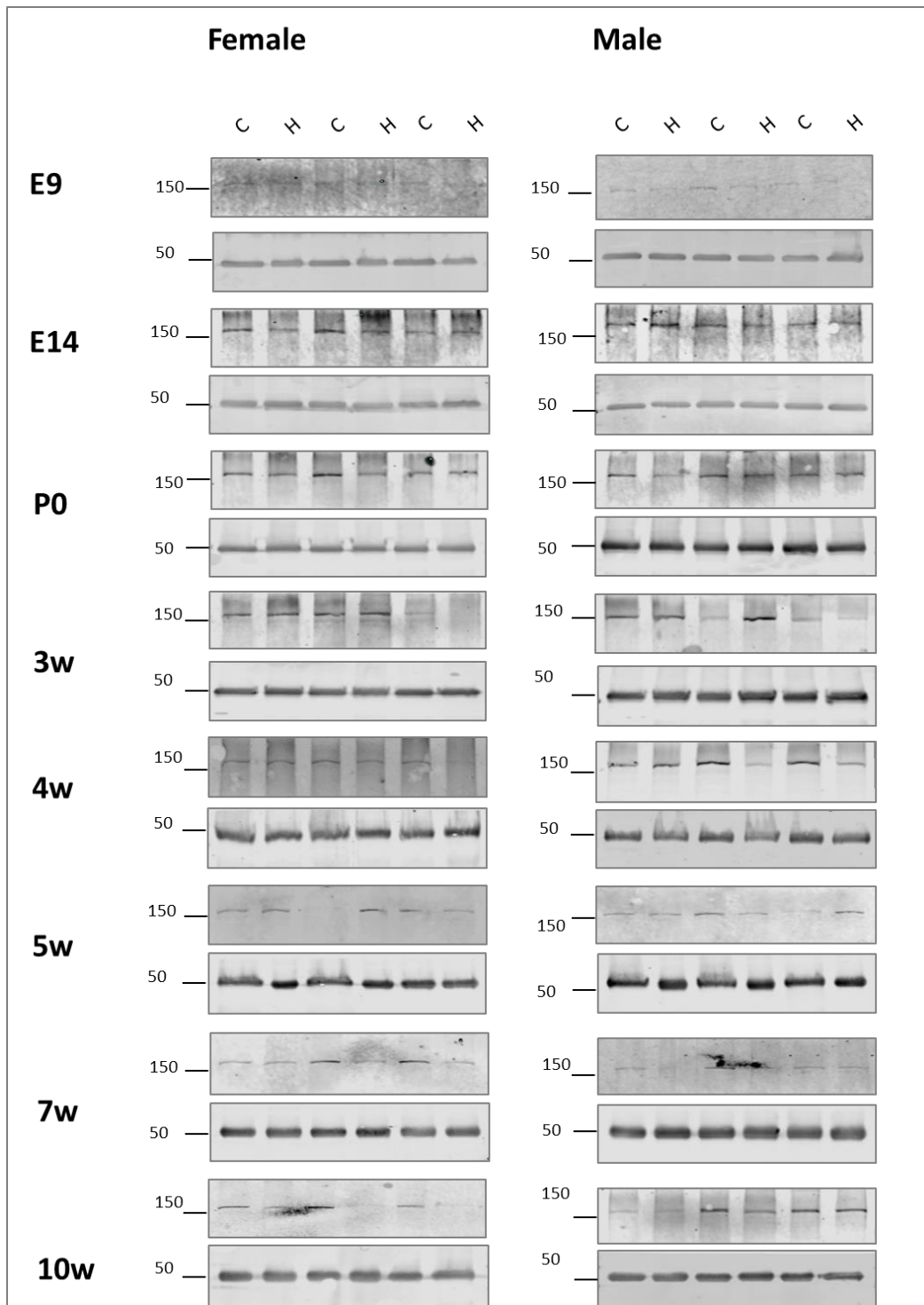


Figure 4.7B: Western blot analysis of total-ROCK protein levels.

Representative blots for total-ROCK (160kD) across eight time points and both sexes. The same membranes were also blotted for α -tubulin as a loading control (50kD). C = Control mouse, H = HD mouse, E = embryonic, P0 = at birth, w = week.

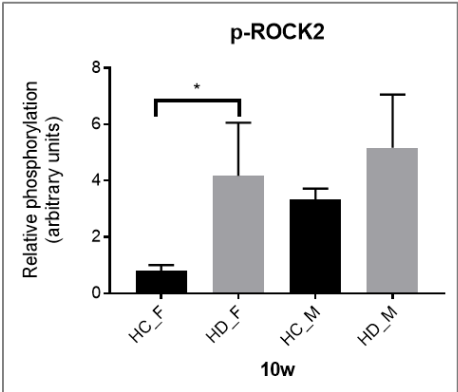
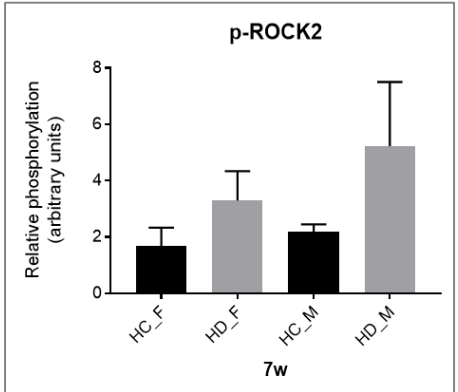
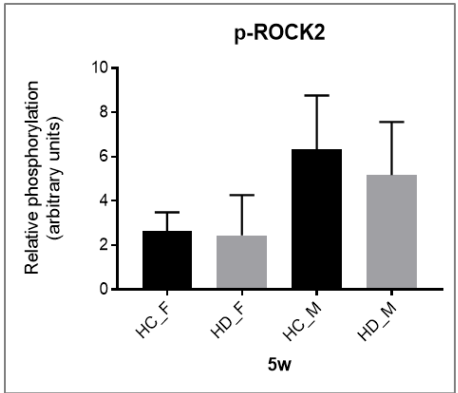
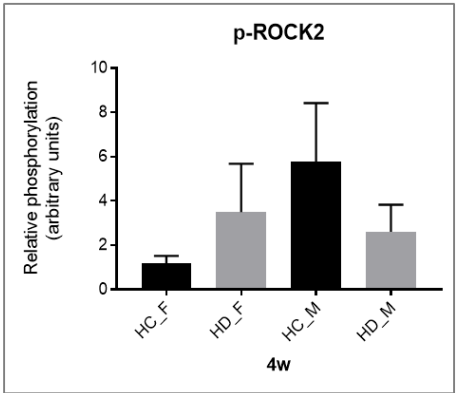
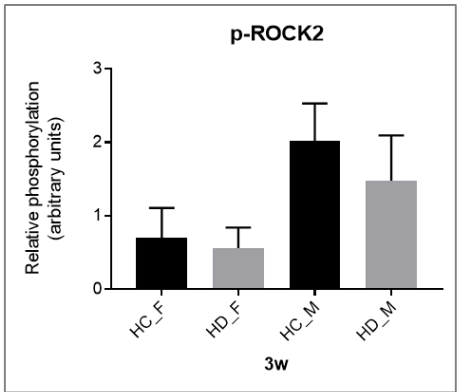
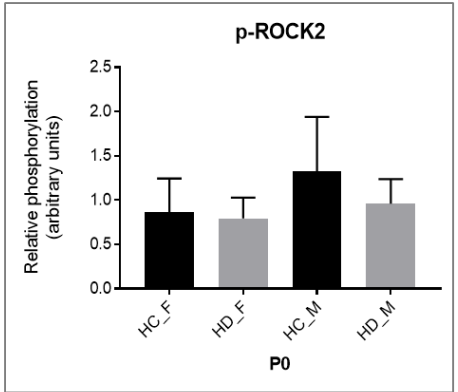
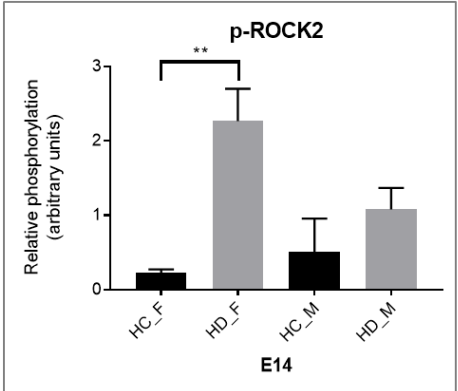
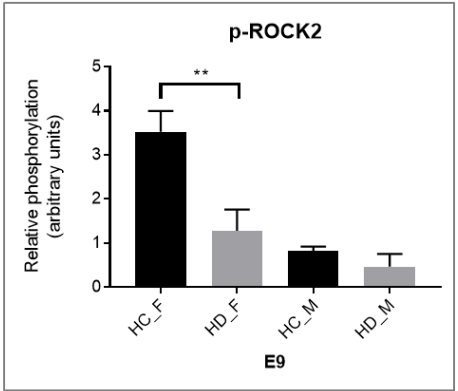


Figure 4.7C: Quantification of phospho-ROCK2 ratio in brain samples of HD versus healthy control (HC) mice.

Shown here are bar-graphs representing the densitometry data of phospho-ROCK2 expression derived from Western blotting experiments using brain tissue lysates from HD and healthy control (HC) mice. The densitometric data were quantified as the ratio of the expression of phospho-ROCK2 (S1366) to total-ROCK2. Protein levels of both phospho-ROCK2 and total-ROCK2 were normalized to α -tubulin expression. Bar graph shows mean \pm standard deviation, *P < 0.05, **P < 0.005, n = 3 experiments, unpaired t-test. HC = Healthy control, HD = Huntington disease. E = embryonic, P0 = at birth, w = week.

4.2.1.1.2 p21 activated kinase (PAK)

The PAK family consists of group I PAKs, including PAK1, PAK2 and PAK3 that are activated by GTP bound, RAC/CDC42. The second, more recently discovered group II PAKs include PAK4, PAK5 (also known as PAK7) and PAK6. The expression of PAK1 and PAK3 is very high in the brain while PAK2 expression is ubiquitous (Fuchsova *et al.*, 2016; Kichina *et al.*, 2010; Kim *et al.*, 2016). PAK1 has been shown to increase the aggregation of mHtt, thereby, modulating its toxicity (Luo *et al.*, 2008). The inhibition of PAK1 is also protective in HD (Ma *et al.*, 2012). When activated, PAK1 is a known regulator of the actin cytoskeleton and dendritic spine morphology (Kichina *et al.*, 2010; Luo *et al.*, 2008). Its role in the loss of dendritic spines and cognitive deficits in AD have been well established (Ma *et al.*, 2012). PAK1 regulates the actin cytoskeleton through LIMK1, which ultimately regulates cofilin (Kichina *et al.*, 2010; Zhou *et al.*, 2009) . It has been suggested that ROCK2 is mainly important for basal cofilin regulation, whereas PAK1 is specifically important for activity-dependent cofilin regulation (Asrar *et al.*, 2009) (Figure 4.6). Apart from cytoskeletal dynamics, PAK1 has other roles in cell motility, the cell cycle, cell survival and death (Kichina *et al.*, 2010; Parvathy *et al.*, 2016). PAK1 T423 is a conserved site in its activation loop, which is activated by kinases (3-phospho-inositide dependent kinase-1 (PDK1)) and deactivated by phosphatases (Serine-threonine phosphatase PP2A). Autophosphorylation of T423 (T402 for PAK 2 and T421 for PAK 3) is required for the activation of PAK.

An equal amount of protein was analyzed by Western blotting using phosphospecific

antibodies and normalized to total protein levels. Representative Western blots for both sexes are shown below with phospho-PAK1 represented in Figure 4.8A and total PAK in Figure 4.8B. Assessments of the relative phosphorylation confirmed that phosphorylation of PAK1-T423 was significantly decreased in the lysates derived from the whole brains of HD mice at E9 and E14 in both sexes. The 3w time point shows the opposite results for both sexes. Females show an increase and males show a decrease in the protein levels of PAK, revealing a sex difference. There was an increase in the relative expression of PAK in 4w males and 10w males however, the comparative analysis of males and females at birth, 5w and 7w did not show any significant differences compared to the peptide array results (Table 4.4). That data was also confirmed by the WB results, as shown in the graphs below (Figure 4.8C).

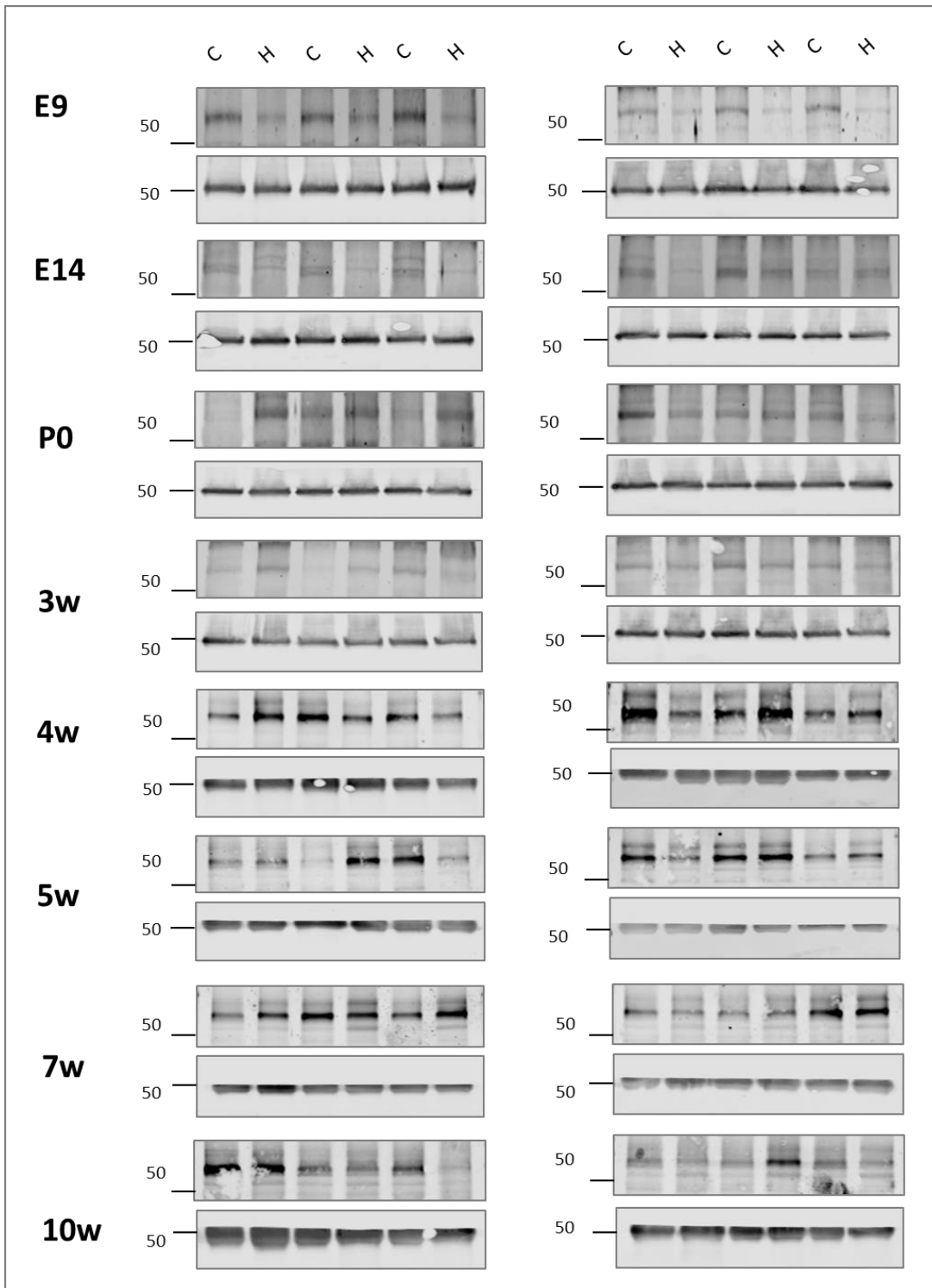


Figure 4.8A: Western blot analysis of phospho-PAK protein levels.

Representative blots for phospho-PAK (65kD) across eight time points and both sexes. The same membranes were also blotted for α -tubulin as a loading control (50kD). C = Control mouse, H = HD mouse, E = embryonic, P0 = at birth, w = week.

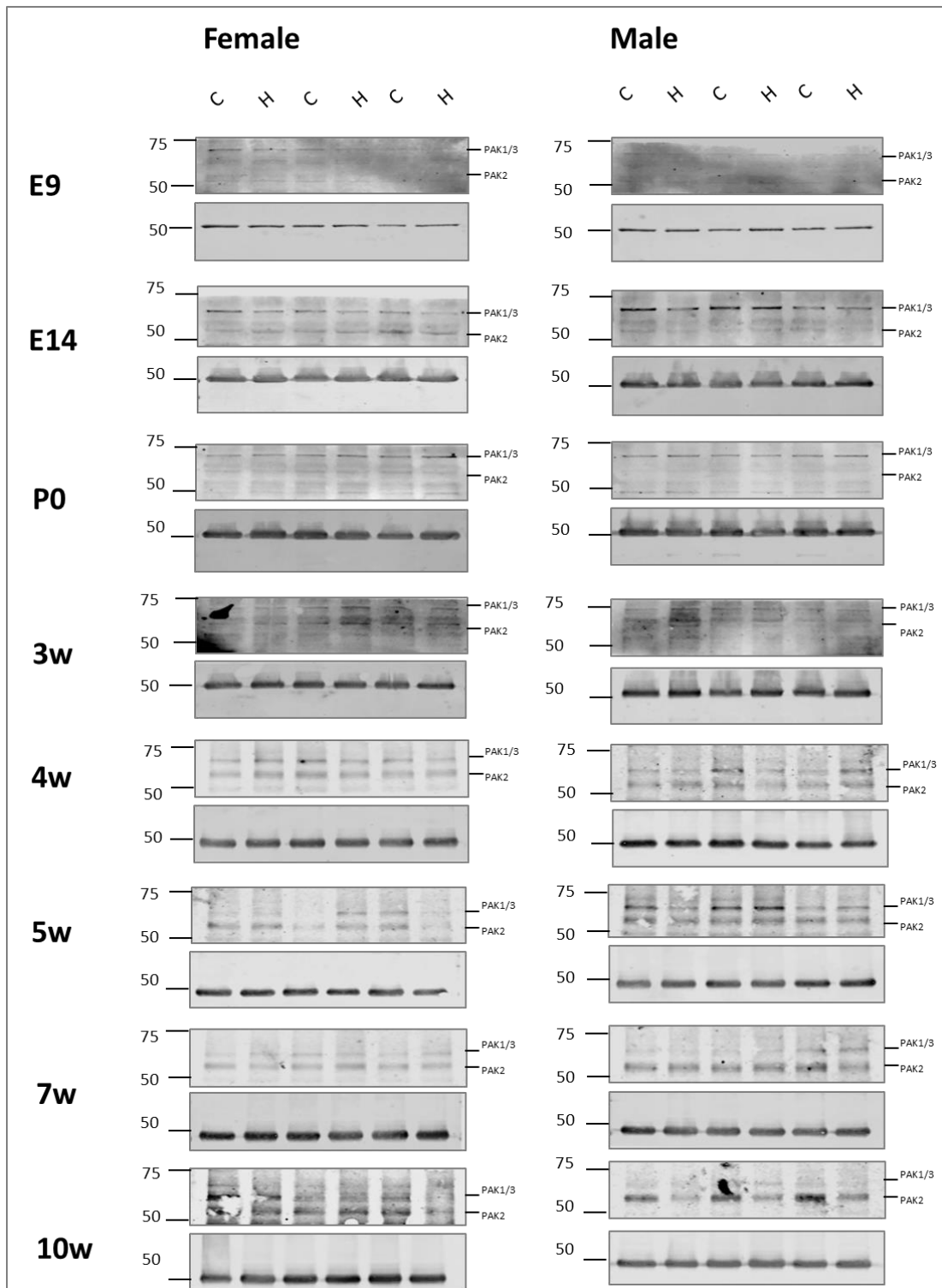


Figure 4.8B: Western blot analysis of total-PAK1/2/3 protein levels.

Representative blots for total-PAK1/3 (68kD) and total-PAK2 (61kD) across eight time points and both sexes normalized to α -tubulin (50kD). C = Control mouse, H = HD mouse, E = embryonic, P0 = at birth, w = week.

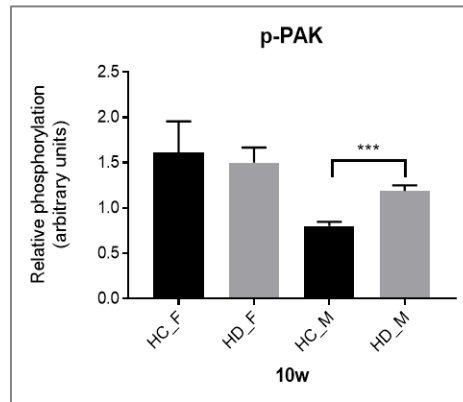
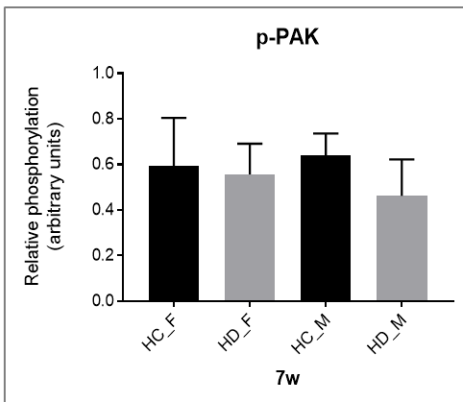
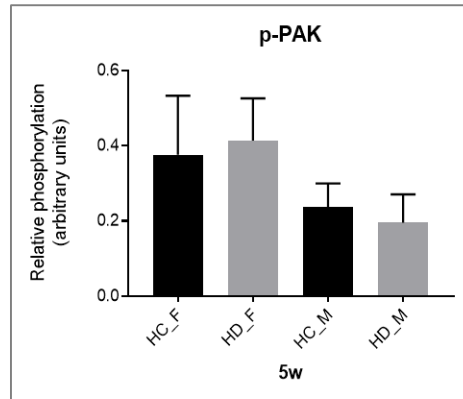
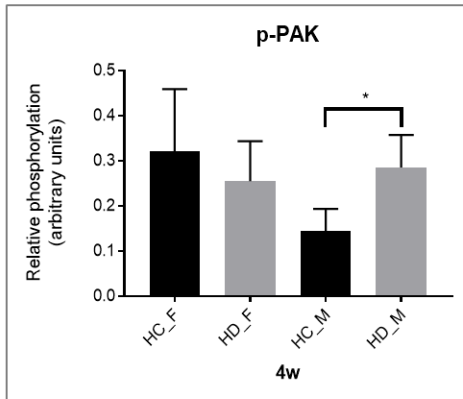
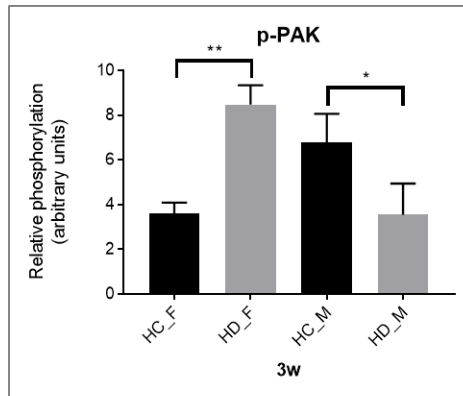
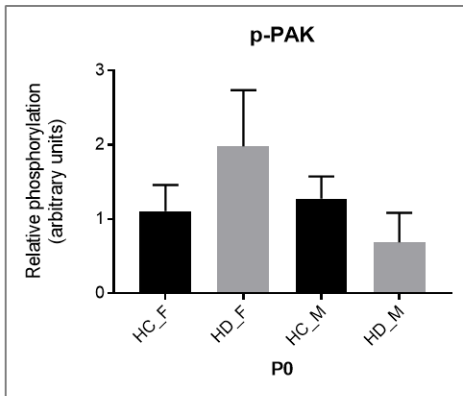
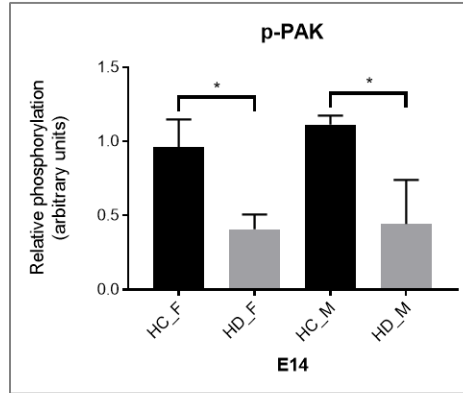
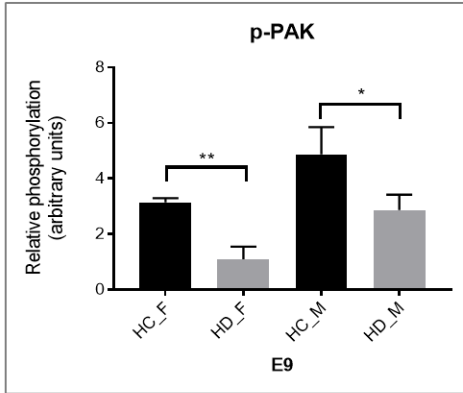


Figure 4.8C: Quantification of phospho-PAK ratio in brain samples of HD versus healthy control (HC) mice.

Shown here are bar-graphs representing densitometry data of phospho-PAK expression derived from Western blotting experiments using brain tissue lysates of HD and healthy control (HC) mice. The densitometric data were quantified as the ratio of the expression of phospho-PAK (T423) to total PAK. Protein levels of both phospho-PAK and total PAK were normalized to α -tubulin expression. Bar graph shows mean \pm standard deviation, *P < 0.05, **P < 0.005, ***P < 0.001, n = 3 experiments, unpaired t-test. HC = Healthy control, HD = Huntington disease, E = embryonic, P0 = at birth, w = week.

4.2.1.1.3 LIMK1

The LIM kinase family of serine/threonine kinases includes LIMK1 and LIMK2 that play a key role in actin and microtubule dynamics (Cuberos *et al.*, 2015; Dong *et al.*, 2012; Meng *et al.*, 2002). Both kinases are related, with the former being highly expressed in the brain and the latter being ubiquitously expressed. The LIM kinases are activated by Rho kinase (ROCK) and PAK1 and 4, which leads to the modulation of cofilin (Ohashi *et al.*, 2000). These upstream kinases phosphorylate LIMK1 T508 within the activation loop which is the site of its activation (Narayanan *et al.*, 2016; Ohashi *et al.*, 2000). The role of LIMK in microtubule dynamics in neural networks has not been studied well due to the complexities of the nervous system (Cuberos *et al.*, 2015). The transient overexpression of LIMK1 accelerates axon formation in mice and a prolonged overexpression of LIMK1 leads to axon retraction (Dong *et al.*, 2012).

Representative Western blots for both sexes are shown below with phospho-LIMK1 represented in Figure 4.9A and total LIMK1 in Figure 4.9B. The antibodies did not detect any expression at E9 for both phospho and total protein. Assessments of the relative phosphorylation confirmed that LIMK1 T508 was significantly decreased in lysates derived from the striatum of female HD mice at 3w. The relative phosphorylation in 4w female and male HD mice exhibited a significant decrease. Males at 7w showed a significant reduction in the expression of LIMK1 compared to females with HD, indicating a sex difference. At 10w, both sexes showed a significant reduction in the relative phosphorylation of LIMK1. No significant changes were observed in the relative phosphorylation at the earlier time points or at 5w (Figure 4.9C).

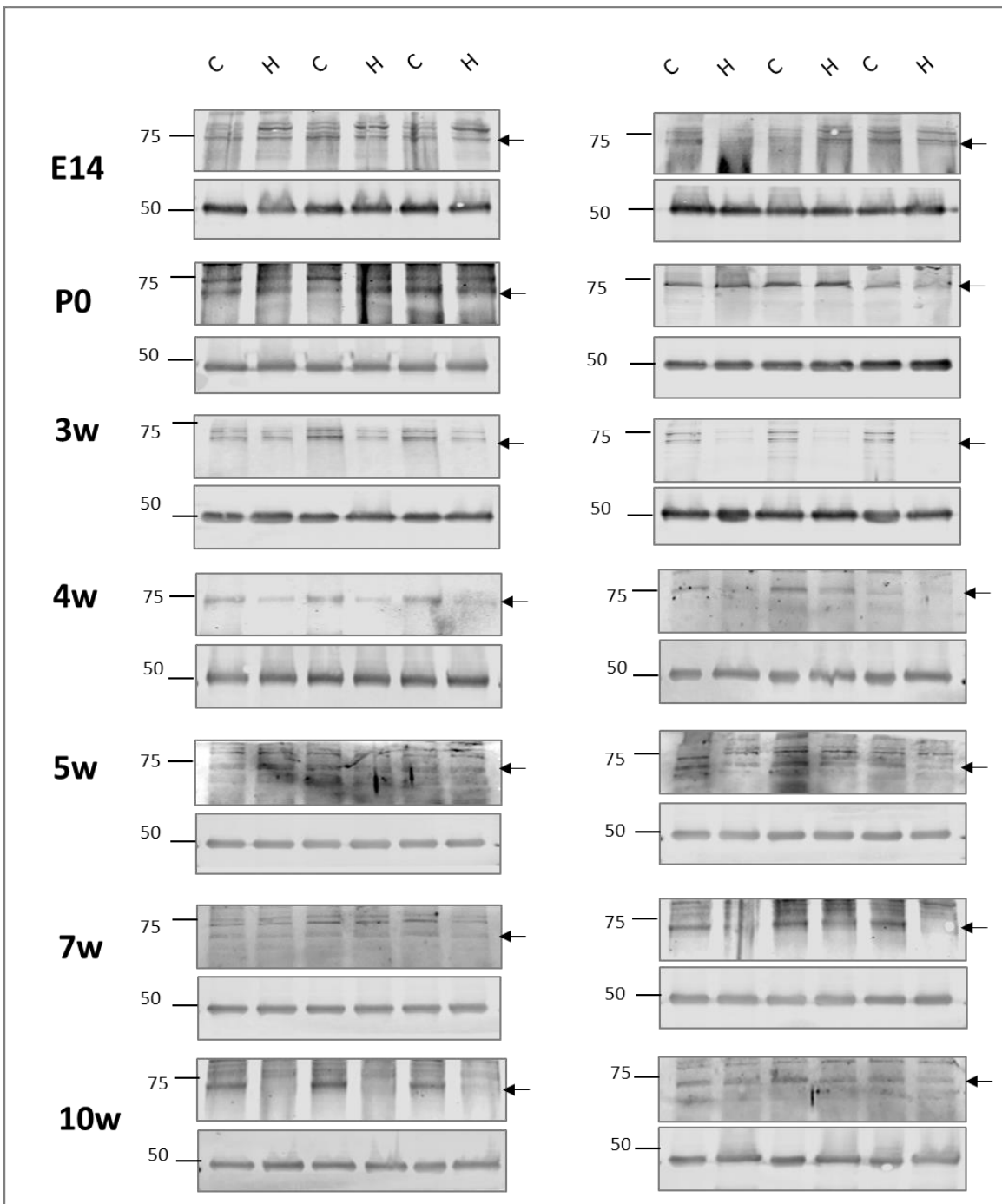


Figure 4.9A: Western blot analysis of phospho-LIMK protein levels.

Representative blots for phospho-LIMK1 (73kD) across seven time points and both sexes. The same membranes were also blotted for α -tubulin as a loading control (50kD). C = Control mouse, H = HD mouse, E = embryonic, P0 = at birth, w = week.

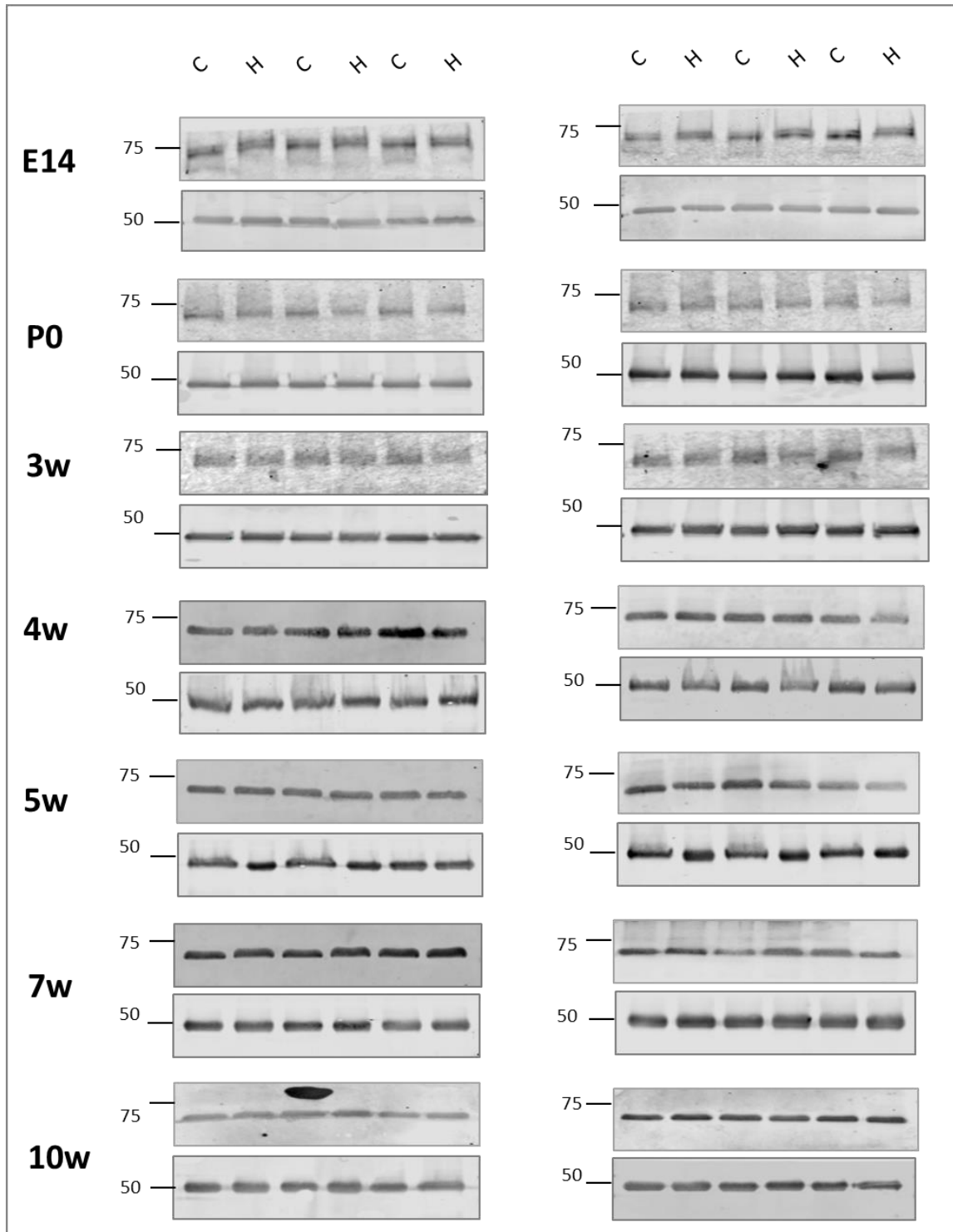


Figure 4.9B: Western blot analysis of total-LIMK protein levels.

Representative blots for total-LIMK1 (73kD) across seven time points and both sexes. The same membranes were also blotted for α -tubulin as a loading control (50kD). C = Control mouse, H = HD mouse, E = embryonic, P0 = at birth, w = week.

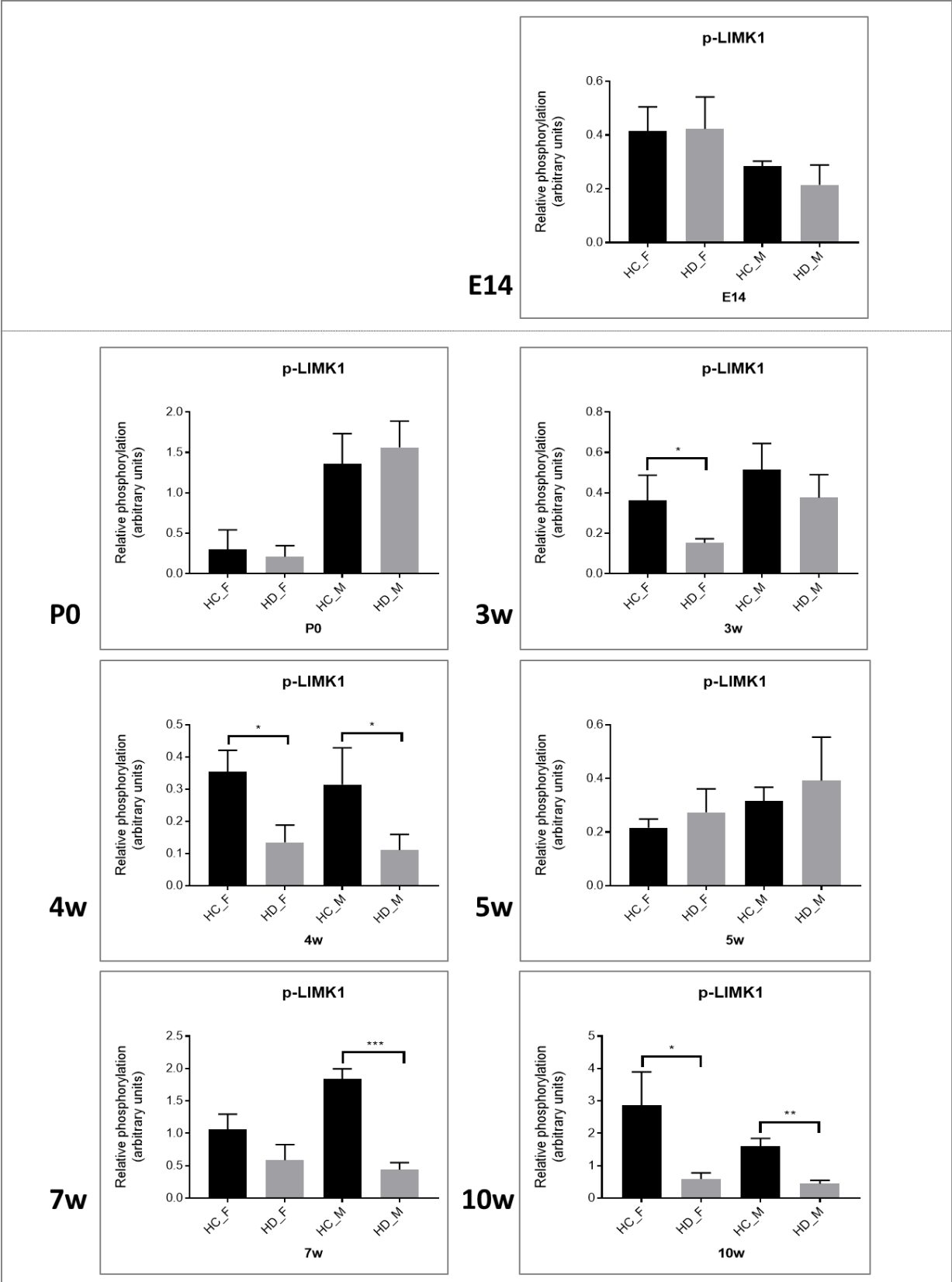


Figure 4.9C: Quantification of phospho-LIMK1 ratio in brain samples of HD versus healthy control mice.

Shown here are bar-graphs representing the densitometry data of phospho-LIMK1 expression derived from Western blotting experiments using brain tissue lysates of HD and healthy control (HC) mice. The densitometric data were quantified as the ratio of the expression of phospho-LIMK1 to total-LIMK1. Protein levels of both phospho-LIMK1 and total-LIMK1 were normalized to α -tubulin expression. Bar graph shows mean \pm standard deviation, *P < 0.05, **P < 0.005, ***P < 0.001, n = 3 experiments, unpaired t-test. HC = Healthy control, HD = Huntington disease, E = embryonic, P0 = at birth, w = week.

4.2.1.1.4 Cofilin

Cofilin plays an important role in actin dynamics by modulating actin polymerization and depolymerization. Apart from the severing activity it also induces dendritic nucleation and debranching. Cofilin is found in various compartments of the cells, including the cytoplasm and nucleoplasm, and forms stable heteropolymers with F-actin in the nucleus (Wioland *et al.*, 2017). Cofilin that is not phosphorylated at S3 is involved in the reversible interactions with F and G-actin. These interactions are involved in the regulation of cofilin after activation or its positioning in the cellular compartment (Bamburg and Bernstein, 2016; Munsie and Truant, 2012). The phosphorylation of cofilin at S3 leads to its deactivation leading to depolymerizing actin filaments. Conversely, the dephosphorylation of cofilin allows its binding to actin thereby promoting its polymerization. Slingshot (SSH) is the major phosphatase responsible for dephosphorylating cofilin at S3. The regulation of LIMK and SSH affects the phosphorylation of cofilin at S3 and ultimately its interaction with actin. Protein kinase D (PKD) inactivates SSH1L, a member of the SSH family, and activates LIMK1; therefore, inhibiting cofilin dephosphorylation. Notably calcineurin triggers cofilin dephosphorylation through the activation of SSH1L, whereas Ca²⁺/calmodulin dependent protein kinase II (CaMKII) negatively regulates SSH1L (Wang *et al.*, 2005). This indicated that calcineurin and CaMKII act as molecular switches controlling Ca²⁺-dependent cofilin activation (Figure 4.6).

Representative Western blots for both sexes are shown below with phospho-cofilin represented in Figure 4.10A and total cofilin in Figure 4.10B. Assessments of the relative

phosphorylation confirmed that cofilin S3 was significantly increased in the lysates derived from the whole brains of females, and decreased in male HD mice at E9 thus, indicating a sex difference. The phosphorylation of cofilin in females indicates that the depolymerization of actin and the reduced phosphorylation in males leads to actin polymerization. At E14, there was an increase in the relative phosphorylation in whole brain samples from females with HD. At 3w both the male and female striatal samples exhibited increases in the relative phosphorylation of cofilin. At 4w the cofilin levels decreased in the female HD striatum. Both the male and female relative expression levels of cofilin were reduced at 5w. At 7w only females and at 10w only males showed a reduction in the relative phosphorylation of cofilin, suggesting a sex difference in disease progression. There was no change observed at birth, as shown in the Figure 4.10C.

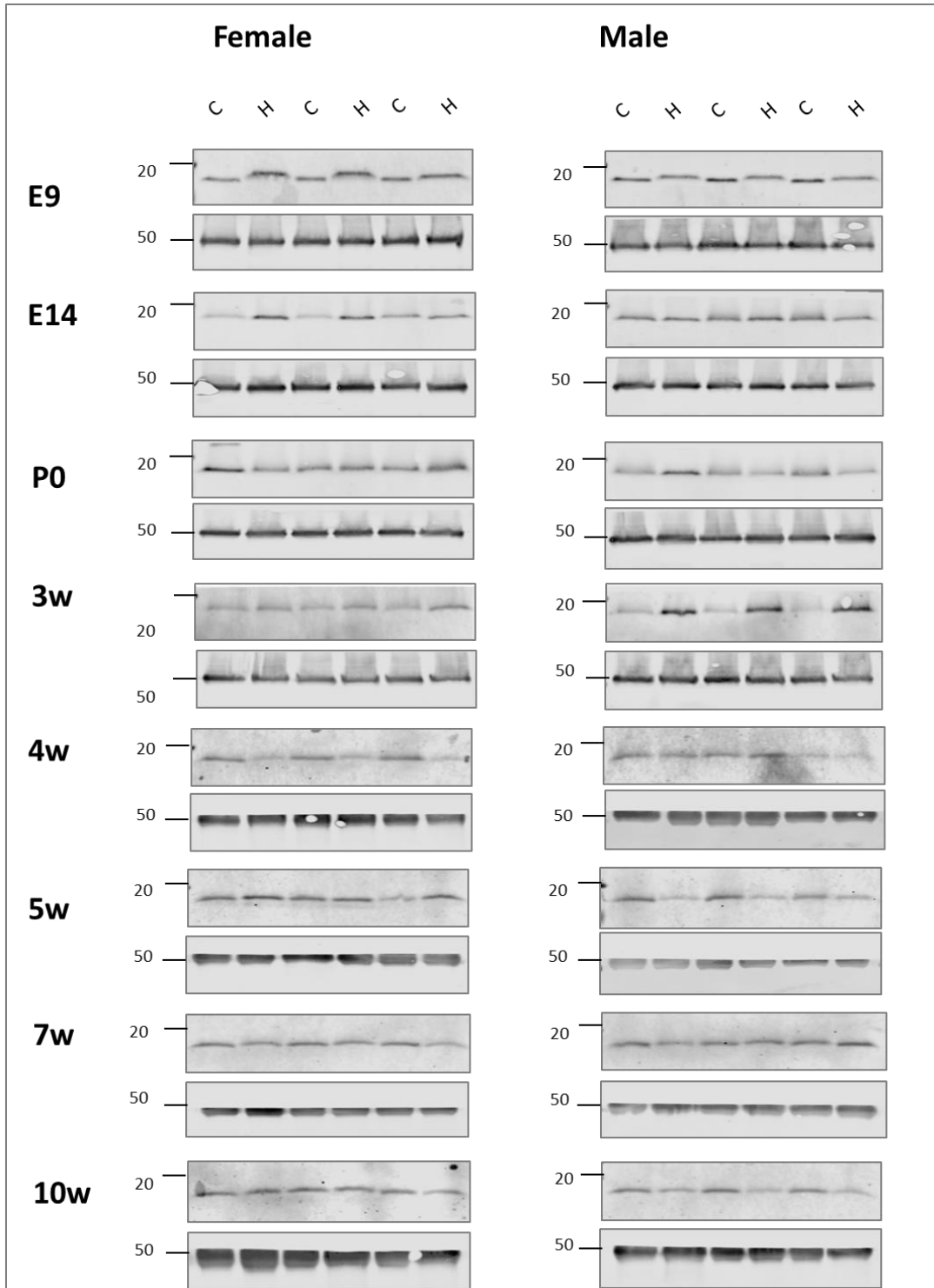


Figure 4.10A: Western blot analysis of phospho-cofilin protein levels.

Representative blots for phospho-cofilin (19kD) across eight time points and both sexes. The same membranes were also blotted for α -tubulin as a loading control (50kD). C = Control mouse, H = HD mouse, E = embryonic, P0 = at birth, w = week.

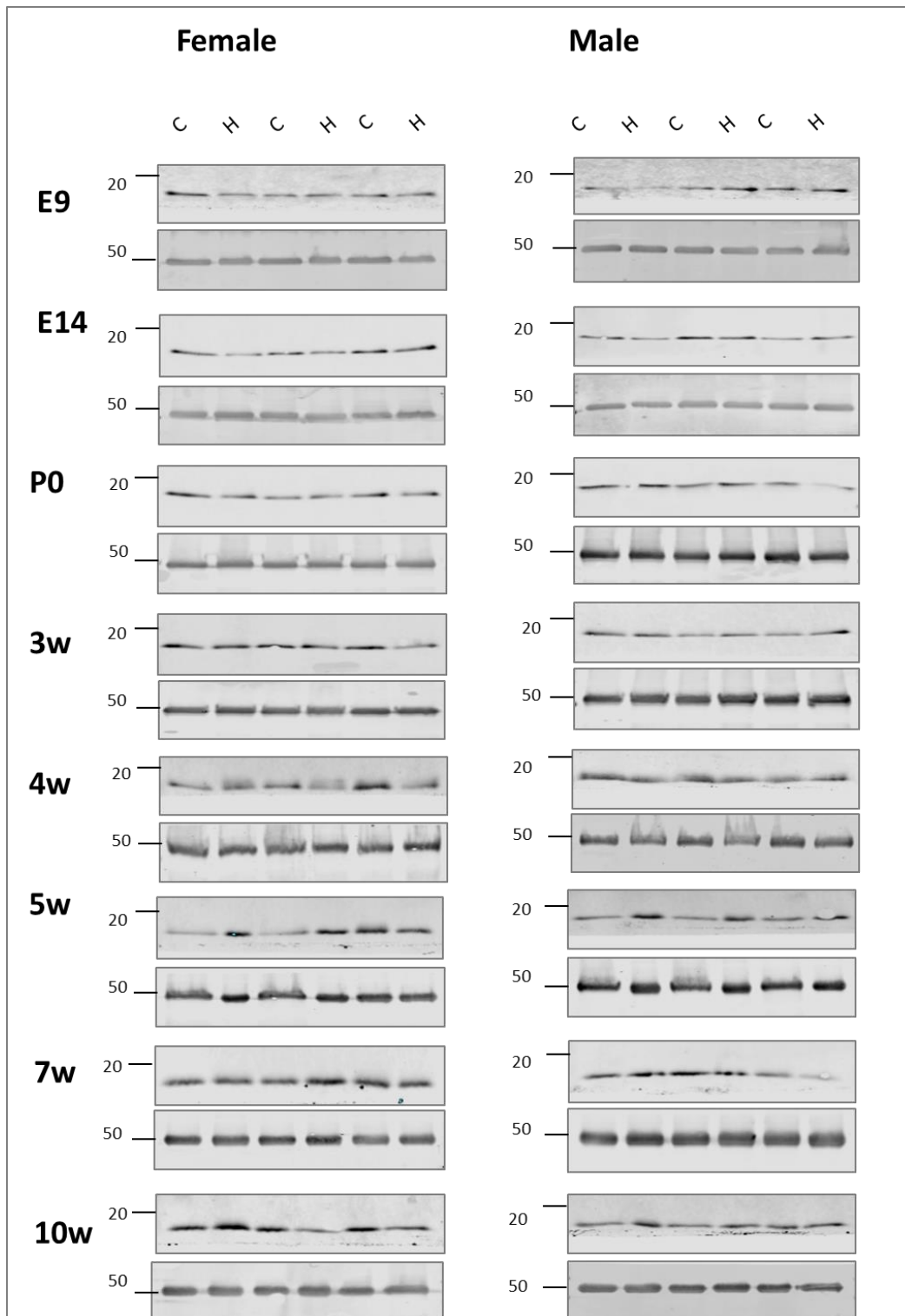


Figure 4.10B: Western blot analysis of total-cofilin protein levels.

Representative blots for total-cofilin (19kD) across eight time points and both sexes. The same membranes were also blotted for α -tubulin as a loading control (50kD). C = Control mouse, H = HD mouse, E = embryonic, P0 = at birth, w = week.

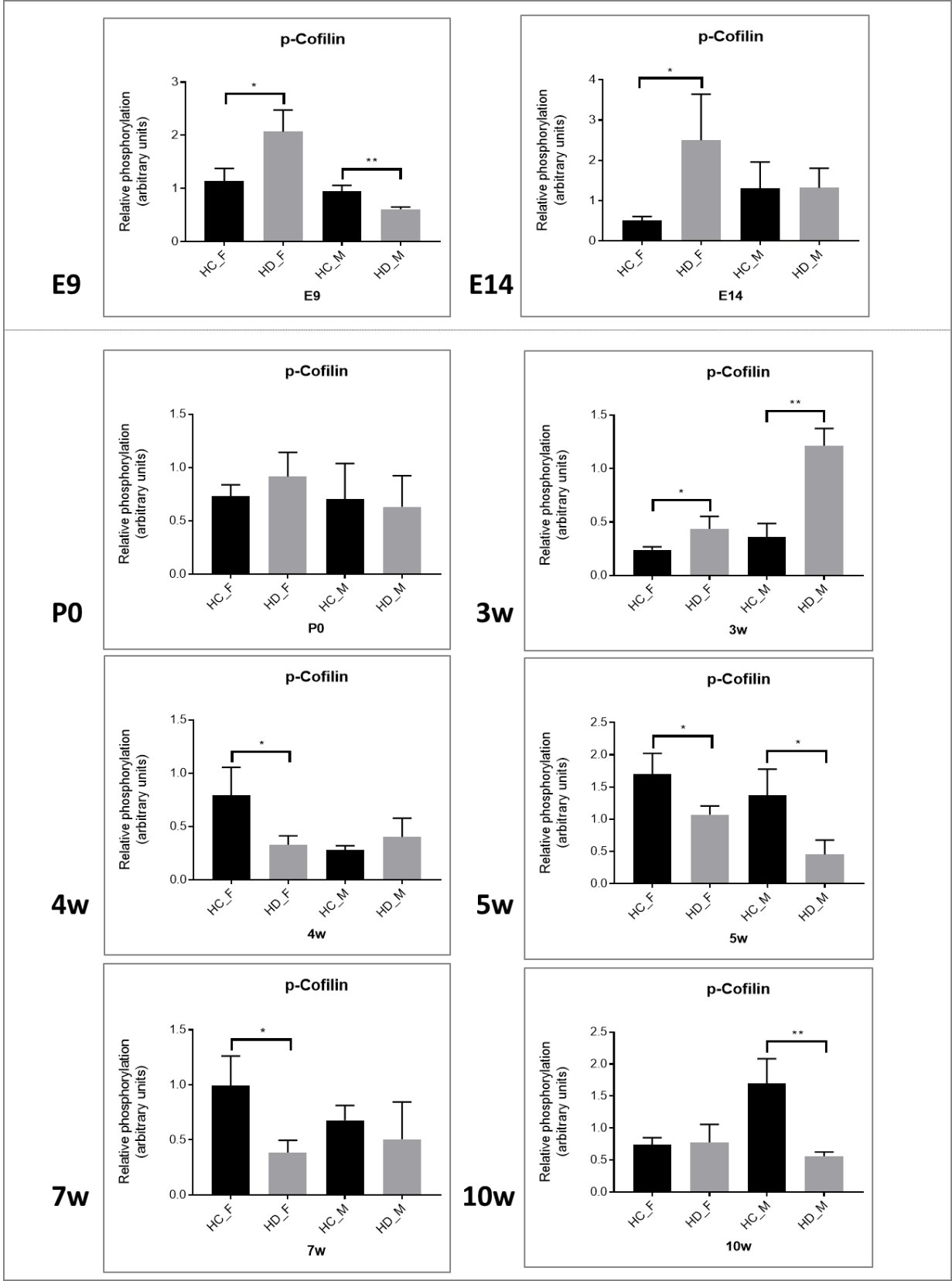


Figure 4.10C: Quantification of phospho-cofilin ratio in brain samples of HD versus healthy control mice.

Shown here are bar-graphs representing densitometry data of phospho-cofilin expression derived from Western blotting experiments using brain tissue lysates of HD and healthy control (HC) mice. The densitometric data were quantified as the ratio of the expression of phospho-cofilin to total cofilin. Protein levels of both phospho-cofilin and total cofilin were normalized to α -tubulin expression. Bar graph shows mean \pm standard deviation, *P < 0.05, **P < 0.005, n = 3 experiments, unpaired t-test. HC = Healthy control, HD = Huntington disease, E = embryonic, P0 = at birth, w = week.

4.2.1.1.5 Slingshot

The Slingshot (SSH) family of protein phosphatases include three members, namely SSH1, SSH2 and SSH3. The regulation of cofilin is controlled by LIMKs and SSH phosphatases through phosphorylation (inactivation) and dephosphorylation (activation) at S3, respectively. The regulation between phospho-cofilin and cofilin level determines actin polymerization in growth cone motility, neurite outgrowth and axon guidance (Ohta *et al.*, 2003). One study showed that SSH1 is activated by ROS, which subsequently activated the cofilin proteins that form cofilin rods and cause neurite atrophy (Kim *et al.*, 2009) (Figure 4.6). Calcium mediates the activation of SSH via the activation of calcineurin (Wang *et al.*, 2005). Phosphorylation of SSH1 at S978 increases its phosphatase activity.

Representative Western blots for both sexes are shown below with phospho-SSH1L represented in Figure 4.11A and total SSH1L in Figure 4.11B. The expression of phospho and total-SSH1L were not detected at E9. Assessment of the relative phosphorylation confirmed that SSH1L at S978 was significantly decreased in the lysates derived from the whole brain of female HD mice at E14 and correspond to the increase in cofilin phosphorylation. The relative phosphorylation at birth in males was significantly decreased in HD striatum samples. At 3w, both sexes had increased expression of SSH1L compared to control samples. At 5w there is a significant increase in the expression of SSH1L in male. The analysis showed that the rest of the striatal samples did not exhibit a significant difference in the relative phosphorylation status of SSH1L (Figure 4.11C).

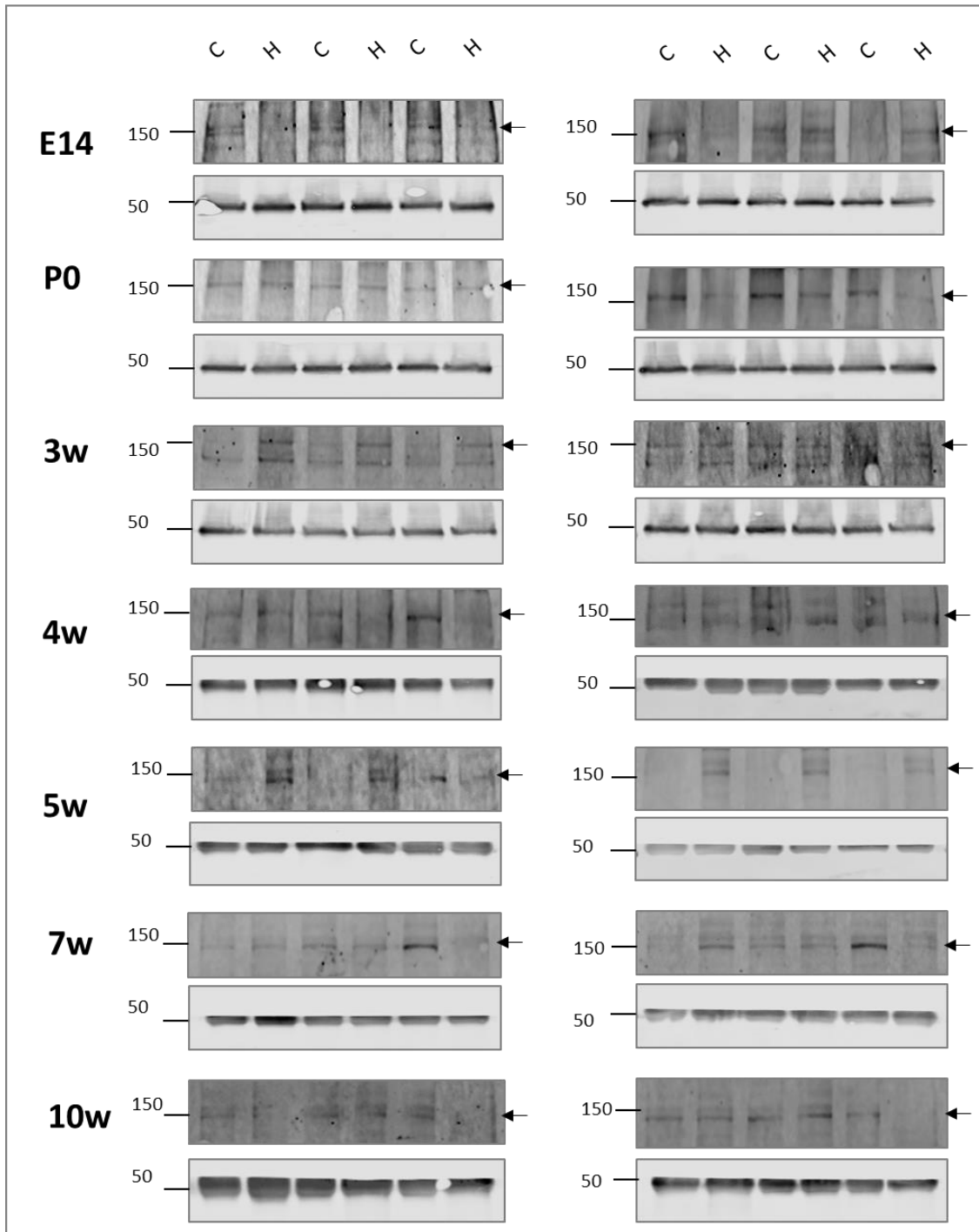


Figure 4.11A: Western blot analysis of phospho-SSH1L protein levels.

Representative blots for phospho-SSH1L (150kD) across eight time points and both sexes. The same membranes were also blotted for α -tubulin as a loading control (50kD). No expression was observed at E9. C = Control mouse, H = HD mouse, E = embryonic, P0 = at birth, w = week. Arrow indicates the band that was used for quantification.

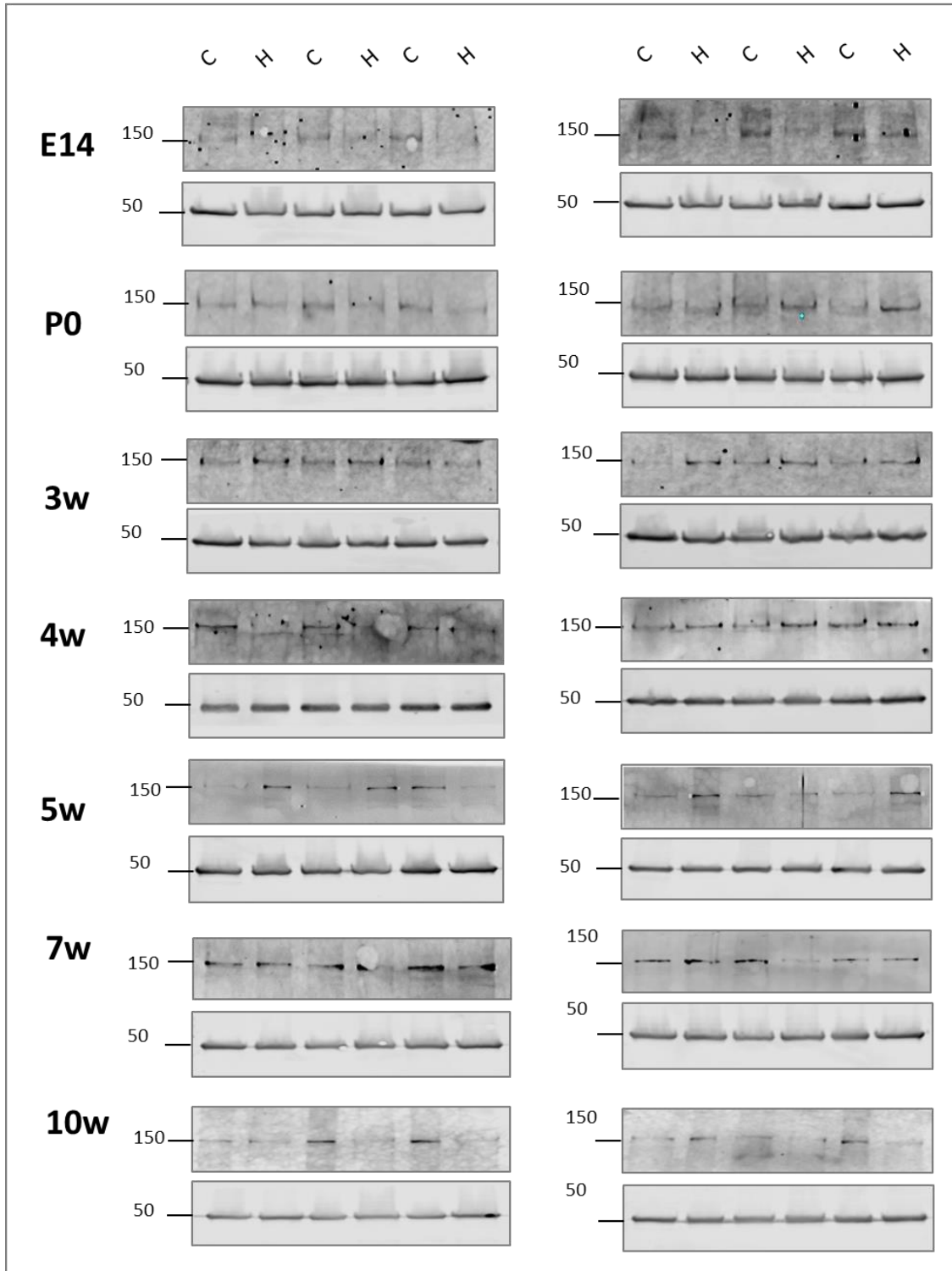


Figure 4.11B: Western blot analysis of total-SSH1L protein levels.

Representative blots for total-SSH1L (150kD) across eight time points and both sexes. The same membranes were also blotted for α -tubulin as a loading control (50kD). No expression was observed at E9. C = Control mouse, H = HD mouse, E = embryonic, P0 = at birth, w = week.

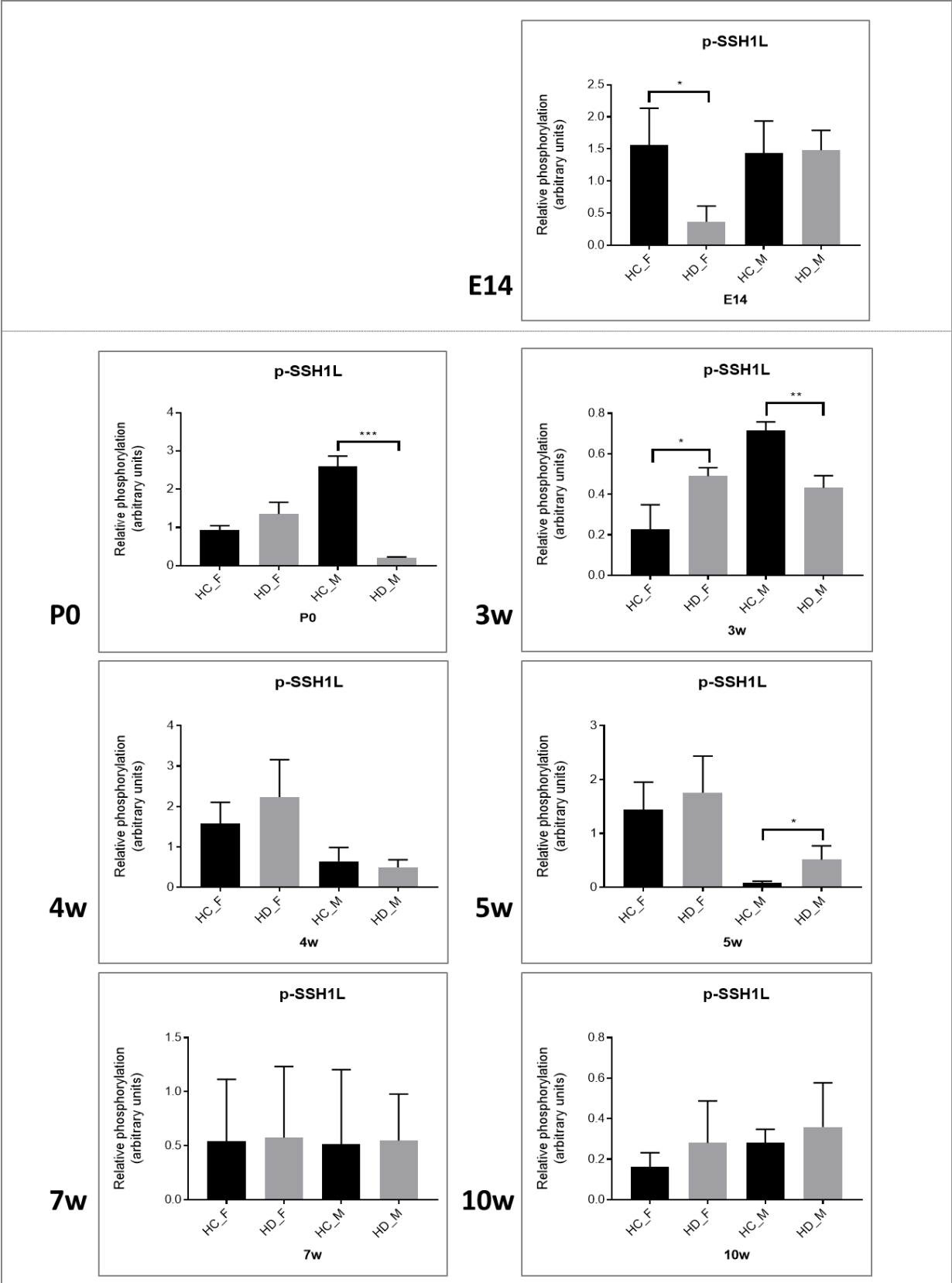


Figure 4.11C: Quantification of phospho-SSH1L ratio in brain samples of HD versus healthy control mice.

Shown here are bar-graphs representing densitometry data of phospho-SSH1L expression derived from Western blotting experiments using brain tissue lysates of HD and healthy control (HC) mice. The densitometric data were quantified as the ratio of the expression of phospho-SSH1L to total SSH1L. Protein levels of both phospho-SSH1L and total SSH1L were normalized to α -tubulin expression. Bar graph shows mean ratio \pm SD, *P < 0.05, **P < 0.005, ***P < 0.001, n = 3 experiments, unpaired t-test. HC = Healthy control, HD = Huntington disease, E = embryonic, P0 = at birth, w = week.

4.2.1.1.6 Profilin-1

Profilin is an actin binding protein with four isoforms with tissue-specific expressions (Burnett *et al.*, 2008). Profilin 1 is expressed in all tissues, profilin 2 is specifically expressed in the brain, and profilins 3 / 4 are expressed in the testis. Profilin 1 binds to Htt protein causing a progressive loss of mHtt seen in the cortex of HD patients by reducing its aggregation (Burnett *et al.*, 2008; Posey *et al.*, 2018). The loss of profilin further leads to the imbalance in the F/G actin ratio, which ultimately affects actin polymerization (Burnett *et al.*, 2008). ROCK1 phosphorylates profilin 1 at S138 and reduces its affinity for G-actin (Narayanan *et al.*, 2016). This prevents the interaction of profilin 1 with Htt; thus, preventing the inhibition of mHtt aggregation (Burnett *et al.*, 2008; Shao *et al.*, 2008).

Representative Western blots for both sexes are shown below with phospho-profilin 1 represented in Figure 4.12A and total profilin in Figure 4.12B. Assessments of relative phosphorylation confirmed that profilin S138 was significantly decreased in the lysates derived from the whole brains of female HD mice at E9, which was similar to the peptide array output (Table 4.4). Phosphorylation increases were observed in the HD brains of both sexes at E14, again agreeing with the direction observed in the peptide array outputs. At 3w, the shift was observed in both sexes showed a significant increase in HD samples. At 7w, a difference was observed between male and females where only the male HD mice showed a significant difference between HD and HC. At 10w, both the female and male HD lysates exhibited a reduction in the expression of profilin 1. There were no significant changes in expression observed in the 4 and 5w samples, as shown in Figure 4.15C.

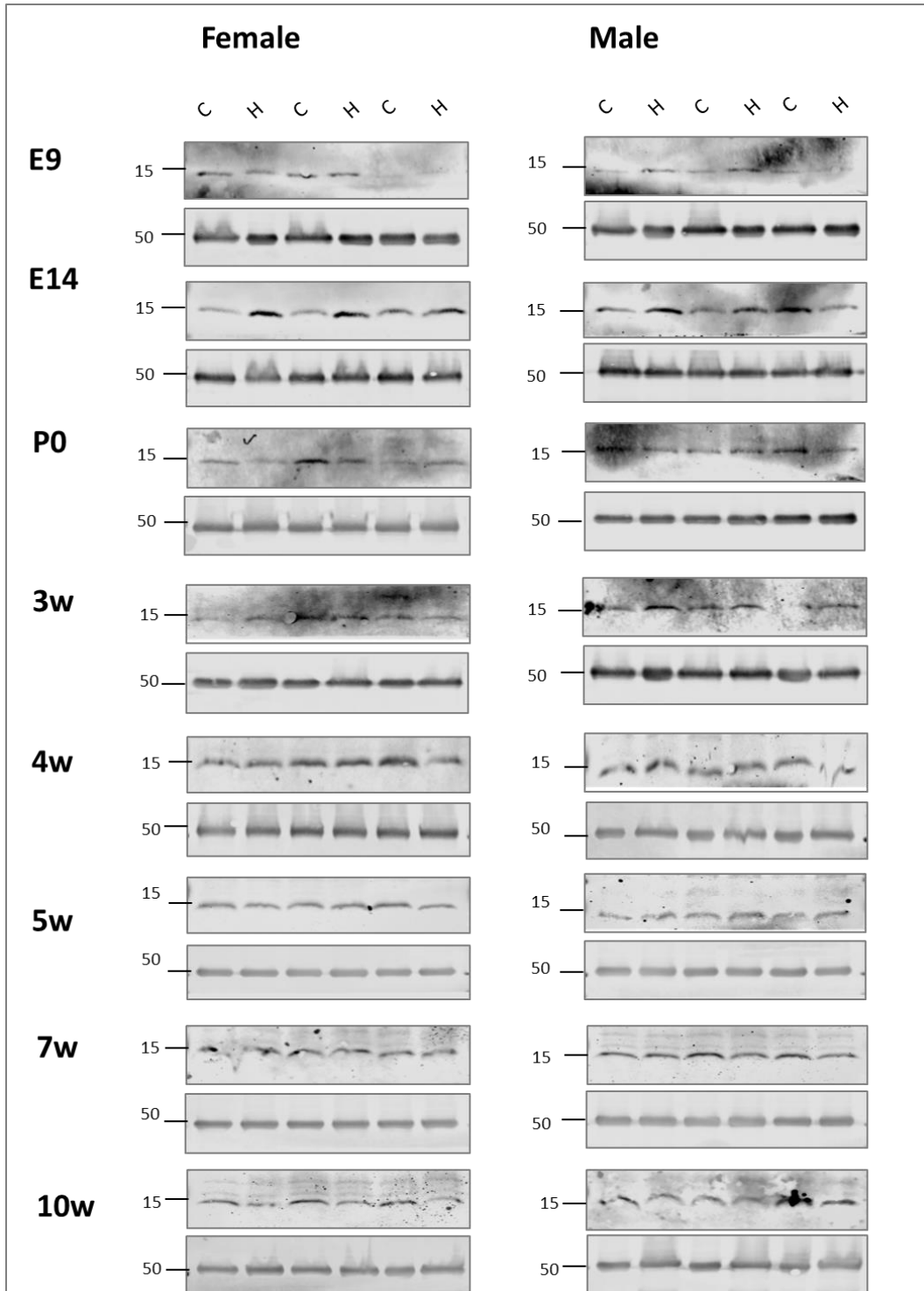


Figure 4.12A: Western blot analysis of phospho-profilin protein levels.

Representative blots for phospho-profilin (15kD) across eight time points and both sexes. The same membranes were also blotted for α -tubulin as a loading control (50kD). C = Control mouse, H = HD mouse, E = embryonic, P0 = at birth, w = week.

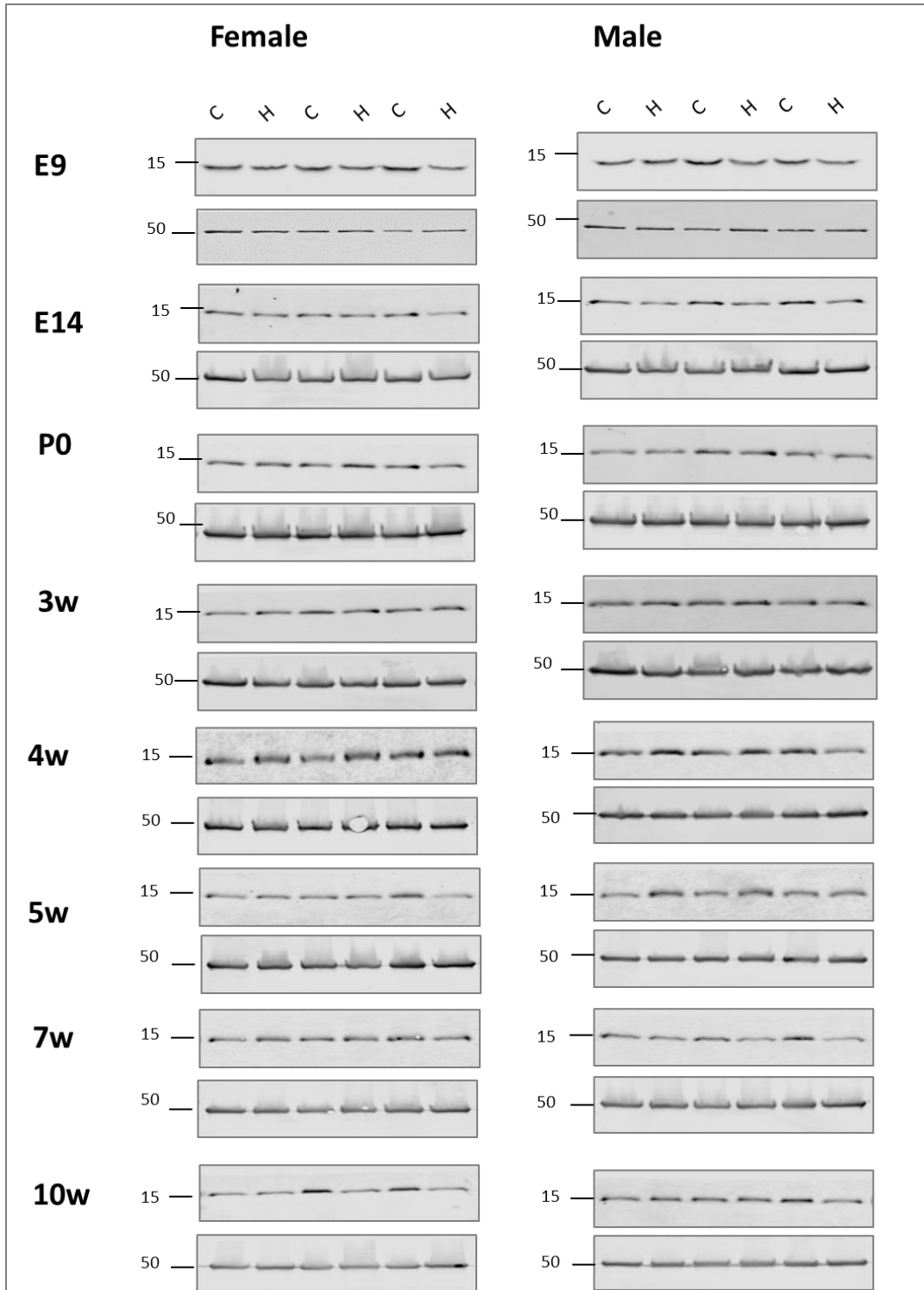


Figure 4.12B: Western blot analysis of total-profilin protein levels.

Representative blots for total-profilin (15kD) across eight time points and both sexes. The same membranes were also blotted for α -tubulin as a loading control (50kD). C = Control mouse, H = HD mouse, E = embryonic, P0 = at birth, w = week.

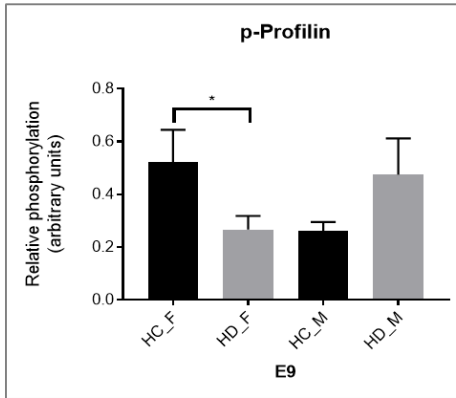
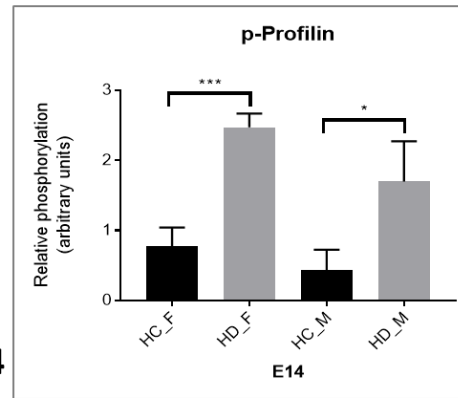
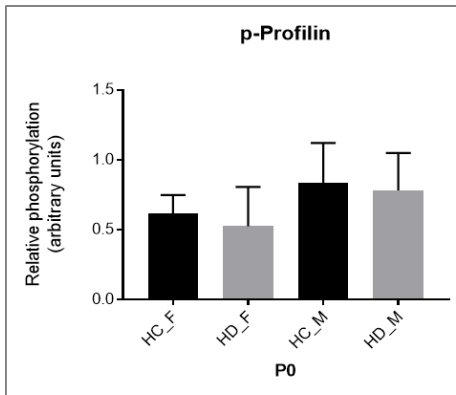
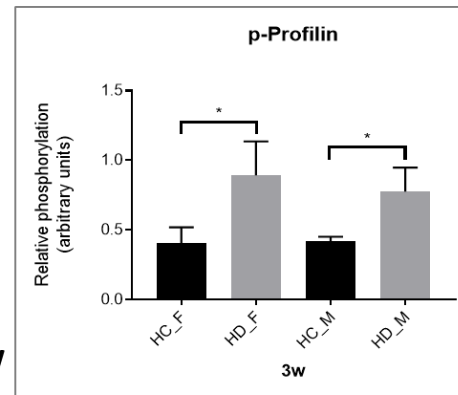
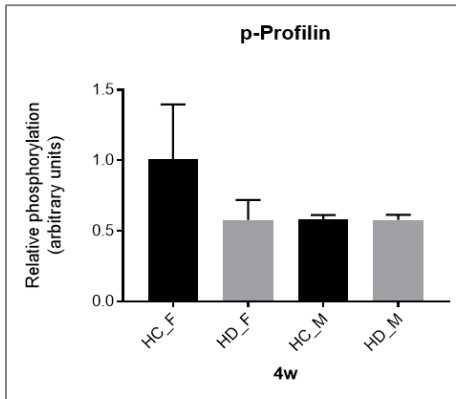
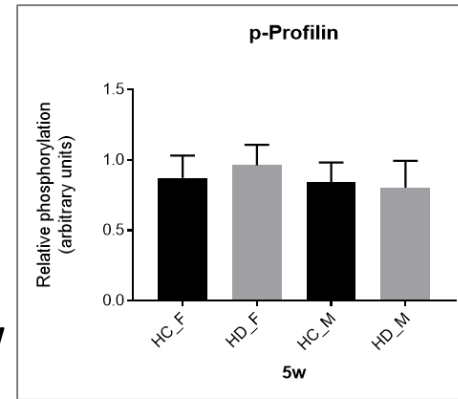
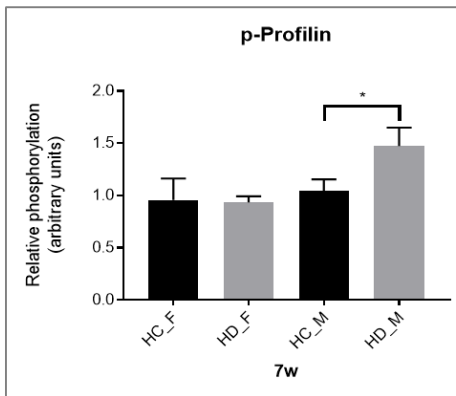
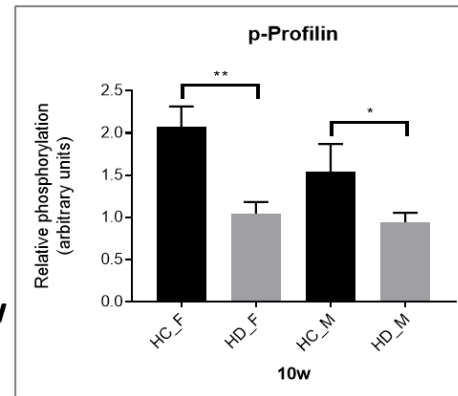
E9**E14****P0****3w****4w****5w****7w****10w**

Figure 4.12C: Quantification of phospho-profilin 1 ratio in brain samples of HD versus healthy control mice.

Shown are bar-graphs representing densitometry data of phospho-profilin 1 expression derived from Western blotting experiments using brain tissue lysates of HD and healthy control (HC) mice. The densitometric data were quantified as the ratio of the expression of phospho-profilin 1 to total-profilin. Protein levels of both phospho-profilin 1 and total-profilin were normalized to α -tubulin expression. Quantitative data were compared between groups using t-tests (males-M and females-F). Bar graph shows mean \pm standard deviation, *P < 0.05, **P < 0.005, ***P < 0.001, n = 3 experiments, unpaired t-test. HC = Healthy control, HD = Huntington disease, E = embryonic, P0 = at birth, w = week.

4.2.1.1.7 AKT1

AKT is a Serine/Threonine kinase whose activation occurs downstream of PI3K, and has many multifunctional key nodes downstream. AKT has three isoforms named AKT 1, 2 and 3 and is considered a master regulator for a number of biological processes such as proliferation, cell survival, growth, and neurogenesis (Colin *et al.*, 2005; Lievens *et al.*, 2008; Maddika *et al.*, 2008; Sugiyama *et al.*, 2019). PI3K activation leads to the phosphorylation of two key residues on AKT1, including T308 in the activation loop, and S473 in a C-terminal hydrophobic motif (Manning and Toker, 2017). The phosphorylation of both residues are required to attain maximum functionality by the kinase. PP2A and PTEN are major phosphatases that directly inactivate AKT (Phadngam *et al.*, 2016). The appearance of this particular isoform in the significantly differentiated peptide array dataset was recognized as important and appropriate for validation.

Representative Western blots for both sexes are shown below with phospho-AKT1 represented in Figure 4.13A and total AKT1 in Figure 4.13B. Assessments of the relative phosphorylation confirmed that phospho-AKT1 S473 was significantly increased in the lysates derived from the whole brain of both sexes HD mice at E9. The relative phosphorylation at birth was also significantly increased in females and males. At 3w, there was an increase in the relative phosphorylation of AKT1 in females and at 5w there was a decrease in the relative phosphorylation in males. Those findings were opposite to the results obtained by the peptide array (Table 4.4). At 10w phosphorylation was increased in males. The results from the later time points suggest a sex difference. E14, 4w and 7w did not show any significant changes in AKT1 phosphorylation, as seen in the Figure 4.13C.

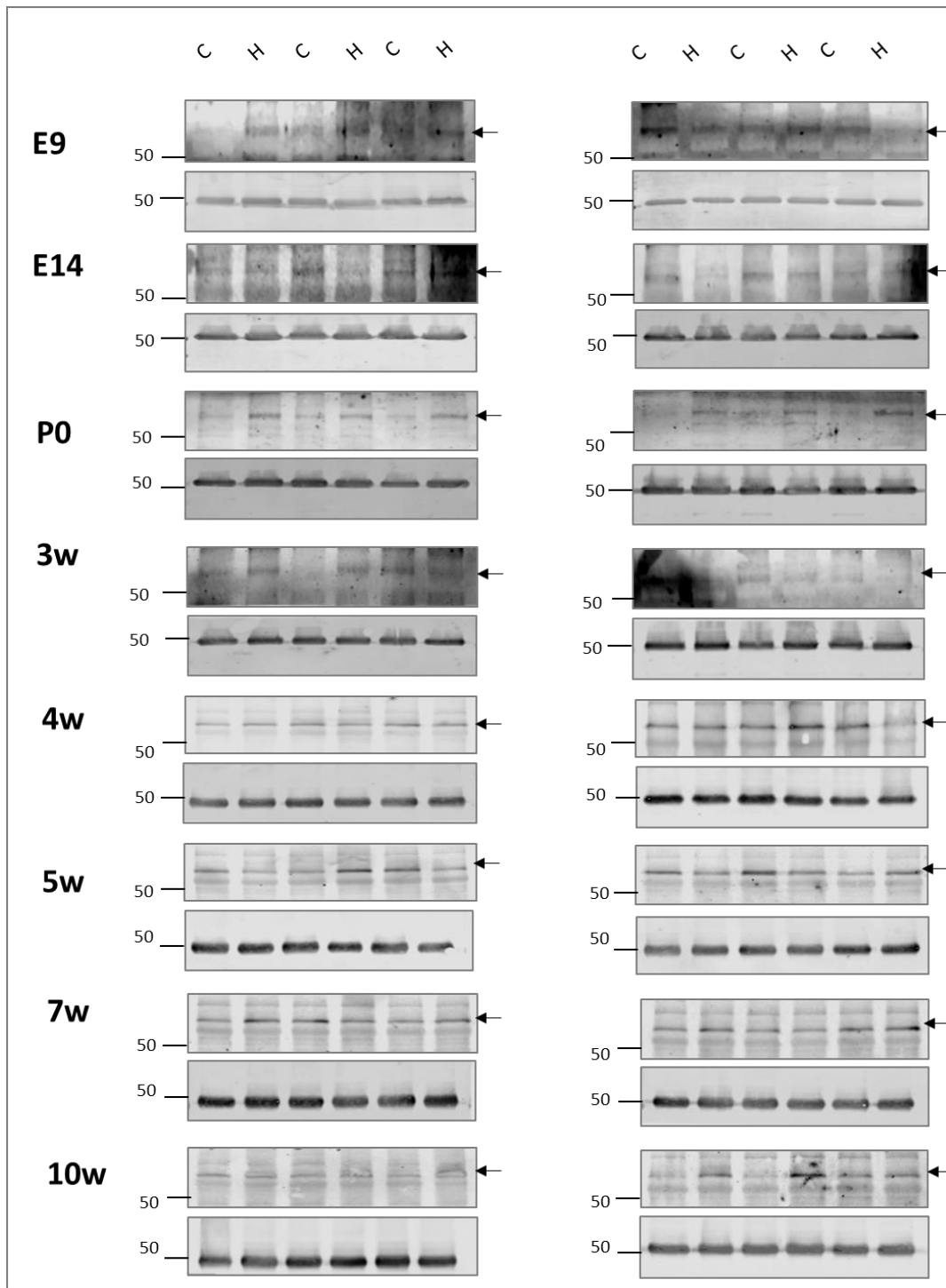


Figure 4.13A: Western blot analysis of phospho-AKT1 protein levels.

Representative blots for phospho-AKT1 (60kD) across eight time points and both sexes. The same membranes were also blotted for α -tubulin as a loading control (50kD). C = Control mouse, H = HD mouse, E = embryonic, P0 = at birth, w = week. Arrow indicates the band that was used for quantification.

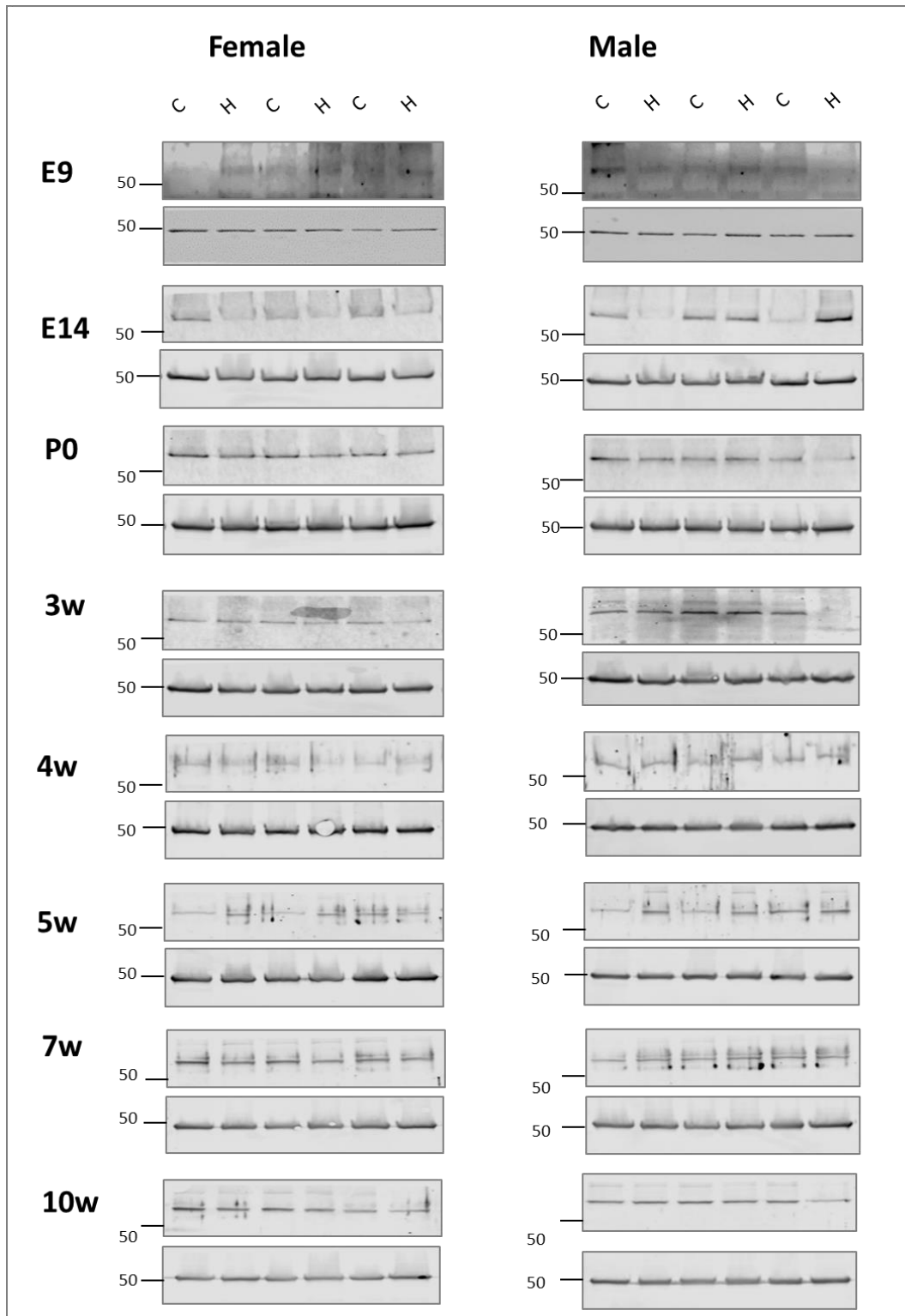


Figure 4.13B: Western blot analysis of total-AKT1 protein levels.

Representative blots for total-AKT1 (60kD) across eight time points and both sexes normalized to α -tubulin (50kD). C = Control mouse, H = HD mouse, E = embryonic, P0 = at birth, w = week.

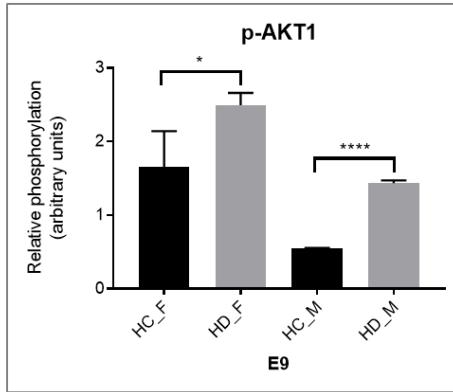
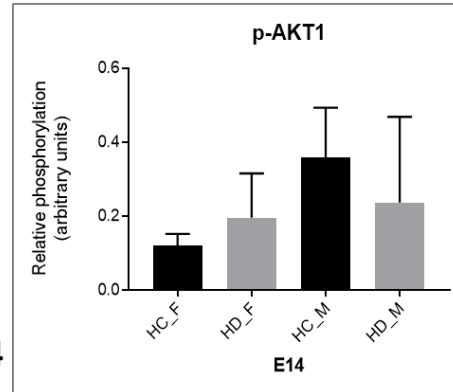
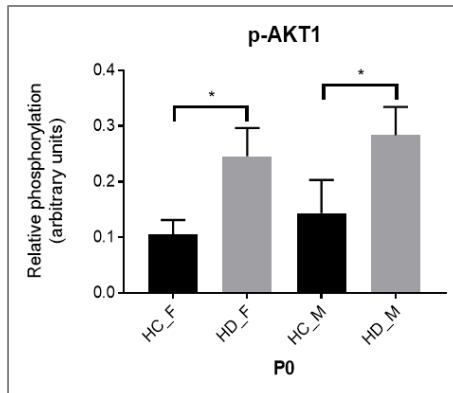
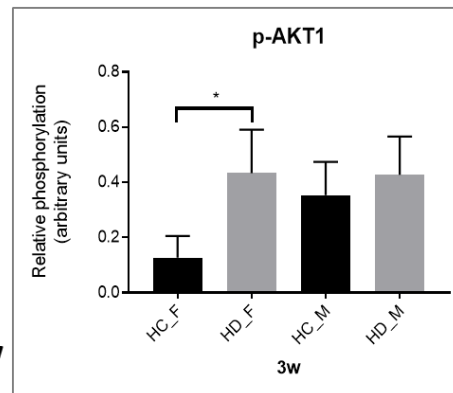
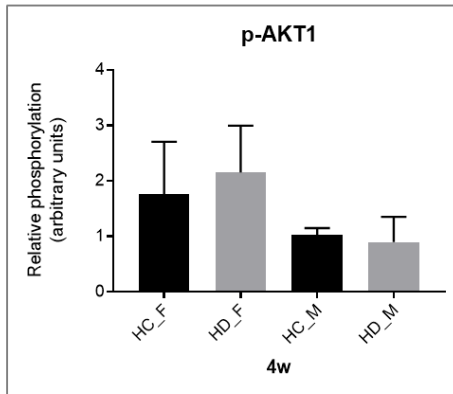
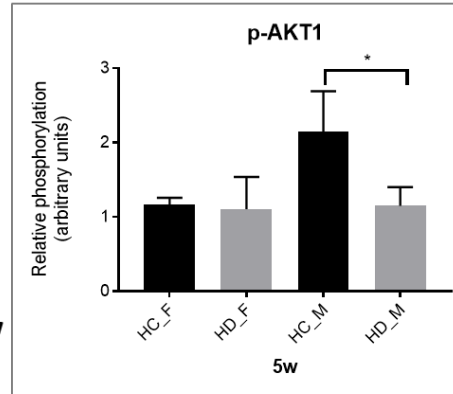
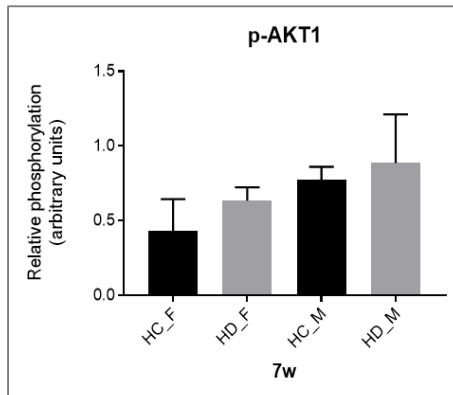
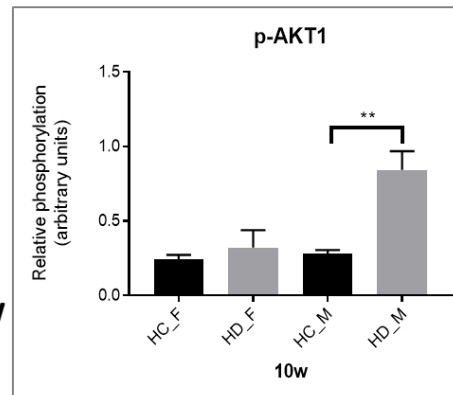
E9**E14****P0****3w****4w****5w****7w****10w**

Figure 4.13C: Quantification of phospho-AKT1 ratio in brain samples of HD versus healthy control mice.

Shown here are bar-graphs representing densitometry data of phospho-AKT1 expression derived from Western blotting experiments using brain tissue lysates from HD and healthy control (HC) mice. The densitometric data were quantified as the ratio of the expression of phospho-AKT1 to total AKT1. Protein levels of both phospho-AKT1 and total AKT1 were normalized to α -tubulin expression. Quantitative data were compared between groups using t-tests (males-M and females-F). Bar graph shows mean \pm standard deviation, *P < 0.05, **P < 0.005, ***P < 0.001, n = 3 experiments, unpaired t-test. HC = Healthy control, HD = Huntington disease, E = embryonic, P0 = at birth, w = week.

Analysis of the effects of the peptides involved in cytoskeletal signaling suggests that the phosphorylation of the upstream kinases, ROCK2 and PAK1, were dysregulated at the embryonic stage of development. The phosphorylation of the kinase and phosphatase upstream of actin (LIMK1, SSH1L) along with cofilin and profilin were found to be dysregulated around the same time as mHtt appeared in the brain, or at later stages of disease. These are tabulated for a comprehensive summary and the ease of visualization in Table 4.4. Therefore it can be suggested that there is evidence of both neurodevelopmental changes, as well as sex specific differences in the progression of the disease which is observed as the dysregulated kinase signaling.

Table 4.14: Summary of the significantly hyper- (pink) and hypo- (green) phosphorylated proteins based on Western blot results.

	E9		E14		P0		3w		4w		5w		7w		10w	
	F	M	F	M	F	M	F	M	F	M	F	M	F	M	F	M
ROCK2																
PAK																
LIMK1																
Cofilin																
SSH1L																
Profilin																
AKT1																

4.2.2 NetworKIN

Western blot analyses was used in an attempt to independently validate the peptide array data following which I decided to identify the upstream kinases responsible for phosphorylating these targets, by using online tools. NetworKIN platform was used to predict candidate kinases upstream of the phosphosites determined from peptide array analyses utilizing neural tissue from HD mice. Significantly hyper-phosphorylated or hypo-phosphorylated phosphosites from the peptide array were used to predict upstream kinases for all the time points and both sexes using NetworKIN. The resulting predicted annotations were filtered using a NetworKIN confidence score cut-off of 3.0 and a NetworKIN score-difference cut-off of 4.0. (Linding *et al.*, 2008). The score-difference defines the maximum difference between the best prediction and the second-best prediction. The identified kinases for hyper- and hypo-phosphorylated phosphosites were plotted on a mammalian kinase-dendrogram generated using KinMap_{beta}. A cut-off score of 30 was used for the NetworKIN output which generated a list of predicted kinases that were represented on the dendrogram as shown in Figure 3.13.

4.2.3 KinMap

As mentioned earlier, a NetworKIN cut off score was used to short list the kinases to be represented on a dendrogram (or kinome tree) generated by KinMap. The kinome tree allows the visualization of the different kinases from a complex dataset (Eid *et al.*, 2017) to gain a better understanding of the biology from high throughput data. The kinases were represented on the kinome tree in the form of a circle or square. A circle was used to represent the female dataset and squares for males. The candidate kinases predicted to target the upregulated phosphosites are represented in red and downregulated phosphosites are represented in green. The color blue was used for upregulated phosphosites observed in only one sex with and yellow for downregulated phosphosites observed in only one sex. The size of the circles or squares is determined by the NetworKIN score, with a higher score having a larger representation on the dendrogram i.e. regulating more peptides on the array. Manning *et al.* used the underlying sequences to divide nearly 540 kinases into eight typical and 13 atypical groups (Manning *et al.*, 2002) as listed earlier.

After shortlisting the kinases with the NetworKIN a cut-off score of 30 these kinases were

then uploaded on the KinMap online tool used to generate dendrograms, visually representing the kinases. Based on the peptide array results KinMap represented the predicted kinases that were predicted to be dysregulated in HD mice (Supplementary Figures 1.1-1.8). Panel A shows the kinases dysregulated in females and the panel B represents males. The dendrograms show subtle differences in the predicted kinases, and indicate towards sex and developmental differences within the disease process. The difference in the upstream predicted kinases is represented in the dendrograms in the appendix and supplementary table S8 highlights them. These results emphasize the importance of cytoskeletal system dynamics and upstream kinases regulating the disease process. PAKs and GSKs are involved in cytoskeletal dynamics and are upstream of actin and microtubules, respectively. The roles of Ephrins on the other hand have been well studied in neural development, cytoskeletal dynamics, axon guidance and synaptogenesis (Boyd *et al.*, 2014; Huot, 2004; Xu and Henkemeyer, 2012). Another prominent family of kinases predicted were the CaMKs, of which one example is Ca²⁺/calmodulin-dependent protein kinase II (CaMKII), which negatively regulates SSH1L activity, and thus, plays an important role in actin cytoskeletal reorganization (Zhao *et al.*, 2012). Ca²⁺-induced cofilin dephosphorylation is mediated by calcineurin-dependent activation of SSH1L, cofilin and LIMK1 (Zhao *et al.*, 2012). ATM, which is an upstream predicted kinase in NSCs was also one of the upstream kinases identified in the murine dataset. A study has showed that small-molecule inhibitors targeting ATM ameliorates mHtt toxicity in cells and animal models (Cara *et al.*, 2016; Lu *et al.*, 2014). Overall, the findings indicate a dysregulated cytoskeleton, developmental variance and sex differences in the disease progression, which needs further investigation.

4.2.4 Discussion

Decades ago, neurodegeneration was not well understood since the life expectancy of individuals was not as long as it is currently. The 2000's showed an increase in better understanding of the disease process and finding some treatments for neurodegenerative disorders. The auto phosphorylation of ROCK2 at S1366 does not affect its kinase activity, but could be a contributor to protein subcellular localization. ROCK 2 has multiple downstream targets that affect the regulation of cell shape, motility, survival and apoptosis (Koch *et al.*, 2018; Koch *et al.*, 2014; Yan *et al.*, 2019). One of the most important effects of activated ROCK is the regulation of the

actin cytoskeleton through the phosphorylation of LIMK1 and LIMK2. LIMK phosphorylates cofilin, which depolymerizes or severs the actin filament. This arrests neurite outgrowth and leads to an abundance of stable actin filaments. Notably, knockdown of ROCK2 prevents apoptosis and increases AKT activity (Koch *et al.*, 2014). Several studies have also shown an increase in ROCK2 and its downstream targets, including LIMK1 and cofilin in patients with neurodegenerative disorders such as ALS and AD (Chuang *et al.*, 2012; Koch *et al.*, 2018; Koch *et al.*, 2014; Narayanan *et al.*, 2016). Another regulator of the actin cytoskeleton and dendritic spine morphogenesis is the RAC/CDC42-activated kinase, PAK1. PAK1 interacts with Htt and enhances the aggregation of mHtt, thus inducing toxicity, while inhibition of PAK1 protects against HD symptoms (Ma *et al.*, 2012). Studies have shown that PAK1 co-localizes with mHtt aggregates in cell lines and in human HD brains, thus, suggesting that it plays a key role in the expansion of the polyQ tract that leads to the aggregation of mHtt (Luo *et al.*, 2008; Ma *et al.*, 2012). Notably, there is a progressive loss of profilin in presymptomatic HD gene carriers (Burnett *et al.*, 2008). A study reported that the overexpression of profilin abolished mHtt toxicity in cells; thus, extending the life span of *Drosophila* (Posey *et al.*, 2018). Profilin can promote actin polymerization or sequester G-actin, therefore, causing different effects under different conditions. The relative levels of F (polymerized) and G actin (monomeric) are affected in HD following the induction of mHtt, but no changes are observed with WT Htt (Posey *et al.*, 2018). It is interesting to note that profilin was a significantly phosphorylated peptide in the kinome analysis. Its interactions with cofilin makes it a major player in the dysregulation of cytoskeletal regulation in R6/2 HD mice. As depicted by the results LIMK1 cofilin and SSH1L play a major role in actin dynamics in HD. Phosphorylation of cofilin causes its deactivation and the process is reversed by the phosphatase SSH1L. Both PAK and ROCK2 regulate LIMK1, which ultimately affects the actin cytoskeleton, axonal transport, and synaptic disruption. SSH1L is involved in Ca⁺²-mediated cofilin dephosphorylation mediated by calcineurin, which is the major phosphatase in this study which could have a major role in the disease process.

Age related neurodegenerative disorders showed an increase in the DNA damage and dysregulation of energetic mechanism which leads to cell death. Recently both ATM (DNA damage) and PDHK1 (energy metabolism) have been shown to be dysregulated in HD (Lu *et al.*, 2014; Vallee *et al.*, 2018) and they appeared as the predicted upstream kinases in this dataset. It has been shown that mHtt causes an aberrant increase in the ATM signaling in HD and ATM

inhibitors appear to be neuroprotective though the mechanisms of the increase are yet to be understood (Lu *et al.*, 2014). The brain uses 70% of the energy produced hence ATP is the primary determinant of neuronal viability. The inactivation of PDHK1 in HD is due to an increase in the WNT/ β -catenin signaling (Vallee *et al.*, 2018). The kinome profiling predicted by *in silico* analysis that these two kinases are important in the disease process. Hence the regulation of aerobic glycolysis and reduction of ATM signaling should be further studied as they might be useful therapeutic targets for HD.

Finally, the peptide array analyses revealed that a number of phosphorylated peptides could not be validated. This is a drawback of peptide array analysis and needs to be addressed. Furthermore, it has been noted that 50-70% of the information from the peptide arrays is lost due to technical reasons during data normalization (Scholma *et al.*, 2016). Therefore, the use of quasi-stringent t-testing ($P < 0.1/0.2$) in the analyses allowed to reduce the bias due to stringent statistical thresholds (Kindrachuk *et al.*, 2012; Napper *et al.*, 2015; Scholma *et al.*, 2016). These adjustments are required to get a much larger dataset supported by bioinformatics analysis to generate significant biologically relevant result. In conclusion these peptide arrays offer an effective high throughput platform to profile global kinase phosphorylation patterns.

5. GENERAL DISCUSSION

5.1 Cytoskeletal dynamics dysregulated in HD NSCs and R6/2 mice

Kinome profiling has been successfully used to study neurodegenerative disorders (Hoozemans *et al.*, 2012; Meng *et al.*, 2016; Rosenberger *et al.*, 2016) and cytoskeletal dynamics have been previously characterized to be dysregulated in neurodegenerative diseases such as Alzheimer's disease (Eira *et al.*, 2016; Majumder *et al.*, 2017). The objective of this study was to determine the involvement of protein kinases in HD pathogenesis and this study uses kinome profiling to identify the pathways dysregulated in NSCs and R6/2 HD mice. The analysis of both the stem cells and murine tissues determined that the cytoskeletal dynamics as one of the major pathways dysregulated. This was followed by *in silico* analyses of the phosphosites which uncovered upstream kinases such as ATM and GSK3 β which have been previously identified as a therapeutic target for HD (Fernandez-Nogales *et al.*, 2015; Lu *et al.*, 2014). ATM is a DNA damage sensor, and it has been shown that the DNA damage in HD is caused by dysfunction of the mutant huntingtin protein in DNA repair followed by an increase in ROS leading to oxidative stress (Maiuri *et al.*, 2017). GSK3 β on the other hand is reduced in HD brain and plays an important role in reducing ubiquitination-proteosomal degradation and suppressing polyQ protein aggregation (Lee *et al.*, 2016). These results could help in identifying therapeutic targets to treat HD by regulating these kinases. This study allowed us to uncover the different phosphorylation status of the key players in the cytoskeletal dynamics - ROCK2, PAK1, Profilin, AKT1, LIMK1, Cofilin and SSH1L. In general most of the peptides had the same directionality (hyper- or hypophosphorylated) in Westerns as in peptide arrays in most of the developmental stages but. In a few developmental time points it was reversed and the complexity of the signaling is represented in the Table 5.1 with shades of pink being hyper and green as hypophosphorylated.

Table 5.1 Comparative summary of the significantly hyper- (pink) and hypo- (green) phosphorylated proteins based on peptide array and Western blot results of R6/2 mouse model. The darker shades of pink and green are the results which show opposite trends in kinome vs Western and are statistically significant. NE = no expression at specified time point. * indicates the significant P-values, $P \leq 0.05$ (Western blotting) and $P \leq 0.2$ (Kinome analysis).

		E9		E14		P0		3w		4w		5w		7w		10w	
		F	M	F	M	F	M	F	M	F	M	F	M	F	M	F	M
ROCK2	<i>Kinome</i>	*			*	*		*		*	*	*				*	
	<i>Western</i>	*		*												*	
PAK	<i>Kinome</i>	*		*		*		*		*	*				*	*	
	<i>Western</i>	*	*	*	*			*	*	*	*						*
Profilin	<i>Kinome</i>	*	*	*	*	*	*	*	*	*	*	*	*	*	*	*	*
	<i>Western</i>	*		*	*			*	*					*	*	*	*
AKT1	<i>Kinome</i>	*	*	*		*		*	*	*	*	*	*	*	*	*	*
	<i>Western</i>	*	*			*	*	*	*				*	*	*	*	*
LIMK1	<i>Western</i>	NE	NE					*	*	*	*	*	*	*	*	*	*
Cofilin	<i>Western</i>	*	*	*				*	*	*	*	*	*	*	*	*	*
SSH1L	<i>Western</i>	NE	NE	*			*	*	*	*	*	*	*	*	*	*	*

Signaling does not always occur in a linear fashion but via cascades with one protein catalyzing the phosphorylation of a second protein. The number of proteins receiving a signal can multiply very rapidly in each step of the cascade thus amplifying the signal. Some of these cascades have proteins which are involved in multiple pathways and may lead to the compensatory output in one pathway and exaggerated in the other. The native phosphorylation events occurring at the cellular levels require a relevant biological stimuli or the absence of it for a more appropriate representation of physiological kinase activities. In the past a number of low throughput techniques have been used to study a disease process. They analyzed one or few molecules at a time. While such techniques are useful and informative they are time consuming and cannot recapitulate these complex signaling changes. They are not conducive to understanding the intricate biological interactions and cannot generate global patterns of signaling. The disadvantage of high throughput studies is that some of these datasets generate complex patterns which might need an increase in sample size to reduce inconsistent findings or further analysis of the dataset using computational algorithms to derive meaningful data.

The phosphorylation profiles of the protein samples were compared as percentage value. The hyper- and hypo phosphorylated peptides list was generated using the P-value cut off and a percentage was obtained using the total number of peptide printed on the array. The results were depicted separately for both male and females and a combined value as shown in Table 5.2. An important difference observed was between the two sexes at 4w and 7w which developmentally correlated with the appearance of mHtt in the striatum and decreased body weight respectively. The hyperphosphorylated peptides in females at 4w is ~40% and hypophosphorylated ~27% and the values are reversed in males in the same time point. Similarly at 7w hyperphosphorylated peptides in females were ~45% and hypophosphorylated~22% and the values reversed on males. This is indicative of potential sex differences in the development of the disease considering the time points being developmentally significant though further investigation is required for a definitive conclusion.

Table 5.2: The percentage of peptides significantly (de) phosphorylated in the mouse and NSCs. A P-value cut off was used to generate a list of hypo- and hypophosphorylated peptides and a percentage value derived using the total number of peptide printed on the array. The percentage value higher in the hyper- or hypophosphorylated results is highlighted in bold.

<i>HD mice</i> ($p \leq 0.2$)					
<i>Time points</i>	Sex	Hyper-phosphorylated	Total	Hypo-phosphorylated	Total
<i>E9</i>	F	24.6%	51.8%	44.2%	87.1%
	M	27.2%		42.9%	
<i>E14</i>	F	35.7%	72.2%	33.5%	62.9%
	M	36.5%		29.4%	
<i>P0</i>	F	28.5%	52.3%	33.8%	69.7%
	M	23.8%		35.9%	
<i>3w</i>	F	40.7%	74.5%	21.3%	52.8%
	M	33.8%		31.5%	
<i>4w</i>	F	38.9%	66.7%	26.3%	70.9%
	M	27.8%		44.6%	
<i>5w</i>	F	34.9%	70.0%	29.4%	62.1%
	M	35.1%		32.7%	
<i>7w</i>	F	44.9%	67.1%	21.5%	66.3%
	M	22.2%		44.8%	
<i>10w</i>	F	32.7%	63.2%	26.6%	57.1%
	M	30.5%		30.5%	
<i>HD Stem cells</i> ($p \leq 0.1$)					
<i>NSCs</i>	F	16.4%		25.2%	

Huntington Disease mouse models and other studies provided evidence that sex may account for the variability in the disease. The scientific evidence that estrogen is neuroprotective in HD is limited and there are conflicting information available. Some studies suggest female sex is detrimental while others have shown it being neuroprotective (Foroud *et al.*, 1999; Zielonka *et al.*, 2013). The levels of neurotrophic factors (GDNF, BDNF) increases in the striatum upon an increase in the estrogen levels (Campos *et al.*, 2012). Estrogen also decreases the production of ROS by increasing the expression of scavengers like superoxide dismutase, glutathione peroxidase etc. (Wang *et al.*, 2001). Estrogen also protects the mitochondrial membrane potential thereby preventing ATP depletion and suppresses the free radical production (Simpkins *et al.*, 2010). These studies can open avenues for targeted therapy but specific mechanisms of neuroprotection need to be well understood. While the results of this global analysis using peptide array definitely indicate towards differences in the sexes.

MAPK/ERK and PI3K/AKT pathways are downstream targets of 17 β -estradiol an estrogen steroid hormone which exerts neuroprotective effect from ROS, glutamate and misfolded protein toxicity in the neurons (Figure 5.1) (Smith and Dahodwala, 2014). The signal cascades are broadly involved in cell survival and are affected due to a decrease in the ratio of Bcl-2 (pro-survival): BAD (pro-apoptotic) proteins in neurodegenerative disorders. Activation of MAPK/ERK leads to the inhibition of pro-apoptotic proteins such as BAD and GSK3 β (Bourque *et al.*, 2009). Both ER α and ER β receptors localize in the mouse striatum which is the most affected tissue in HD (Kuppers and Beyer, 1999). GSK3 β phosphorylates tau which leads to microtubule dysfunction (Figure 4.3B) followed by disruption in protein trafficking which ultimately leads to the formation of neurofibrillary tangles and finally cell death (Goodenough *et al.*, 2005). Microtubule dynamics can be affected if GSK3 β is inhibited by estrogen via PI3K/AKT which may affected the cytoskeletal signaling as shown in Figure 5.1. The coordination of the actin-microtubule dynamics is required to maintain the neuronal structure and function. These cytoskeletal filaments provide cells with mechanical stability and organization which is lost in neurodegenerative disorders. A larger cohort of animals with equal distribution of both sexes is required to draw definitive conclusions along with further elucidation of mechanisms underlying estrogens role in HD. In summary, sex steroid hormones and the sex chromosomes might play a vital role in the development of the HD through their effects in the basal ganglia networks. A better understanding of the differences in these pathways is integral for the development of biomarkers and new therapies for HD.

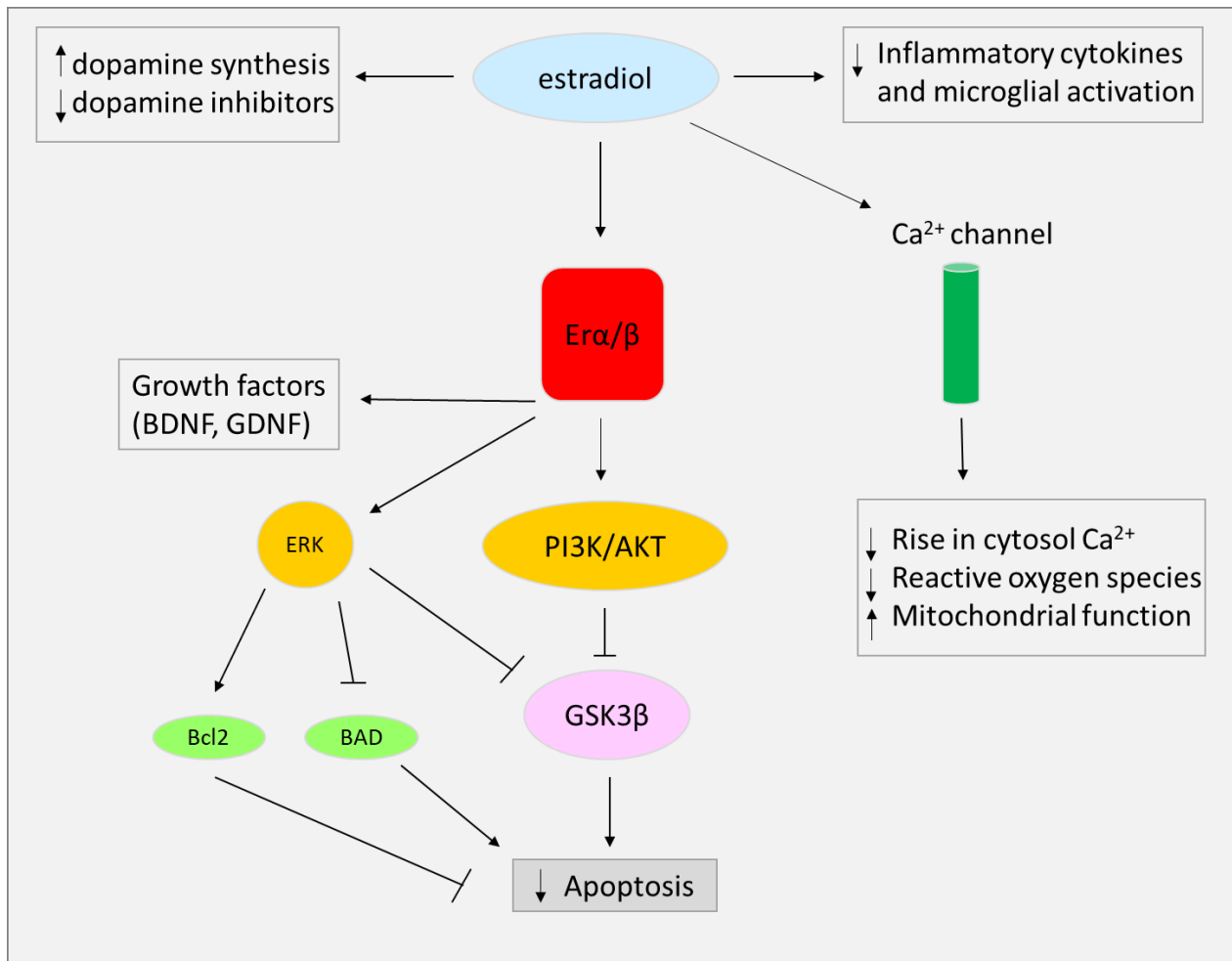


Figure 5.1: Schematic representation of neuroprotective mechanisms of ER signaling. Binding of estrogen receptors (ER) by estradiol activates signal cascades that ultimately decrease apoptosis of neurons. GSK3 β inhibited by estrogen via the PI3K/AKT pathway results in the inhibition of apoptosis (Permission to use from Smith and Dahodwala, 2014).

5.2 Limitations of kinome analysis

Protein phosphorylation is estimated to influence about 30% of the proteome, regulating fundamental cellular processes such as cell proliferation, migration, survival, apoptosis etc. All these processes are mediated by 525 protein kinases. Kinome analysis allows the measurement of intracellular signaling events underlying a disease process. Each kinase has a characteristic recognition pattern which catalyzes a specific residue only if the surrounding sequences match the pattern. This is a caveat with the kinome analysis since a phosphorylatable amino acid may either

be exposed or buried in an intact protein in a conformational context. Kinase have a substrate specificity *in vivo* in a temporal and spatial context. Protein interaction domains exist within the kinase which allow the kinase to recognize specific proteins to bind and phosphorylate. This may further be triggered upon signaling cues such as stimulation with specific ligands that activate upstream receptors. Peptide arrays do not accurately recapitulate these cellular aspects.

In the present study commercially available antibodies against specific kinases / phosphatases and downstream targets were used to independently validate the peptide array results. Other experimental approaches may be used towards further validating and characterizing this dataset such as *in vitro* kinase and phosphatase assays where the appropriate kinase/phosphatase may be immunoprecipitated from the HD mouse brain or NSCs and assessed for activation. Another challenge with kinome analysis is that it examines just one side of the biological process. Protein kinases and phosphatases often act in tandem to perform the phosphorylation and de-phosphorylation process. The peptide arrays just provide information pertaining to only kinases which may be incomplete without the analysis of the phosphatase activity. Adding to this is the fact that the buffer used for kinome analysis may not be able to provide the maximal activity of each and every kinase. The fact that the peptides printed on the array are manually selected renders a level of bias along with the aforementioned constraints therefore adding to the potential limitations of kinome analysis.

5.3 Proteome vs kinome: dysregulation in cytoskeletal dynamics

It is interesting to compare my kinome data with the proteomic analysis from post-mortem patient samples. Systematic quantitative proteomics assessing global changes in HD implicated Rho proteins, actin cytoskeleton signaling and mitochondrial dysfunction signaling as the most altered in HD (Ratovitski *et al.*, 2016). This study utilized the HD human brain tissues to perform quantitative proteomics which directly addresses the changes in protein abundances that occur in the disease state (Ratovitski *et al.*, 2016). The mass-spectrometrically (MS) identified proteins were verified using Western blotting which showed protein expression changes in actin cytoskeleton. Their proteomic analysis indicated that changes in the HD brain are consistent with the dysfunction of actin cytoskeleton remodeling as shown in the Figure 5.2. It is interesting to note that they did not study the rodent samples but despite the difference in the species there was

a consistent pathway dysregulated in post-mortem human samples and in my study using R6/2 HD mice. Another study focusing on the changes in the striatal proteome of YAC128Q mice used liquid chromatography coupled in-line with tandem mass spectrometry (LC-MS/MS) (Wegrzynowicz *et al.*, 2012). They identified proteins related to energy metabolism or cellular transport/cytoskeleton as most prominent among others. The striatal lysates were used to analyze by immunoblotting with antibodies the protein identified in the analyses (Wegrzynowicz *et al.*, 2012). This along with the previous work clearly implicates dysregulated cytoskeletal dynamics in HD and in a number of other neurodegenerative disorders as enlisted in Table 5.1.

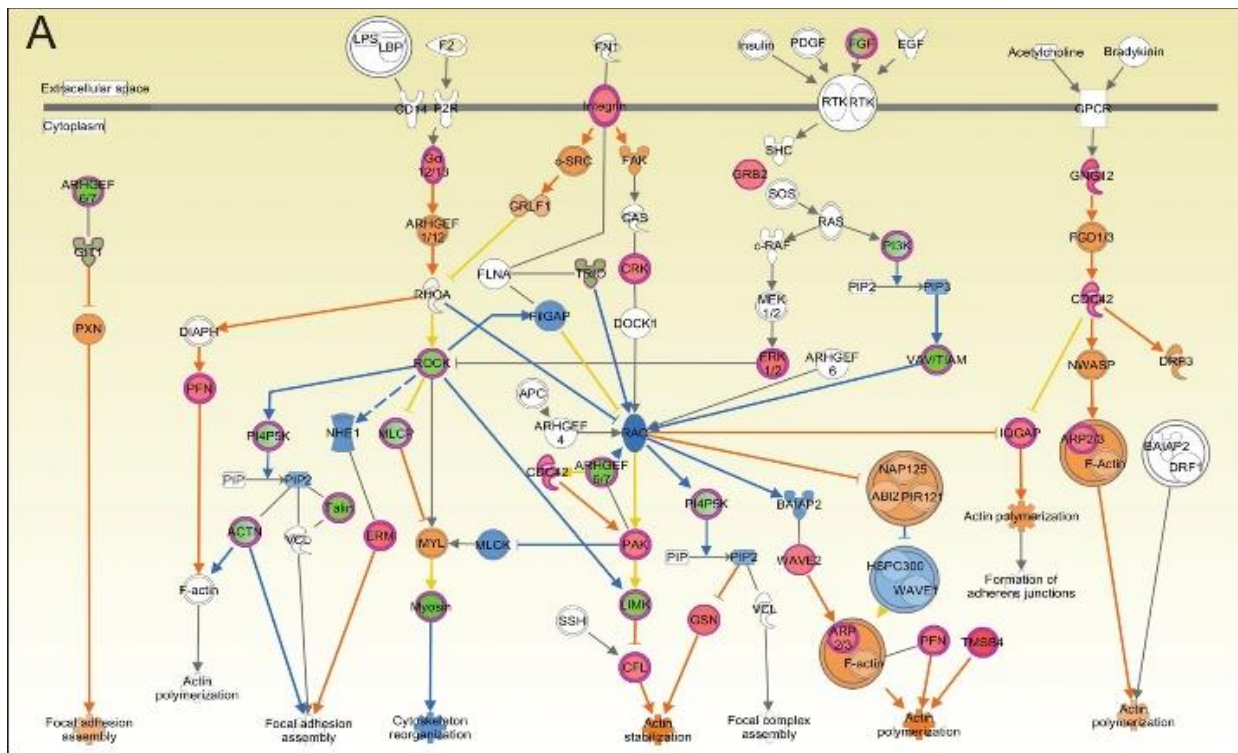


Figure 5.2: Quantitative proteomic analysis shows actin cytoskeleton pathway is enriched in HD relative to control.

Ingenuity pathway analysis (IPA) generated figure based on the MS output from brain tissue samples from twelve post mortem patients (Permission to use from Ratovitski *et al.*, 2016).

Table 5.1: Main cytoskeletal defects observed in neurodegenerative disorders.

Cytoskeleton dysfunction	Molecular dysregulation	Neurodegenerative disorder
Altered microtubule dynamics and axonal transport defects	Decreased α -tubulin acetylation	AD (Zhang et al., 2014) HD (Dompierre et al., 2007) CMT (d'Ydewalle et al., 2011)
	Tau hyper-phosphorylation	AD (Alonso et al., 1996 , Alonso et al., 1997)
	Increased β III tubulin levels	PD (Cartelli et al., 2013)
	GSK3 β hyperactivation	AD (Flaherty et al., 2000)
	Mutations in SOD1	ALS (Strom et al., 2008)
MT severing	Increased tubulin polyglutamylation/recruitment of MT severing enzymes	AD (Zempel et al., 2013)
Axonal transport defects (microtubule independent)	Mutations in molecular motors	ALS (Munch et al., 2004) CMT (Zhao et al., 2001)
	Increased kinesin phosphorylation by GSK3 β	AD (Morfini et al., 2002 , Pigino et al., 2003)
	Mutated Huntingtin	HD (Trushina et al., 2004)
	Protein aggregation	AD (Coleman, 2011 , Goldstein, 2012) PD (Coleman, 2011 , Goldstein, 2012) HD (Coleman, 2011 , Goldstein, 2012)
Actin cytoskeleton dysregulation	Cofilin-actin rods (cofilin hyper-dephosphorylation)	AD (Minamide et al., 2000) HD (Munsie and Truant, 2012)
	Hirano bodies	AD (Schmidt et al., 1989)
	Cofilin inactivation	PD (Bellani et al., 2014)
	Profilin1 mutations	ALS (Wu et al., 2012)
	Dysregulation of Rho GTPases	PD (Zhou et al., 2011) CMT (Delague et al., 2007 , Stendel et al., 2007) HD (Tourette et al., 2014) AD (Mendoza-Naranjo et al., 2007 , Petraatos et al., 2008)

(Eira et al., 2016)

6. CONCLUSIONS

In summary, the peptide array platform provided a means to comprehensively study the rapid changes in the kinome of NSCs and R6/2 mice, to investigate the pathways dysregulated in the disease. The most significant pathway dysregulated in kinome analysis was cytoskeletal signaling. It is evident that this data is purely correlative, but it does offer intriguing insight into disease progression, at least preliminarily, and implicates the activation of apoptotic pathways, calcium signaling and ROS generation as causative or adaptive mechanisms in the dysregulated cytoskeletal dynamics. Profilin balances the F/G actin ratio which ultimately affects the actin polymerization and its activation leads to the aggregation of mHtt. Overall these results indicate that the LIMK1-cofilin-SSH1L dynamics are affected in HD, and that they most likely underlie a reduction in neurite outgrowth (Figure 6.1). This was corroborated by the NeuroLucida 360 analysis shown earlier, where there is a 25% reduction in the neurite length in HD compared to controls (Figure 4.5). Any alterations in cellular cytoskeletal dynamics would clearly have an impact on cellular morphology, transport and synaptic integrity, which would contribute to a degenerative phenotype and neuronal cell death. Thus, the data provides therapeutic targets for treating the disease phenotype. Overall, this temporal study furthered knowledge of the dysregulation of cytoskeletal abnormalities in HD across key developmental time points, and opened avenues for further research in discovering targets for therapeutic intervention.

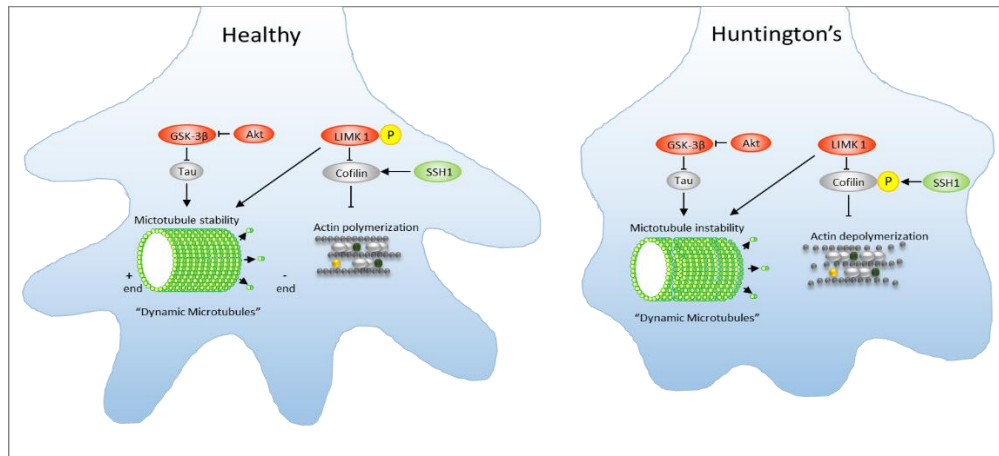


Figure 6.1: Schematic representation of cytoskeletal signaling resulting in neurite reduction in HD.

LIMK1-Cofilin-SSH1L dynamics are affected in HD, and they most likely underlie the reduction in neurite outgrowth by affecting the actin polymerization.

7. FUTURE DIRECTIONS

7.1 Kinome analysis of other neural tissues

Striatum is the most affected tissue in HD, and based on the kinome analysis, it would be interesting to assess the differential phosphorylation status of the same peptides in other neural tissues, including the cortex, hippocampus and cerebellum. Multiple studies have shown that both the striatum and cortex are the most affected tissue subtypes in HD. Most of such research has focused on specific time points, sexes, or large-scale studies that provide data that are relevant to the particular stage of disease, sex, or tissue type. If the key developmental stages in a progressive disease such as HD are missing, the data obtained will be incomplete for the development of therapeutic strategies. Moreover, variations in the number of polyQ repeats affects the onset of disease; thus, complicating the understanding of the disease process and the identification of possible differences between the two sexes. All such factors must also be addressed by future studies. Different neural tissues have different functions, and thus, the combined kinome dataset of all tissues will allow us to better understand the development of disease and disentangle the cross-talk between signaling mechanisms affected at various stages of disease.

7.2 Stem cells

A common approach to investigating the human disease to find therapeutic targets is by performing preliminary experiments using animal models. Rodents are cost effective and an easy option though they are not the perfect model to recapitulate all aspects of human diseases. Nonetheless these models cover a wide range of symptoms of the neurodegenerative condition and allow a better understanding of the disease. Brain pathologies alter the expression of a number of genes and as the different cell types have specific function these molecular changes contribute to cognitive decline and behavioral deficits. The molecular mechanisms in a murine model will definitely be different when compared to a human. The R6/2 transgenic mice contain the exon 1 of the human HD gene with the polyQ repeats. They do not have the genetic background of a human, a reason for why a number of clinical trials have failed.

As discussed previously, the complexity in understanding HD is due to a number of

reasons. i) The different polyQ repeats affects the onset of disease; ii) possible differences in both sexes; and iii) the interplay between the different neural tissues. Personalized medicine is the future of medical practice and HD is ideal candidate. This is so since the repeat size varies among the patients and the disease is more aggressive when inherited from the father as discussed earlier. Since the discovery of the HD gene 25 years ago, the first massive clinical trial to study the effect of a mHtt-lowering drug (RG6042) are about to begin at specific centers around the globe (Mullard, 2019). However, it remains important to understand the subtleties in the disease that cause differences between patients. Patient derived NSCs could play a large role in understanding such subtle differences and facilitate the development of therapeutic strategies (Yamanaka and Blau, 2010). This observational study provided data from the NSCs of one female HD patient with a specific number of polyQ repeats, but a higher number of such patient lines would advance the development of therapeutics and promote an understanding of the complexities. The inclusion of a larger number of patient derived stem cell lines will also enhance patient specific data, which will ultimately assist in dose response and reduced animal trials to achieve the desired results.

7.3 Therapeutic strategies

A recent study showed that intranasal administration of mesenchymal stem cells at four weeks ameliorated the HD phenotype in R6/2 HD mice (Yu-Taeger *et al.*, 2019). They used a non-invasive surgical procedure and utilized the regenerative properties of multipotent mesenchymal stem cells (MSCs) and their ability to migrate to degenerating central nervous system (Yu-Taeger *et al.*, 2019).

This thesis indicates a dysregulated cytoskeletal dynamics and potential for therapeutic intervention. Based on the results of the kinome analysis cofilin / profilin or LIMK1/SSH1L combined therapeutic strategy could be exploited at E14. If cofilin / profilin inhibitors or LIMK1 activator and SSH1L inhibitor is given to a R6/2 mouse as a combination therapeutic it might result in the formation of proper synaptic connections. This might be able to regulate the kinase signaling in HD due to the mutant protein therefore delaying the appearance of symptoms. This along with reducing the accumulation of mutant protein later in life might be beneficial, ameliorating the disease phenotype. Such a trial in a well-established mouse model such as R6/2 can be exploited followed by immunostaining for mHtt and synaptic markers, verifying these results.

REFERENCES

- The Huntington's Disease Collaborative Research Group Akhshi, T.K., Wernike, D., and Piekny, A. (2014). Microtubules and actin crosstalk in cell migration and division. *Cytoskeleton (Hoboken)* *71*, 1-23.
- Andre, V.M., Cepeda, C., and Levine, M.S. (2010). Dopamine and glutamate in Huntington's disease: A balancing act. *CNS Neurosci. Ther.* *16*, 163-178.
- Ardhanareeswaran, K., Mariani, J., Coppola, G., Abyzov, A., and Vaccarino, F.M. (2017). Human induced pluripotent stem cells for modelling neurodevelopmental disorders. *Nat. Rev. Neurol.* *13*, 265-278.
- Arsenault, R., Griebel, P., and Napper, S. (2011). Peptide arrays for kinome analysis: new opportunities and remaining challenges. *Proteomics* *11*, 4595-4609.
- Arsenault, R.J., Li, Y., Bell, K., Doig, K., Potter, A., Griebel, P.J., Kusalik, A., and Napper, S. (2012a). *Mycobacterium avium* subsp. paratuberculosis inhibits gamma interferon-induced signaling in bovine monocytes: insights into the cellular mechanisms of Johne's disease. *Infect. Immun.* *80*, 3039-3048.
- Arsenault, R.J., Li, Y., Maattanen, P., Scruten, E., Doig, K., Potter, A., Griebel, P., Kusalik, A., and Napper, S. (2013a). Altered Toll-like receptor 9 signaling in *Mycobacterium avium* subsp. paratuberculosis-infected bovine monocytes reveals potential therapeutic targets. *Infect. Immun.* *81*, 226-237.
- Arsenault, R.J., Li, Y., Potter, A., Griebel, P.J., Kusalik, A., and Napper, S. (2012b). Induction of ligand-specific PrP (C) signaling in human neuronal cells. *Prion* *6*, 477-488.
- Arsenault, R.J., Napper, S., and Kogut, M.H. (2013b). *Salmonella enterica* Typhimurium infection causes metabolic changes in chicken muscle involving AMPK, fatty acid and insulin/mTOR signaling. *Vet. Res.* *44*, 35-50.
- Asrar, S., Meng, Y., Zhou, Z., Todorovski, Z., Huang, W.W., and Jia, Z. (2009). Regulation of hippocampal long-term potentiation by p21-activated protein kinase 1 (PAK1). *Neuropharmacology* *56*, 73-80.
- Atwal, R.S., Xia, J., Pinchev, D., Taylor, J., Epan, R.M., and Truant, R. (2007). Huntingtin has a membrane association signal that can modulate huntingtin aggregation, nuclear entry and toxicity. *Hum. Mol. Genet.* *16*, 2600-2615.
- Baharani, A., Trost, B., Kusalik, A., and Napper, S. (2017). Technological advances for interrogating the human kinome. *Biochem. Soc. Trans.* *45*, 65-77.
- Bamburg, J.R., and Bernstein, B.W. (2010). Roles of ADF/cofilin in actin polymerization and beyond. *F1000 Biol. Rep.* *2*, 62-69.

- Bamburg, J.R., and Bernstein, B.W. (2016). Actin dynamics and cofilin-actin rods in Alzheimer disease. *Cytoskeleton (Hoboken)* 73, 477-497.
- Barone, E., Mosser, S., and Fraering, P.C. (2014). Inactivation of brain Cofilin-1 by age, Alzheimer's disease and gamma-secretase. *Biochim. Biophys. Acta* 1842, 2500-2509.
- Barone, G., Groom, A., Reiman, A., Srinivasan, V., Byrd, P.J., and Taylor, A.M. (2009). Modeling ATM mutant proteins from missense changes confirms retained kinase activity. *Hum. Mutat.* 30, 1222-1230.
- Bass, J.J., Wilkinson, D.J., Rankin, D., Phillips, B.E., Szewczyk, N.J., Smith, K., and Atherton, P.J. (2017). An overview of technical considerations for Western blotting applications to physiological research. *Scand. J. Med. Sci. Sports* 27, 4-25.
- Beal, M.F., and Ferrante, R.J. (2004). Experimental therapeutics in transgenic mouse models of Huntington's disease. *Nat. Rev. Neurosci.* 5, 373-384.
- Beery, A.K., and Zucker, I. (2011). Sex bias in neuroscience and biomedical research. *Neurosci. Biobehav. Rev.* 35, 565-572.
- Bertram, L., and Tanzi, R.E. (2005). The genetic epidemiology of neurodegenerative disease. *J. Clin. Invest.* 115, 1449-1457.
- Beurel, E., Grieco, S.F., and Jope, R.S. (2015). Glycogen synthase kinase-3 (GSK3): regulation, actions, and diseases. *Pharmacol. Ther.* 148, 114-131.
- Bode, F.J., Stephan, M., Suhling, H., Pabst, R., Straub, R.H., Raber, K.A., Bonin, M., Nguyen, H.P., Riess, O., Bauer, A., *et al.* (2008). Sex differences in a transgenic rat model of Huntington's disease: decreased 17beta-estradiol levels correlate with reduced numbers of DARPP32+ neurons in males. *Hum. Mol. Genet.* 17, 2595-2609.
- Bourque, M., Dluzen, D.E., and Di Paolo, T. (2009). Neuroprotective actions of sex steroids in Parkinson's disease. *Front. Neuroendocrinol.* 30, 142-157.
- Bowater, R.P., and Wells, R.D. (2001). The intrinsically unstable life of DNA triplet repeats associated with human hereditary disorders. *Prog. Nucleic Acid Res. Mol. Biol.* 66, 159-202.
- Boyd, A.W., Bartlett, P.F., and Lackmann, M. (2014). Therapeutic targeting of EPH receptors and their ligands. *Nat. Rev. Drug Discov.* 13, 39-62.
- Breuer, K., Foroushani, A.K., Laird, M.R., Chen, C., Sribnaia, A., Lo, R., Winsor, G.L., Hancock, R.E., Brinkman, F.S., and Lynn, D.J. (2013). InnateDB: systems biology of innate immunity and beyond--recent updates and continuing curation. *Nucleic Acids Res.* 41, 1228-1233.
- Briz, V., and Baudry, M. (2014). Estrogen Regulates Protein Synthesis and Actin Polymerization in Hippocampal Neurons through Different Molecular Mechanisms. *Front. Endocrinol. (Lausanne)* 5, 22-36.

- Brouillet, E., Conde, F., Beal, M.F., and Hantraye, P. (1999). Replicating Huntington's disease phenotype in experimental animals. *Prog. Neurobiol.* *59*, 427-468.
- Budworth, H., and McMurray, C.T. (2013). A brief history of triplet repeat diseases. *Methods Mol. Biol.* *1010*, 3-17.
- Burnett, B.G., Andrews, J., Ranganathan, S., Fischbeck, K.H., and Di Prospero, N.A. (2008). Expression of expanded polyglutamine targets profilin for degradation and alters actin dynamics. *Neurobiol. Dis.* *30*, 365-374.
- Caenepeel, S., Charyczak, G., Sudarsanam, S., Hunter, T., and Manning, G. (2004). The mouse kinome: discovery and comparative genomics of all mouse protein kinases. *Proc. Natl. Acad. Sci. U. S. A.* *101*, 11707-11712.
- Campos, F.L., Cristovao, A.C., Rocha, S.M., Fonseca, C.P., and Baltazar, G. (2012). GDNF contributes to oestrogen-mediated protection of midbrain dopaminergic neurones. *J. Neuroendocrinol.* *24*, 1386-1397.
- Cara, L., Baitemirova, M., Follis, J., Larios-Sanz, M., and Ribes-Zamora, A. (2016). The ATM- and ATR-related SCD domain is over-represented in proteins involved in nervous system development. *Sci. Rep.* *6*, 19050-19064.
- Carroll, J.B., Bates, G.P., Steffan, J., Saft, C., and Tabrizi, S.J. (2015). Treating the whole body in Huntington's disease. *Lancet Neurol.* *14*, 1135-1142.
- Carruth, L.L., Reisert, I., and Arnold, A.P. (2002). Sex chromosome genes directly affect brain sexual differentiation. *Nat. Neurosci.* *5*, 933-934.
- Cattaneo, E., Rigamonti, D., Goffredo, D., Zuccato, C., Squitieri, F., and Sipione, S. (2001). Loss of normal huntingtin function: new developments in Huntington's disease research. *Trends Neurosci.* *24*, 182-188.
- Caviston, J.P., and Holzbaur, E.L. (2009). Huntingtin as an essential integrator of intracellular vesicular trafficking. *Trends Cell Biol.* *19*, 147-155.
- Cereda, E., Barichella, M., Cassani, E., Caccialanza, R., and Pezzoli, G. (2013). Reproductive factors and clinical features of Parkinson's disease. *Parkinsonism Relat. Disord.* *19*, 1094-1099.
- Chandra, A., Johri, A., and Beal, M.F. (2014). Prospects for neuroprotective therapies in prodromal Huntington's disease. *Mov. Disord.* *29*, 285-293.
- Chang, L., and Goldman, R.D. (2004). Intermediate filaments mediate cytoskeletal crosstalk. *Nat. Rev. Mol. Cell Biol.* *5*, 601-613.
- Chelly, J., and Mandel, J.L. (2001). Monogenic causes of X-linked mental retardation. *Nat. Rev. Genet.* *2*, 669-680.

- Chen, X., Grisham, W., and Arnold, A.P. (2009). X chromosome number causes sex differences in gene expression in adult mouse striatum. *Eur. J. Neurosci.* *29*, 768-776.
- Cheng, A., Wang, S., Yang, D., Xiao, R., and Mattson, M.P. (2003). Calmodulin mediates brain-derived neurotrophic factor cell survival signaling upstream of Akt kinase in embryonic neocortical neurons. *J. Biol. Chem.* *278*, 7591-7599.
- Chong, S.S., Almqvist, E., Telenius, H., LaTray, L., Nichol, K., Bourdelat-Parks, B., Goldberg, Y.P., Haddad, B.R., Richards, F., Sillence, D., *et al.* (1997). Contribution of DNA sequence and CAG size to mutation frequencies of intermediate alleles for Huntington disease: evidence from single sperm analyses. *Hum. Mol. Genet.* *6*, 301-309.
- Chuang, H.H., Yang, C.H., Tsay, Y.G., Hsu, C.Y., Tseng, L.M., Chang, Z.F., and Lee, H.H. (2012). ROCKII Ser1366 phosphorylation reflects the activation status. *Biochem. J.* *443*, 145-151.
- Cisbani, G., and Cicchetti, F. (2012). An in vitro perspective on the molecular mechanisms underlying mutant huntingtin protein toxicity. *Cell Death Dis.* *3*, 382-394.
- Colin, E., Regulier, E., Perrin, V., Durr, A., Brice, A., Aebischer, P., Deglon, N., Humbert, S., and Saudou, F. (2005). Akt is altered in an animal model of Huntington's disease and in patients. *Eur. J. Neurosci.* *21*, 1478-1488.
- Colin, E., Zala, D., Liot, G., Rangone, H., Borrell-Pages, M., Li, X.J., Saudou, F., and Humbert, S. (2008). Huntingtin phosphorylation acts as a molecular switch for anterograde/retrograde transport in neurons. *EMBO J.* *27*, 2124-2134.
- Consortium, H.D.i. (2012). Induced pluripotent stem cells from patients with Huntington's disease show CAG-repeat-expansion-associated phenotypes. *Cell Stem Cell* *11*, 264-278.
- Cuberos, H., Vallee, B., Vourc'h, P., Tastet, J., Andres, C.R., and Benedetti, H. (2015). Roles of LIM kinases in central nervous system function and dysfunction. *FEBS Lett.* *589*, 3795-3806.
- Cummings, D.M., Alaghband, Y., Hickey, M.A., Joshi, P.R., Hong, S.C., Zhu, C., Ando, T.K., Andre, V.M., Cepeda, C., Watson, J.B., *et al.* (2012). A critical window of CAG repeat-length correlates with phenotype severity in the R6/2 mouse model of Huntington's disease. *J. Neurophysiol.* *107*, 677-691.
- Czech, D.P., Lee, J., Sim, H., Parish, C.L., Vilain, E., and Harley, V.R. (2012). The human testis-determining factor SRY localizes in midbrain dopamine neurons and regulates multiple components of catecholamine synthesis and metabolism. *J. Neurochem.* *122*, 260-271.
- Daigle, J., Van Wyk, B., Trost, B., Scruten, E., Arsenault, R., Kusalik, A., Griebel, P.J., and Napper, S. (2014). Peptide Arrays for Kinome Analysis of Livestock Species. *Front. Vet. Sci.* *1*, 4-19.
- Darlington, R.B., Dunlop, S.A., and Finlay, B.L. (1999). Neural development in metatherian and eutherian mammals: variation and constraint. *J. Comp. Neurol.* *411*, 359-368.

- Dawe, H.R., Minamide, L.S., Bamburg, J.R., and Cramer, L.P. (2003). ADF/cofilin controls cell polarity during fibroblast migration. *Curr. Biol.* *13*, 252-257.
- Dayalu, P., and Albin, R.L. (2015). Huntington disease: pathogenesis and treatment. *Neurol. Clin.* *33*, 101-114.
- DeGuire, S.M., Ruggeri, F.S., Fares, M.B., Chiki, A., Cendrowska, U., Dietler, G., and Lashuel, H.A. (2018). N-terminal Huntingtin (Htt) phosphorylation is a molecular switch regulating Htt aggregation, helical conformation, internalization, and nuclear targeting. *J. Biol. Chem.* *293*, 18540-18558.
- Dewing, P., Chiang, C.W., Sinchak, K., Sim, H., Fernagut, P.O., Kelly, S., Chesselet, M.F., Micevych, P.E., Albrecht, K.H., Harley, V.R., *et al.* (2006). Direct regulation of adult brain function by the male-specific factor SRY. *Curr. Biol.* *16*, 415-420.
- Dewing, P., Shi, T., Horvath, S., and Vilain, E. (2003). Sexually dimorphic gene expression in mouse brain precedes gonadal differentiation. *Brain Res. Mol. Brain Res.* *118*, 82-90.
- Dickstein, D.L., Dickstein, D.R., Janssen, W.G., Hof, P.R., Glaser, J.R., Rodriguez, A., O'Connor, N., Angstman, P., and Tappan, S.J. (2016). Automatic Dendritic Spine Quantification from Confocal Data with Neurolucida 360. *Curr. Protoc. Neurosci.* *77*, 1271-12721.
- DiProspero, N.A., Chen, E.Y., Charles, V., Plomann, M., Kordower, J.H., and Tagle, D.A. (2004). Early changes in Huntington's disease patient brains involve alterations in cytoskeletal and synaptic elements. *J. Neurocytol.* *33*, 517-533.
- Dong, Q., Ji, Y.S., Cai, C., and Chen, Z.Y. (2012). LIM kinase 1 (LIMK1) interacts with tropomyosin-related kinase B (TrkB) and Mediates brain-derived neurotrophic factor (BDNF)-induced axonal elongation. *J. Biol. Chem.* *287*, 41720-41731.
- dos Remedios, C.G., Chhabra, D., Kekic, M., Dedova, I.V., Tsubakihara, M., Berry, D.A., and Nosworthy, N.J. (2003). Actin binding proteins: regulation of cytoskeletal microfilaments. *Physiol. Rev.* *83*, 433-473.
- Duyao, M.P., Auerbach, A.B., Ryan, A., Persichetti, F., Barnes, G.T., McNeil, S.M., Ge, P., Vonsattel, J.P., Gusella, J.F., Joyner, A.L., *et al.* (1995). Inactivation of the mouse Huntington's disease gene homolog Hdh. *Science* *269*, 407-410.
- Ehrnhoefer, D.E., Sutton, L., and Hayden, M.R. (2011). Small changes, big impact: posttranslational modifications and function of huntingtin in Huntington disease. *Neuroscientist* *17*, 475-492.
- Eid, S., Turk, S., Volkamer, A., Rippmann, F., and Fulle, S. (2017). KinMap: a web-based tool for interactive navigation through human kinome data. *BMC Bioinformatics* *18*, 16-22.
- Eira, J., Silva, C.S., Sousa, M.M., and Liz, M.A. (2016). The cytoskeleton as a novel therapeutic target for old neurodegenerative disorders. *Prog. Neurobiol.* *141*, 61-82.

- Endo, M., Ohashi, K., and Mizuno, K. (2007). LIM kinase and slingshot are critical for neurite extension. *J. Biol. Chem.* 282, 13692-13702.
- Fentress, J.C., Stanfield, B.B., and Cowan, W.M. (1981). Observation on the development of the striatum in mice and rats. *Anat. Embryol. (Berl)* 163, 275-298.
- Fernandez-Nogales, M., Hernandez, F., Miguez, A., Alberch, J., Gines, S., Perez-Navarro, E., and Lucas, J.J. (2015). Decreased glycogen synthase kinase-3 levels and activity contribute to Huntington's disease. *Hum. Mol. Genet.* 24, 5040-5052.
- Ferrante, R.J. (2009). Mouse models of Huntington's disease and methodological considerations for therapeutic trials. *Biochim. Biophys. Acta* 1792, 506-520.
- Fife, C.M., McCarroll, J.A., and Kavallaris, M. (2014). Movers and shakers: cell cytoskeleton in cancer metastasis. *Br. J. Pharmacol.* 171, 5507-5523.
- Fifkova, E., and Delay, R.J. (1982). Cytoplasmic actin in neuronal processes as a possible mediator of synaptic plasticity. *J. Cell Biol.* 95, 345-350.
- Figiel, M., Szlachcic, W.J., Switonski, P.M., Gabka, A., and Krzyzosiak, W.J. (2012). Mouse Models of Polyglutamine Diseases: Review and Data Table. Part I. *Mol. Neurobiol.* 46, 393-429.
- Finlay, B.L., and Darlington, R.B. (1995). Linked regularities in the development and evolution of mammalian brains. *Science* 268, 1578-1584.
- Fischbeck, K.H. (2001). Polyglutamine expansion neurodegenerative disease. *Brain Res. Bull.* 56, 161-163.
- Fodor, S.P., Read, J.L., Pirrung, M.C., Stryer, L., Lu, A.T., and Solas, D. (1991). Light-directed, spatially addressable parallel chemical synthesis. *Science* 251, 767-773.
- Foroud, T., Gray, J., Ivashina, J., and Conneally, P.M. (1999). Differences in duration of Huntington's disease based on age at onset. *J. Neurol. Neurosurg. Psychiatry* 66, 52-56.
- Frank, R. (2002). The SPOT-synthesis technique. Synthetic peptide arrays on membrane supports-principles and applications. *J. Immunol. Methods* 267, 13-26.
- Fuchsova, B., Alvarez Julia, A., Rizavi, H.S., Frasch, A.C., and Pandey, G.N. (2016). Expression of p21-activated kinases 1 and 3 is altered in the brain of subjects with depression. *Neuroscience* 333, 331-344.
- Gauthier, L.R., Charrin, B.C., Borrell-Pages, M., Dompierre, J.P., Rangone, H., Cordelieres, F.P., De Mey, J., MacDonald, M.E., Lessmann, V., Humbert, S., *et al.* (2004). Huntingtin controls neurotrophic support and survival of neurons by enhancing BDNF vesicular transport along microtubules. *Cell* 118, 127-138.
- Genetic Modifiers of Huntington's Disease Consortium. (2019). CAG Repeat Not Polyglutamine Length Determines Timing of Huntington's Disease Onset. *Cell* 178, 887-900.

- Geysen, H.M., Meloen, R.H., and Barteling, S.J. (1984). Use of peptide synthesis to probe viral antigens for epitopes to a resolution of a single amino acid. *Proc. Natl. Acad. Sci. U. S. A.* *81*, 3998-4002.
- Goel, R.K., Paczkowska, M., Reimand, J., Napper, S., and Lukong, K.E. (2018). Phosphoproteomics analysis identifies novel candidate substrates of the non-receptor tyrosine kinase, SRMS. *Mol. and Cell. Prot.* *17*, 925-947.
- Goldberg, J.L. (2003). How does an axon grow? *Genes Dev.* *17*, 941-958.
- Goldstein, L.S., and Yang, Z. (2000). Microtubule-based transport systems in neurons: the roles of kinesins and dyneins. *Annu. Rev. Neurosci.* *23*, 39-71.
- Goodenough, S., Schleusner, D., Pietrzik, C., Skutella, T., and Behl, C. (2005). Glycogen synthase kinase 3beta links neuroprotection by 17beta-estradiol to key Alzheimer processes. *Neuroscience* *132*, 581-589.
- Gordon-Weeks, P.R. (1987). The cytoskeletons of isolated, neuronal growth cones. *Neuroscience* *21*, 977-989.
- Gratuze, M., Cisbani, G., Cicchetti, F., and Planel, E. (2016). Is Huntington's disease a tauopathy? *Brain* *139*, 1014-1025.
- Gunning, P., O'Neill, G., and Hardeman, E. (2008). Tropomyosin-based regulation of the actin cytoskeleton in time and space. *Physiol. Rev.* *88*, 1-35.
- Gunning, P.W., Hardeman, E.C., Lappalainen, P., and Mulvihill, D.P. (2015). Tropomyosin - master regulator of actin filament function in the cytoskeleton. *J. Cell Sci.* *128*, 2965-2974.
- Guo, L., Xiao, Y., Fan, M., Li, J.J., and Wang, Y. (2014a). Profiling Global Kinome Signatures of the Radioresistant MCF-7/C6 Breast Cancer Cells Using MRM-based Targeted Proteomics. *J. Prot. Res.* *14*, 193-201.
- Guo, Q., Bin, H., Cheng, J., Seefelder, M., Engler, T., Pfeifer, G., Oeckl, P., Otto, M., Moser, F., Maurer, M., *et al.* (2018). The cryo-electron microscopy structure of huntingtin. *Nature* *555*, 117-120.
- Guo, W., Ji, Y., Wang, S., Sun, Y., and Lu, B. (2014b). Neuronal activity alters BDNF-TrkB signaling kinetics and downstream functions. *J. Cell Sci.* *127*, 2249-2260.
- Gurniak, C.B., Perlas, E., and Witke, W. (2005). The actin depolymerizing factor n-cofilin is essential for neural tube morphogenesis and neural crest cell migration. *Dev. Biol.* *278*, 231-241.
- Gusella, J.F., Wexler, N.S., Conneally, P.M., Naylor, S.L., Anderson, M.A., Tanzi, R.E., Watkins, P.C., Ottina, K., Wallace, M.R., Sakaguchi, A.Y., *et al.* (1983). A polymorphic DNA marker genetically linked to Huntington's disease. *Nature* *306*, 234-238.

- Haddad, M.S., and Cummings, J.L. (1997). Huntington's disease. *Psychiatr. Clin. North Am.* *20*, 791-807.
- Hall, A. (2012). Rho family GTPases. *Biochem. Soc. Trans.* *40*, 1378-1382.
- Harjes, P., and Wanker, E.E. (2003). The hunt for huntingtin function: interaction partners tell many different stories. *Trends Biochem. Sci.* *28*, 425-433.
- Heng, J.I., Chariot, A., and Nguyen, L. (2010). Molecular layers underlying cytoskeletal remodelling during cortical development. *Trends Neurosci.* *33*, 38-47.
- Henty-Ridilla, J.L., Juanes, M.A., and Goode, B.L. (2017). Profilin Directly Promotes Microtubule Growth through Residues Mutated in Amyotrophic Lateral Sclerosis. *Curr. Biol.* *27*, 3535-3543.
- Hersch, S.M., and Ferrante, R.J. (2004). Translating therapies for Huntington's disease from genetic animal models to clinical trials. *NeuroRx* *1*, 298-306.
- Hoozemans, J.J., Hilhorst, R., Ruijtenbeek, R., Rozemuller, A.J., and van der Vies, S.M. (2012). Protein kinase activity profiling of postmortem human brain tissue. *Neurodegener. Dis.* *10*, 46-48.
- Hornbeck, P.V., Kornhauser, J.M., Tkachev, S., Zhang, B., Skrzypek, E., Murray, B., Latham, V., and Sullivan, M. (2012). PhosphoSitePlus: a comprehensive resource for investigating the structure and function of experimentally determined post-translational modifications in man and mouse. *Nucleic Acids Res.* *40*, 261-270.
- Huber, W., von Heydebreck, A., Sultmann, H., Poustka, A., and Vingron, M. (2002). Variance stabilization applied to microarray data calibration and to the quantification of differential expression. *Bioinformatics* *1*, 96-104.
- Huntington, H.S.G. (1996). Unified Huntington's disease rating scale : reliability and consistency. *Mov. Disord.* *11*, 136-142.
- Huot, J. (2004). Ephrin signaling in axon guidance. *Prog. Neuropsychopharmacol. Biol. Psychiatry* *28*, 813-818.
- Imarisio, S., Carmichael, J., Korolchuk, V., Chen, C.W., Saiki, S., Rose, C., Krishna, G., Davies, J.E., Tfofi, E., Underwood, B.R., *et al.* (2008). Huntington's disease: from pathology and genetics to potential therapies. *Biochem. J.* *412*, 191-209.
- Jaffe, A.B., and Hall, A. (2005). Rho GTPases: biochemistry and biology. *Annu. Rev. Cell Dev. Biol.* *21*, 247-269.
- Jalal, S., Arsenault, R., Potter, A.A., Babiuk, L.A., Griebel, P.J., and Napper, S. (2009). Genome to kinome: species-specific peptide arrays for kinome analysis. *Sci. Signal.* *2*, 1-12.
- Johnson, S.A., and Hunter, T. (2005). Kinomics: methods for deciphering the kinome. *Nat. Methods* *2*, 17-25.

- Kato, M., Li, J., Chuang, J.L., and Chuang, D.T. (2007). Distinct structural mechanisms for inhibition of pyruvate dehydrogenase kinase isoforms by AZD7545, dichloroacetate, and radicicol. *Structure* 15, 992-1004.
- Kerschbamer, E., and Biagioli, M. (2015). Huntington's Disease as Neurodevelopmental Disorder: Altered Chromatin Regulation, Coding, and Non-Coding RNA Transcription. *Front. Neurosci.* 9, 509-514.
- Kiaei, M., Balasubramaniam, M., Govind Kumar, V., Shmookler Reis, R.J., Moradi, M., and Varughese, K.I. (2018). ALS-causing mutations in profilin-1 alter its conformational dynamics: A computational approach to explain propensity for aggregation. *Sci. Rep.* 8, 13102-13112.
- Kichina, J.V., Goc, A., Al-Husein, B., Somanath, P.R., and Kandel, E.S. (2010). PAK1 as a therapeutic target. *Expert Opin. Ther. Targets* 14, 703-725.
- Kikuchi, T., Morizane, A., Doi, D., Magotani, H., Onoe, H., Hayashi, T., Mizuma, H., Takara, S., Takahashi, R., Inoue, H., *et al.* (2017). Human iPS cell-derived dopaminergic neurons function in a primate Parkinson's disease model. *Nature* 548, 592-610.
- Kim, G.H., Kim, J.E., Rhie, S.J., and Yoon, S. (2015). The Role of Oxidative Stress in Neurodegenerative Diseases. *Exp. Neurobiol.* 24, 325-340.
- Kim, H., Oh, J.Y., Choi, S.L., Nam, Y.J., Jo, A., Kwon, A., Shin, E.Y., Kim, E.G., and Kim, H.K. (2016). Down-regulation of p21-activated serine/threonine kinase 1 is involved in loss of mesencephalic dopamine neurons. *Mol. Brain* 9, 45-58.
- Kim, J.S., Huang, T.Y., and Bokoch, G.M. (2009). Reactive oxygen species regulate a slingshot-cofilin activation pathway. *Mol. Biol. Cell* 20, 2650-2660.
- Kindrachuk, J., Arsenault, R., Kusalik, A., Kindrachuk, K.N., Trost, B., Napper, S., Jahrling, P.B., and Blaney, J.E. (2012). Systems kinomics demonstrates Congo Basin monkeypox virus infection selectively modulates host cell signaling responses as compared to West African monkeypox virus. *Mol. Cell. Prot.* 11, 1-12.
- Kindrachuk, J., Wahl-Jensen, V., Safronetz, D., Trost, B., Hoenen, T., Arsenault, R., Feldmann, F., Traynor, D., Postnikova, E., Kusalik, A., *et al.* (2014). Ebola virus modulates transforming growth factor beta signaling and cellular markers of mesenchyme-like transition in hepatocytes. *J. Virol.* 88, 9877-9892.
- Kobayashi, M., Nishita, M., Mishima, T., Ohashi, K., and Mizuno, K. (2006). MAPKAPK-2-mediated LIM-kinase activation is critical for VEGF-induced actin remodeling and cell migration. *EMBO J.* 25, 713-726.
- Koch, J.C., Tatenhorst, L., Roser, A.E., Saal, K.A., Tonges, L., and Lingor, P. (2018). ROCK inhibition in models of neurodegeneration and its potential for clinical translation. *Pharmacol. Ther.* 189, 1-21

- Koch, J.C., Tonges, L., Barski, E., Michel, U., Bahr, M., and Lingor, P. (2014). ROCK2 is a major regulator of axonal degeneration, neuronal death and axonal regeneration in the CNS. *Cell Death Dis.* 5, 1-12.
- Koutsis, G., Karadima, G., Kladi, A., and Panas, M. (2013). The challenge of juvenile Huntington disease: to test or not to test. *Neurology* 80, 990-996.
- Kovtun, I.V., Therneau, T.M., and McMurray, C.T. (2000). Gender of the embryo contributes to CAG instability in transgenic mice containing a Huntington's disease gene. *Hum. Mol. Genet.* 9, 2767-2775.
- Kovtun, I.V., Welch, G., Guthrie, H.D., Hafner, K.L., and McMurray, C.T. (2004). CAG repeat lengths in X- and Y-bearing sperm indicate that gender bias during transmission of Huntington's disease gene is determined in the embryo. *J. Biol. Chem.* 279, 9389-9391.
- Koyuncu, S., Saez, I., Lee, H.J., Gutierrez-Garcia, R., Pokrzywa, W., Fatima, A., Hoppe, T., and Vilchez, D. (2018). The ubiquitin ligase UBR5 suppresses proteostasis collapse in pluripotent stem cells from Huntington's disease patients. *Nat. Commun.* 9, 2886-2908.
- Kremer, B., Almqvist, E., Theilmann, J., Spence, N., Telenius, H., Goldberg, Y.P., and Hayden, M.R. (1995). Sex-dependent mechanisms for expansions and contractions of the CAG repeat on affected Huntington disease chromosomes. *Am. J. Hum. Genet.* 57, 343-350.
- Kuppers, E., and Beyer, C. (1999). Expression of estrogen receptor-alpha and beta mRNA in the developing and adult mouse striatum. *Neurosci. Lett.* 276, 95-98.
- La Spada, A.R., Paulson, H.L., and Fischbeck, K.H. (1994). Trinucleotide repeat expansion in neurological disease. *Ann. Neurol.* 36, 814-822.
- Labots, M., Gotink, K.J., Dekker, H., Azijli, K., van der Mijn, J.C., Huijts, C.M., Piersma, S.R., Jimenez, C.R., and Verheul, H.M. (2016). Evaluation of a tyrosine kinase peptide microarray for tyrosine kinase inhibitor therapy selection in cancer. *Exp. Mol. Med.* 48, 279-290.
- Landles, C., and Bates, G.P. (2004). Huntingtin and the molecular pathogenesis of Huntington's disease. Fourth in molecular medicine review series. *EMBO Rep.* 5, 958-963.
- Lecker, S.H., Goldberg, A.L., and Mitch, W.E. (2006). Protein degradation by the ubiquitin-proteasome pathway in normal and disease states. *J. Am. Soc. Nephrol.* 17, 1807-1819.
- Li, J.Y., Popovic, N., and Brundin, P. (2005). The use of the R6 transgenic mouse models of Huntington's disease in attempts to develop novel therapeutic strategies. *NeuroRx* 2, 447-464.
- Li, S.H., Gutekunst, C.A., Hersch, S.M., and Li, X.J. (1998). Interaction of huntingtin-associated protein with dynactin P150Glued. *J. Neurosci.* 18, 1261-1269.
- Li, S.H., and Li, X.J. (2004a). Huntingtin-protein interactions and the pathogenesis of Huntington's disease. *Trends Genet.* 20, 146-154.

- Li, S.H., and Li, X.J. (2004b). Huntingtin and its role in neuronal degeneration. *Neuroscientist* 10, 467-475.
- Li, Y., Arsenault, R.J., Trost, B., Slind, J., Griebel, P.J., Napper, S., and Kusalik, A. (2012). A systematic approach for analysis of peptide array kinome data. *Sci. Signal* 5, 12-29.
- Lievens, J.C., Iche, M., Laval, M., Faivre-Sarrailh, C., and Birman, S. (2008). AKT-sensitive or insensitive pathways of toxicity in glial cells and neurons in *Drosophila* models of Huntington's disease. *Hum. Mol. Genet.* 17, 882-894.
- Linding, R., Jensen, L.J., Ostheimer, G.J., van Vugt, M.A., Jorgensen, C., Miron, I.M., Diella, F., Colwill, K., Taylor, L., Elder, K., *et al.* (2007). Systematic discovery of in vivo phosphorylation networks. *Cell* 129, 1415-1426.
- Linding, R., Jensen, L.J., Pasculescu, A., Olhovsky, M., Colwill, K., Bork, P., Yaffe, M.B., and Pawson, T. (2008). NetworKIN: a resource for exploring cellular phosphorylation networks. *Nucleic Acids Res.* 36, 695-699.
- Liot, G., Zala, D., Pla, P., Mottet, G., Piel, M., and Saudou, F. (2013). Mutant Huntingtin alters retrograde transport of TrkB receptors in striatal dendrites. *J. Neurosci.* 33, 6298-6309.
- Liu, Z., Zhou, T., Ziegler, A.C., Dimitrion, P., and Zuo, L. (2017). Oxidative Stress in Neurodegenerative Diseases: From Molecular Mechanisms to Clinical Applications. *Oxid. Med. Cell. Longev.* 2017, 1-12.
- Lu, X.H., Mattis, V.B., Wang, N., Al-Ramahi, I., van den Berg, N., Fratantoni, S.A., Waldvogel, H., Greiner, E., Osmand, A., Elzein, K., *et al.* (2014). Targeting ATM ameliorates mutant Huntingtin toxicity in cell and animal models of Huntington's disease. *Sci. Transl. Med.* 6, 178-191.
- Luo, S., Mizuta, H., and Rubinsztein, D.C. (2008). p21-activated kinase 1 promotes soluble mutant huntingtin self-interaction and enhances toxicity. *Hum. Mol. Genet.* 17, 895-905.
- Ma, Q.L., Yang, F., Frautschy, S.A., and Cole, G.M. (2012). PAK in Alzheimer disease, Huntington disease and X-linked mental retardation. *Cell. Logist.* 2, 117-125.
- Maattanen, P., Taschuk, R., Ross, L., Marciniuk, K., Bertram, L., Potter, A., Cashman, N.R., and Napper, S. (2013a). PrP(Sc)-specific antibodies do not induce prion disease or misfolding of PrP(C) in highly susceptible Tga20 mice. *Prion* 7, 434-439.
- Maattanen, P., Trost, B., Scruten, E., Potter, A., Kusalik, A., Griebel, P., and Napper, S. (2013b). Divergent immune responses to *Mycobacterium avium* subsp. *paratuberculosis* infection correlate with kinome responses at the site of intestinal infection. *Infect. Immun.* 81, 2861-2872.
- MacDonald, M.E., Ambrose, C.M., Duyao, M.P., Myers, R.H., Lin, C., Srinidhi, L., Barnes, G., Taylor, S.A., James, M., and Groot, N. (1993). A novel gene containing a trinucleotide repeat that is expanded and unstable on Huntington's disease chromosomes. The Huntington's Disease Collaborative Research Group. *Cell* 72, 971-983.

- Maddika, S., Ande, S.R., Wiechec, E., Hansen, L.L., Wesselborg, S., and Los, M. (2008). Akt-mediated phosphorylation of CDK2 regulates its dual role in cell cycle progression and apoptosis. *J. Cell Sci.* *121*, 979-988.
- Maekawa, M., Ishizaki, T., Boku, S., Watanabe, N., Fujita, A., Iwamatsu, A., Obinata, T., Ohashi, K., Mizuno, K., and Narumiya, S. (1999). Signaling from Rho to the actin cytoskeleton through protein kinases ROCK and LIM-kinase. *Science* *285*, 895-898.
- Majumder, P., Roy, K., Singh, B.K., Jana, N.R., and Mukhopadhyay, D. (2017). Cellular levels of Grb2 and cytoskeleton stability are correlated in a neurodegenerative scenario. *Dis. Model. Mech.* *10*, 655-669.
- Mandelkow, E.M., Drewes, G., Biernat, J., Gustke, N., Van Lint, J., Vandenheede, J.R., and Mandelkow, E. (1992). Glycogen synthase kinase-3 and the Alzheimer-like state of microtubule-associated protein tau. *FEBS Lett.* *314*, 315-321.
- Mangiarini, L., Sathasivam, K., Seller, M., Cozens, B., Harper, A., Hetherington, C., Lawton, M., Trotter, Y., Lehrach, H., Davies, S.W., *et al.* (1996). Exon 1 of the HD gene with an expanded CAG repeat is sufficient to cause a progressive neurological phenotype in transgenic mice. *Cell* *87*, 493-506.
- Manning, B.D., and Toker, A. (2017). AKT/PKB Signaling: Navigating the Network. *Cell* *169*, 381-405.
- Manning, G., Whyte, D.B., Martinez, R., Hunter, T., and Sudarsanam, S. (2002). The protein kinase complement of the human genome. *Science* *298*, 1912-1934.
- Matus, A., Ackermann, M., Pehling, G., Byers, H.R., and Fujiwara, K. (1982). High actin concentrations in brain dendritic spines and postsynaptic densities. *Proc. Natl. Acad. Sci. U. S. A.* *79*, 7590-7594.
- McCullough, L.D., de Vries, G.J., Miller, V.M., Becker, J.B., Sandberg, K., and McCarthy, M.M. (2014). NIH initiative to balance sex of animals in preclinical studies: generative questions to guide policy, implementation, and metrics. *Biol. Sex Differ.* *5*, 15-22.
- Medina, M., Garrido, J.J., and Wandosell, F.G. (2011). Modulation of GSK-3 as a Therapeutic Strategy on Tau Pathologies. *Front. Mol. Neurosci.* *4*, 24-34.
- Menalled, L., El-Khodori, B.F., Patry, M., Suarez-Farinas, M., Orenstein, S.J., Zahasky, B., Leahy, C., Wheeler, V., Yang, X.W., MacDonald, M., *et al.* (2009). Systematic behavioral evaluation of Huntington's disease transgenic and knock-in mouse models. *Neurobiol. Dis.* *35*, 319-336.
- Meng, G., Zhong, X., and Mei, H. (2016). A Systematic Investigation into Aging Related Genes in Brain and Their Relationship with Alzheimer's Disease. *PLoS One* *11*, 4-21.
- Meng, Y., Zhang, Y., Tregoubov, V., Janus, C., Cruz, L., Jackson, M., Lu, W.Y., MacDonald, J.F., Wang, J.Y., Falls, D.L., *et al.* (2002). Abnormal spine morphology and enhanced LTP in LIMK-1 knockout mice. *Neuron* *35*, 121-133.

- Miller, J.P., Holcomb, J., Al-Ramahi, I., de Haro, M., Gafni, J., Zhang, N., Kim, E., Sanhueza, M., Torcassi, C., Kwak, S., *et al.* (2010). Matrix metalloproteinases are modifiers of huntingtin proteolysis and toxicity in Huntington's disease. *Neuron* 67, 199-212.
- Miller, M.L., Jensen, L.J., Diella, F., Jorgensen, C., Tinti, M., Li, L., Hsiung, M., Parker, S.A., Bordeaux, J., Sicheritz-Ponten, T., *et al.* (2008). Linear motif atlas for phosphorylation-dependent signaling. *Sci. Signal* 1, 1-12.
- Minamide, L.S., Striegl, A.M., Boyle, J.A., Meberg, P.J., and Bamberg, J.R. (2000). Neurodegenerative stimuli induce persistent ADF/cofilin-actin rods that disrupt distal neurite function. *Nat. Cell Biol.* 2, 628-636.
- Mitchison, T., and Kirschner, M. (1988). Cytoskeletal dynamics and nerve growth. *Neuron* 1, 761-772.
- Moser, R., Xu, C., Kao, M., Annis, J., Lerma, L.A., Schaupp, C.M., Gurley, K.E., Jang, I.S., Biktasova, A., Yarbrough, W.G., *et al.* (2014). Functional kinomics identifies candidate therapeutic targets in head and neck cancer. *Clin. Cancer Res.* 20, 4274-4288.
- Mouneimne, G., DesMarais, V., Sidani, M., Scemes, E., Wang, W., Song, X., Eddy, R., and Condeelis, J. (2006). Spatial and temporal control of cofilin activity is required for directional sensing during chemotaxis. *Curr. Biol.* 16, 2193-2205.
- Mu, S., Wang, J., Zhou, G., Peng, W., He, Z., Zhao, Z., Mo, C., Qu, J., and Zhang, J. (2014). Transplantation of induced pluripotent stem cells improves functional recovery in Huntington's disease rat model. *PLoS One* 9, 1-10.
- Mueller, K.A., Glajch, K.E., Huizenga, M.N., Wilson, R.A., Granucci, E.J., Dios, A.M., Tousley, A.R., Iuliano, M., Weisman, E., LaQuaglia, M.J., *et al.* (2018). Hippo Signaling Pathway Dysregulation in Human Huntington's Disease Brain and Neuronal Stem Cells. *Sci. Rep.* 8, 1-13.
- Mullard, A. (2019). Pioneering antisense drug heads into pivotal trials for Huntington disease. *Nat. Rev. Drug Discov.* 18, 161-163.
- Mulongo, M., Prysliak, T., Scruten, E., Napper, S., and Perez-Casal, J. (2014). In vitro infection of bovine monocytes with *Mycoplasma bovis* delays apoptosis and suppresses production of gamma interferon and tumor necrosis factor alpha but not interleukin-10. *Infect. Immun.* 82, 62-71.
- Munsie, L.N., Desmond, C.R., and Truant, R. (2012). Cofilin nuclear-cytoplasmic shuttling affects cofilin-actin rod formation during stress. *J. Cell Sci.* 125, 3977-3988.
- Munsie, L.N., and Truant, R. (2012). The role of the cofilin-actin rod stress response in neurodegenerative diseases uncovers potential new drug targets. *Bioarchitecture* 2, 204-208.
- Nakagawa, O., Fujisawa, K., Ishizaki, T., Saito, Y., Nakao, K., and Narumiya, S. (1996). ROCK-I and ROCK-II, two isoforms of Rho-associated coiled-coil forming protein serine/threonine kinase in mice. *FEBS Lett.* 392, 189-193.

- Napper, S., Dadgar, S., Arsenault, R.J., Trost, B., Scruten, E., Kusalik, A., and Shand, P. (2015). Induction of tissue- and stressor-specific kinomic responses in chickens exposed to hot and cold stresses. *Poult. Sci.* *94*, 1333-1345.
- Narayanan, K.L., Chopra, V., Rosas, H.D., Malarick, K., and Hersch, S. (2016). Rho Kinase Pathway Alterations in the Brain and Leukocytes in Huntington's Disease. *Mol. Neurobiol.* *53*, 2132-2140.
- Nasir, J., Floresco, S.B., O'Kusky, J.R., Diewert, V.M., Richman, J.M., Zeisler, J., Borowski, A., Marth, J.D., Phillips, A.G., and Hayden, M.R. (1995). Targeted disruption of the Huntington's disease gene results in embryonic lethality and behavioral and morphological changes in heterozygotes. *Cell* *81*, 811-823.
- Nekrasov, E.D., Vigont, V.A., Klyushnikov, S.A., Lebedeva, O.S., Vassina, E.M., Bogomazova, A.N., Chestkov, I.V., Semashko, T.A., Kiseleva, E., Suldina, L.A., *et al.* (2016). Manifestation of Huntington's disease pathology in human induced pluripotent stem cell-derived neurons. *Mol. Neurodegener.* *11*, 27-42.
- Nelson, T.J., Martinez-Fernandez, A., and Terzic, A. (2010). Induced pluripotent stem cells: developmental biology to regenerative medicine. *Nat. Rev. Cardiol.* *7*, 700-710.
- Niwa, R., Nagata-Ohashi, K., Takeichi, M., Mizuno, K., and Uemura, T. (2002). Control of actin reorganization by Slingshot, a family of phosphatases that dephosphorylate ADF/cofilin. *Cell* *108*, 233-246.
- Nopoulos, P.C. (2016). Huntington disease: a single-gene degenerative disorder of the striatum. *Dialogues Clin. Neurosci.* *18*, 91-98.
- Norremolle, A., Sorensen, S.A., Fenger, K., and Hasholt, L. (1995). Correlation between magnitude of CAG repeat length alterations and length of the paternal repeat in paternally inherited Huntington's disease. *Clin. Genet.* *47*, 113-117.
- Nyarko, J.N.K., Quartey, M.O., Pennington, P.R., Heistad, R.M., Dea, D., Poirier, J., Baker, G.B., and Mousseau, D.D. (2018). Profiles of beta-Amyloid Peptides and Key Secretases in Brain Autopsy Samples Differ with Sex and APOE epsilon4 Status: Impact for Risk and Progression of Alzheimer Disease. *Neuroscience* *373*, 20-36.
- Ohashi, K., Nagata, K., Maekawa, M., Ishizaki, T., Narumiya, S., and Mizuno, K. (2000). Rho-associated kinase ROCK activates LIM-kinase 1 by phosphorylation at threonine 508 within the activation loop. *J. Biol. Chem.* *275*, 3577-3582.
- Ohta, Y., Kousaka, K., Nagata-Ohashi, K., Ohashi, K., Muramoto, A., Shima, Y., Niwa, R., Uemura, T., and Mizuno, K. (2003). Differential activities, subcellular distribution and tissue expression patterns of three members of Slingshot family phosphatases that dephosphorylate cofilin. *Genes Cells* *8*, 811-824.
- Orr, H.T., and Zoghbi, H.Y. (2007). Trinucleotide repeat disorders. *Annu. Rev. Neurosci.* *30*, 575-621.

- Palidwor, G.A., Shcherbinin, S., Huska, M.R., Rasko, T., Stelzl, U., Arumughan, A., Foulle, R., Porras, P., Sanchez-Pulido, L., Wanker, E.E., *et al.* (2009). Detection of alpha-rod protein repeats using a neural network and application to huntingtin. *PLoS Comput. Biol.* 5, 1-11.
- Parikh, K., and Peppelenbosch, M.P. (2010). Kinome profiling of clinical cancer specimens. *Cancer Res.* 70, 2575-2578.
- Parsons, M.P., Kang, R., Buren, C., Dau, A., Southwell, A.L., Doty, C.N., Sanders, S.S., Hayden, M.R., and Raymond, L.A. (2014). Bidirectional control of postsynaptic density-95 (PSD-95) clustering by Huntingtin. *J. Biol. Chem.* 289, 3518-3528.
- Parvathy, M., Sreeja, S., Kumar, R., and Pillai, M.R. (2016). Potential role of p21 Activated Kinase 1 (PAK1) in the invasion and motility of oral cancer cells. *BMC Cancer* 1, 293-300.
- Pennuto, M., Palazzolo, I., and Poletti, A. (2009). Post-translational modifications of expanded polyglutamine proteins: impact on neurotoxicity. *Hum. Mol. Genet.* 18, 40-47.
- Peppelenbosch, M.P. (2012). Kinome profiling. *Scientifica (Cairo)* 2012, 1-14.
- Petrilli, A., Copik, A., Posadas, M., Chang, L.S., Welling, D.B., Giovannini, M., and Fernandez-Valle, C. (2014). LIM domain kinases as potential therapeutic targets for neurofibromatosis type 2. *Oncogene* 33, 3571-3582.
- Phadngam, S., Castiglioni, A., Ferraresi, A., Morani, F., Follo, C., and Isidoro, C. (2016). PTEN dephosphorylates AKT to prevent the expression of GLUT1 on plasmamembrane and to limit glucose consumption in cancer cells. *Oncotarget* 7, 84999-85020.
- Posey, A.E., Ruff, K.M., Harmon, T.S., Crick, S.L., Li, A., Diamond, M.I., and Pappu, R.V. (2018). Profilin reduces aggregation and phase separation of huntingtin N-terminal fragments by preferentially binding to soluble monomers and oligomers. *J. Biol. Chem.* 293, 3734-3746.
- Pouladi, M.A., Morton, A.J., and Hayden, M.R. (2013). Choosing an animal model for the study of Huntington's disease. *Nat. Rev. Neurosci.* 14, 708-721.
- Pringsheim, T., Wiltshire, K., Day, L., Dykeman, J., Steeves, T., and Jette, N. (2012). The incidence and prevalence of Huntington's disease: a systematic review and meta-analysis. *Mov. Disord.* 27, 1083-1091.
- Proschel, C., Blouin, M.J., Gutowski, N.J., Ludwig, R., and Noble, M. (1995). Limk1 is predominantly expressed in neural tissues and phosphorylates serine, threonine and tyrosine residues in vitro. *Oncogene* 11, 1271-1281.
- Quartey, M.O., Nyarko, J.N.K., Pennington, P.R., Heistad, R.M., Chaharyn, B.M., Wei, Z., Bainbridge, D., Baker, G.B., and Mousseau, D.D. (2019). Age- and sex-dependent profiles of APP fragments and key secretases align with changes in despair-like behavior and cognition in young APPSwe/Ind mice. *Biochem. Biophys. Res. Commun.* 511, 454-459.

Quigley, J. (2017). Juvenile Huntington's Disease: Diagnostic and Treatment Considerations for the Psychiatrist. *Curr. Psychiatry Rep.* 19, 9-13.

Ramaswamy, S., McBride, J.L., and Kordower, J.H. (2007). Animal models of Huntington's disease. *ILAR J.* 48, 356-373.

Ratovitski, T., Chaerkady, R., Kammers, K., Stewart, J.C., Zavala, A., Pletnikova, O., Troncoso, J.C., Rudnicki, D.D., Margolis, R.L., Cole, R.N., *et al.* (2016). Quantitative Proteomic Analysis Reveals Similarities between Huntington's Disease (HD) and Huntington's Disease-Like 2 (HDL2) Human Brains. *J. Proteome Res.* 15, 3266-3283.

Ratovitski, T., O'Meally, R.N., Jiang, M., Chaerkady, R., Chighladze, E., Stewart, J.C., Wang, X., Arbez, N., Roby, E., Alexandris, A., *et al.* (2017). Post-Translational Modifications (PTMs), Identified on Endogenous Huntingtin, Cluster within Proteolytic Domains between HEAT Repeats. *J. Proteome Res.* 16, 2692-2708.

Raymond, L.A. (2017). Striatal synaptic dysfunction and altered calcium regulation in Huntington disease. *Biochem. Biophys. Res. Commun.* 483, 1051-1062.

Ring, K.L., An, M.C., Zhang, N., O'Brien, R.N., Ramos, E.M., Gao, F., Atwood, R., Bailus, B.J., Melov, S., Mooney, S.D., *et al.* (2015). Genomic Analysis Reveals Disruption of Striatal Neuronal Development and Therapeutic Targets in Human Huntington's Disease Neural Stem Cells. *Stem Cell Reports* 5, 1023-1038.

Robert, A., Hookway, C., and Gelfand, V.I. (2016). Intermediate filament dynamics: What we can see now and why it matters. *Bioessays* 38, 232-243.

Robertson, A.J., Trost, B., Scruten, E., Robertson, T., Mostajeran, M., Connor, W., Kusalik, A., Griebel, P., and Napper, S. (2014). Identification of developmentally-specific kinotypes and mechanisms of Varroa mite resistance through whole-organism, kinome analysis of honeybee. *Front. Genet.* 5, 139-151.

Romarowski, A., Battistone, M.A., La Spina, F.A., Puga Molina Ldel, C., Luque, G.M., Vitale, A.M., Cuasnicu, P.S., Visconti, P.E., Krapf, D., and Buffone, M.G. (2015). PKA-dependent phosphorylation of LIMK1 and Cofilin is essential for mouse sperm acrosomal exocytosis. *Dev. Biol.* 405, 237-249.

Roos, R.A., Vegter-van der Vlis, M., Hermans, J., Elshove, H.M., Moll, A.C., van de Kamp, J.J., and Bruyn, G.W. (1991). Age at onset in Huntington's disease: effect of line of inheritance and patient's sex. *J. Med. Genet.* 28, 515-519.

Rosenberger, A.F., Hilhorst, R., Coart, E., Garcia Barrado, L., Naji, F., Rozemuller, A.J., van der Flier, W.M., Scheltens, P., Hoozemans, J.J., and van der Vies, S.M. (2016). Protein Kinase Activity Decreases with Higher Braak Stages of Alzheimer's Disease Pathology. *J. Alzheimers Dis.* 49, 927-943.

Ross, C.A., and Akimov, S.S. (2014). Human-induced pluripotent stem cells: potential for neurodegenerative diseases. *Hum. Mol. Genet.* 23, 17-26.

- Ross, C.A., and Tabrizi, S.J. (2011). Huntington's disease: from molecular pathogenesis to clinical treatment. *Lancet Neurol.* *10*, 83-98.
- Rossman, K.L., Der, C.J., and Sondek, J. (2005). GEF means go: turning on RHO GTPases with guanine nucleotide-exchange factors. *Nat. Rev. Mol. Cell Biol.* *6*, 167-180.
- Sainath, R., and Gallo, G. (2015). Cytoskeletal and signaling mechanisms of neurite formation. *Cell Tissue Res.* *359*, 267-278.
- Saudou, F., and Humbert, S. (2016). The Biology of Huntingtin. *Neuron* *89*, 910-926.
- Scholma, J., Fuhler, G.M., Joore, J., Hulsman, M., Schivo, S., List, A.F., Reinders, M.J., Peppelenbosch, M.P., and Post, J.N. (2016). Improved intra-array and interarray normalization of peptide microarray phosphorylation for phosphoproteome and kinome profiling by rational selection of relevant spots. *Sci. Rep.* *6*, 1-13.
- Schulte, J., and Littleton, J.T. (2011). The biological function of the Huntingtin protein and its relevance to Huntington's Disease pathology. *Curr. Trends Neurol.* *5*, 65-78.
- Schulte, J., Sepp, K.J., Wu, C., Hong, P., and Littleton, J.T. (2011). High-content chemical and RNAi screens for suppressors of neurotoxicity in a Huntington's disease model. *PLoS One* *6*, 23841-23854.
- Semaka, A., Kay, C., Doty, C., Collins, J.A., Bijlsma, E.K., Richards, F., Goldberg, Y.P., and Hayden, M.R. (2013). CAG size-specific risk estimates for intermediate allele repeat instability in Huntington disease. *J. Med. Genet.* *50*, 696-703.
- Shao, J., Welch, W.J., Diprospero, N.A., and Diamond, M.I. (2008). Phosphorylation of profilin by ROCK1 regulates polyglutamine aggregation. *Mol. Cell. Biol.* *28*, 5196-5208.
- Siani, F., Greco, R., Levandis, G., Ghezzi, C., Daviddi, F., Demartini, C., Vegeto, E., Fuzzati-Armentero, M.T., and Blandini, F. (2017). Influence of Estrogen Modulation on Glia Activation in a Murine Model of Parkinson's Disease. *Front. Neurosci.* *11*, 306-317.
- Simpkins, J.W., Yi, K.D., Yang, S.H., and Dykens, J.A. (2010). Mitochondrial mechanisms of estrogen neuroprotection. *Biochim. Biophys. Acta* *1800*, 1113-1120.
- Simunovic, F., Yi, M., Wang, Y., Stephens, R., and Sonntag, K.C. (2010). Evidence for gender-specific transcriptional profiles of nigral dopamine neurons in Parkinson disease. *PLoS One* *5*, 1-14.
- Skotte, N.H., Andersen, J.V., Santos, A., Aldana, B.I., Willert, C.W., Norremolle, A., Waagepetersen, H.S., and Nielsen, M.L. (2018). Integrative Characterization of the R6/2 Mouse Model of Huntington's Disease Reveals Dysfunctional Astrocyte Metabolism. *Cell. Rep.* *23*, 2211-2224.
- Smith, K.M., and Dahodwala, N. (2014). Sex differences in Parkinson's disease and other movement disorders. *Exp. Neurol.* *259*, 44-56.

- Soosairajah, J., Maiti, S., Wiggan, O., Sarmiere, P., Moussi, N., Sarcevic, B., Sampath, R., Bamberg, J.R., and Bernard, O. (2005). Interplay between components of a novel LIM kinase-slingshot phosphatase complex regulates cofilin. *EMBO J.* *24*, 473-486.
- Stoyas, C.A., and La Spada, A.R. (2018). The CAG-polyglutamine repeat diseases: a clinical, molecular, genetic, and pathophysiologic nosology. *Handb. Clin. Neurol.* *147*, 143-170.
- Sugiyama, M.G., Fairn, G.D., and Antonescu, C.N. (2019). Akt-ing Up Just About Everywhere: Compartment-Specific Akt Activation and Function in Receptor Tyrosine Kinase Signaling. *Front. Cell. Dev. Biol.* *7*, 70-94.
- Sutherland, J.J., Gao, C., Cahya, S., and Vieth, M. (2013). What general conclusions can we draw from kinase profiling data sets? *Biochim. Biophys. Acta* *1834*, 1425-1433.
- Szebenyi, G., Morfini, G.A., Babcock, A., Gould, M., Selkoe, K., Stenoiien, D.L., Young, M., Faber, P.W., MacDonald, M.E., McPhaul, M.J., *et al.* (2003). Neuropathogenic forms of huntingtin and androgen receptor inhibit fast axonal transport. *Neuron* *40*, 41-52.
- Szlachcic, W.J., Switonski, P.M., Krzyzosiak, W.J., Figlerowicz, M., and Figiel, M. (2015). Huntington disease iPSCs show early molecular changes in intracellular signaling, the expression of oxidative stress proteins and the p53 pathway. *Dis. Model. Mech.* *8*, 1047-1057.
- Szlachcic, W.J., Wiatr, K., Trzeciak, M., Figlerowicz, M., and Figiel, M. (2017). The Generation of Mouse and Human Huntington Disease iPSC Cells Suitable for In vitro Studies on Huntingtin Function. *Front. Mol. Neurosci.* *10*, 253-269.
- Takahashi, H., Koshimizu, U., and Nakamura, T. (1998). A novel transcript encoding truncated LIM kinase 2 is specifically expressed in male germ cells undergoing meiosis. *Biochem. Biophys. Res. Commun.* *249*, 138-145.
- Takahashi, K., and Yamanaka, S. (2013). Induced pluripotent stem cells in medicine and biology. *Development* *140*, 2457-2461.
- Takano, H., and Gusella, J.F. (2002). The predominantly HEAT-like motif structure of huntingtin and its association and coincident nuclear entry with dorsal, an NF-kB/Rel/dorsal family transcription factor. *BMC Neurosci.* *3*, 1-13.
- Tartari, M., Gissi, C., Lo Sardo, V., Zuccato, C., Picardi, E., Pesole, G., and Cattaneo, E. (2008). Phylogenetic comparison of huntingtin homologues reveals the appearance of a primitive polyQ in sea urchin. *Mol. Biol. Evol.* *25*, 330-338.
- Telenius, H., Kremer, B., Goldberg, Y.P., Theilmann, J., Andrew, S.E., Zeisler, J., Adam, S., Greenberg, C., Ives, E.J., Clarke, L.A., *et al.* (1994). Somatic and gonadal mosaicism of the Huntington disease gene CAG repeat in brain and sperm. *Nat. Genet.* *6*, 409-414.
- Thomas, E.A. (2006). Striatal specificity of gene expression dysregulation in Huntington's disease. *J. Neurosci. Res.* *84*, 1151-1164.

- Tourette, C., Li, B., Bell, R., O'Hare, S., Kaltenbach, L.S., Mooney, S.D., and Hughes, R.E. (2014). A large scale Huntingtin protein interaction network implicates Rho GTPase signaling pathways in Huntington disease. *J. Biol. Chem.* *289*, 6709-6726.
- Trost, B., Arsenault, R., Griebel, P., Napper, S., and Kusalik, A. (2013a). DAPPLE: a pipeline for the homology-based prediction of phosphorylation sites. *Bioinformatics* *29*, 1693-1695.
- Trost, B., Kindrachuk, J., Maattanen, P., Napper, S., and Kusalik, A. (2013b). PIIKA 2: an expanded, web-based platform for analysis of kinome microarray data. *PLoS One* *8*, 1-12.
- Trost, B., Maleki, F., Kusalik, A., and Napper, S. (2016). DAPPLE 2: a Tool for the Homology-Based Prediction of Post-Translational Modification Sites. *J. Proteome Res.* *15*, 2760-2767.
- Trushina, E., Heldebrant, M.P., Perez-Terzic, C.M., Bortolon, R., Kovtun, I.V., Badger, J.D., 2nd, Terzic, A., Estevez, A., Windebank, A.J., Dyer, R.B., *et al.* (2003). Microtubule destabilization and nuclear entry are sequential steps leading to toxicity in Huntington's disease. *Proc. Natl. Acad. Sci. U. S. A.* *100*, 12171-12176.
- Vallee, A., Lecarpentier, Y., Guillevin, R., and Vallee, J.N. (2018). Aerobic glycolysis in amyotrophic lateral sclerosis and Huntington's disease. *Rev. Neurosci.* *29*, 547-555.
- van Dyck, C.H., Seibyl, J.P., Malison, R.T., Laruelle, M., Wallace, E., Zoghbi, S.S., Zea-Ponce, Y., Baldwin, R.M., Charney, D.S., and Hoffer, P.B. (1995). Age-related decline in striatal dopamine transporter binding with iodine-123-beta-CITSPECT. *J. Nucl. Med.* *36*, 1175-1181.
- Van Wyk, B., Snider, M., Scruten, E., van Drunen Littel-van den Hurk, S., and Napper, S. (2016). Induction of functional interferon alpha and gamma responses during acute infection of cattle with non-cytopathic bovine viral diarrhea virus. *Vet. Microbiol.* *195*, 104-114.
- Velier, J., Kim, M., Schwarz, C., Kim, T.W., Sapp, E., Chase, K., Aronin, N., and DiFiglia, M. (1998). Wild-type and mutant huntingtins function in vesicle trafficking in the secretory and endocytic pathways. *Exp. Neurol.* *152*, 34-40.
- Wang, J., Green, P.S., and Simpkins, J.W. (2001). Estradiol protects against ATP depletion, mitochondrial membrane potential decline and the generation of reactive oxygen species induced by 3-nitropropionic acid in SK-N-SH human neuroblastoma cells. *J. Neurochem.* *77*, 804-811.
- Wang, Y., Shibasaki, F., and Mizuno, K. (2005). Calcium signal-induced cofilin dephosphorylation is mediated by Slingshot via calcineurin. *J. Biol. Chem.* *280*, 12683-12689.
- Warby, S.C., Doty, C.N., Graham, R.K., Carroll, J.B., Yang, Y.Z., Singaraja, R.R., Overall, C.M., and Hayden, M.R. (2008). Activated caspase-6 and caspase-6-cleaved fragments of huntingtin specifically colocalize in the nucleus. *Hum. Mol. Genet.* *17*, 2390-2404.
- Wegrzynowicz, M., Holt, H.K., Friedman, D.B., and Bowman, A.B. (2012). Changes in the striatal proteome of YAC128Q mice exhibit gene-environment interactions between mutant huntingtin and manganese. *J. Prot. Res.* *11*, 1118-1132.

- Wioland, H., Guichard, B., Senju, Y., Myram, S., Lappalainen, P., Jegou, A., and Romet-Lemonne, G. (2017). ADF/Cofilin Accelerates Actin Dynamics by Severing Filaments and Promoting Their Depolymerization at Both Ends. *Curr. Biol.* 27, 1956-1967.
- Wood, H. (2018). Huntington disease - a neurodevelopmental disorder? *Nat. Rev. Neurol.* 14, 632-633.
- Wood, N.I., Carta, V., Milde, S., Skillings, E.A., McAllister, C.J., Ang, Y.L., Duguid, A., Wijesuriya, N., Afzal, S.M., Fernandes, J.X., *et al.* (2010). Responses to environmental enrichment differ with sex and genotype in a transgenic mouse model of Huntington's disease. *PLoS One* 5, 1-16.
- Wooten, G.F., Currie, L.J., Bovbjerg, V.E., Lee, J.K., and Patrie, J. (2004). Are men at greater risk for Parkinson's disease than women? *J. Neurol. Neurosurg. Psychiatry* 75, 637-639.
- Wright, G.E.B., Collins, J.A., Kay, C., McDonald, C., Dolzhenko, E., Xia, Q., Bečanović, K., Semaka, A., Nguyen, C.M., Trost, B., *et al.* (2019). Length of uninterrupted CAG repeats, independent of polyglutamine size, results in increased somatic instability and hastened age of onset in Huntington disease. *bioRxiv*, 178, 887–900.
- Xie, C., Liu, Y.Q., Guan, Y.T., and Zhang, G.X. (2016). Induced Stem Cells as a Novel Multiple Sclerosis Therapy. *Curr. Stem Cell Res. Ther.* 11, 313-320.
- Xu, N.J., and Henkemeyer, M. (2012). Ephrin reverse signaling in axon guidance and synaptogenesis. *Semin. Cell Dev. Biol.* 23, 58-64.
- Yamanaka, S., and Blau, H.M. (2010). Nuclear reprogramming to a pluripotent state by three approaches. *Nature* 465, 704-712.
- Yan, J., Pan, Y., Zheng, X., Zhu, C., Zhang, Y., Shi, G., Yao, L., Chen, Y., and Xu, N. (2019). Comparative Study of ROCK1 and ROCK2 in Hippocampal Spine Formation and Synaptic Function. *Neurosci. Bull.* 35, 649-660.
- Yang, J., Li, S., He, X.B., Cheng, C., and Le, W. (2016). Induced pluripotent stem cells in Alzheimer's disease: applications for disease modeling and cell-replacement therapy. *Mol. Neurodegener.* 11, 39-50.
- Yang, N., Higuchi, O., Ohashi, K., Nagata, K., Wada, A., Kangawa, K., Nishida, E., and Mizuno, K. (1998). Cofilin phosphorylation by LIM-kinase 1 and its role in Rac-mediated actin reorganization. *Nature* 393, 809-812.
- Yu-Taeger, L., Stricker-Shaver, J., Arnold, K., Bambynek-Dziuk, P., Novati, A., Singer, E., Lourmati, A., Fabian, C., Magg, J., Riess, O., *et al.* (2019). Intranasal Administration of Mesenchymal Stem Cells Ameliorates the Abnormal Dopamine Transmission System and Inflammatory Reaction in the R6/2 Mouse Model of Huntington Disease. *Cells* 8, 1-22.

- Yuan, J., Xu, B.Z., Qi, S.T., Tong, J.S., Wei, L., Li, M., Ouyang, Y.C., Hou, Y., Schatten, H., and Sun, Q.Y. (2010). MAPK-activated protein kinase 2 is required for mouse meiotic spindle assembly and kinetochore-microtubule attachment. *PLoS One* 5, 1-13.
- Zeitlin, S., Liu, J.P., Chapman, D.L., Papaioannou, V.E., and Efstratiadis, A. (1995). Increased apoptosis and early embryonic lethality in mice nullizygous for the Huntington's disease gene homologue. *Nat. Genet.* 11, 155-163.
- Zhang, N., An, M.C., Montoro, D., and Ellerby, L.M. (2010). Characterization of Human Huntington's Disease Cell Model from Induced Pluripotent Stem Cells. *PLoS Curr.* 2, 1-16.
- Zhao, J.W., Gao, Z.L., Ji, Q.Y., Wang, H., Zhang, H.Y., Yang, Y.D., Xing, F.J., Meng, L.J., and Wang, Y. (2012). Regulation of cofilin activity by CaMKII and calcineurin. *Am. J. Med. Sci.* 344, 462-472.
- Zhao, L., Ma, Q.L., Calon, F., Harris-White, M.E., Yang, F., Lim, G.P., Morihara, T., Ubeda, O.J., Ambegaokar, S., Hansen, J.E., *et al.* (2006). Role of p21-activated kinase pathway defects in the cognitive deficits of Alzheimer disease. *Nat. Neurosci.* 9, 234-242.
- Zhou, Z., Meng, Y., Asrar, S., Todorovski, Z., and Jia, Z. (2009). A critical role of Rho-kinase ROCK2 in the regulation of spine and synaptic function. *Neuropharmacol.* 56, 81-89.
- Zielonka, D., Marinus, J., Roos, R.A., De Michele, G., Di Donato, S., Putter, H., Marcinkowski, J., Squitieri, F., Bentivoglio, A.R., and Landwehrmeyer, G.B. (2013). The influence of gender on phenotype and disease progression in patients with Huntington's disease. *Parkinsonism Relat. Disord.* 19, 192-197.

APPENDIX

Supplementary Table 1: List of peptides from a previously designed peptide array with peptides their uniprot ID and phosphosites. This array was used to study signaling changes in the NSCs.

Supplementary Table 2: PIKA 2 output from the peptide array experiment for NSCs. Columns represents the name, uniprot ID, target phosphosite followed by their respective P-value and fold change.

Supplementary Table 3: InnateDB output for the peptide array analysis of NSCs. The first sheet represents the output for upregulated peptides (up) and the second sheet downregulated peptides (down).

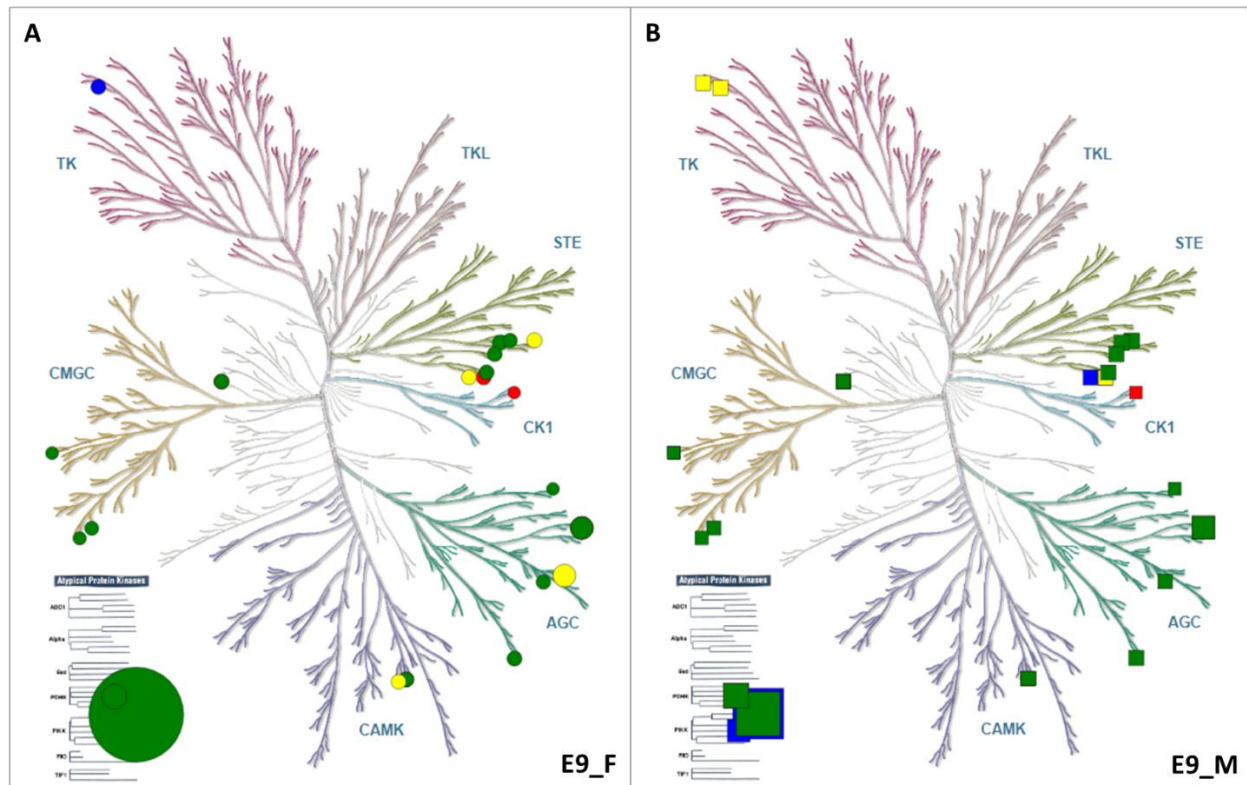
Supplementary Table 4: List of peptides for the customized peptide array to study the kinase signaling in R6/2 neural tissue. The name of the peptide is followed by it uniprot ID and target phosphosite.

Supplementary Table 5: PIKA 2 output from the peptide array experiment for murine neural tissue. Columns represents the name, uniprot ID, target phosphosite followed by their respective P-value and fold change. Each time point and sex is represented in a separate sheet.

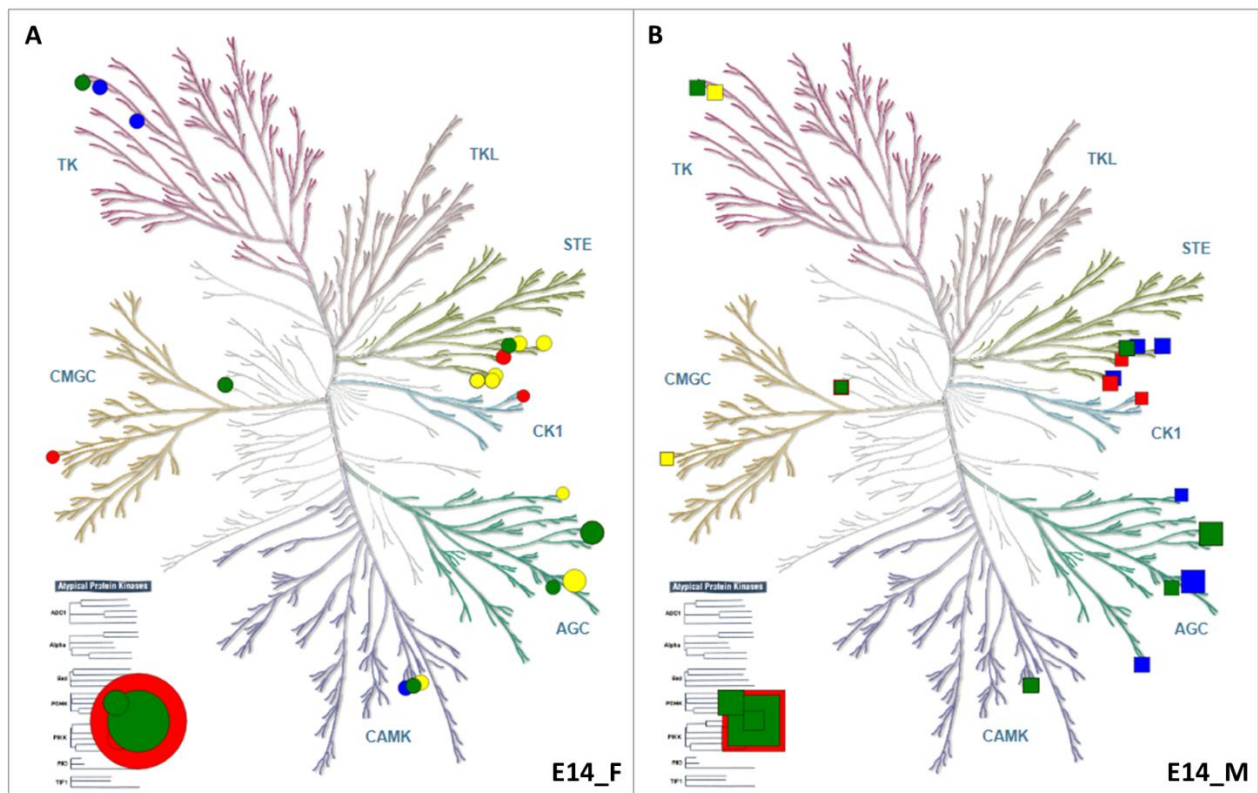
Supplementary Table 6: InnateDB output for the peptide array analysis of murine neural tissues. The excel sheet represents the output for upregulated peptides. Each time point and sex is represented in a separate sheet.

Supplementary Table 7: InnateDB output for the peptide array analysis of murine neural tissues. The excel sheet represents the output for downregulated peptides. Each time point and sex is represented in a separate sheet.

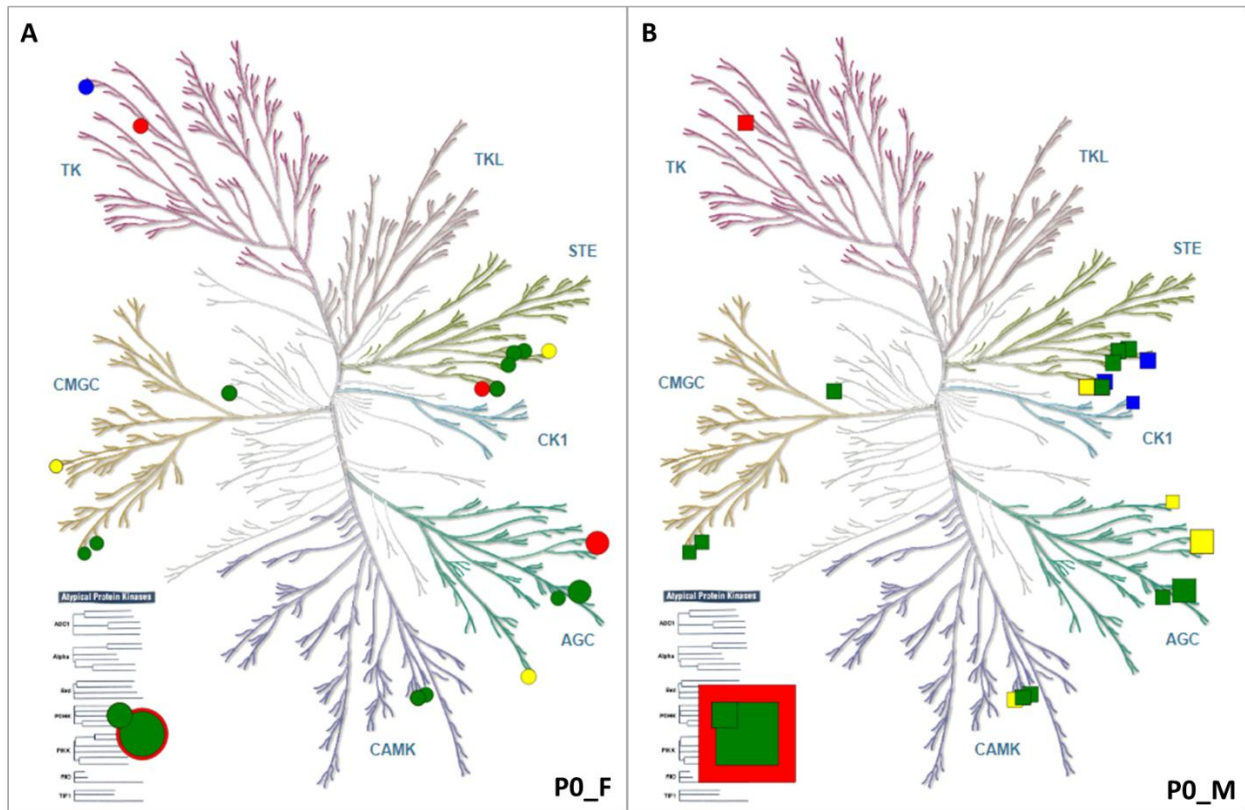
Supplementary Table 8: List of predicted kinases identified by NetworKIN. Shown in this Table are the predicted kinases for upregulated and downregulated peptides. They are further divided based on sex and the eight time points of the study. The predicted kinases are ranked based on the NetworKIN score. Bold represents the kinases specific to a sex.



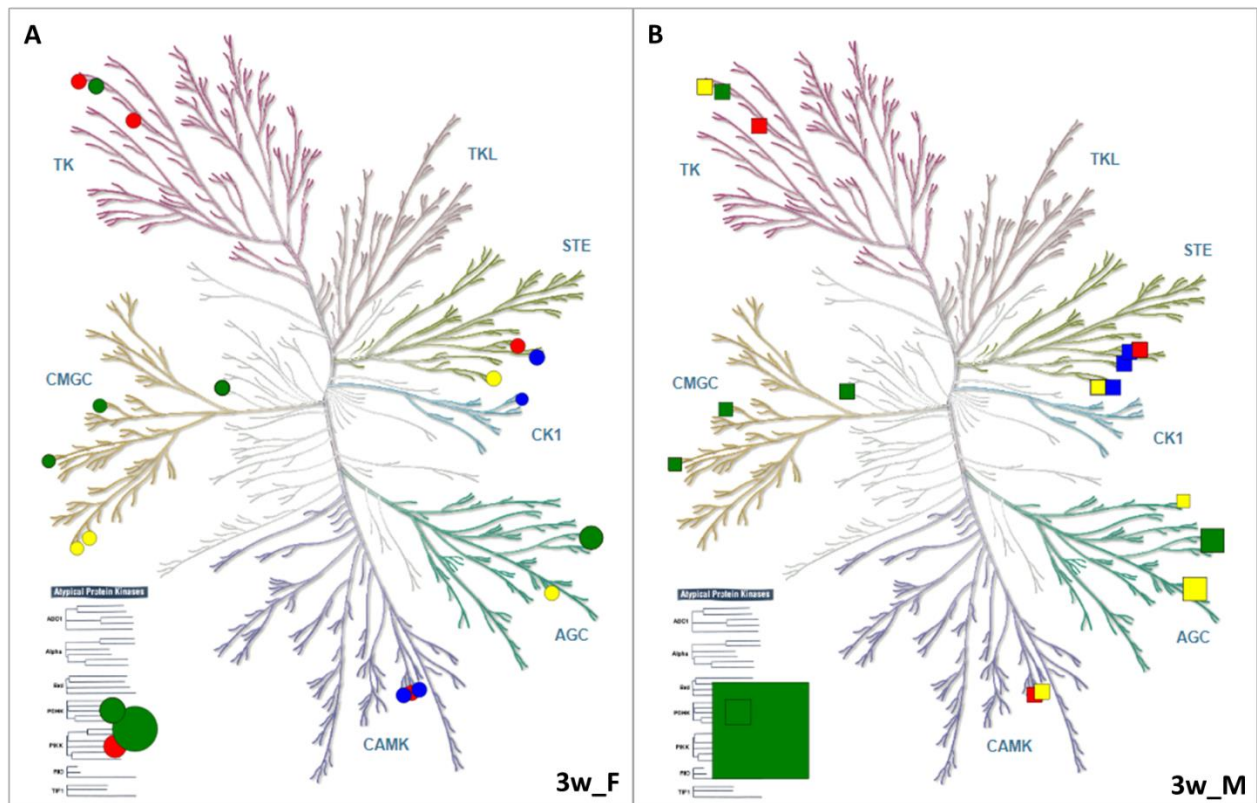
Supplementary Figure 1.1. Identification of candidate kinases predicted to target the upregulated and downregulated phosphosites in the striatal tissue of R6/2 HD mice at embryonic day 9: Dendrogram of the human kinome constructed using KinMap (Eid *et al.*, 2017), highlighting the candidate kinases predicted to target the upregulated and downregulated phosphosites in the whole brain of females (A) and males (B) at embryonic day 9 (E9). Candidate kinases were identified by NetworKIN (Linding *et al.*, 2007) analysis. Red=upregulated, Green=downregulated, Blue=upregulated in either M/F, Yellow= downregulated in either M/F.



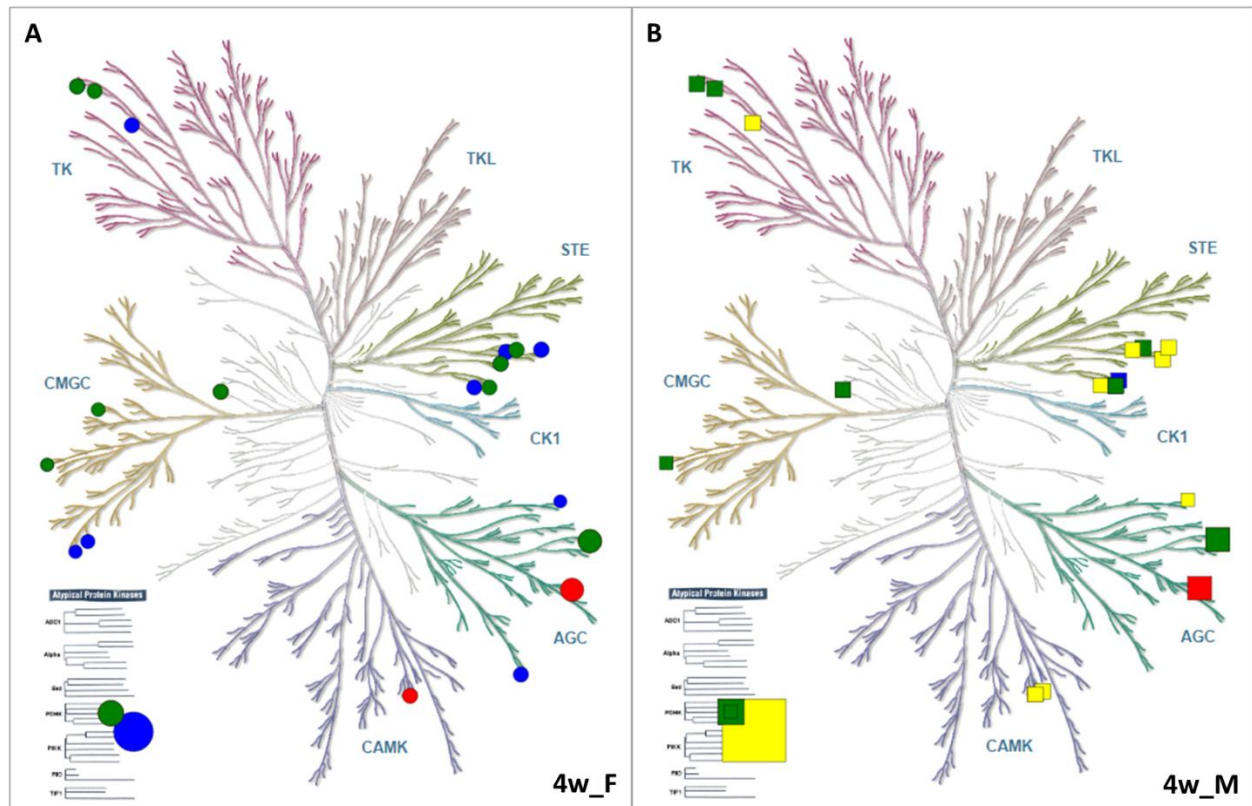
Supplementary Figure 1.2. Identification of candidate kinases predicted to target the upregulated and downregulated phosphosites in the striatal tissue of R6/2 HD mice at embryonic day 14: Dendrogram of the human kinome constructed using KinMap (Eid *et al.*, 2017), highlighting the candidate kinases predicted to target the upregulated and downregulated phosphosites in the whole brain of females (A) and males (B) at embryonic day 14 (E14). Candidate kinases were identified by NetworKIN (Linding *et al.*, 2007) analysis. Red=upregulated, Green=downregulated, Blue=upregulated in either M/F, Yellow=downregulated in either M/F.



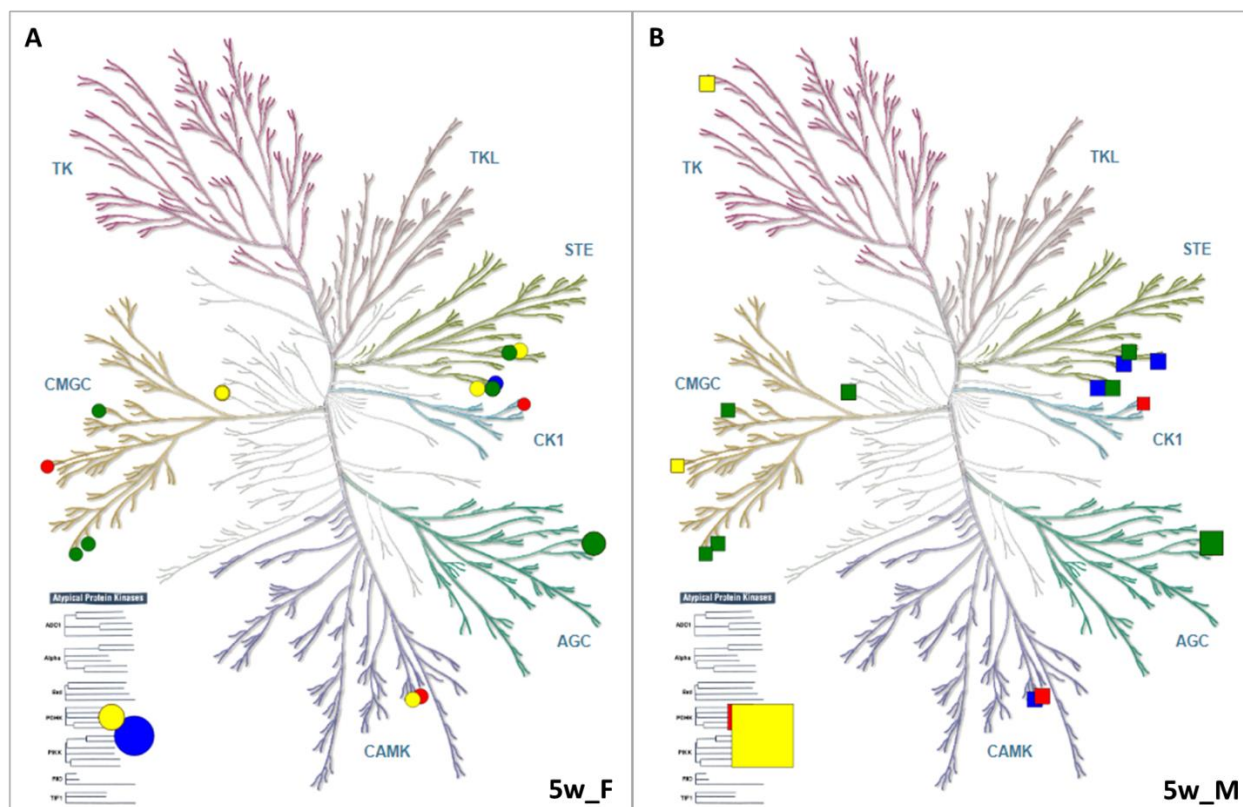
Supplementary Figure 1.3. Identification of candidate kinases predicted to target the upregulated and downregulated phosphosites in the striatal tissue of newborn R6/2 HD mice: Dendrogram of the human kinome constructed using KinMap (Eid *et al.*, 2017), highlighting the candidate kinases predicted to target the upregulated and downregulated phosphosites in the striatal tissue of females (A) and males (B) at birth (P0). Candidate kinases were identified by NetworkKIN (Linding *et al.*, 2007) analysis. Red=upregulated, Green=downregulated, Blue=upregulated in either M/F, Yellow= downregulated in either M/F.



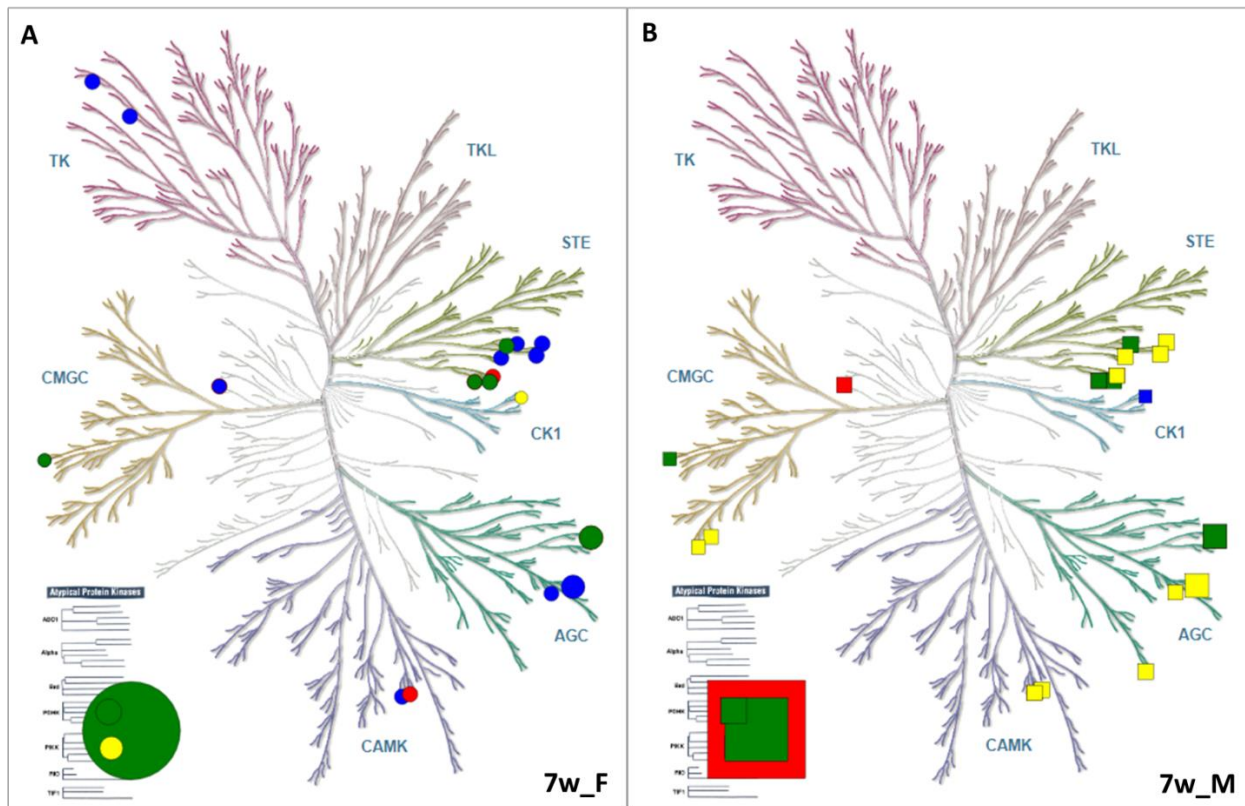
Supplementary Figure 1.4. Identification of candidate kinases predicted to target the upregulated and downregulated phosphosites in the striatal tissue of 3-week-old R6/2 HD mice: Dendrogram of the human kinome constructed using KinMap (Eid *et al.*, 2017), highlighting the candidate kinases predicted to target the upregulated and downregulated phosphosites in the striatal tissue of females (A) and males (B) at week 3 (3w). Candidate kinases were identified by NetworKIN (Linding *et al.*, 2007) analysis. Red=upregulated, Green=downregulated, Blue=upregulated in either M/F, Yellow= downregulated in either M/F.



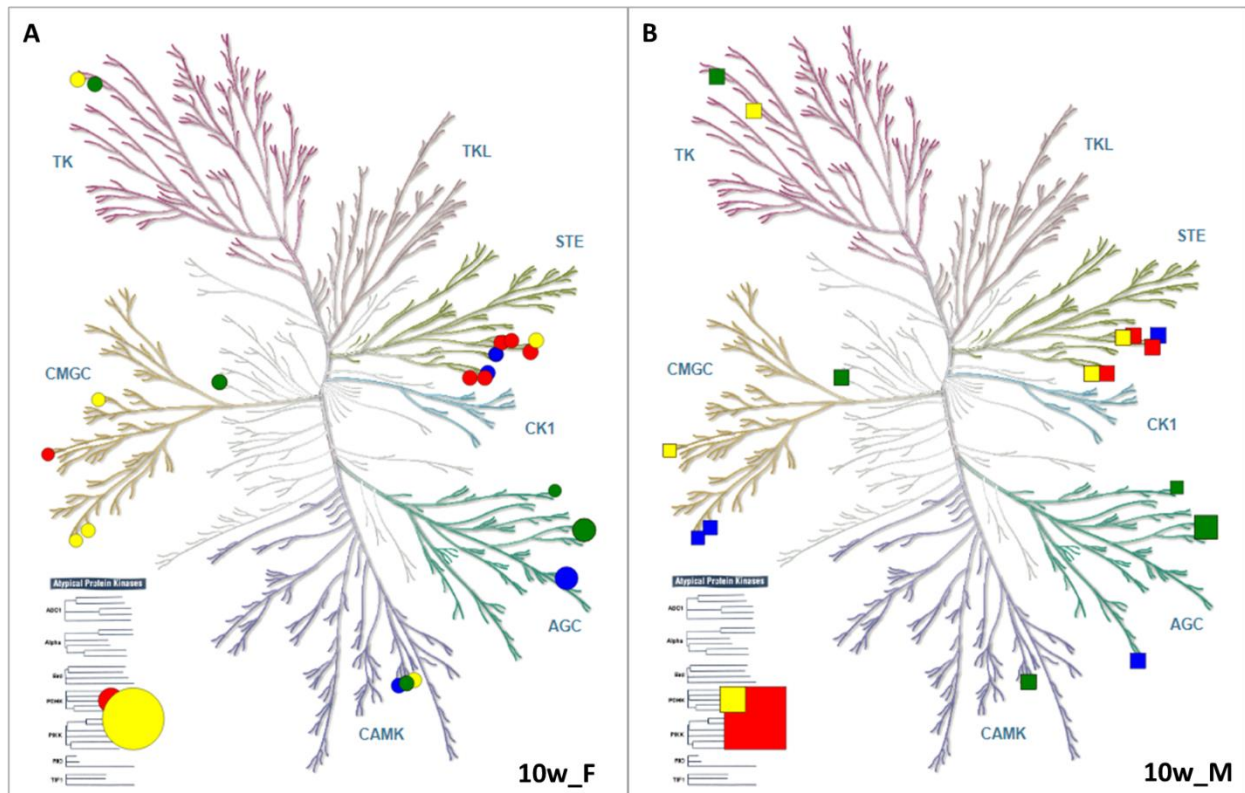
Supplementary Figure 1.5 Identification of candidate kinases predicted to target the upregulated and downregulated phosphosites in the striatal tissue of 4-week-old R6/2 HD mice: Dendrogram of the human kinome constructed using KinMap (Eid *et al.*, 2017), highlighting the candidate kinases predicted to target the upregulated and downregulated phosphosites in the striatal tissue of females (A) and males (B) at week 4 (4w). Candidate kinases were identified by NetworKIN (Linding *et al.*, 2007) analysis. Red=upregulated, Green=downregulated, Blue=upregulated in either M/F, Yellow= downregulated in either M/F.



Supplementary Figure 1.6 Identification of candidate kinases predicted to target the upregulated and downregulated phosphosites in the striatal tissue of 5-week-old R6/2 HD mice: Dendrogram of the human kinome constructed using KinMap (Eid *et al.*, 2017), highlighting the candidate kinases predicted to target the upregulated and downregulated phosphosites in the striatal tissue of females (A) and males (B) at week 5 (5w). Candidate kinases were identified by NetworKIN (Linding *et al.*, 2007) analysis. Red=upregulated, Green=downregulated, Blue=upregulated in either M/F, Yellow= downregulated in either M/F.



Supplementary Figure 1.7 Identification of candidate kinases predicted to target the upregulated and downregulated phosphosites in the striatal tissue of 7-week-old R6/2 HD mice: Dendrogram of the human kinome constructed using KinMap (Eid *et al.*, 2017), highlighting the candidate kinases predicted to target the upregulated and downregulated phosphosites in the striatal tissue of females (A) and males (B) at week 7 (7w). Candidate kinases were identified by NetworKIN (Linding *et al.*, 2007) analysis. Red=upregulated, Green=downregulated, Blue=upregulated in either M/F, Yellow= downregulated in either M/F.



Supplementary Figure 1.8 Identification of candidate kinases predicted to target the upregulated and downregulated phosphosites in the striatal tissue of 10-week-old R6/2 HD mice: Dendrogram of the human kinome constructed using KinMap (Eid *et al.*, 2017), highlighting the candidate kinases predicted to target the upregulated and downregulated phosphosites in the striatal tissue of females (A) and males (B) at week 10 (10w). Candidate kinases were identified by NetworKIN (Linding *et al.*, 2007) analysis. Red=upregulated, Green=downregulated, Blue=upregulated in either M/F, Yellow= downregulated in either M/F.